

A Prototype Radio Detector for the IceCube Surface Enhancement

**Ein Radio-Detektor Prototyp für die Erweiterung des IceCube
Oberflächendetektors**

Zur Erlangung des akademischen Grades eines
Doktors der Naturwissenschaften
von der KIT-Fakultät für Physik
des Karlsruher Instituts für Technologie (KIT)

genehmigte
Dissertation

von Max Renschler (M.Sc.)
aus Rastatt, Deutschland

Tag der mündlichen Prüfung: 13.12.2019

Referent: Prof. Dr. Ralph Engel

Korreferent: Prof. Dr. Marc Weber

Betreuer: Dr. Andreas Haungs

A PROTOTYPE RADIO DETECTOR FOR THE ICECUBE SURFACE ENHANCEMENT

Even after more than a century of extensive research on cosmic rays, important questions remain unanswered. These include the sources of high-energy cosmic rays with energies above 10^{14} eV, their mass composition, and the acceleration mechanisms that boost charged particles to energies far beyond of what mankind has ever reached. The IceCube experiment, located at the geographic South Pole, is the world-leading high-energy neutrino detector. With its surface array IceTop, the IceCube experiment explores cosmic rays up to EeV energies. The IceTop Enhancement will extend the IceTop array with new detectors during the next years. The deployment of radio antennas into the IceTop array was proposed in order to significantly improve the measurements of cosmic-ray air showers, the search for neutrinos with IceCube, the testing of hadronic interaction models and the extension into new research fields like the search for PeV gammas from the Galactic Center.

This thesis focuses on the development of the first prototype radio detector for the proposed IceTop radio extension. This radio detector will be part of a hybrid detector station consisting of scintillation detectors and radio antennas. As an antenna candidate, the SKALA radio antenna was tested and the antenna's low-noise amplifier was characterized for low temperatures down to -70°C . A new antenna mount, suitable for the South Pole environmental conditions, was designed and test deployments were performed within the KIT hybrid engineering array. The characterization of the antenna's low-noise amplifier and measurements of the antennas within the engineering array confirmed the antenna's ability to operate under South Pole conditions. A concept for a hybrid particle and radio data acquisition system (DAQ) was developed and radio front-end electronics were designed, built and characterized to include the radio-antenna readout into the DAQ. Two prototype antennas were deployed at the South Pole together with a first-version hybrid DAQ in January 2019. Latest data received from the deployed antennas at the South Pole prove the functionality of the prototype radio detector and provide important information on the radio background and radio noise emitted from nearby man-made sources. Additional background measurements performed during the antenna deployment at the South Pole indicate that the Galactic noise dominates the radio background at the measurement site for frequencies up to 250 MHz which is an important requirement to decrease the radio energy threshold. Information gained during the development of the prototype radio detectors and from the first radio measurements at the South Pole enable the next steps towards the planned radio detector array for the IceTop Enhancement. The performed tests on the developed prototype show that the designed system can be scaled up to a full, valuable IceCube hybrid detector system for cosmic-ray studies at the South Pole.

EIN RADIO-DETEKTOR PROTOTYP FÜR DIE ERWEITERUNG DES ICECUBE OBERFLÄCHENDETEKTORS

Nach mehr als einem Jahrhundert der Erforschung kosmischer Strahlung sind wichtige Fragen noch immer unbeantwortet. Unklar sind die Objekte der kosmischen Beschleuniger, die Massenzusammensetzung der kosmischen Strahlung sowie die Beschleunigungsmechanismen, die geladene Teilchen zu Energien beschleunigen, die weit über denen liegen, die die Menschheit je erzeugen konnte. Das IceCube Neutrino Observatorium ist der weltweit größte Neutrinodetektor und befindet sich am geografischen Südpol. IceCube trägt mit seinem Oberflächendetektor IceTop direkt zur Vermessung von Luftschauern der kosmischen Strahlung bei. Der IceTop Detektor wird in den nächsten Jahren durch neue Detektoren erweitert (IceTop Enhancement). Die Implementierung von Radiomessungen der ausgedehnten Luftschauer im IceTop Detektor ist geplant. Die Messung von Radiostrahlung kann die Vermessung kosmischer Strahlung, die Suche nach Neutrinos und das Verständnis hadronischer Wechselwirkungsmodelle verbessern und öffnet neue Forschungsfelder, wie die Suche nach PeV Gammastrahlung aus dem galaktischen Zentrum.

Im Laufe dieser Dissertation wurde der erste Prototyp eines Radiodetektors für den Einsatz in IceTop entwickelt. Dieser Radiodetektor ist Teil eines hybriden Detektorsystems bestehend aus Szintillationsdetektoren und Radioantennen. Als Antenne wird die SKALA Antenne verwendet, die während dieser Arbeit getestet wurde. Der Antennenverstärker wurde bis zu tiefsten Temperaturen von -70°C charakterisiert. Eine neue Antennenhalterung wurde entwickelt und innerhalb des hybriden Testdetektors am KIT getestet, um die Antenne im Hinblick auf die besonderen klimatischen Bedingungen am Südpol zu optimieren. Die Charakterisierungsmessungen und erste Radiomessungen mit den Antennen im Testdetektor bestätigen die Tauglichkeit der Antenne für den Einsatz am Südpol. Innerhalb dieser Arbeit wurde das Konzept einer hybriden Datenerfassung entwickelt und Elektronik zur Prozessierung von Radiosignalen entworfen, gebaut und charakterisiert. Zwei Prototyp-Antennen zusammen mit einer ersten Version der hybriden Datenerfassung wurden im Januar 2019 am Südpol installiert. Neueste Daten der Antennen am Südpol beweisen die Funktionsfähigkeit der installierten Detektoren und liefern wichtige Erkenntnisse über die Radio-Untergrundsituation vor Ort und mögliche Störquellen. Untergrundmessungen während des Antennenaufbaus am Südpol zeigen, dass das galaktische Rauschen der dominierende Untergrund im Detektorgelände ist. Dies ist eine wichtige Voraussetzung dafür, die Energieschwelle der Radiodetektion zu verringern. Das Wissen, das während der Entwicklung des Prototyp-Radiodetektors und durch die Analyse erster Messdaten erworben wurde, ermöglicht wichtige Schritte hin zu einem finalen Radiodetektor für IceTop. Die durchgeführten Tests des Prototypen zeigen, dass mit dem entworfenen System ein vollständiger und hochwertiger hybrider Detektor am Südpol realisierbar ist.

CONTENTS

1	INTRODUCTION	1
2	COSMIC RAYS	7
2.1	The cosmic-ray energy spectrum	7
2.2	Extensive cosmic-ray air showers and their detection	11
2.3	Measuring cosmic rays with radio antennas	15
2.3.1	Radio emission in cosmic-ray air showers	15
2.3.2	Benefits of using radio for detecting cosmic rays	17
2.3.3	A radio extension for the IceTop array	19
3	THE ICECUBE NEUTRINO OBSERVATORY	21
3.1	The IceCube detector	21
3.2	IceTop	26
3.3	IceTop Enhancement	29
3.3.1	Scintillator prototype station	30
3.3.2	The benefits of including radio detection into IceTop	32
3.4	Summary	36
4	THE DATA ACQUISITION SYSTEM	37
4.1	A South Pole Data Acquisition System for the IceTop Enhancement	38
4.2	The RadioTAXI DAQ	40
4.3	Implementation of the radio signal processing into the hybrid Radio-TAXI DAQ	41
4.4	The hybrid UberTAXI DAQ	43
4.5	Summary	44
5	THE PROTOTYPE ANTENNA	47
5.1	The measurement of cosmic-ray signals with radio antennas	48
5.2	The SKALA antenna	49
5.3	Mechanical antenna structure	52
5.4	Low-temperature LNA characterization	53
5.4.1	Measurement setup	54
5.4.2	LNA characterization results	57
5.4.3	Network analyzer measurements	59
5.5	Conclusion and remarks	62
6	THE HYBRID ENGINEERING ARRAY	65
6.1	Introducing the hybrid engineering array	65
6.2	The radio array	66
6.3	Radio background measurements	68
6.4	The search for cosmic-ray signals	70
6.4.1	Direction reconstruction of radio signals	71

6.4.2	Beamforming and cross-correlation beam analysis	73
6.5	Conclusion, prospects and remarks	75
7	RADIO FRONT-END ELECTRONICS	77
7.1	Requirements on the radio front-end electronics	77
7.2	A detailed view to the Radio front-end board	79
7.3	Characterization measurements	82
7.3.1	Low-temperature characterization	82
7.3.2	Characterization results	83
7.3.3	Temperature dependencies	85
7.4	Integration into the DAQ system	89
7.4.1	Influence of the front-end electronics on the background noise	90
7.4.2	Test of the full signal chain	91
7.5	Conclusion	97
8	ANTENNA DEPLOYMENT AT THE SOUTH POLE	99
8.1	Deployment of the antennas	99
8.2	Deployment of the DAQ	101
8.3	Station layout after deployment in season 2018–19	102
8.4	Snow accumulation on and around the antenna over time	105
8.5	Hardware failure of the deployed DAQ system	108
8.6	Summary	109
9	RADIO BACKGROUND MEASUREMENTS AT THE SOUTH POLE	111
9.1	Noise in radio measurements	111
9.2	The Cane model and implications for the measured antenna frequency spectrum	113
9.3	Prediction of the measured Galactic-noise frequency spectrum	115
9.4	Background measurements setup	117
9.5	The radio background at the South Pole	118
9.6	Dynamic background spectrum at the South Pole	121
9.7	The search for Galactic noise	122
9.8	Comparison with earlier measurements	126
9.9	Conclusion	127
10	PRELIMINARY ANALYSIS OF RADIO DATA FROM THE PROTOTYPE DETECTORS	129
10.1	Radio waveforms received by the South Pole prototype station	129
10.2	The preliminary background frequency spectrum	132
10.3	Conclusion	136
11	CONCLUSION AND OUTLOOK	139
	Appendix	143
A	APPENDIX	145
A.1	An improved amplification circuit for the radio front-end electronics	145

A.2	Gain measurements with different input attenuation	146
A.3	The calibration source RSG 1000	146
A.4	South Pole antenna transport	147
A.5	Fit Results background measurement time variation	148
A.6	Report of the deployment campaign at the South Pole 2018–19	148

BIBLIOGRAPHY	161
--------------	-----

INTRODUCTION

Starting with the balloon flights of Victor Hess in the year 1912, the exploration of cosmic rays is ongoing for more than 100 years. Cosmic rays are ionized nuclei ranging from single protons up to fully ionized iron nuclei and high-energy photons (gamma rays) that penetrate the Earth's atmosphere. For energies of the primary cosmic-ray particle higher than 10^{14} eV, a direct detection of cosmic-ray particles is not practical anymore due to their decreasing flux. Above this energy, cosmic rays are measured indirectly by measuring the extensive air shower (EAS) they generate in the Earth's atmosphere. Since the first direct detection of cosmic-ray particles by Hess [1] and the detection of air showers in the 1930s by Kolhörster *et al* [2], cosmic rays were measured by large detector arrays up to energies of several 10^{20} eV. The energy spectrum of cosmic rays measured with many different experiments during the last decades follows a power law and shows several spectral features that provide hints on their origin although no individual sources were found until today. The direct measurement of low-energy cosmic rays with $E \leq 10^{14}$ eV using balloon-borne and space-borne detectors shows a mass composition very similar to the solar spectrum and suggests a galactic origin of low-energy cosmic rays. Going higher in energy, cosmic-ray particles can only be measured indirectly due to their decreasing flux by detecting the particle cascade they produce when they interact with matter in the upper atmosphere. The spectrum's index softens at 10^{15} eV [3] which is called the 'knee' of the spectrum followed by a second knee at 10^{17} eV [4]. It is assumed that a transition of galactic to extra-galactic cosmic rays starts at these energies. The actual reason why the galactic cosmic-ray flux decreases is still under discussion. The most promising explanations are a limit of acceleration energy of galactic sources, which are assumed to be mostly supernova remnants, and a loss of high-energy particles into the surrounding space due to a limitation of the galactic confinement that prevents charged particles to leave the Galaxy. A spectrum hardening at 10^{19} eV (the 'ankle') is commonly seen as the final transition of galactic to extra-galactic sources. Recent results of the Pierre Auger Observatory prove an extra-galactic origin of cosmic rays with energies higher than $8 \cdot 10^{18}$ eV [5]. For highest energies above 10^{19} eV, the cosmic-ray flux starts to fall off, which could again be due to a limitation in energy of extra-galactic sources or a result of propagation effects of high-energy particles traveling through the universe. Thus, although great results were obtained during the last decades, many open questions remain like the galactic and extra-galactic sources of cosmic rays, the acceleration mechanisms, the mass composition for high energies and the reason for the suppression of the flux of highest-energy particles. These open questions can only be answered

by improving cosmic-ray measurements not only in sheer number of detected particles but also in more accurate measurements of cosmic rays, especially regarding an improved sensitivity in the mass of the primary particle.

Individual sources, source characteristics, and information about acceleration mechanisms require more information than cosmic rays alone can provide. A more complete picture can be gained when investigating the sky not only in the cosmic-ray channel but also looking for high-energy photons, electromagnetic emission, neutrinos, and gravitational waves [6] in a multi-messenger approach.

The IceCube neutrino observatory located at the geographic South Pole is the world-leading detector of high-energy neutrinos reaching Earth from sources in our Galaxy and from beyond. To achieve this, 1 km^3 of glacier ice in depths deeper than 1400 m under the surface is instrumented with photosensors to detect Cherenkov light emitted by leptons produced in neutrino interactions. IceCube detected the most-energetic neutrinos ever measured with energies of several PeV. By sharing and receiving event alerts with other experiments, interesting objects and events in the universe can be investigated in multiple detector channels enabling a multi-messenger observation. Doing so, one of the first observations of a multi-messenger event succeeded in 2017 initiated by an IceCube alert based on a high-energy neutrino detection coming from the blazar *TXS 0506+056* [7]. IceCube is not only a neutrino detector but also measures cosmic rays with its surface detector array IceTop that covers the 1 km^2 footprint of the IceCube in-ice detector. In the search for astrophysical neutrinos with IceCube, the IceTop detector acts as a veto array to distinguish particles generated by cosmic-ray air showers, the main background in IceCube, from astrophysical neutrinos.

IceTop does not only serve as an important veto detector in the search for neutrinos but itself contributes extensively to cosmic-ray research. The IceTop detector covers an energy range of primary cosmic rays of several TeV up to EeV energies and is therefore sensitive to the very interesting region of the knees and the ankle in the energy spectrum that is assumed to represent the transition between galactic and extra-galactic sources. The unique combination of the IceTop detector and the in-ice detector part allows for a combined measurement of shower particles at the ground level and high-energy muons inside the South Pole ice that are produced in the very beginning of the air shower. This very special combination of measurements of air-showers opens possibilities for improved mass-composition analysis of cosmic rays and can lead to a better understanding of the hadronic interactions happening during the shower development in the atmosphere.

IceTop consists of 162 ice-Cherenkov detectors spread in pairs over the 1 km^2 footprint of the IceTop array. Since the completion of the detector deployment in 2010, the IceTop tanks got buried in snow which affects especially the measurement of the electromagnetic particle component of air showers. To investigate the effect of snow on the existing detectors and to enhance the capabilities of the IceTop array, new detec-

tors are introduced into the surface array during the IceTop Enhancement. Scintillation detectors will be used to measure the particle component of air showers. With these detectors, the effect of snow accumulation on the IceTop tanks can be directly investigated by comparing results from the new scintillation detectors and the buried IceTop tanks.

In addition to scintillation detectors, the deployment of radio antennas is foreseen. Current plans include the deployment of 96 radio antennas inside the footprint of IceTop. The measurement of radio emission, which is generated during the development of the shower through the atmosphere, can heavily increase the abilities of the IceTop array. Radio emission is a direct measure of the shower's electromagnetic component. The radio measurement provides an own estimation of the shower maximum X_{max} and contributes to a second, independent estimation of the shower maximum combining the electromagnetic component measured with radio antennas and the number of muons measured with particle detectors. The shower maximum is an indicator of the nature and mass of the primary particle, so radio detection can directly increase mass-composition accuracy. Also, radio improves the measurement of inclined air-showers: Since radio emission propagates without attenuation through the atmosphere, the detection of radio signals is still possible even if other particle components of the shower already died out on their way to the observation level. This enables, amongst others, the search for PeV-gammas from the Galactic Center which are predicted by measurements of the HESS telescope [8]. The Galactic Center is visible from the IceTop site year-round at an inclination of 61° . Highly inclined gamma-ray showers can be measured and analyzed with a combination of muon detectors and radio antennas. Last, a multi-component measurement of EAS can help to validate current hadronic interaction models that are of great importance for the interpretation of EAS measurements. To lower the energy threshold for radio detection of cosmic-ray signals, the target measurement bandwidth of the IceCube radio extension is with 100–190 MHz higher than the 'usual' measurement bandwidth of 30–80 MHz used by current cosmic-ray radio experiments like Tunka-Rex [9] or the Auger radio engineering array [10]. Assuming the Galactic noise (radio emission generated by sources in our Galaxy and neighboring galaxies) as the dominating radio background, the signal-to-noise ratio can be increased by measuring in higher frequencies since the Galactic-noise spectrum is more steeply falling with frequency than the cosmic-ray induced radio spectrum. The requirement of dominating Galactic noise is essential for a successful measurement at higher frequencies.

The radio technique can help to answer the open questions in cosmic-ray research. To improve the capabilities of radio measurements, going to a higher frequency bandwidths above 100 MHz is necessary that requires a radio-quiet environment which can be found at the South Pole. This work is about the development of a prototype radio detector for the IceTop Enhancement that exploits these higher frequency bandwidths.

Within the frame of this thesis, the deployment of two prototype antennas together with a hybrid particle and radio detector data acquisition system (DAQ) in January 2019 at the South Pole was realized. The Information that were gained during the detector development and from first radio measurements at the South Pole enable next steps towards a deployment of an array of radio detectors in the IceTop array.

As antenna, the prototype version-2 of the SKALA antenna developed by the Square Kilometer Array collaboration [11] is used. The SKALA antenna is a log-periodic dipole array that has a wide bandwidth starting at 70 MHz and a large sky coverage with a good acceptance for signals down to zenith angles of 70° . As the DAQ system, the TAXI DAQ was expanded for the possibility of sampling radio signals of two antennas. The TAXI DAQ is already in use in a prototype scintillation-detector array at the South Pole and digitizes incoming signals using domino-ring-sampler chips (*DRS4*).

A brief introduction into the research fields of cosmic-ray physics and extensive air showers induced by cosmic-ray particles in the atmosphere is given in chapter 2 together with a summary of the detection methods of cosmic rays. A special focus is given to the radio detection of cosmic rays.

Chapter 3 introduces the IceCube experiment and its IceTop detector array. The IceTop Enhancement will be presented in detail together with the prototype scintillation-detector array deployed during the South Pole summer season 2017–18. Again, a focus is given to the implementation of the radio detection into the IceTop array and the improvements radio can provide for the measurements of cosmic rays with IceCube.

Including radio antennas into the IceTop array requires a DAQ system that can process and digitize signals from radio antennas. Signal processing is especially important for the interpretation of radio signals since effects on the measured frequency spectrum can influence the measurement result in a much greater way than it is the case for particle detectors. A concept on how to include the radio-signal processing and digitization into the *DRS4*-based TAXI DAQ system was developed within the frame of this thesis and is presented together with a detailed description of the TAXI DAQ in chapter 4.

The SKALA antenna candidate is introduced in chapter 5. The chapter provides information about the general characteristics of the antenna and presents a new antenna mounting structure that was designed within the frame of this thesis. Due to the special environmental conditions prevailing at the South Pole, the antenna mounting has to withstand extremely cold temperatures, high UV radiation and should not get buried in snow within several years. These considerations require a new design of the antenna mounting usable for a several-years long operation at the South Pole. Tests and characterization of the antenna, especially the antenna's low-noise amplifier, were performed before the antenna deployment to confirm the antenna's ability to operate under South Pole conditions. The characterization of the low-noise amplifier down to -70°C will be presented in the last section of chapter 5.

To perform test measurements with new prototype detectors for the IceCube Enhancement, the IceScint scintillation detectors and the SKALA radio antennas, and to test and improve the detector DAQ, a hybrid engineering array was deployed within the frame of this thesis. The possibility to make first measurements with the SKALA antennas in the engineering array, test DAQ systems and prepare the antenna deployment were key steps for the deployment of prototype antennas in January 2019. The hybrid engineering array will be introduced in chapter 6 with a special focus on radio measurements performed with SKALA antennas.

To be able to digitize radio signals with the TAXI DAQ, new radio front-end electronics were designed during this thesis and are presented in chapter 7. The radio front-end includes bias tees to power the antenna's LNA, filter stages and an additional amplification before the radio signals are digitized with the TAXI DAQ. Extensive characterization measurements of the radio front-end were performed down to -70°C to investigate possible temperature-dependent effects together with tests of the full DAQ system including the radio front-end electronics and the TAXI DAQ.

Two prototype radio antennas together with a hybrid TAXI DAQ were deployed at the South Pole in January 2019. Chapter 8 reports about the details of the deployment and the final layout of the prototype detector station inside the IceTop array. Also, information will be given on the snow accumulation on the antenna structure and around the antenna. These information are important since snow on the antenna metal structure can modify the antenna response and the directive pattern in an uncontrollable way. Snow accumulation around the antenna due to the antenna structure would decrease the time of operation until maintenance is necessary, e.g. a lift of the antenna structure. Both effects should be avoided as good as possible and lessons learned from the deployed antenna structures can improve future versions of antenna mountings.

The radio background is of great importance for every cosmic-ray radio experiment. The proposed decrease of the radio energy threshold for the IceCube radio extension by measuring in a higher bandwidth above 100 MHz is only possible if the radio background at the measurement site is dominated by Galactic noise. Due to this, information about the prevailing radio background inside the IceTop array are of great importance and can directly influence the predicted energy limits of the array. During the deployment of prototype antennas at the South Pole, background measurements were performed which are presented in chapter 9. This includes an analysis of the measured data in regards to contributions of the Galactic noise.

Due to an unforeseeable hardware failure of the deployed RadioTAXI DAQ, the measurement with the deployed radio antennas at the South Pole was only possible starting September 2019. In chapter 10 a first analysis of the most recent data received from the South Pole is presented before the work of this thesis is summarized in chapter 11.

The phenomena of cosmic rays were discovered in the year 1912 by V.F. Hess during several balloon flights up to heights of 5 km [1]. He found the ionizing radiation to increase with height and concluded on radiation penetrating the Earth's atmosphere from space instead of being emitted by the Earth itself as it was the general opinion at that time. The detection of cosmic-ray air showers succeeded by operating Geiger counters with a distance of several meters between the counters in coincidence. W. Kolhörster and P. Auger individually reported on measurements with this setup concluding that secondary particles of a cosmic-ray induced air showers hit the remote detectors at the same time [2, 12].

Since then, cosmic-ray experiments grew significantly, not only in pure size but also in detection methods. In the beginning of cosmic-ray measurements, simple Geiger counters and, after the introduction of photomultiplier tubes (PMT), scintillation detectors were used to detect particles on the ground. Today, a variety of different technologies and detectors is available like particle detectors based on scintillation or Cherenkov radiation with PMT or silicon photomultiplier readout, telescopes measuring air-Cherenkov and fluorescence light emitted during the shower development or the detection of air-showers by their radio emission. The latter is the youngest detection channel in terms of regular operation in experiments.

Below, a brief introduction into the field of cosmic rays and cosmic-ray induced air showers will be given. The applied detection methods in modern cosmic-ray experiments will be introduced focusing on radio detection.

2.1 THE COSMIC-RAY ENERGY SPECTRUM

The energy of cosmic-ray particles is spread over a wide range of energies up to 10^{20} eV, as measurements of the cosmic-ray energy spectrum by various experiments show in Figure 2.1. The energy spectrum is shown for energies from 10^{14} eV for which a direct detection of the cosmic-ray particle is still possible up to the highest energies measured with the biggest cosmic-ray experiments currently operating, the Pierre Auger Observatory located in Argentina and the Telescope Array with its site in Utah, USA. Due to the low flux for high-energy cosmic rays, these experiments measure high-energy cosmic rays indirectly by detecting extensive air showers produced by cosmic-ray particles interacting with matter in the atmosphere. For energies below 10^{10} eV, the spectrum is dominated by the geomagnetic cut-off and solar modulation that prevent charged cosmic rays to reach the Earth [14].

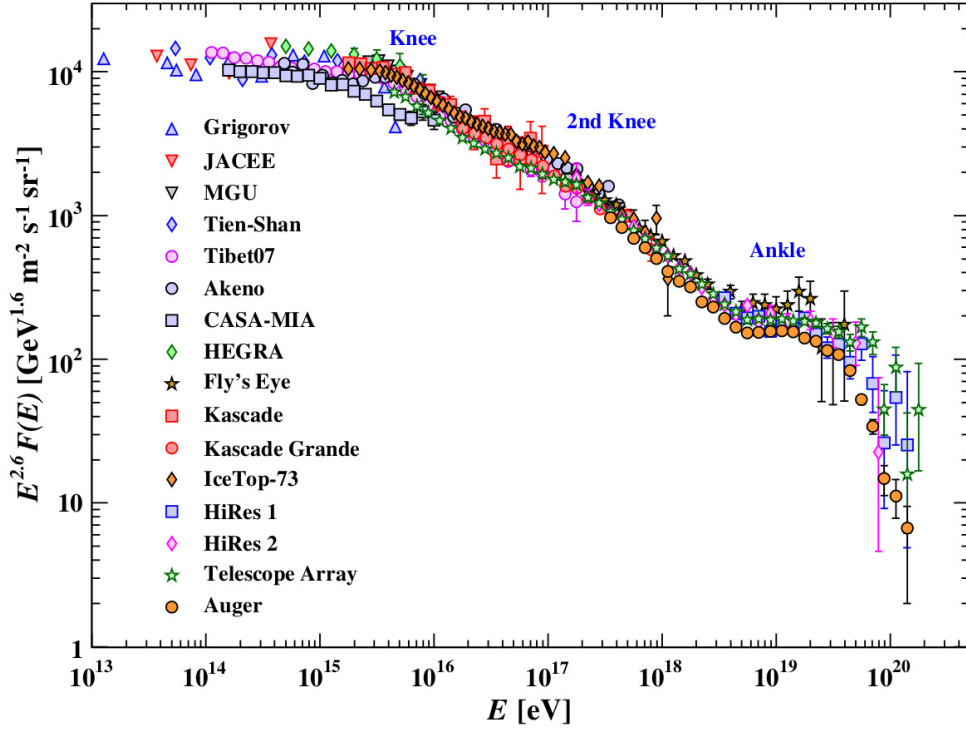


Figure 2.1: The cosmic-ray energy spectrum measured by many experiments over several decades of energy between 10^{14} – 10^{20} eV. (Picture taken from [13])

For higher energies, the cosmic-ray energy spectrum follows a power-law [3] with a changing spectral indices γ of the form

$$\frac{dN}{dE} \sim E^{-\gamma}. \quad (2.1)$$

Cosmic rays with energies below 10^{18} eV can be assumed to be mostly produced in our Galaxy. These cosmic rays are mainly accelerated in supernova remnants up to energies of several PeV. Energies higher than that can be reached by reacceleration of galactic cosmic rays in the galactic wind or by taking other possible sources like γ -ray bursts into account [15]. At energies of about 10^{15} eV (the ‘knee’ in the energy spectrum), the spectral index of the cosmic-ray flux changes from $\gamma = 2.7$ for energies below circa 10^{15} to $\gamma = 3$ after the knee transition energy. A possible explanation is that cosmic rays, which are produced in our Galaxy, are no longer magnetically confined due to their increasing Lamor radius that at some point extends over the expanse of our Galaxy. Since the Lamor radius decreases with the charge of the particle, additional knees should occur for heavier primaries which were observed by the KASCADE-Grande experiment at $8 \cdot 10^{16}$ eV and are shown in the energy spectrum as ‘second knee’ [4]. Alternatively, the spectrum hardening at 10^{15} eV and the ‘second

knee' structure can be interpreted as a limitation in energy of galactic sources. Between energies of 10^{17} – 10^{18} eV a transition from galactic cosmic rays to extra-galactic cosmic rays is assumed [16]. At an energy of $10^{18.5}$, the spectrum softens again to a spectral index of about $\gamma = 2.5$ which is seen as the final transition between a galactic and an extra-galactic origin. This assumption is reinforced by a recent study performed by the Auger Observatory which found a dipole-like anisotropy of the arrival direction of cosmic rays with energies above 8 EeV [5]. The dipole orientation is not aligned with the Galactic plane which indicates an extra-galactic origin of cosmic rays at these energies. Sources of these ultra-high-energy cosmic rays could be active galaxy nuclei (AGNs) and starburst galaxies [17]. At highest energies above 10^{19} eV, the cosmic-ray spectrum steeply falls off which can be explained by a limitation of the maximum acceleration of extra-galactic sources or by the interaction of high-energy protons with the cosmic microwave background (CMB). The latter effect is named after its explorers Greisen, Zatsepin and Kuzmin (GZK) and describes the interaction of high-energy protons with a CMB-photon as

$$p + \gamma_{\text{CMB}} \rightarrow \Delta^+ \rightarrow p + \pi^0 \quad (2.2)$$

$$p + \gamma_{\text{CMB}} \rightarrow \Delta^+ \rightarrow n + \pi^+. \quad (2.3)$$

For heavier nuclei, photo-disintegration would result in a spectrum cut-off around 10^{20} similar to the GZK cut-off for protons [18]. Measurements by the Auger Observatory and the Telescope Array indicate that the spectrum's cut-off follows the behavior predicted by the GZK effect [19] [20]. However, results of Auger show a too heavy mean mass of high-energy cosmic rays at the cut-off energy for explaining the flux suppression by GZK only.

The mass composition for low-energy cosmic rays can be directly measured by balloon-borne experiments like CREAM [24] or space-borne experiments like AMS-02 [25] by measuring the mass and the charge of the cosmic-ray particle as it travels through the detector. The direct measurement allows for a very precise composition measurement of the cosmic-ray particles, as can be seen in the low-energy part in Fig. 2.2 (left). For energies below 10^{12} eV, the flux is dominated by protons (85%) followed by Helium nuclei (12%) and heavier particles (1–2%), electrons, positrons and photons [26].

The flux for high-energy cosmic rays drops significantly which makes a direct measurement of the primary particles impossible. The mass composition of high-energy cosmic rays is measured by detecting extensive air showers (EAS) generated by cosmic rays in the Earth's atmosphere and concluding indirectly on the mass of the primary particle (see the following section 2.2). Thus, mass composition measurements of high energy particles become less accurate. In Fig. 2.2 (left), a global spline fit of the composition of the cosmic-ray flux over several magnitudes of energy is shown for several experiments. In this analysis, the measured spectra of the presented measurements were cross-calibrated to obtain overlapping energy spectra and a common energy scale was fixed using direct measurements [21]. For energies around 10^{15} – 10^{17} eV the fits

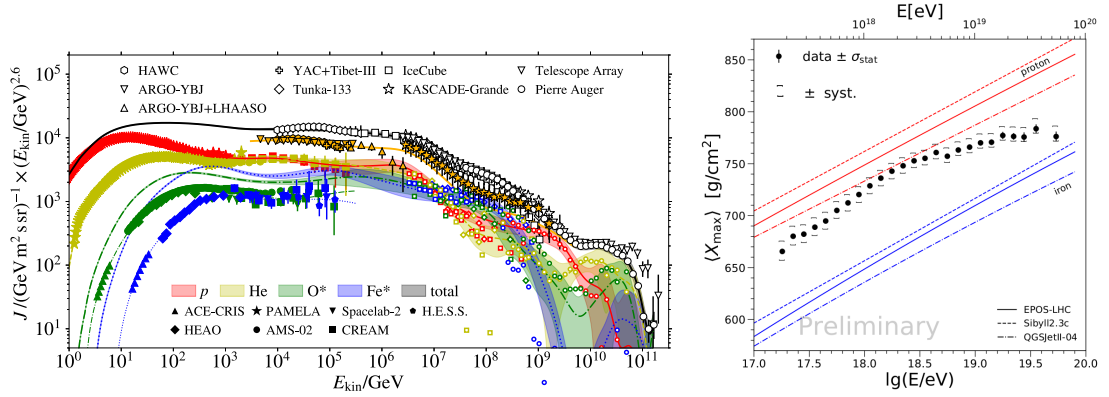


Figure 2.2: **Left:** All-particle flux (black thick solid line), flux contribution by protons (red solid line), helium (yellow dashed line), oxygen group and oxygen elemental (green dash-dotted thick and thin line), iron group and iron elemental (blue dotted thick and thin line). The presented data points are scaled in energy to be able to combine all measurements. Data points of composition measurements from air showers are shown without error bars for clarity. (Figure from [21], updated Figure taken from [22]). **Right:** Average atmospheric depth of the shower maximum measured by the Auger Observatory. (Figure taken from [23])

on the different mass groups show the different particle ‘knees’ which shift to higher energies with heavier particles. This energy range is fully covered by the IceCube experiment and its IceTop surface array that measures cosmic-ray particles with energies between 10^{14} – 10^{18} eV. For energies of 10^{18} – 10^{19} eV, the results indicate a light mass composition of primary particles. This trend is visible in the measurement of the average slant depth of the shower maximum $\langle X_{max} \rangle$, which is an indicator for the mass of the primary particle. In Fig. 2.2 (right), average $\langle X_{max} \rangle$ results measured by the Auger Observatory are shown. In the plot, the measured $\langle X_{max} \rangle$ is shown together with the limits for proton and iron showers simulated with different hadronic interaction models. For energies around 10^{18} eV, the average cosmic-ray mass approaches the proton limit which is also observed by the Telescope Array [27]. For higher energies, the composition measured by Auger shifts again to heavier primaries which is not seen in measurements of the Telescope Array that observes a lighter composition for highest energies than Auger [28]. However, both measurements agree within systematic uncertainties. A comparison of the predicted limits of the hadronic interaction models in 2.2 (right) shows the deviation of the model predictions of the proton and iron limits and the direct influence on the interpretation of the measurement.

After the study of high-energy cosmic rays for several decades, the origin of cosmic rays in terms of single sources is still unknown. This holds also true for the actual acceleration mechanisms which boost cosmic-ray particles to energies several magnitudes higher than what humankind has ever reached in man-made accelerators. One key element is the study of the composition of high-energy cosmic rays which suf-

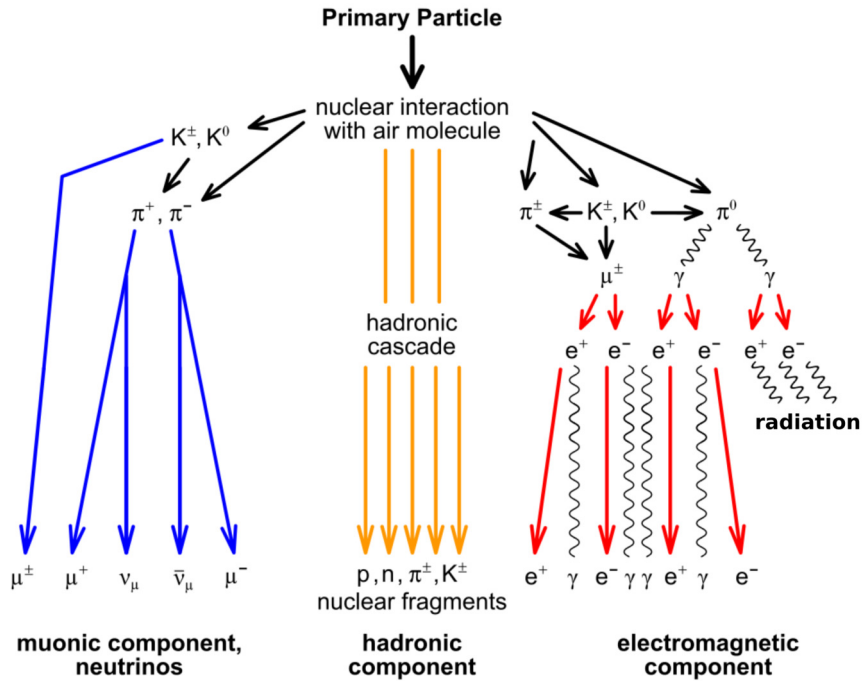


Figure 2.3: Sketch of the subdivision of an EAS into its three components, the muonic component, the hadronic component and the electromagnetic component. The radiation of photons and lower-frequency electromagnetic emission are summarized under the term 'radiation' that is directly connected to the electromagnetic component of the shower. (Figure adopted from [3])

fers from systematic uncertainties and low statistics for ultra-high energy cosmic rays. These open questions can only be answered with more accurate high-energy cosmic-ray measurements.

2.2 EXTENSIVE COSMIC-RAY AIR SHOWERS AND THEIR DETECTION

The flux of primary cosmic-ray particles decreases with energy and the direct detection and measurement of cosmic rays with energies higher than about 100 TeV is not feasible anymore. The properties of high-energy cosmic rays are deduced from the measurement of secondary particles and electromagnetic emission produced by a cosmic-ray particle hitting molecules in the Earth's atmosphere and in secondary processes. When a high-energy cosmic ray interacts with molecules in the upper atmosphere, secondary particles are produced that again interact with atmospheric matter and build up a cascade of secondary particles, an extensive air shower (EAS). An EAS can be subdivided into three components which are shown in a sketch in Fig. 2.3.

In hadronic interactions of the primary particle and its secondary hadronic particles

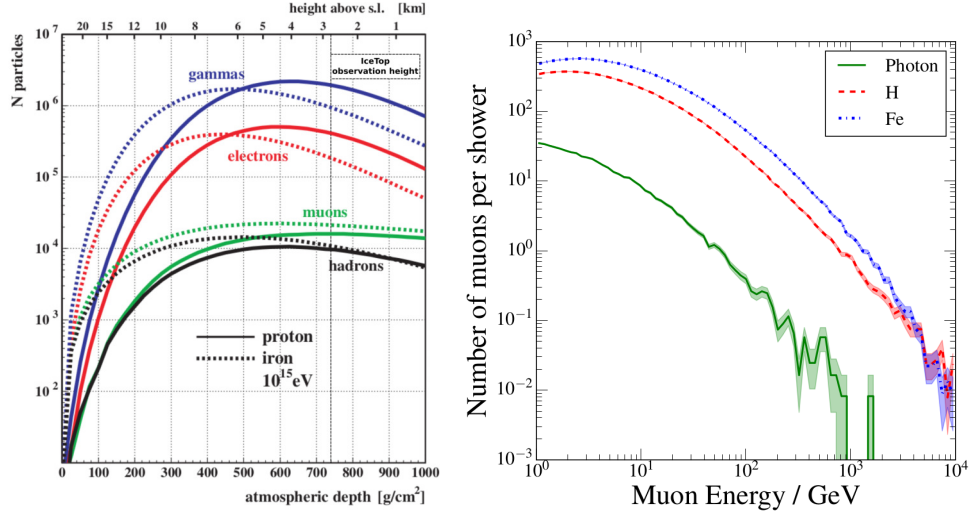


Figure 2.4: Left: Evolution of the average number of shower particles of the three shower components for two shower simulations for a proton and an iron primary particle. The IceTop observation height is circa 2.8 km and included in the plot for comparison. (Figure adapted from [3]) Right: Number of muon particles per muon energy for a nearly vertical 1 PeV proton, iron and photon showers simulated with CORSIKA. (Figure from [29])

with matter in the atmosphere, mostly kaons and pions are produced. Before undergoing further interactions, these kaons and pions can decay into muons and neutrinos which make up the muonic shower component. This is the most penetrating shower component and high-energy muons are the shower particles that can still be detected underground after kilometers of stone, water or ice. Pions and kaons that do not decay form the hadronic shower component together with other hadrons like protons and neutrons. The main part of the primary particle energy, about 90% depending on the energy of the primary particle and the observation height, goes into the electromagnetic shower component that is mainly initialized by the decay of neutral pions into photon pairs. Generated photons then produce electrons via pair-production and generated electrons again produce photons via bremsstrahlung. With this, the number of electrons, positrons, and photons increases up to millions of particles. The electromagnetic cascade stops when the energy of the photons undergoes the threshold for pair production (about 1 MeV). At this point, the number of shower particles reached its maximum and the corresponding depth of the shower in the atmosphere is called the shower maximum X_{max} . Additional electromagnetic emission is generated by electrons and positrons of the electromagnetic component: high-energy electrons with a velocity greater than the speed of light in the air produce Cherenkov radiation, excited Nitrogen molecules emit fluorescence light and charge variations during the showers way through the atmosphere produce radio emission (see sec. 2.3).

The longitudinal shower profile, especially the position of the shower maximum X_{max} ,

is sensitive in the primary particle energy and the mass of the primary particle. The longitudinal profile of an EAS can be described by the Gaisser-Hillas function [30] for the number of electrons N_e per atmospheric depth X that follows

$$N_e(X) = N_e^{\text{max}} \cdot \left(\frac{X - X_0}{X_{\text{max}} - X_0} \right)^{\frac{X_{\text{max}} - X_0}{\lambda}} \cdot e^{-\frac{X_{\text{max}} - X}{\lambda}} \quad (2.4)$$

with the atmospheric depth of the first interaction X_0 and an attenuation parameter for electrons λ that is circa 70 g cm^{-2} . The term $(X_{\text{max}} - X_0)$ is sensitive to the primary energy E_0 and the nature and mass of the primary particle. The term $(X_{\text{max}} - X)$ represents the current development of the shower and increases with the logarithm of the primary energy $\ln(E_0)$. A heavy primary with mass number A can be approximated as A individual nuclei with a reduced energy of each E_0/A . Since the shower maximum X_{max} scales with the logarithm of the energy, X_{max} is proportional to the logarithmic mass of the primary particle $\ln(A)$. In other words, light particles penetrate deeper into the atmosphere before the first interaction, heavy particles develop at smaller atmospheric depths (higher up in the atmosphere).

The effect of this is shown in Fig. 2.4 (left), in which the particle numbers of CORSIKA [31] simulations of 10^{15} eV proton and iron primaries are compared. Since the proton shower penetrates deeper into the atmosphere before the first interaction, the shower maximum shifts to higher atmospheric depths. Absorption effects due to the longer way of the particles through the atmosphere mostly affect the electromagnetic component (e^+ , e^- , γ) compared to the muonic component that is about the same in number of particles for both showers at the detection level. So, the ratio between electrons and muons or the total number of charged particles is a good estimator for the mass of the primary particle. It has to be mentioned, that shower-to-shower fluctuations lead to different depths of X_{max} for individual showers with the same primary particle and introduce systematic uncertainties. For the IceCube experiment with a height of the surface detector of circa 2.8 km , shower-to-shower fluctuations can result in not-yet fully developed showers of high-energy protons at the observation level. Showers initiated by gamma rays develop deeper in the atmosphere than proton showers and are poor in the number of muons. This can be seen in Fig. 2.4 (right) that shows the number of muons over the muon energy for showers with proton, iron, and gamma primary each with an energy of 1 PeV .

Cosmic-ray air showers can be measured using several detection mechanisms in different channels like particle, photon or radio detection. In Fig. 2.5 a sketch of detection methods is shown to summarize the possibilities. The obvious approach is to detect secondary particles which reach the ground, like electrons, muons and hadronic particles, with particle detectors. Usually, scintillation detectors or Cherenkov detectors with a water or ice medium are used for this task. Particle detectors can be buried or shielded to enable a separation of the electron and muon measurement as it was done

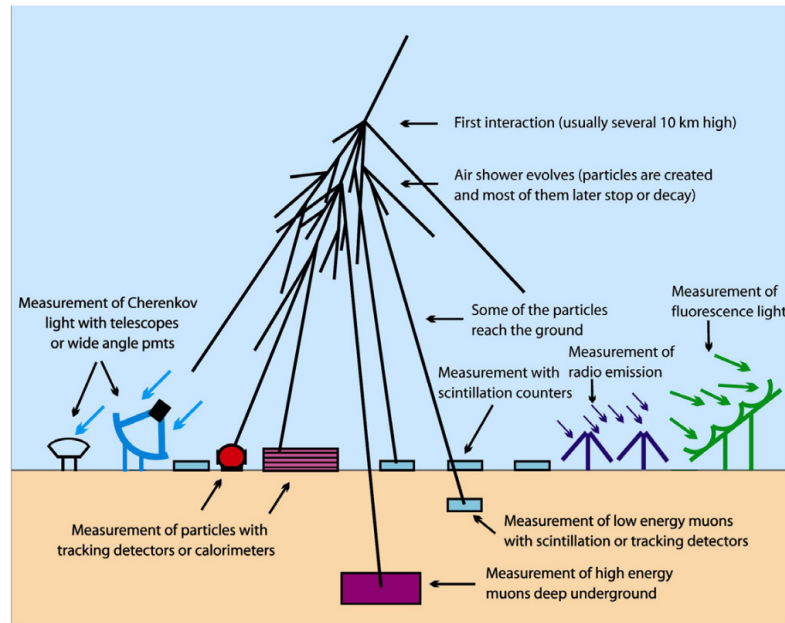


Figure 2.5: Overview of the different technologies to detect particles and radiation from a cosmic-ray air shower (Figure from [32])

for the KASCADE experiment or the AMIGA experiment that is part of the Auger Observatory [33, 34]. Observing the lateral distribution of the air-shower particles on the ground with particle detectors enables the measurements of the direction and energy of the primary particle. The statistical mass composition can be determined by measuring the muon/electron ratio (see Fig. 2.4 (left)) although the results are poor compared to hybrid detector approaches that combine different detection channels like particle and fluorescence light measurements. A more accurate measurement of the longitudinal shower development and especially of the height of the shower maximum X_{\max} is of great importance for the mass composition analysis. This can be obtained by detecting the Cherenkov light emitted by electrons in the shower. A dedicated imaging air-Cherenkov telescope (IACT) is the High Energy Stereoscopic System (HESS) telescope located in Namibia or the Tunka-133 Cherenkov telescope array that measures Cherenkov radiation of EAS simultaneously with the detection of shower particles and radio emission by the Tunka detector array and its Tunka-Rex radio detector [35]. Also, fluorescence light can be measured that is emitted isotropically by excited nitrogen molecules in the air. Monitoring the fluorescence light emission during the development of the shower through the atmosphere enables a direct measurement of the longitudinal development and the shower maximum. Measuring air showers with particle detectors and fluorescence telescopes is realized in the two largest cosmic-ray experiments, the Auger Observatory and the Telescope Array [36, 37]. The greatest drawback of detecting EAS with Cherenkov or fluorescence telescopes is the very lim-

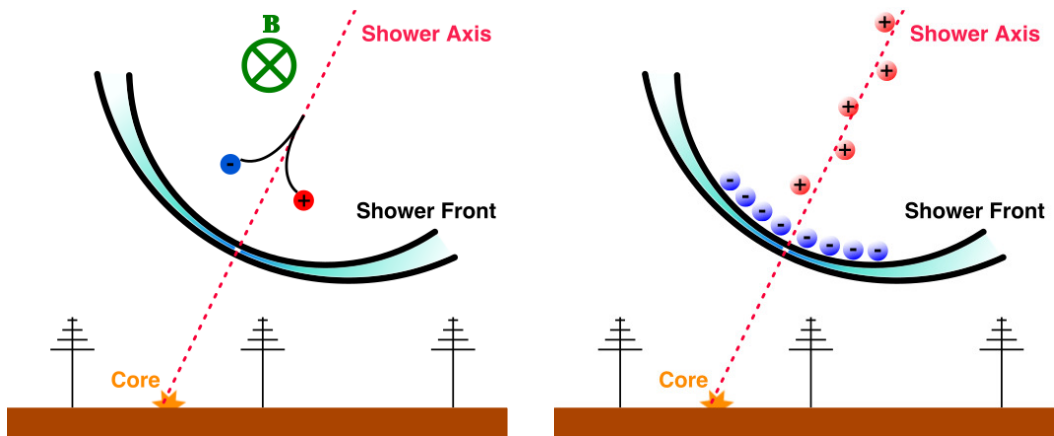


Figure 2.6: The two emission mechanisms of radio radiation during the development of an air shower through the atmosphere. **Left:** Geomagnetic effect. **Right:** Askaryan effect. (Figures from [40])

ited measurement time since these techniques require cloudless and dark nights to operate.

Last, the measurement of air showers with radio antennas evolved during the last decade to a promising new detection channel. The mechanisms of radio emission during the development of an EAS, its detection and benefits of using radio detection compared to other methods will be discussed in the next section.

2.3 MEASURING COSMIC RAYS WITH RADIO ANTENNAS

The idea of detecting EAS using radio antennas was expressed by Askaryan in 1962 [38] and first radio signals from cosmic-ray air showers were detected by Jelly *et al.* in 1965 [39]. Due to the strong requirements on electronics and computing power, it took several decades after the first detection of radio emission until the evolution of digital electronics and signal processing allowed for an precise measurement and accurate interpretation of measured analog signals of the cosmic-ray radio emission. Due to this, radio detection of EAS is still a rather young but advancing field of research and already comes with important benefits for the detection of high-energy cosmic rays.

2.3.1 Radio emission in cosmic-ray air showers

The two main effects of radio emission during an EAS development are the geomagnetic effect and the Askaryan effect which is the one Askaryan originally introduced in 1962 (see Fig. 2.6). For particle showers in air, the geomagnetic effect dominates over the Askaryan effect which contributes only to approximately 10% in the measured radio signal. The geomagnetic radio emission is generated by electrons and positrons

in the air shower which are moving through the Earth's magnetic field. Electrons and positrons are accelerated in opposite directions through the Lorentz force as they move with the shower. During the development of the shower, the number of electrons and positrons deflected by the magnetic field rises until the shower reached its maximum and drops after this resulting in a time-varying net current during the shower process. This leads to electromagnetic emission in the MHz frequency range. The generation of this radio emission is comparable to a Hertz dipole and the radio emission is linearly polarized in the direction perpendicular to the direction of the geomagnetic field. Radio emission generated by the Askaryan effect is the result of a net charge-excess in the shower front. During the development of the shower in the atmosphere, the ambient medium is ionized by shower particles. Since the heavy ionized matter is left behind while the ionization electrons move along with the shower front, a negative charge excess builds up in the shower front that can be as large as 20–30% compared to the total number of electrons and positrons [41, 42]. This charge excess is largest along the shower axis and grows in strength while the air shower develops through the atmosphere until the shower maximum. Due to the emission mechanism, Askaryan radiation is radially polarized towards the shower axis. Askaryan radio emission is a subdominant effect for showers in air but is dominating for showers in dense material. For the lateral distribution of radio emission on the ground and the interpretation of the radio energy in terms of energy of the primary particle, coherency of the radio emission during the development of the air shower plays an important role. If radio radiation is emitted coherently during the shower process, the received electric-field amplitudes scale linearly with the particle number which allows a direct calculation of the energy of the primary particle. Furthermore, coherency highly influenced the lateral distribution of the electric field strength on the ground. Since the refractive index n in the air is not exactly 1 but changes with atmospheric depth up to $n = 1.0003$ at sea level, the velocity of radio waves can be slower than the speed of ultra-relativistic electrons traveling with the shower front. Due to this, radio emission is most coherent and the electric-field strength is highest at the Cherenkov angle of $\theta_C = \cos^{-1}(1/n)$ which is approximately $\theta_C = 1^\circ$ in air. The Cherenkov-ring structure in the radio footprint gets more prominent with increasing observation bandwidth since coherency conditions get sharper for smaller wavelengths. This behavior can be seen in Fig. 2.7 where the lateral distribution of the received power of radio emission is shown over the distance to the shower for several frequency bandwidths simulated with CoREAS [43]. The received power is highest when measured in the Cherenkov ring [41]. The bandwidth of radio emission ranges from low MHz frequencies up to GHz frequencies. In the MHz bandwidth, the dominating, natural radio background originates from sources in our Galaxy and nearby neighboring galaxies, mainly the Galactic Center in our Milky Way as the brightest source of MHz radio emission seen from Earth, and is called Galactic noise. The Galactic noise sets the energy threshold for low frequencies in radio detectors but its strength decreases with frequency. At a certain

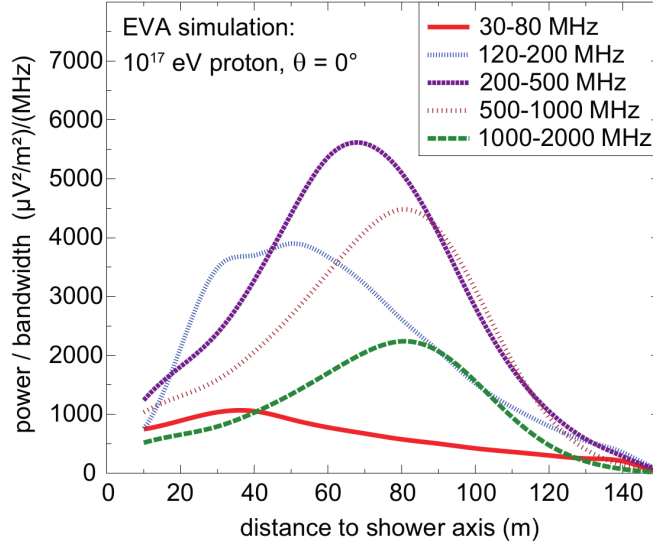


Figure 2.7: Signal strength of the measured radio emission over the distance to the shower core for a vertical proton-shower simulation in different measurement bandwidths. (Figure from [41])

frequency, Galactic noise becomes less dominant than artificial noise that is, in the end, the frequency-independent thermal noise of the measuring electronics. Below this intersection frequency, the EAS radio emission spectrum falls less steeply than the background-dominating spectrum of the Galactic noise. In this frequency range, the energy threshold of radio detection can be lowered by measuring at higher frequencies where the Galactic noise is less strong [44]. This can lower the energy threshold from several tens to hundreds of PeV down to single PeV energies.

2.3.2 Benefits of using radio for detecting cosmic rays

The integration of radio detection into cosmic-ray experiments, especially if it is combined with particle detectors measuring the muonic component, increases the accuracy of the measurement, the mass composition and the number of detected events.

The electric field strength of an EAS radio signal is proportional to the number of electrons that again is proportional to the energy of the primary particle. The radiation energy of an EAS is, therefore, a direct and universal primary-energy indicator. Since the radiation energy of air showers is well-known and can be simulated accurately for different measurement sites, the measured radiation energy does not only improve the actual primary-energy result but can also be used to cross-check the energy scale of different cosmic-ray detectors [45]. This was successfully realized for the Tunka-133 and KASCADE-Grande cosmic-ray experiments by using their radio extensions Tunka-Rex and LOPES [46].

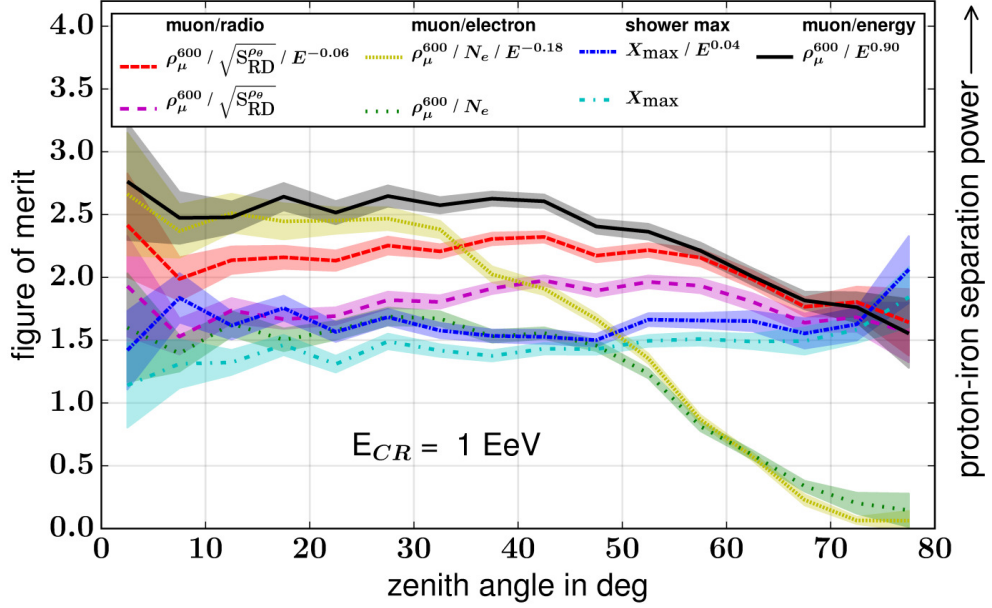


Figure 2.8: Figure of merit for proton-iron separation power of different shower observables and combinations. $\sqrt{S_{RD}^{\rho\Theta}}$ is the radiation energy E_{rad} corrected for dependencies on the arrival direction. Mass estimators are shown with correction for their dependence on the true primary energy and without which provides a more realistic view on the actual separation power. (Figure from [47])

Including radio detection also increases the accuracy of mass-composition studies of the detected air showers. The radio signal of an EAS is sensitive to the depth of the shower maximum X_{max} since this is assumed to dominantly contribute to the received radio signal. So, the radio technique provides an own estimation of X_{max} and also serves as a measurement of the electromagnetic shower component which can be combined with the number of muons measured with conventional particle detectors to estimate a second and independent assumption of X_{max} . By combining both results, the accuracy of the X_{max} measurement can be increased. Unlike any interpretation of shower properties based on particle numbers measured with particle detectors, the radio-signal interpretation is not dependent on hadronic interaction models that are a great source of uncertainty in cosmic-ray measurements. Therefore, the information that radio detectors can add to the overall shower result is less polluted with systematic uncertainties arising from different choices of hadronic interaction models. The radio technique becomes especially powerful at inclined air showers. Here, particle detectors suffer from a dying-out of the electromagnetic particle component of the shower due to the longer way through the atmosphere. When the shower finally reached the ground, only the muonic shower component is left which is insufficient for an accurate mass composition analysis. Radio emission that was emitted during

the shower development until the shower maximum is only slightly attenuated in the atmosphere and can be detected on the ground also for very high shower inclinations. In Fig. 2.8, an analysis of Holt *et al.* shows the improvement in proton-iron separation power when the measured density of muons (ρ_{μ}^{600}) and the measured radiation energy ($\sqrt{S_{RD}^{\rho e}}$) are combined. Especially for zenith angles higher than 30° , a combination of muon density and radiation energy beats the 'classic' approach of comparing the muon and the electron density and remains stable up to highest inclinations of 77° .

2.3.3 A radio extension for the IceTop array

Adding radio antennas to a particle-detector array to measure the radio emission during an EAS comes with various benefits. As it was shown above, radio increases the general accuracy of the cosmic-ray measurement, improves significantly the mass-separation capability of the detector, and increases the sensitivity for highly inclined showers. Although also air-Cherenkov and fluorescence detectors provide these capabilities, the advantage of radio detectors is their high effective measurement time which is only interrupted by thunderstorms and their cost-effective and fast deployment.

This work is about the preparation for the deployment of a radio extension for the IceTop surface array of the IceCube experiment located at the South Pole. This location requires the deployment and operation of radio detectors in a unique environment with extreme temperatures, strict limitation of resources (electrical power) and rough terrain. An easy and fast deployment of detectors in the snow and a guaranteed operation of the detectors especially during the South Pole winter, when temperatures drop to -70°C and physical maintenance is not possible, are additional requirements that play a key role.

In the next chapter, the IceCube experiment will be introduced and plans of adding scintillation detectors and radio antennas to the existing IceTop array will be discussed in detail. With a focus on the abilities of the radio detection, the possible improvements and additional capabilities for the IceTop array coming with a radio extension will be investigated in section 3.3.2.

THE ICECUBE NEUTRINO OBSERVATORY

The IceCube neutrino observatory is a neutrino detector located at the geographic South Pole near the Amundsen-Scott South Pole station. The IceCube experiment measures neutrinos using a 1 km^3 ice volume instrumented with photomultiplier tubes (PMTs) to detect Cherenkov light emitted by secondary particles originating from neutrino interactions with matter. With this, the measurement of neutrinos with energies starting from a few TeV up to PeV energies is possible. These are the most-energetic neutrinos measured until now [48, 49]. In addition to the in-ice detector, IceCube is equipped with a surface detector, IceTop, that is used for calibration and veto purposes for the in-ice detector and contributes to the research of cosmic rays with energies up to several EeV.

3.1 THE ICECUBE DETECTOR

A sketch of the IceCube detector is presented in Fig. 3.1 showing the detector with its different components. Neutrinos are detected using a 1 km^3 ice volume located about 1450 m deep in the South Pole ice. The ice volume is instrumented with 5160 PMTs spread over 86 strings that have been deployed with an average spacing of 125 m in the ice. The strings are equipped with digital optical modules (DOMs) with a vertical spacing of 17 m. Each DOM houses a 25 cm diameter PMT and readout electronics [51]. The instrumented volume starts at a depth of 1450 m leaving the upper ice layer not instrumented to use this as a natural shielding against low-energy muons produced in cosmic-ray air showers. Eight out of the total 86 detector strings are belonging to the DeepCore extension which improves the measurement of low-energy neutrinos down to energies of about 10 GeV [52]. For this, the eight DeepCore strings are deployed as a more dense detector array with a string spacing of 70 m and a vertical spacing of the DOMs of 7 m between ice depths of 2100–2450 m.

Neutrinos are detected with IceCube by measuring charged leptons produced during charged-current (CC) interactions of neutrinos with a target nucleus N or by measuring the cascade generated by the nucleus recoil after a neutral-current (NC) interaction of a neutrino with a target nucleus

$$\nu_l + N \xrightarrow{W^\pm} l + X \quad (\text{CC}) \quad (3.1)$$

$$\nu_l + N \xrightarrow{Z^0} \nu_l + N \quad (\text{NC}). \quad (3.2)$$

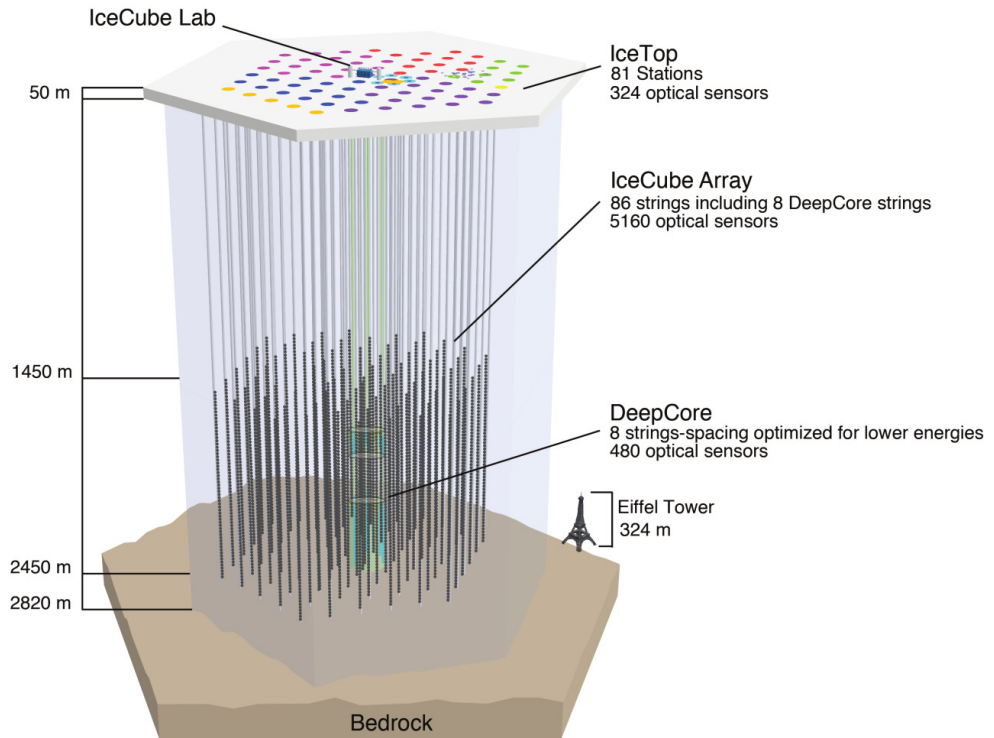


Figure 3.1: Sketch of the IceCube detector showing the in-ice detector and the IceTop surface array. The Eiffel tower is shown for comparison. (Figure from [50])

In CC interactions, a neutrino ν_l produces a lepton of the same family l that propagates through the ice. If the generated lepton exceeds a certain energy threshold it produces Cherenkov radiation. Leptons produced in these reactions can be distinguished by the signals they produce in the detector visible in Fig. 3.2. Muons produce extended track-like events while electrons produce cascade-like events. Taus should be distinguishable from other neutrino generations by detecting a double-bang event showing the tau production and the tau decay as cascade-like events connected by a track-like signature in a resolvable distance if the energy of the tau is large enough [53].

Neutral-current interactions can be performed by all three neutrino generations which leave a cascade-like signal in the detector. In neutral-current interactions, the neutrino deposits some of its energy and momentum in the target particle and leaves the detector again after the interaction. Here, no information can be gained about the primary-neutrino flavor. The direction reconstruction of the primary neutrino works best for the track-like events of muon neutrinos while an energy reconstruction is easiest for fully contained events which are mostly cascade-like events of electrons, low-energy taus, and neutral-current interactions.

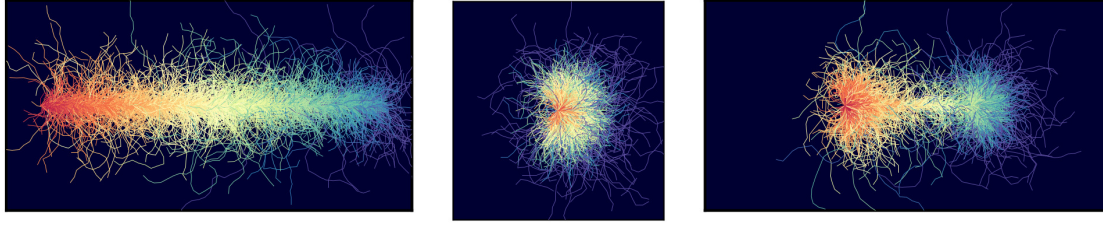


Figure 3.2: Light-emission signatures of muons, electrons and taus produced in a neutrino interaction in the ice. Colors indicate the emission time: red to blue represents early to late photon emission. **Left:** Muon signature (track-like). **Middle:** Electron signature (cascade-like). **Right:** Tau signature (Two cascade-like bumps connected by a track-like signature). (Figures from [54])

Last, high-energy electron anti-neutrinos can be detected by their Glashow resonance signal. A resonant reaction of $\bar{\nu}_e + e^- \rightarrow W^-$ is expected for anti-neutrinos at an energy of 6.3 PeV. The decay of the produces W^- into $\bar{\nu}_\mu \mu$ or $\bar{\nu}_\tau \tau$ pairs would then be visible as a track-like signature of the muon or the tau without a starting cascade-like signature as it would be produced from the remaining nucleus in a CC reaction (nucleus X in formula 3.1).

THE ICECUBE UPGRADE The IceCube detector will be upgraded in the very near future to improve the measurement of low-energy neutrinos and decrease the neutrino detection limit below what is already possible with the IceCube Deep Core. The ‘IceCube Upgrade’ adds seven new strings to the IceCube in-ice detector which are located inside of the IceCube Deep Core area (see Fig. 3.3). The deployment of the upgrade is foreseen for the antarctic summer season 2022–23. The Upgrade strings will have a spacing of 20 m and are equipped with different DOM versions with a spacing on the string of 3 m both of which are circa three times denser than the spacing of strings and DOMs of the Deep Core (75 m horizontal, 7 m vertical). With this, the detection limit for neutrinos can be lowered to GeV energies and various improvements for the standard neutrino search with IceCube are possible. Calibration devices that are deployed on the Upgrade strings enable a deeper investigation of glacier ice properties, which is one of the main sources of systematic uncertainty of current in-ice measurements, and a better understanding of the overall detector response. These results can be applied to old measurements taken with IceCube during the last 10 years to improve the angular and spatial resolution in a reanalysis of the entire data set.

Lowering the energy threshold for neutrino measurements to GeV opens new fields of physics for the IceCube experiment that were inaccessible before. Studies of neutrino oscillation with high sensitivity are possible that profit from the higher event statistics of low-energy neutrinos and the improved spatial resolution of events in the ice. Here,

Gen2 is shown to give an impression of the planned extension. The actual layout, as well as the final size of IceCube-Gen2, is not yet finalized. An increase of detector volume is directly linked to an improved sensitivity in high-energy neutrinos with energies of multiple PeVs which will have a great impact on the neutrino research with IceCube. First, the investigation of neutrino flavor and oscillation becomes easier for high-energy neutrinos. The signature of a tau neutrino, which is a double cascade-like event connected by a track, becomes easier to resolve for higher energies since the track length of the produced tau lepton between the production and annihilation cascade increases. Electron anti-neutrinos can be detected using the Glashow resonance predicting a resonant interaction $\bar{\nu}_e + e^- \rightarrow W^-$ for an energy of the anti-neutrino of 6.3 PeV. An improved investigation of the measured neutrino flavor leads to a better understanding of the neutrino production mechanism in the source. Increasing the sensitivity for high-energy neutrinos can also improve the knowledge of propagation mechanisms of high-energy cosmic rays (protons) through the universe. Protons with energies over 10^{20} eV can interact with photons of the cosmic microwave background (CMB) and produce an additional pion which is called the GZK effect (see equations 2.2,2.3). This mechanism is one candidate explanation of the flux suppression for ultra-high energy cosmic rays. So-called GZK-neutrinos are produced in the pion decay after a GZK reaction with PeV energies. Measuring these GZK neutrinos leads to a better understanding of the cosmic-ray flux suppression at the highest energies and can also give important information about the mass of these cosmic-ray particles.

With an increase of in-ice detector volume, also the IceTop array has to be extended to cover at least the footprint of the in-ice detector. This is improving cosmic-ray measurements from PeV to several EeV energies but also increases the number of events contained in both the IceTop and the in-ice detector. Since atmospheric muons with energies above circa 400 GeV can be measured in the ice and give precious information about the shower development and the primary particle, a higher fraction of contained events and a wider angular acceptance will increase the understanding of cosmic rays.

IceCube-Gen2 might also include the in-ice radio detection of neutrinos with radio antennas which are deployed in holes under the snow surface similar to the IceCube DOMs but in lower depths of only several hundreds of meters. The downward-pointing in-ice antennas detect radio signals generated during neutrino-induced parti-

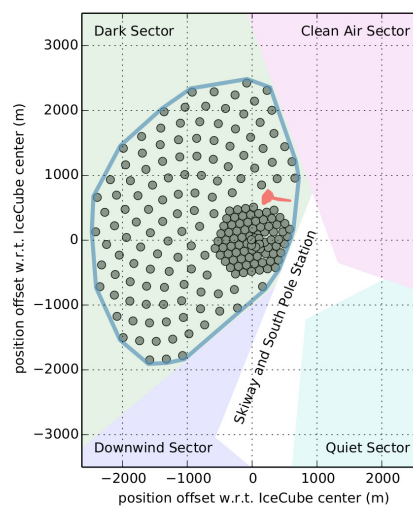


Figure 3.4: Sketch of a possible layout of the next generation IceCube detector, IceCube-Gen2. (Figure from [56])

cle showers in the ice. The radio emission of in-ice particle showers is strongly dominated by the Askaryan effect. Two collaborations, the Askaryan Radio Array (ARA) collaboration [57] and the Antarctic Ross Ice-Shelf Antenna Neutrino Array (ARIANNA) collaboration [58], started efforts on developing this technique of neutrino detection with the aim to cover large ice volumes in the order of hundreds of cubic kilometers with a relative small number of detector stations. ARA prototype stations are located at the IceCube site, ARIANNA stations were deployed on the Ross Ice Shelf in Antarctica. Joint efforts of both collaborations to realize an in-ice radio array at the IceCube site are ongoing [59].

3.2 ICETOP

Since neutrinos are detected via charged leptons produced in neutrino interactions, the main background while searching for neutrino signals are high-energy leptons produced in other interactions, with muons produced in cosmic-ray air showers above the snow surface as the dominating background. To provide a veto for air-shower muons, IceCube consists of an additional surface detector array called IceTop.

The IceTop detector covers the area of the in-ice IceCube detector of 1 km^2 and is located directly above the IceCube strings (see Fig. 3.1). IceTop consists of 81 stations with two ice-Cherenkov tanks each. The IceTop stations are mostly aligned with the in-ice strings with the same station spacing of 125 m and a 10 m distance between the two tanks of a station like it can be seen in Fig. 3.5 [50]. In the middle of the array, three detectors at intermediate positions form an in-fill array together with the surrounding regular-spaced stations for a denser shower sampling.

Two ice-Cherenkov tanks of the IceTop array can be seen in Fig 3.5 (left). Each ice-Cherenkov tank has a height of 1.1 m and an inner diameter of 1.82 m. The tanks are filled with bubble-free ice up to a height of 0.9 m. The tanks inside-walls are coated with a reflective coating made of zirconium dioxide (150 tanks) and Tyvek (12 tanks). For each tank, two PMTs are detecting photons generated in the ice with one in high-gain mode and the other one in low-gain mode. The PMT and readout electronics of the IceTop tanks are the same DOMs as deployed in the ice to minimize efforts for new technology development and infrastructure.

Due to the two-detector station design, each detector can produce two different triggers, a soft-local-coincidence (SLC) trigger if only one of the two detectors of the station detected an event and a hard-local-coincidence (HLC) trigger when an event was detected in both detectors. For a detection of an air-shower event with IceCube, 6 HLC triggers (three triggered detector stations) have to occur in $6 \mu\text{s}$. In normal operation, event data from all detectors with an SLC and HLC trigger are transferred to the IceCube lab. For HLC triggers, additionally, the recorded waveform is sent to the ICL. A global trigger decision is made on the ICL server machines that perform a first rough analysis, select physically interesting events and cut event data (i.e. the recorded

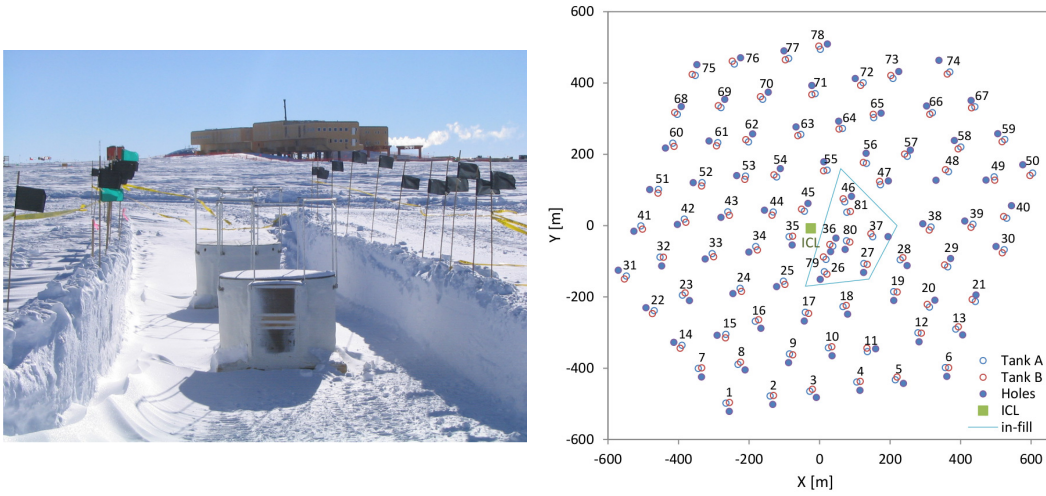


Figure 3.5: **Left:** Picture of a IceTop detector station consisting of two ice-Cherenkov detectors at the South Pole. The Amundsen-Scott South Pole station is visible in the back (Picture from [60]). **Right:** Map of the IceTop stations and the in-ice strings ('Holes'). Each IceTop station consists of two detectors. In the middle of the IceTop array is the IceCube Lab (ICL) (Figure from [50]).

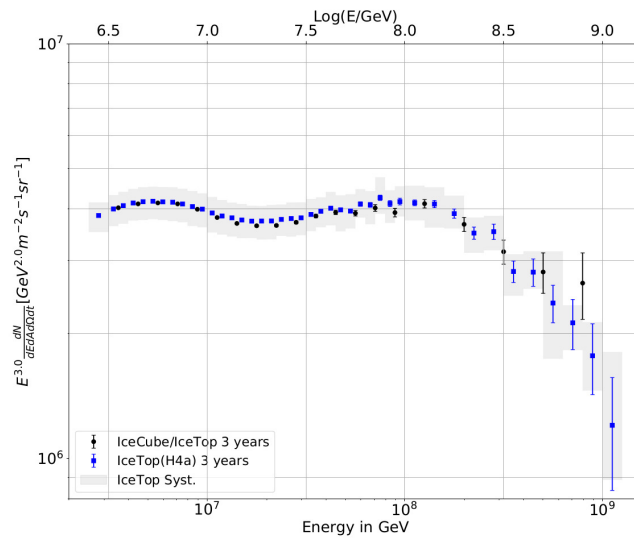


Figure 3.6: Cosmic-ray energy spectrum measured with IceCube after three years of operation. The IceTop-only analysis is shown in blue, the combined analysis of IceTop and the IceCube in-ice detector is shown in black. Due to the harder selection criteria for a combined analysis (e.g. showers have to hit both the IceTop and the in-ice detector), statistics are lower for the combined analysis. (Figure from [61])

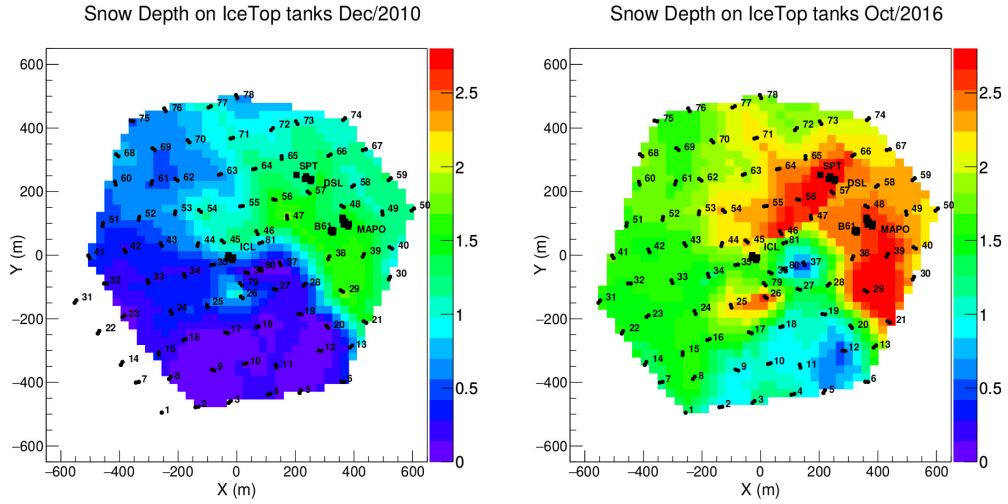


Figure 3.7: Measured height of snow accumulation on the IceTop tanks for years 2010 and 2016. (Figure from [63])

waveforms) depending on the physical interest before transmitting to the North [50]. All recorded events are stored on magnetic tape at the South Pole. In this configuration, the IceTop detector is able to measure cosmic-ray air showers with energies from 300 TeV (100 TeV in the denser infill array) up to EeV energies [62]. Due to the high altitude of the IceTop detector, the shower signal measured in the IceTop tanks is dominated by the electromagnetic shower component. Shower-to-shower fluctuations have the effect that air showers produced by high-energy protons not always reach their shower maximum at the altitude of IceTop.

The unique feature of the IceTop surface array is the ability to measure in coincidence with the IceCube in-ice detectors that add information about shower particles which travel 1450 m through the ice to the overall picture of the measured air shower. At this depth, these are only muons with energies above 400 GeV. A combined analysis profits from the improved direction reconstruction available by measuring the high-energy muon tracks in the ice and a possibly enhanced mass sensitivity if both information are combined. Events with signals in both detectors, of course, need to have a sufficiently low inclination angle to deposit energy in both detectors that limits the number of available events compared to all air showers detectable with IceTop. The cosmic-ray energy spectrum measured with IceCube for three years of operation is shown in Fig. 3.6 for a reconstruction with IceTop alone as well as for a combined analysis of IceTop and IceCube.

During deployment, the IceTop tanks were buried and the tanks top-surface was leveled with the snow to minimize effects of temperature variation and snow accumulation around the tank. Since the snow height is increasing with about 0.2 m per year on average, the IceTop detectors got buried in the snow. In Fig. 3.7, the increase of

snow accumulation on the IceTop detectors is shown that is for some detectors more than 2.5 m until the year 2016. This additional and increasing snow layer affects the measurement results of IceTop and especially increases the energy threshold for measuring cosmic-ray air showers. To investigate the effect of snow accumulation on the IceTop tanks, new scintillation detectors and radio antennas will be introduced into the IceTop array within the IceTop Enhancement.

3.3 ICETOP ENHANCEMENT

To improve the existing IceTop surface array and also to start work on research and development for new detector technologies for a future, extended surface array of the next generation of IceCube, IceCube-Gen2, the existing IceTop array will be equipped with new particle and radio detectors during the next years [64] [65]. The IceTop Enhancement extends the IceTop array by introducing scintillation detectors and radio antennas inside the current footprint of IceTop. The deployment of the IceTop Enhancement will start in parallel with the preparation for the IceCube Upgrade drilling and will be completed afterwards. In addition to particle and radio detectors, the operation of imaging air-Cherenkov telescopes (IceAct) is under discussion [66]. IceAct consists of small telescopes with a 61-pixel SiPM readout that was tested during prototype deployments in the last years at the South Pole [67].

The main motivation of including scintillation detectors into the IceTop array is to investigate the effect of snow accumulation on the already deployed IceTop tanks (see Fig. 3.7) [68]. Snow building up on the IceTop tanks changes the electron-muon fraction measured with the detectors and, with this, manipulates results of the cosmic-ray mass composition. Scintillation detectors are fast and relatively easy to deploy and can be used to investigate this effect by providing a comparison measurement of the same showers without effects of snow above the detectors. Additionally, the proposed scintillation detector improves the measurement of cosmic rays with IceTop. The scintillator array is fully efficient down to energies of 1 PeV and can extend the lower energy threshold of the IceTop detector by an order of magnitude to 10^{14} eV [69]. In Fig. 3.8 (right), the simulated reconstruction efficiency and simulated trigger efficiency compared to the IceTop trigger efficiency indicate the improvement of the trigger efficiency especially for low-energy showers of the scintillation detectors. The radio part of the Enhancement will be discussed in detail in the following section 3.3.2.

In Fig. 3.8 (left), the proposed layout of the Enhancement is shown. The scintillation detectors and radio antennas of the Enhancement are grouped into 32 stations consisting of eight scintillation detectors and three radio antennas. With this, 256 scintillation detectors and 96 radio antennas in total will be added to the existing 162 IceTop tanks. The 32 stations are covering the whole area of the IceTop array and provide a much denser detector spacing than the IceTop tanks alone. One data acquisition (DAQ) system will read out the signals of all eight scintillation detectors and three radio anten-

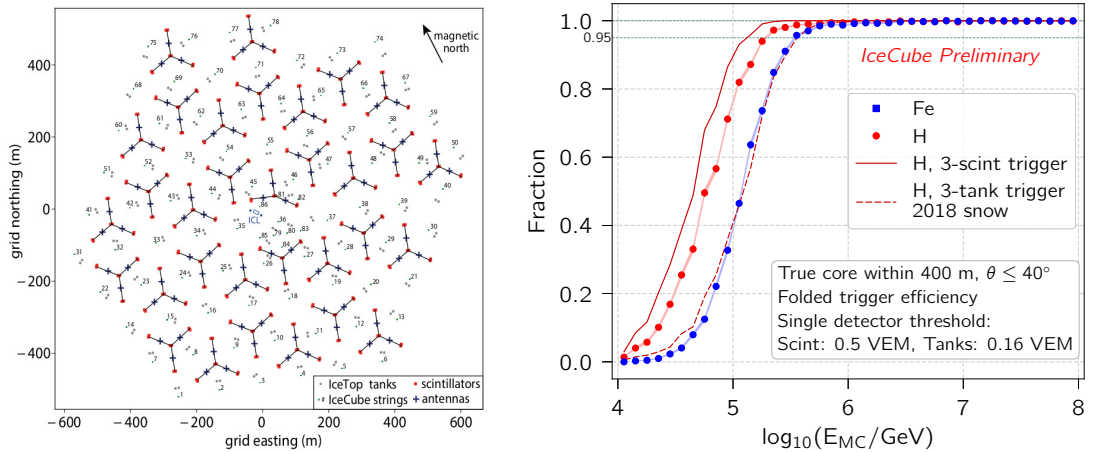


Figure 3.8: **Left:** Proposed layout of the IceTop Enhancement. The map is showing 32 detector stations located inside the footprint of IceTop. Each station consists of eight scintillation detectors (in pairs of two) and three radio antennas in the center of the station arms. **Right:** Simulated reconstruction and trigger efficiency of the scintillation-detector part of the IceTop Enhancement. The reconstruction efficiency is shown for proton and iron primaries. The trigger efficiency is shown for proton primaries for the scintillation-detector array and the IceTop detector array with snow heights of 2018. The same trigger conditions were used for simulating the trigger efficiencies of both detectors to be able to compare the efficiency. (Figure from [70])

nas in each station. For this, the latest version of the TAXI DAQ [71] is used. The TAXI DAQ system will be presented in detail in chapter 4.

A trigger decision is generated per station and recorded signals are then sent to the IceCube Lab main servers. For the final station-DAQ version, it is foreseen that the station trigger can be based on the radio signal, the scintillation-detector events or a mix of both. For this, the fast trigger lines of the eight scintillation detectors and a signal-over-threshold trigger for the six radio channels (two polarizations for each of the three antennas) are evaluated with the DAQs field-programmable gate array (FPGA). Using the full abilities provided by an FPGA, even more advanced trigger decisions i.e. based on a first evaluation of radio data or a radio direction reconstruction on the station level are possible.

The proposed deployment plans of the IceTop Enhancement foresee a deployment of the scintillation detectors, the radio antennas and the DAQ in two phases during the South Pole summer seasons 2020–21 and 2021–22.

3.3.1 Scintillator prototype station

A prototype scintillation-detector station has been deployed in the season 2017–18 that has been extended by two prototype radio antennas in season 2018–19 in the frame-

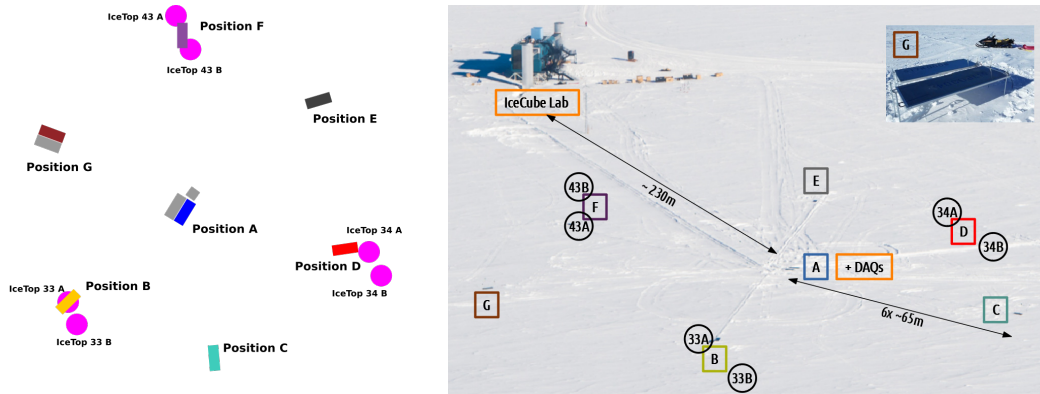


Figure 3.9: Left: Not-to-scale map of the prototype scintillation-detector station deployed in season 2017–18. Right: Aerial view of the prototype scintillation-detector station with marked detector positions of the scintillation detectors and the IceTop detectors. (Figure from [73])

work of this thesis. A map of the deployed scintillation-detector station is shown in Fig. 3.9. The prototype scintillation detector array consists of two different scintillation-detector designs with two different DAQ systems. Both detector systems have a scintillation detector with a silicon-photomultiplier (SiPM) readout in common. The designs differ in the approach when and how to digitize the recorded signals and how detailed the detector output should be. In a first detector design developed by the University of Wisconsin (UW), the detector signals are digitized and integrated directly in the scintillation-detector electronics [72]. If the scintillation detector detects an event, only the timestamp and the integrated charge for different gains are transferred to the DAQ system without the possibility to also record the sampled waveform. The second scintillation-detector type deployed in the prototype station is developed by the Karlsruhe Institute of Technology (KIT) and follows the approach to sample and digitize the detector signals in a central TAXI DAQ [68]. Here, the analog detector signals are transferred to the TAXI where they are sampled and digitized. An integration of the signal is happening in the TAXI FPGA. From here, the integrated charge and also the actual recorded waveform can be sent to the main ICL DAQ. To save bandwidth and storage, the waveform transfer would be switched off in normal operation and would only happen for testing or especially interesting events.

Both detector systems were successfully operating during the year 2018 and cosmic-ray air showers were recorded with both systems in coincidence with the IceTop detector. Coincident events reconstructed with the prototype scintillation detectors and IceTop show comparable direction-reconstruction results with agreements for the zenith and azimuth reconstruction within the limited angular resolution of the prototype station [73]. Test measurements with both detector systems and a comparison of the measurement results and detector abilities led to a final scintillation-detector design for the deployment in the IceTop Enhancement that combines the advantages of both

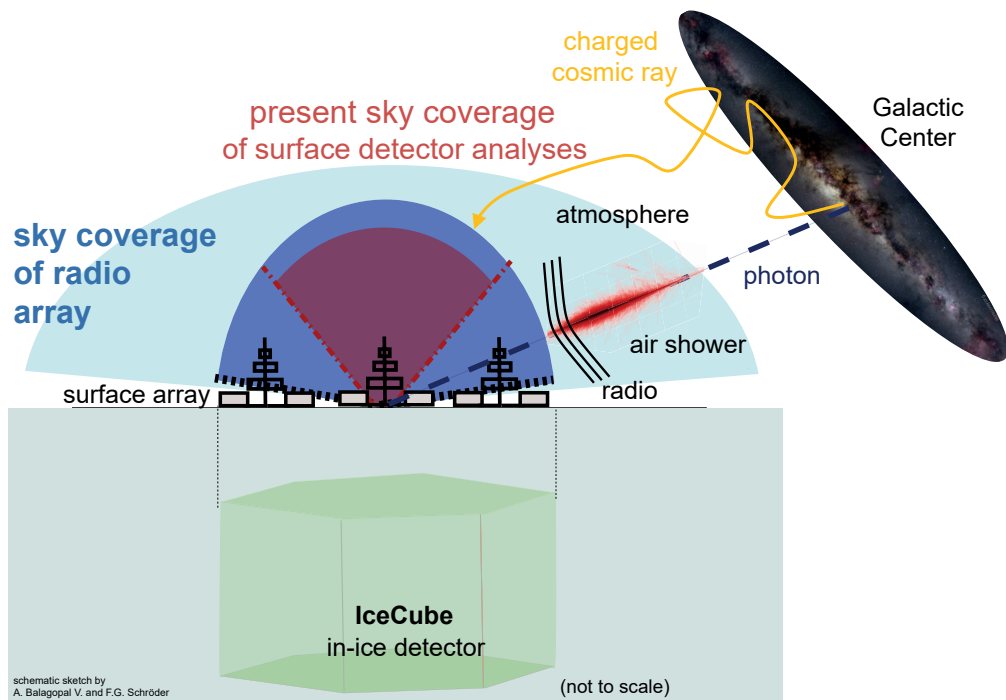


Figure 3.10: Sketch of the sky coverage of the particle and radio detectors with an illustration of the Galactic Center that is visible from the IceTop site year-round at an inclination of 61° . (Figure from [74])

systems. The mechanical detector design, as well as the TAXI DAQ concept (now for sampling and digitizing the signals of three radio antennas), will be taken from the KIT detector design while the detector electronics will be taken from the UW detector design. This decreases the costs and bandwidth consumption of the detectors while leaving the trigger and reconstruction efficiency as proposed. Also, DAQ resources which got available by combining both detector designs can be used for the radio detection of EAS which further reduces the costs for development and deployment of a hybrid particle and radio detector significantly.

3.3.2 *The benefits of including radio detection into IceTop*

The original IceTop detector was planned and build as pure particle-detector measuring cosmic-ray air showers with ice-Cherenkov tanks. First efforts to include a radio detection of cosmic rays into the IceTop array were started with the radio air-shower test array (RASTA) but did not lead to a persistent deployment of radio antennas at the South Pole [75]. The IceTop Enhancement provides a perfect possibility to include state-of-the-art radio detection into the IceTop array while minimizing efforts and costs

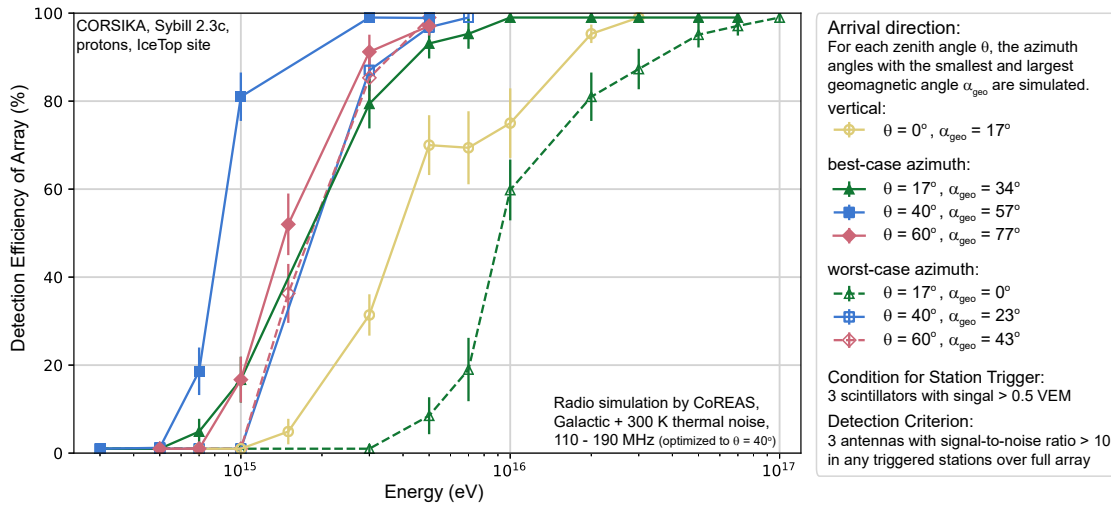


Figure 3.11: Simulation study of the radio efficiency in a measurement bandwidth of 100–190 MHz with Galactic and thermal (300 K) noise contribution for best and worst case scenarios. In the worse-case scenario, the shower direction is parallel to the magnetic field and the geomagnetic effect is mostly disabled. (Figure from [74])

of the radio detectors and their deployment since the radio detection is highly combined with new scintillation detectors.

Combining radio and particle detectors for the search for cosmic rays comes in general with great benefits for the measurement since the radio emission is a direct measure of the electromagnetic component of the shower, improves reconstruction and composition results and is detectable even for highly inclined air showers [41, 42, 47]. Especially for the IceTop detector, radio detection offers rich improvements due to the purpose of IceTop as veto detector and the unique position of the IceTop array at the South Pole.

VETO CAPABILITIES OF ICETOP One of the main purposes of the IceTop array is to veto cosmic-ray events during the search for astrophysical neutrinos. As shown in a sketch of the field-of-views of the different detector types in Fig. 3.10, the sky coverage of the IceTop array will significantly improve if radio antennas can be used for air-shower detection. Particle detectors lose efficiency for inclined air showers since the shower components die out and a trigger generation becomes more difficult. Radio detectors stay efficient until high shower inclinations, e.g. the SKALA antenna as the antenna candidate of the IceTop radio array is sensitive for inclinations up to 70° [76]. Additionally, if an inclined air shower hits the IceCube in-ice detector but cannot be vetoed by IceTop, the shower core lies most probably outside of the IceTop array footprint. Here, radio detection benefits from the increase of the radio-footprint size on the ground that increases a detection probability using radio detectors. Using the ability

of the proposed hybrid-detector and DAQ system to generate trigger decisions also based on radio detectors, hybrid trigger decisions and even more advanced triggers using the DAQ FPGA to pre-process the data are essential to enable these features.

COSMIC-RAY MEASUREMENTS Including radio detectors into a particle-detector array comes with several benefits for the measurements of cosmic-ray air shower. Like it was already mentioned, the radio signal of an air shower is directly linked to the electromagnetic component of the shower and can be used to increase mass-composition accuracy since radio can provide an own estimation of the shower maximum X_{\max} . Here, radio can profit from lower systematic uncertainties compared to particle detectors that have to rely on hadronic interaction models. This feature becomes especially important when inclined air showers are measured for which the electromagnetic particle-component died out before it reaches the ground level. Here, radio detection is the best possibility to measure the electromagnetic component by detecting the radio emission reaching the ground. This enables a mass-composition analysis that else would not be possible. Other possible detector systems like Cherenkov and fluorescence telescopes suffer from a low duty cycle of around 25%, limitations of power consumption and the harsh environmental conditions at the South Pole [77]. Radio detection at the South Pole becomes even more efficient when using a higher frequency bandwidth than the standard band of 30–80 MHz used by LOPES, AEAR (at the Pierre Auger Observatory) or Tunka-Rex. Simulation studies show, that the energy threshold for radio can be lowered significantly when the radio signal is analyzed in a higher frequency bandwidth like 100–190 MHz and the Galactic noise dominates the radio background [44]. The IceCube radio extension would be the first radio detector that exploits higher frequencies for the measurement of cosmic rays and can, therefore, help to expand the knowledge about radio emission during EAS. Besides, it might be the first cosmic-ray radio experiment that can measure radio emission generated purely by the sub-dominant Askaryan effect which happens when showers move parallel to the Earth's magnetic field. In Fig. 3.11, a study on the radio detection efficiency is shown assuming a trigger provided by the scintillation detectors. The detection efficiency, assuming three antennas in all triggered stations with a signal-to-noise ratio greater 10, goes down to PeV energies which is a magnitude lower than former energy limits on radio detection. For this study, the background model and the waveform normalization described by Balagopal *et al.* in [44] were used. Measurements of the radio background at the actual measurement site are essential for refining the energy threshold. Also, the measurement of the radio emission of air showers allows the cross-check and calibration of the absolute energy scale of IceCube with other cosmic-ray experiments measuring the shower's radio component like AERA and Tunka-Rex [45, 46]. More accurate cosmic-ray measurements with radio antennas also help in the measurement of high-energy neutrinos with the IceCube in-ice detector. First, the Ice-Top surface detector is used to calibrate the in-ice detector part by using high-energy

muons generated in an air-shower that travel through the in-ice detector. More accurate air-shower measurements increase the calibration capabilities of IceTop since the expected muon direction, energy and flux can be estimated more precise. Second, neutrinos generated in air showers are one of the main background signals of the IceCube in-ice detector. A better understanding of the atmospheric background is possible with better air-shower measurements and by that will improve IceCube neutrino results.

PEV GAMMAS FROM THE GALACTIC CENTER A cosmic-ray radio detector at the South Pole enables the search for PeV gammas that could be produced in the Galactic Center (GC) [44]. Measurements by the HESS telescope indicate a PeVatron [8] in the center of our Galaxy that can be seen from the IceTop array year-round at an inclination of around 61° (see Fig. 3.10). PeV gammas that are emitted from the GC produce an air shower when they hit the Earth's atmosphere that can be measured with particle detectors and radio antennas. Due to the high inclination of showers from the GC, the particles of the electromagnetic shower component (e^+ , e^-) cannot be measured anymore at ground level which prevents an analysis of the primary-particle mass or type. Using radio detectors, the electromagnetic component can be recovered by measuring the shower's radio emission and a separation between a hadronic primary particle and a high-energy photon is possible. For the latter, a strong electromagnetic component together with a low number of muons is expected since a gamma-ray shower has a strong electromagnetic component but only weak contributions in the muonic and hadronic components. Simulation studies suggest, that several PeV gammas can be measured during a one-year measurement with low PeV energies at which the radio array is fully efficient [44].

HADRONIC INTERACTION MODELS Including radio antennas into the IceTop/IceCube detector will improve possible tests of hadronic interaction models which are one of the weak points in today's cosmic-ray measurements. Since valid data to adjust hadronic interaction models is only available from collider experiments up to energies of about 10^{17} eV, interaction processes during cosmic-ray air showers with higher energies are extrapolated. This comes with systematic uncertainties and deviations from measurement results of current models like a muon deficit for high-energy cosmic-ray air showers in the prediction of the models [78]. The IceCube detector with its IceTop surface array and the IceTop enhancement provides a globally unique detector combination to test hadronic interaction models. IceTop tanks and scintillation detectors together provide information about the muonic and electromagnetic shower components. Radio detectors enable a second, precise measurement of the electromagnetic component and increase the possibility to distinguish proton-initiated showers from heavier primaries. Finally, the IceCube in-ice detector provides unique information about high-energy muons produced in the beginning of the air shower development.

With this set of information, hadronic interaction models can be tested more precise than it is possible with current studies based on an average mass composition [79].

3.4 SUMMARY

The IceCube neutrino observatory is the world-leading high-energy neutrino detector observing galactic and extra-galactic neutrinos of up to several PeVs in energy. The main background during the search for astrophysical neutrinos are muons and atmospheric neutrinos produced during cosmic-ray air showers happening in the South Pole atmosphere and entering the in-ice detector. The IceTop cosmic-ray detector covers the IceCube footprint on the surface to veto cosmic-ray events and to contribute to cosmic-ray science. IceTop is equipped with ice-Cherenkov tanks which got buried in snow throughout the years of operation. With the proposed IceTop Enhancement, new detectors are introduced into the IceTop array to investigate the effects of snow accumulation on the existing detectors, to improve the veto capabilities of IceTop, and to increase the capabilities to study cosmic rays from TeV to EeV energies. The IceTop Enhancement consists of scintillation detectors and radio antennas. Especially the possibility to detect and measure the radio emission from air showers with state-of-the-art technology offers rich improvements for the IceTop array. Among these are a much larger sky coverage to veto cosmic rays for the neutrino search and a more accurate measurement of cosmic-ray air showers with an improved ability to study mass composition. Also, radio improves the test of hadronic interaction models using all available information with a combined IceCube/IceTop analysis and enables the search for PeV gammas from the Galactic Center. The IceTop Enhancement together with the near-future IceCube Upgrade will be important steps towards a new generation IceCube neutrino observatory, the IceCube-Gen2.

Work on research and development began on a radio detector for the IceTop Enhancement during this thesis with the aim to deploy a prototype detector station in season 2018–19. With this prototype, important information about mechanical and conceptual requirements of a radio detector at this unique location can be gained and first measurements of the radio-background situation at the site are enabled which are of great importance for the detector layout and ongoing simulation studies.

THE DATA ACQUISITION SYSTEM

Data acquisition (DAQ) systems convert analog measurement signals like voltage or current into digital values to process and store the measured data. For this, the analog signal is measured in samples of a certain time width, digitized with an analog-to-digital (ADC) converter that has a digitization depth of several bits, and sent to further computing units like field-programmable gate arrays (FPGAs) or CPUs. The sample time width, or the equivalent sampling frequency, defines the frequency resolution of the digitized signal. According to the Nyquist–Shannon sampling theorem [80], the highest resolvable frequency f_{\max} can at maximum be only half of the sampling frequency f_s to obtain all information that can be measured with a f_s frequency resolution:

$$f_{\max} < \frac{f_s}{2}. \quad (4.1)$$

This is especially important for a DAQ measuring radio emission where the bandwidth of the measurement and the recorded frequency spectrum are essential for interpreting the measurement results. The digitizing depth, or sampling depth, of the ADC defines the resolution of the digitized signal. Assuming a 1 V dynamic range of an ADC, a sampling depth of 10 bits leads to a division of the 1 V input range into $2^{10} = 1024$ parts of 1 mV width while a higher sampling depth of 14 bits results in 16384 parts leading to a much finer voltage resolution of 0.06 mV. For radio measurements, in which radio signals are measured over the radio background, the lowest ADC bits are usually monitoring the background noise. The exact number of ‘noise-bits’ depends on the amplification of the radio signal before digitization. Assuming a 14-bit ADC and a radio background that reaches up to the fourth ADC bit, the effective dynamic range for measuring cosmic-ray signals is reduced to 10 bits resembling circa 1000 ADC values. Since the amplitude of the measured radio signal goes linearly with the energy of the primary particle, this roughly resembles a dynamic range of the radio energy measurement of about 1000.

A DAQ system digitizes analog data and sends it to the next-higher processing stage. In addition, it might also produce trigger decisions and communicate with other DAQ systems. I.e. we can think of a DAQ that distributes a trigger signal in case of an event to also collect the data of surrounding detectors. The details of a DAQ system, the conditions that lead to a trigger decision and the trigger distribution and data collecting vary, of course, from experiment to experiment. The IceCube experiment follows the philosophy that individual detector triggers are generated in every single DOM in the ice and in the IceCube tanks and sent to the main DAQ running on the IceCube server

machines on the surface. The main DAQ evaluates the incoming triggers and forms events out of trigger coincidences.

This is different from what is foreseen as DAQ approach on the station level of the IceTop Enhancement. One station of the IceTop Enhancement consists of several detectors of different types (eight scintillation detectors, three radio antennas). Scintillation detectors generate a detector trigger signal when an event occurred in the detector and send a fast trigger signal and the received data via separate lines to the station DAQ. Here, a first trigger decision is taken based on the signals of the eight connected scintillation detectors. Depending on this first decision, data from radio antennas are read out or not and the station event is sent to the IceCube servers. This is especially important regarding the data taking and transmission for radio antennas. Since the whole radio waveform has to be recorded and sent for a proper analysis, a readout of the radio data for every single scintillation trigger would lead to an unreasonable amount of radio data of about 1 TB/day that would have to be sent, at least partly, via satellite link to the northern hemisphere.

The DAQ system operating in the prototype scintillator array at the South Pole (2018), the hybrid prototype array including two radio antennas (2019), and the future stations of the IceTop Enhancement is the TAXI DAQ that will be introduced in detail in this chapter.

4.1 A SOUTH POLE DATA ACQUISITION SYSTEM FOR THE ICETOP ENHANCEMENT

The Transportable Array for eXtremely large area Instrumentation studies (TAXI) [71] DAQ system developed by DESY Zeuthen digitizes incoming detector signals, manages the slow control of connected detectors and communicates with the outside world in all KIT detector stations deployed at the South Pole until now. The TAXI DAQ has been dynamically changing and was adopted to the needs over the time of this thesis depending on the number and type of detectors and requirements on the system by surrounding infrastructure. Before introducing the TAXI DAQ in detail in the following section, a short overview of the different TAXI versions is provided.

The original TAXI DAQ of the first generation is a 24-channel digitizer designed for a 12 V bias voltage. To adapt the TAXI DAQ to South Pole requirements, a second generation of the TAXI DAQ was designed (IceTAXI) that can handle a 24 V operation voltage with the ability to sample eight scintillation detectors. Only the required eight of the 24 input channels were implemented in this version. The IceTAXI was deployed together with the prototype scintillation detectors as their DAQ system in season 2017–18 and was successfully operating for one year. To be able to also read out radio antennas with the TAXI DAQ, a third generation of the DAQ based on the IceTAXI system but with the full number of 24 operating input channels was designed and build (RadioTAXI). The purpose of the RadioTAXI system was to read out eight

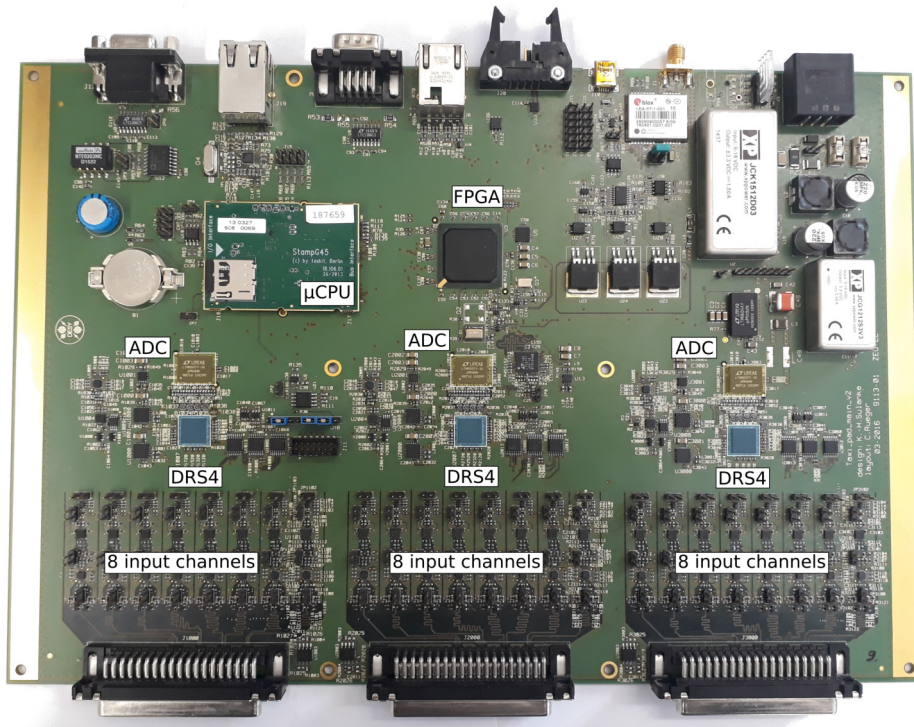


Figure 4.1: Image of the TAXI DAQ board. The TAXI DAQ has 24 input channels that are sampled and digitized using *DRS4* sampling chips with following 8-channel and 14-bit analog-to-digital converters.

scintillation detectors together with two prototype antennas. The RadioTAXI DAQ was deployed together with two prototype antennas in season 2018–19 at the South Pole. For future seasons, the scintillation detectors will digitize the measured signal already in the detector and digitization with the TAXI system is no longer needed. Due to this, a fourth generation of TAXI is under development at DESY Zeuthen that uses all 24 input channels to sample the signals of three radio antennas and provides a digital interface to eight scintillation detectors (UberTAXI). The UberTAXI system will be deployed together with modified scintillation detectors and additional radio antennas in season 2019–20 at the South Pole.

The work during this thesis focused on the third-generation RadioTAXI and included the development and integration of the radio-antenna readout into the DAQ, the preparation of the DAQ for the deployment and the actual deployment of the DAQ in season 2018–19 at the South Pole. If not otherwise noted, the following section relates to the RadioTAXI DAQ.

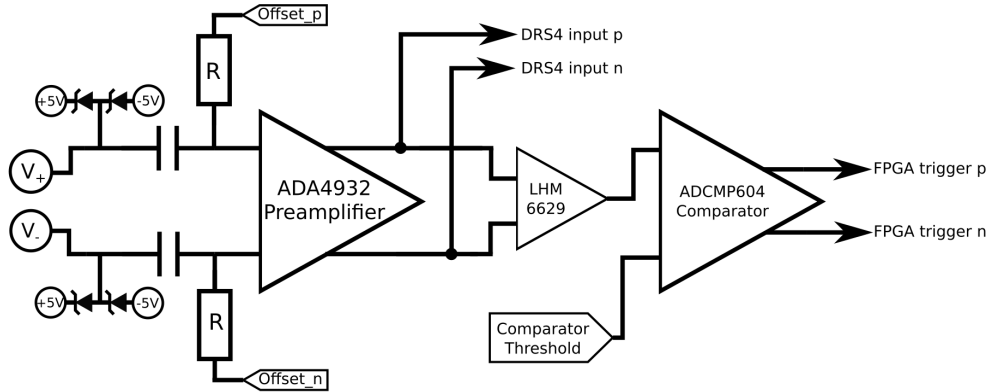


Figure 4.2: Simplified sketch of a TAXI input channel. The TAXI analog input is the same for scintillation-detector signals and radio-antenna signals.

4.2 THE RADIOTAXI DAQ

The RadioTAXI DAQ is used to sample and digitize the signals of eight scintillation detectors and two radio antennas. In Fig. 4.1 an image of the RadioTAXI board is shown. The RadioTAXI DAQ can sample and digitize 24 input channels in parallel. For this, Domino Ring Sampler *DRS4* chips sample the incoming signal with a variable sampling rate of 0.7–5 GHz [81]. For the operation in the IceTop surface stations, a sampling rate of 1.0 GHz was chosen. Each *DRS4* chip has eight input channels that can be sampled in parallel or can be cascaded to one, two or four effective channels. The TAXI board houses three *DRS4* chips with their input channels grouped to three individual *Sub-D 37* input connectors. Each *DRS4* channel is storing the sampled values in a domino ring buffer with a length of 1024 sampling cells. The *DRS4* is sampling the incoming signal continuously and overwrites old sample information after a ring-buffer cycle of 1024 cells. If a trigger signal is propagated to the *DRS4*, it stops sampling and outputs the content of the sampling cells of all channels with a 33 MHz clock speed. The output can be multiplexed to read out one channel after another or can be realized in parallel to reduce dead time during the readout. For RadioTAXI, the parallel readout of all eight *DRS4* channels in parallel is implemented. To digitize the samples, an eight-channel analog-to-digital converter (ADC) *LTM9007* with a sampling depth of 14 bits is used. The digitized samples are transferred to a *Spartan-6* FPGA.

A simplified sketch of the RadioTAXI analog electronics of one input channel is shown in Fig. 4.2. The differential signal enters the RadioTAXI analog electronics via the input connectors visible in Fig. 4.1. A protection against voltage peaks is implemented with Schottky diodes after the differential-signal inputs. Following this, the input signal is AC-coupled to the further analog circuit. The signal baseline can be adjusted by setting voltage offsets for the positive and the negative signal polarization. The offsets are

set by controlling a digital-to-analog converter (DAC). Regarding the measurement of radio signals, the baseline adjustment is an important feature since radio signals are oscillating around the baseline whereas scintillation detector signals only have a positive signal contribution. Since the TAXI DAQ was primarily designed for measuring photo-multiplier tubes (PMT) and silicon photomultiplier (SiPM) signals, the default baseline is set to the lower edge of the voltage range of the *DRS4* and has to be lifted to half of the voltage range for the sampling of radio signals. Following the baseline-offset inputs, the amplifier *ADA4932* is used as a unity gain amplifier before the signal is split up to the *DRS4* inputs and the comparator. The *ADA4932* amplifier has a bandwidth of 560 MHz when set to an amplification of 1. This bandwidth is sufficient for the targeted frequency range of about 100–190 MHz. If a higher bandwidth is needed, the *ADA4932* amplifier can be replaced by the pin-compatible *ADA4927* with a bandwidth up to 2.3 GHz which was also tested during this thesis (see Fig. 7.12). Leaving the *ADA4932* amplifier, the signal is divided into two paths with one leaving the circuit into the *DRS4* inputs and the other one connected to the following comparator circuit. Before entering the comparator, the signal is amplified with a *LHM6620* amplifier with a gain of 10 and a bandwidth of 900 MHz. The single-ended output signal enters a comparator that produced a trigger signal if the incoming signal is above an adjustable comparator threshold. The trigger signal is sent to the FPGA which handles the trigger processing and the final trigger generation which is then enabling the readout of the *DRS4* sampling chips. Due to this, more complex trigger conditions than just a simple signal-over-threshold trigger can be realized. Most obvious is a coincidence trigger that only enables the *DRS4* readout if a certain number of detectors saw an event.

4.3 IMPLEMENTATION OF THE RADIO SIGNAL PROCESSING INTO THE HYBRID RADIOTAXI DAQ

At the beginning of this thesis, a concept of how to implement the processing of radio signals into the TAXI DAQ was developed which is shown as a block diagram in Fig. 4.3. This hybrid DAQ concept allows the processing and sampling of two radio antennas together with eight scintillation detectors. Implementing radio signal processing into TAXI comes with the need for additional radio-specific electronics like bias tees to power the antenna's low-noise amplifier (see chap. 5), filters, and additional amplifiers. The radio trace length should be long enough to not only record the actual cosmic-ray signal but also as much background noise as possible to improve the analysis of the signal, i.e. the identification of radio frequency interference (RFI) in the signal and a more precise frequency spectrum. Last, the readout of the radio signal sampled with the TAXI *DRS4* sampling chips needs to be triggered by the scintillation detectors using a coincidence trigger to reduce data throughput which would be unrealistically high if the radio data would be recorded for every single scintillation-detector event.

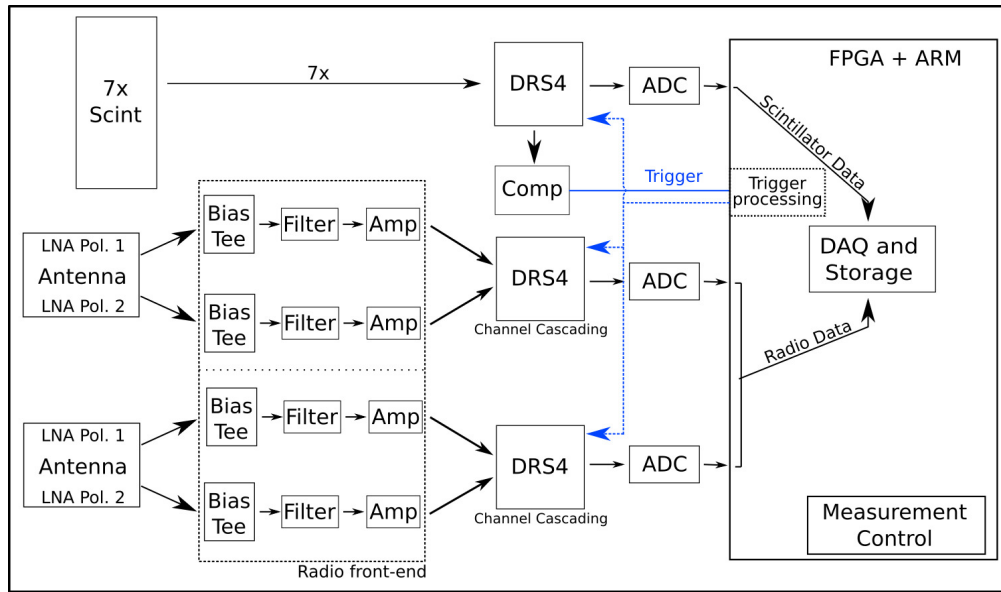


Figure 4.3: Block diagram of the radio signal processing with RadioTAXI. Preamplifiers in the TAXI analog inputs shown in Fig. 4.2 are not included in this block diagram for clarity.

As shown in the block diagram in Fig 4.3, one of the three TAXI *DRS4* chips samples the signals of the seven deployed scintillation detectors. The other two *DRS4* chips sample the signals of two radio antennas with two polarization each. Only the eight input channels of the first *DRS4* (of which seven are connected to scintillation detectors) are equipped with comparators and can generate signal-over-threshold triggers which are transferred to the FPGA. The comparators of the other two *DRS4* inputs have been dismantled to use their FPGA connection as a communication interface between the FPGA and the scintillation detectors. A *DRS4* readout trigger is generated in the FPGA based on coincident scintillation-detector events which resembles an air-shower event. The number of coinciding scintillation-detector events to generate a trigger as well as the coincidence time window can be set remotely. After a trigger decision, a trigger signal is transferred to the *DRS4* trigger inputs to read out the radio and scintillator data of this shower event. The *DRS4* chips sampling the radio signals are driven in channel-cascading mode with a cascading of four *DRS4* channels to one effective channel with a four times larger sampling length of 4096 sampling cells which corresponds to about $4.1 \mu\text{s}$ at a sampling rate of 1.0 GHz. To enable the channel-cascading feature of the *DRS4*, the radio input signal has to be fanned out into the four cascaded *DRS4* channels. The read-out data is digitized with ADCs and transferred to the FPGA which handles the communication with the ARM μCPU of TAXI.

To avoid modifying the actual RadioTAXI printed circuit board (PCB), additional radio-specific components were placed on an extra radio front-end board. One front-end

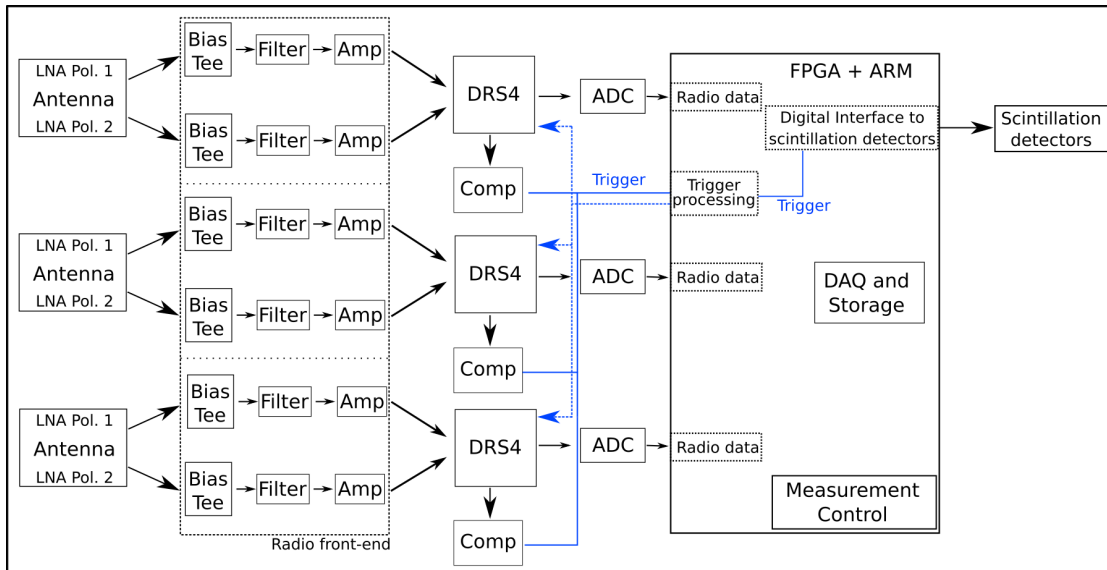


Figure 4.4: Block diagram of the radio signal processing with UberTAXI. Preamplifiers in the TAXI analog inputs shown in Fig. 4.2 are not included in this block diagram for clarity.

board houses two identical circuits for two antenna polarization of one antenna. For each polarization, the front-end electronics include a bias-tee to power the antenna LNA, a protection against electrostatic discharge (ESD), filters and a fanout into four parallel amplifiers. The fanned out and amplified signal is then guided to the Radio-TAXI inputs. The radio front-end electronics, as well as their characterization for low temperatures, will be presented in detail in chapter 7.

The DAQ hardware was designed and developed following this concept and deployed at the South Pole in January 2019.

4.4 THE HYBRID UBERTAXI DAQ

Future designs of the scintillation-detector electronics foresee a digitization of the SiPM signal directly in the detector electronics inside the detector panel. Thus, a fourth generation of the TAXI DAQ is needed that can provide a digital interface to the eight scintillation detectors of one detector station (UberTAXI). This change enables the possibility to add a third antenna to each station by sampling its signals with the first *DRS4* sampling chip that was used for the scintillation detector signals before. A conceptual block diagram of the UberTAXI is shown in Fig. 4.4. In this design, all three *DRS4* chips are used to sample the six polarization of three connected antennas. For each antenna polarization, a comparator provides a signal-over-threshold trigger based on the radio signal that can be evaluated by the UberTAXI's FPGA to make a global trigger decision. Trigger signals of the scintillation detectors are provided

via a fast trigger connection from each scintillation detector to the UberTAXI. Radio and scintillation-detector based triggers can be realized together with more advanced mixed-detector trigger decisions that might be more efficient in some cases, e.g. for the search for PeV gammas from the Galactic Center. Another feature of the UberTAXI is a default baseline at the half of the voltage range of the *DRS4* that is set by applying a common-mode voltage to the output of the *AD4932* amplifier. For the RadioTAXI, lifting the baseline from the lower edge of the *DRS4* voltage range was realized by applying an offset voltage before the *AD4932* amplifier. Due to the higher DC voltage seen by the amplifier using this solution, possible saturation effects of the amplifier might change its frequency behavior, i.e. decrease the amplifiers frequency bandwidth. This possible source of unwanted frequency behavior is disabled when setting the baseline as a common-mode voltage at the amplifier.

With this new TAXI design, also the radio-specific hardware needs to be adapted to the new layout which means especially an expansion of the radio front-end electronics for one more antenna. The future concept foresees a new design of the radio front-end that is capable of processing all three radio antennas with only one additional PCB. The new radio front-end will be directly connected to the TAXI inputs. This saves additional cables and an interface PCB connecting the radio front-end to the TAXI inputs like it is needed for the current RadioTAXI design (see chapter 7). This next version of the radio front-end electronics was under development at the end of this thesis and is not part of this work.

4.5 SUMMARY

The TAXI DAQ system samples and digitizes the analog signals of scintillation detectors and radio antennas of the deployed prototype detector station at the South Pole. The TAXI DAQ can sample 24 analog input signals with sampling frequencies from 0.7–5 GHz and stores the samples in 1024 sampling cells per channel. The sampling cells are digitized using 8-channel ADCs with 14-bit sampling depth. The *DRS4* readout is enabled by a trigger decision based on a signal-over-threshold trigger evaluated by an FPGA. Different generations of the TAXI DAQ were developed over the last years. The current generation-3 RadioTAXI, that was deployed at the South Pole in January 2019 together with two prototype antennas, is equipped with three *DRS4* sampling chips. RadioTAXI digitizes the signals of the seven deployed scintillation detectors with one *DRS4* chip and uses the other two *DRS4* chips to sample radio-antenna signals. The radio-*DRS4* chips are operated in 1:4 channel cascading mode to increase the trace length to 4096 samples per antenna polarization. The trigger decision is based on scintillation-detector events but can be extended in next generations of the DAQ to also take radio events or mixed-detector events into account.

With the new detector electronics of future scintillation detectors, the digitization of scintillation-detector signals in the TAXI DAQ becomes obsolete. In a next generation,

all three *DRS4* chips will be used to sample signals of three antennas. Communication and a fast trigger connection to the scintillation detectors will be realized with a digital interface. Doing so, the integration of radio antennas into the array of the IceTop enhancement will be realized as cost-effectively and straightforward as possible.

THE PROTOTYPE ANTENNA

Radio detectors can improve the IceTop detector in various ways as discussed in sec. 3.3.2. To achieve these improvements, an antenna with a good acceptance for highly inclined signals, a high gain, and a wide bandwidth is needed. Additionally, the antenna structure has to withstand the harsh environmental conditions at the South Pole which consist of very cold temperatures down to -70°C and a high UV radiation. An antenna candidate that fulfills these requirements is the SKALA antenna [82] which is developed by the Square Kilometer Array collaboration [11].



Figure 5.1: Left: SKALA version-1 antenna deployed at KIT. Right: SKALA version-2 antenna deployed at KIT

In the following chapter, the antenna will be introduced and modifications to the antenna's mechanical design to meet the South Pole environmental conditions will be presented. To test the antenna's ability to measure at very low temperatures, the antenna low-noise amplifier (LNA) was characterized at low temperatures down to -70°C . This measurement shall also clarify whether a temperature monitoring and LNA gain correction is necessary for the operation at the South Pole. The characterization results will be discussed in the last section of this chapter and can be found in a bachelor's thesis dedicated to the characterization of the LNA [83].

5.1 THE MEASUREMENT OF COSMIC-RAY SIGNALS WITH RADIO ANTENNAS

Radio emission is produced during the development of an extensive air shower (EAS) in the atmosphere via the geomagnetic effect and the Askaryan effect (see section 2.3). Radio emission propagates nearly without attenuation through the atmosphere and can be measured on the ground using radio antennas. The frequency spectrum of the EAS radio emission is broadband and can be measured in frequencies of a few MHz up to GHz [84]. With the measurement bandwidth also the antenna design changes. In a receiving antenna, a current is induced by an incoming electromagnetic wave in the antenna metal lobes and a voltage can be measured at the antenna terminals. The antenna output impedance for the target frequency bandwidth has to be adjusted to the input impedance of the receiver or the signal cable to minimize losses due to impedance mismatching. The impedance matching can be realized by using, i.e., baluns (balanced-unbalanced transformers) after the antenna terminals. The length of the antenna lobes defines the resonance frequency (or the equivalent resonance wavelength) of the antenna. Regarding a standard half-wave dipole antenna, the resonance wavelength λ_R is defined by the length of the dipole L with $L = \lambda_R/2$. For frequencies that differ from the resonance frequency and are not odd multiples of $\lambda_R/2$, the antenna impedance changes and it comes to an impedance mismatch between the antenna output and the receiver leading to an attenuation for these frequencies. The gain G of an antenna is therefore dependent on frequency and also on the incoming direction of the electromagnetic wave. The frequency-dependent antenna gain is given in zenith and azimuth angles $G(f, \theta, \phi)$. The directional dependence of the gain can be described using directive patterns in which the gain is plotted over the incoming direction of the signal (see Fig. 5.2). For a receiving antenna, the effective area A_{eff} indicates the maximum power P_{max} , the antenna can pick up from a plane wave with a power density S

$$P_{max} = A_{eff} \cdot S. \quad (5.1)$$

The effective area is strongly correlated to the gain of the antenna and, like the gain, dependent on the signal's frequency (or wavelength) and direction

$$A_{eff} = \frac{\lambda^2}{4\pi} \cdot G. \quad (5.2)$$

The effective area has values in the range of several m^2 depending on the antenna, the incoming direction of the signal, and the frequency. For example, the effective area of the SKALA antenna introduced below for a vertical signal at 100 MHz is circa $4 m^2$. The voltage signal received by an antenna is small and has to be amplified. This amplification happens as close to the antenna terminals as possible to decrease noise coupling into signal lines and resistive effects. To achieve this, antennas are equipped with low-noise amplifiers (LNA) directly at the feeding point of the antenna. After the

first amplification with the LNA, the radio signal is sent via coaxial cables to the next electronic stages where it is filtered and additionally amplified, if needed. To power the LNA, bias tees are used that introduce a DC voltage in the signal cable to the antenna. The LNA is powered with this DC voltage and radio signals are sent on top of the DC voltage over the signal line. The DC voltage and the actual radio signal are separated inside the bias tee using a blocking capacitor in the signal way.

5.2 THE SKALA ANTENNA

The *SKA Log-periodic Antenna SKALA* is developed by the Square Kilometer Array (SKA) collaboration for its low-frequency antenna array which shall cover a bandwidth of 50–350 MHz [11]. SKA requirements on its antenna are a high sensitivity, a large sky coverage and low receiver noise which all shall be achieved at low cost and low power consumption. This makes the antenna also very suitable for an operation in a cosmic-ray detector array at the South Pole. The SKALA antenna is at this moment under active development and a final version of the antenna has not been released. However, several prototype versions of the antenna exist and prototype version-1 and version-2 were tested and operated during this thesis (see Fig. 5.1). Prototype version-2 antennas are foreseen to be used as radio antennas for the full surface array with, in total, 96 antennas. Thus, the following introduction will focus on this second prototype version.

THE ANTENNA The SKALA antenna is a log-periodic dipole array (LPDA) consisting of several half-wave dipole elements tuned to different resonant frequencies. The spacing of the dipoles follows a logarithmic function which gives the antenna type its name. Compared to other antenna types used for cosmic-ray measurements like Butterfly antennas, SALLA (short/small aperiodic loaded loop antenna) antennas or dipole antennas, LPDAs cover a large frequency bandwidth, have a high gain and are fairly independent of the ground conditions. Regarding the purpose of the antenna as a cosmic-ray detector measuring very small signals at the South Pole, these characteristics make the antenna an ideal candidate.

For comparison, directive patterns of the SKALA version-2 prototype antenna are shown together with the directive pattern of the SALLA antenna for 90 MHz [85] in Fig. 5.2. The SALLA antenna is a cost-effective and robust antenna with a very low dependency on prevailing ground conditions. The SALLA antenna has been designed for the Tunka-Rex experiment in which it was operated successfully over many years [87], and it was selected for the Auger radio extension [88]. The robust antenna design of the SALLA antenna and the insensitivity to different grounds would make the antenna also suitable for an operation in IceTop but comparing the directive pattern in Fig. 5.2 it is visible that the SALLA antenna has a much smaller gain compared to the SKALA antenna. Additionally, the SALLA gain drops for inclinations higher

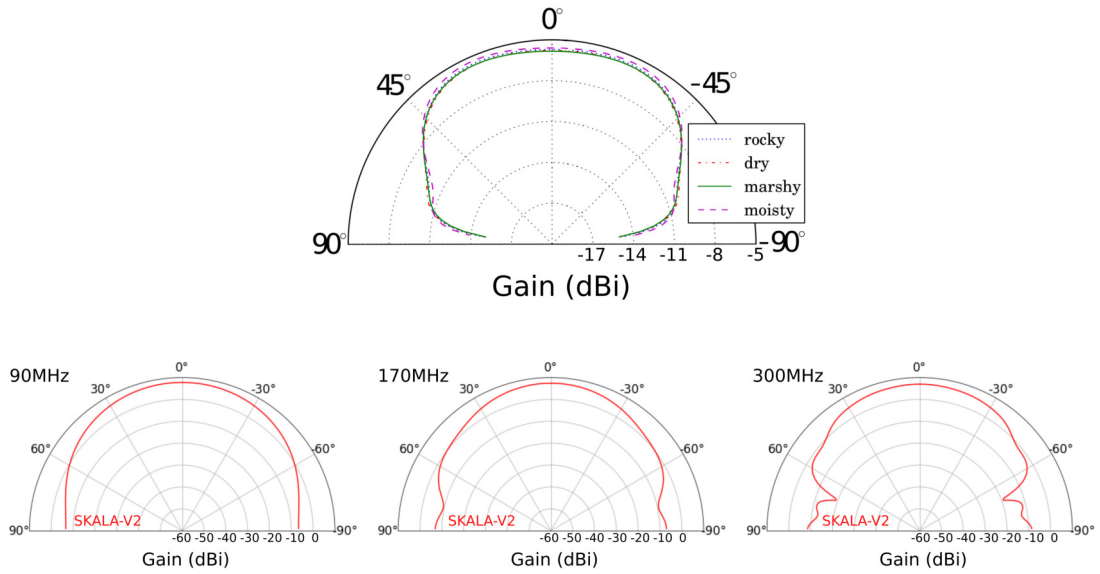


Figure 5.2: Top: Directive pattern of the SALLA antenna for different ground conditions. (Adopted from [85]). **Bottom:** SKALA directive patterns in dB, H-Plane, for frequencies 90 MHz (right), 170 MHz (middle), 300 MHz (left). (Adapted from [86])

than about 45° . The SKALA has, in general, a stronger gain that remains above 0 dBi for inclination angles lower than 60° which is important regarding the search for PeV gamma rays arriving at an inclination of about 61° from the Galactic Center and the general increase of sky coverage aimed for with the antenna array.

In Fig. 5.3, simulated directive patterns of the SKALA prototype version-1 for different grounds are shown for frequencies of 70 MHz and 150 MHz. For realistic scenarios like a soil ground (red) or a metal mesh over soil (green) the antenna gain is low for inclinations lower than $\pm 90^\circ$ which corresponds to a reflection of a down-going radio signal at the ground. The response of the antenna for different ground types does only change slightly. These antenna characteristics are important for an operation at the South Pole since the ground conditions of the antenna will change over time. The snow level will increase with about 20 cm/year on average and the snow-surface structures will change due to winds and snowdrifts. Also, the reflection of radio signals at the snow surface or below is unknown and may distort the measured signal if the antenna is too sensitive for up-going radiation. The simulated antenna gain for frequencies from 50–350 MHz is plotted in Fig. 5.4 for zenith angles θ of 0° and 60° . The overall gain drops for higher zenith angles as it can also be seen in the directive antenna patterns in Fig. 5.2. Dips in the antenna gain result from the antenna layout and are affected by the choice of number and resonance frequency of dipole elements.

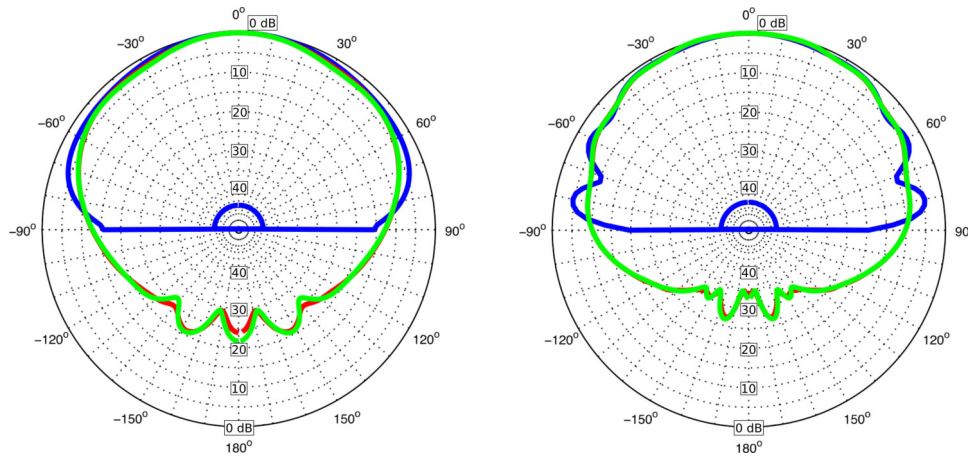


Figure 5.3: SKALA version-1 directive pattern (45° -cut between E-plane and H-plane) for different ground conditions: infinite ground (blue), soil (red), mesh over soil (green). **Left:** Directive pattern for a frequency of 70 MHz. **Right:** Directive pattern for a frequency of 150 MHz. (Figures adopted from [82])

THE LOW-NOISE AMPLIFIER The antenna low-noise amplifier (LNA) sits in the top part of the antenna inside a plastic housing (see Fig. 5.5, left). Both antenna polarizations are amplified with one LNA each. The amplification of the signals of one antenna polarization inside the LNA is realized in two stages. In Fig. 5.5 (right), a sketch of the LNA amplification stages is shown. In the first stage, the differential amplifier *TQP3M9039* is used to amplify the signal of each antenna arm independently. After a transformation of both antenna-arm signals to one single-ended signal using the Balun *B0205F50200AHF*, the resulting single-ended signal is amplified in a second stage using the amplifier *PSA-5451+* to obtain the final amplification level. The LNA is equipped with ESD protection diodes in both signal paths before the input into the first amplifier stage [89]. The LNA output is a $50\ \Omega$ -terminated, single-ended signal.

In Fig. 5.6 a gain simulation of the SKALA prototype version-2 LNA is shown [82]. The LNA response was simulated for an LNA connected to the antenna impedance. The overall gain of the LNA is above 40dB for frequencies higher than 100 MHz. Oscillations in the gain pattern occur since the antenna impedance changes with frequency and an impedance matching between antenna and LNA is not always possible. The LNA amplification decreases for frequencies lower 60 MHz. For high frequencies up to 600 MHz, the LNA gain remains over 30 dB. Tests of the LNA and a characterization for low temperatures were performed at KIT and will be presented in section 5.4.

For the measurement of cosmic-ray signals in high-frequency bandwidths, the noise temperature of the electronics becomes the limiting factor for signal detection. Thus, a noise temperature as low as possible is necessary to decrease the lower energy threshold. The noise temperature is a measure of the power of noise introduced in the signal and is usually given in units of Kelvin. In Fig. 5.7, measurements and simulations of the

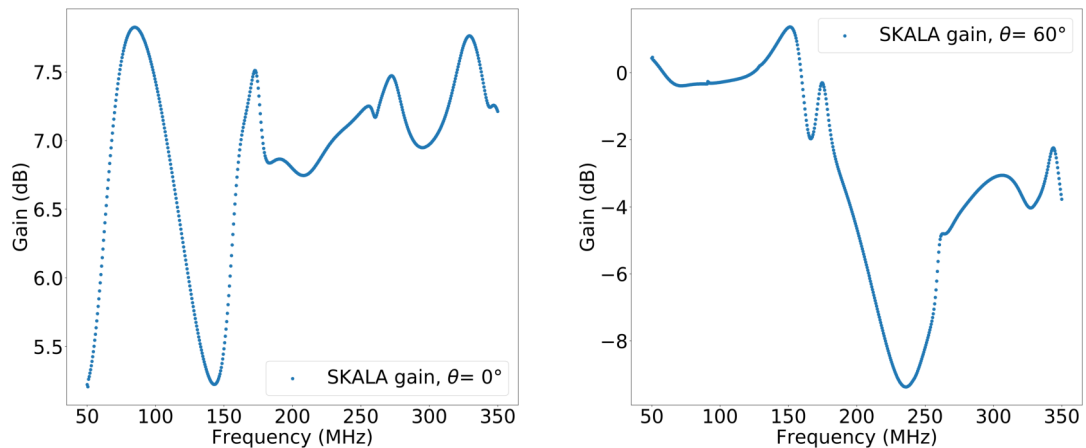


Figure 5.4: Gain of the SKALA version-2 antenna for zenith angles of 0° and 60° .

LNA noise temperature are shown. With a $50\ \Omega$ input signal to the LNA (red curve in Fig. 5.7), the noise measurement shows a noise temperature under 60 K for frequencies higher 100 MHz. Simulations of the LNA loaded with the SKALA antenna impedance (green curve) show a noise temperature of about 30 K. This result can be compared to the LNA noise temperature of the already mentioned SALLA antenna with 200 K to point out the improvement in reducing the LNA noise temperature [90].

5.3 MECHANICAL ANTENNA STRUCTURE

The mechanical structure of the SKALA antenna is designed for an operation in the environment of Australia and South Africa. In this design, the height of the antenna above ground¹ is about 30 cm and the antenna is secured by a concrete base plate. For a deployment at the South Pole, this design has to be adopted to meet the environmental conditions prevailing there. In particular, these are extreme temperatures lower than -70°C and a high UV radiation during the South Pole summer. Regarding a constant increase of the snow level of about 20 cm/year on average, an increase of the antenna height is needed which could even lead to a liftable antenna structure.

For the deployment of two prototype radio antennas at the South Pole in season 2018–19, a new mechanical structure of the antenna was designed using suitable materials. In Fig. 5.8, CAD models of the antenna structures are shown. The antenna mechanical structure has been designed in three different heights above ground (total height above ground) of 0.3 m (1.8 m), 0.7 m (2.3 m) and 1.7 m (3.3 m). By deploying different-size antennas, the snow accumulation around the antenna and effects in the measured signal due to snow burying the antenna can be investigated with the prototype array.

¹ In the following, the height of the antenna above ground is defined as the distance between the lowest antenna lobe and the ground level

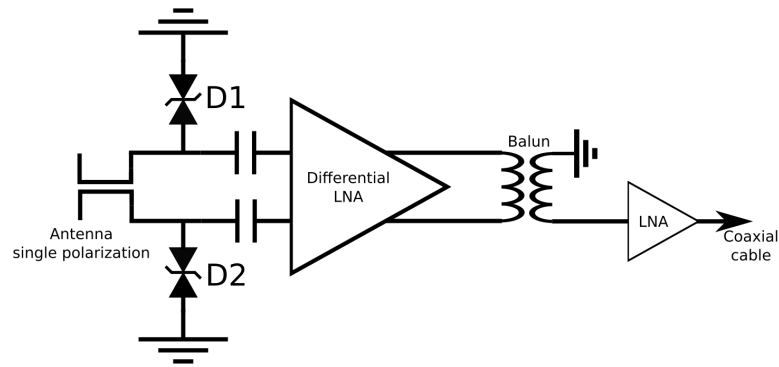


Figure 5.5: Left: Image of the SKALA LNA sitting in the LNA housing on the top of the antenna. Right: Simplified schematic of antenna LNA.

The antenna design consists of four antenna legs prolonging the antenna arms to the ground and a middle pole that serves as stabilization and as a cable guide. The antenna mechanical structure is attached to a base made out of plywood. The base is secured at the ground using snow spikes with a length of 1 m and a diameter of 2.5 cm which are driven into the snow surface. The antenna legs, the middle pole and snow spikes are made out of glass-fiber reinforced plastic material (GFK). The antenna arms are attached to the legs using GFK adapters. GFK can resist very low temperatures and is not damaged by UV radiation which makes it an ideal material for a deployment at the South Pole. Fig. 5.9 shows the SKALA antenna in the smallest South Pole design during a test deployment at KIT and in Fig. 5.10 close-ups of the interface sections are shown. For the deployment at the South Pole, screws securing the interface of different structure parts were replaced by cottor pins like it is shown in the most right picture in Fig. 5.10. Cottor pins enable an easy and fast deployment without the need for tools that is also possible while wearing gloves at the South Pole. The white plastic parts that stabilize the antenna structure on the top and the bottom of the antenna, as well as the LNA housing, were not replaced by new-material designs. These parts are made out of ASA¹ plastic which has a high UV resistance and good weather stability. Stress tests of the plastic parts during multiple temperature cycles from 20°C down to -70°C and back did not reveal any cracks or breaks in the plastic material.

5.4 LOW-TEMPERATURE LNA CHARACTERIZATION

The antenna LNA sits in the top part of the antenna inside a plastic housing. Due to its position, the LNA will be exposed to the full range of temperature variation at the

¹ Acrylonitrile styrene acrylate

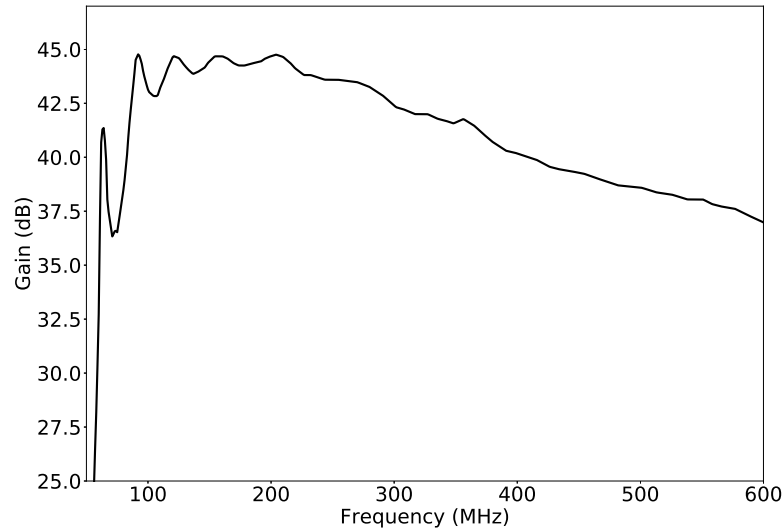


Figure 5.6: Simulated gain of the SKALA version-2 LNA. The LNA was simulated as loaded with the SKALA-antenna impedance. (Figure adapted from [76])

South Pole of several tens of degrees with lowest temperatures of under -70°C . At this moment, a temperature monitoring of the LNA is not foreseen but information about the ambient temperature at the measurement site are accessible if a rough temperature correction is required. To investigate the LNA behavior at different temperatures, characterization measurements of the LNA were performed within a temperature range of $+20^{\circ}\text{C}$ to -70°C . Since information about the temperature dependence of the LNA gain are crucial for decreasing the measurement uncertainty, the measured gain results were cross-checked by measurements with a network analyzer that will be presented at the end of this section.

5.4.1 Measurement setup

As shown in the LNA schematics (see Fig. 5.5), the LNA is directly connected to the antenna arms of one polarization. After the amplification of the signals of the two antenna arms, the signal exits the LNA as a 50Ω -terminated single-ended signal. To characterize the LNA, a calibration pulse was used as a reference signal. The calibration source was connected to the LNA using a 50Ω coaxial cable of which the signal and ground wires were directly soldered to the two LNA inputs. Fig. 5.11 shows a sketch of the measurement setup for the LNA characterization measurements and the connection of the attenuated reference-source signal to the LNA inputs.

As the calibration source, the frequency generator *RSG 1000* was used which emits a linearly decreasing frequency spectrum that reaches up to 1 GHz. The measurements were performed with the LNA placed inside the temperature chamber *VT 7021* that

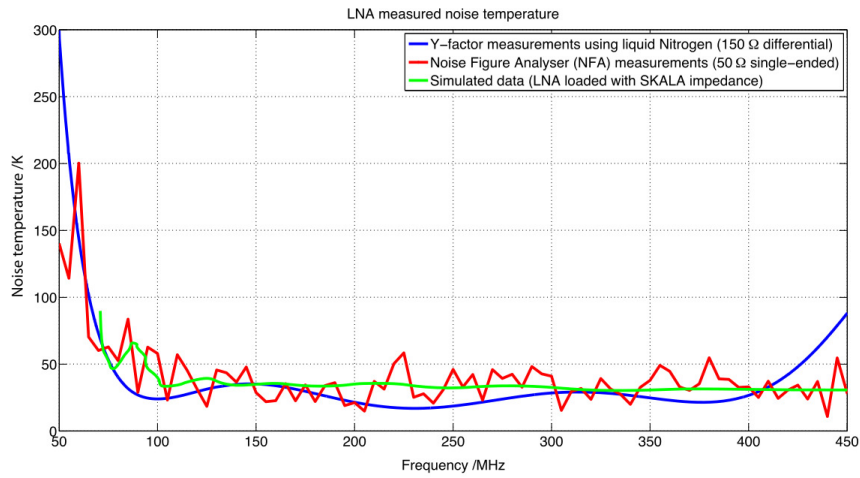


Figure 5.7: Simulated and measured noise temperature of the SKALA version-1 LNA. For the simulation, the LNA was loaded with the antenna impedance (green) and goes up to about 40 K in the measurement bandwidth starting at 100 MHz. (Figure from [82])

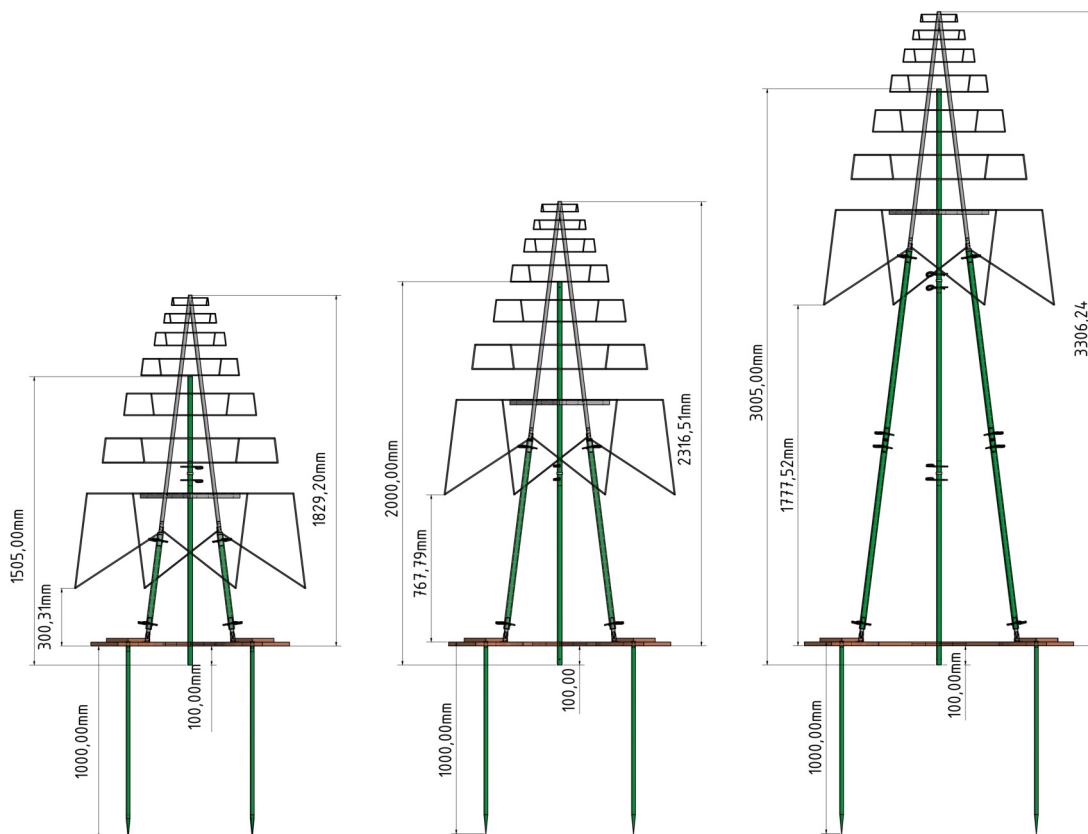


Figure 5.8: CAD designs of the South Pole antenna structure. The CAD models are scaled the same to allow a direct comparison of the height of the different designs.



Figure 5.9: SKALA version-2 antenna in the South Pole design deployed in the hybrid engineering array at KIT without middle pole and snow spikes.



Figure 5.10: Details of the SKALA version-2 South Pole mechanical structure. **Left:** Connection between antenna arm and GFK leg. **Middle left:** Connection between GFK leg and antenna foot. **Middle right:** Connection between two GFK legs using a GFK adapter. **Right:** Final connection of a GFK leg to the antenna foot using a cottor pin.

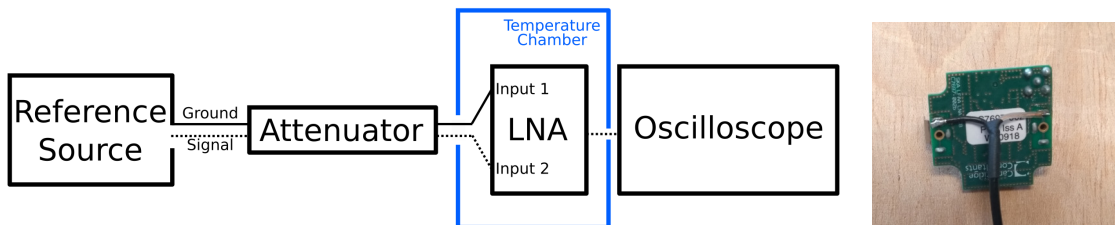


Figure 5.11: **Left:** Sketch of the measurement setup for characterizing the LNA. For measuring the attenuated output of the reference source, the oscilloscope was attached directly the attenuator output. **Right:** Attachment of the signal cable from the attenuator output to the LNA inputs. The signal line and the ground line of the coaxial cable are soldered to the LNA inputs.

can cool down to -72°C . The LNA output signal was recorded using a *WaveRunner 6Zi* oscilloscope with a sampling rate of 20 GS/s. The calibration source and the oscilloscope were placed outside of the temperature chamber and cable connections to the LNA were connected via through-puts of the temperature-chamber walls.

The LNA gain is determined by measuring the input reference pulse $\chi(s)_{\text{Pulse}}$ and the reference pulse amplified by the LNA electronics $\chi(s)_{\text{LNA}}$. A fast Fourier transformation is performed on both signals giving the Fourier transformation of the input reference pulse $F(f)_{\text{Pulse}}$ and of the LNA-amplified signal $F(f)_{\text{LNA}}$. Since $\chi(s)$ is a measured signal consisting of samples n , $\chi[n]$, the discrete Fourier transformation is used giving a Fourier transformation sampled in bins k , $F[k]$:

$$F[k] = \sum_{n=0}^{N-1} e^{2\pi i k \frac{n}{N}} \chi[n] \quad (5.3)$$

The Fourier transform $F[k]$ is in units of voltage. It can be transformed into decibels by using the formula

$$F[k]_{\text{dB}} = 20 \cdot \log_{10}(F[k]). \quad (5.4)$$

Since the measured samples represent voltage values, the prefactor 20 is chosen to transform them into decibel units. The difference of the Fourier transformations in decibel of the calibration signal $F[k]_{\text{Pulse,dB}}$ and the LNA-amplified signal $F[k]_{\text{LNA,dB}}$ is the gain of the LNA in decibel

$$G[k] = F[k]_{\text{LNA,dB}} - F[k]_{\text{Pulse,dB}} \quad (5.5)$$

of the sample k which can be calculated to a frequency value.

Since the LNA has a high gain of over 40 dB, the reference source signal has to be attenuated. The amplitude of the output signal of the reference source is fixed and a variable attenuation was realized by using commercial attenuators in the input-signal line. Measurements were performed with different attenuation levels of the reference-source signal from -32 dB to -58 dB to investigate and exclude possible saturation effects of the LNA during the characterization.

5.4.2 LNA characterization results

The LNA gain was measured for frequencies up to 1 GHz and temperatures from 20°C to -70°C . In Fig. 5.12 the gain measurements at three different temperatures, -70°C , -25°C and 20°C , are shown. The presented gain is the average value over 600 gain measurements at each temperature together with the standard deviation. In the lower plot of Fig. 5.12, the gain difference of the -25°C and the $+20^{\circ}\text{C}$ measurement against the lowest temperature measurement at -70°C is shown.

For all temperatures, the LNA gain stays above 35 dB for frequencies from 100 MHz

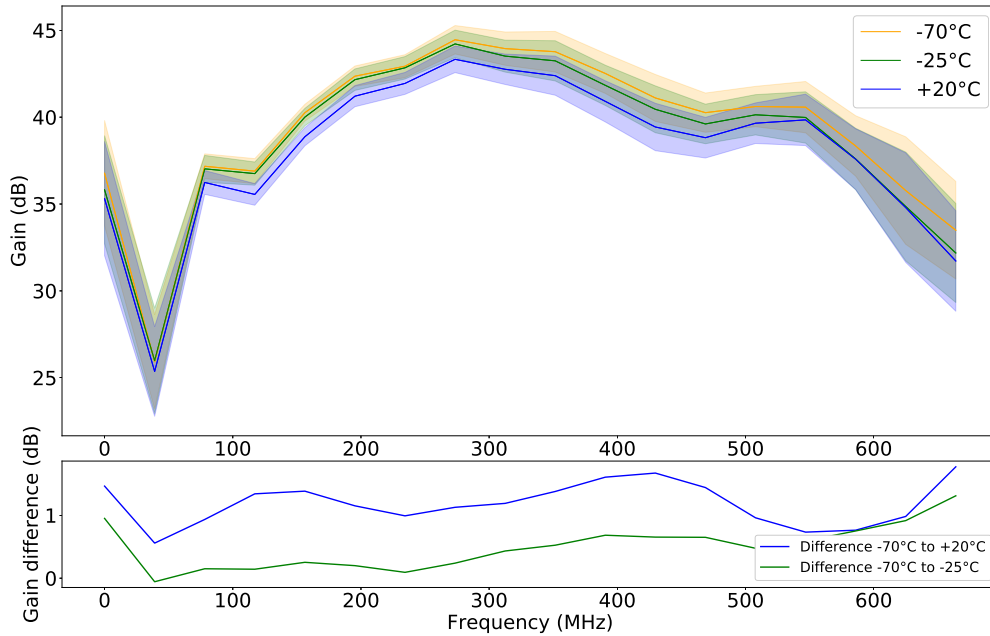


Figure 5.12: Results of the LNA characterization measurement at different temperatures. The upper plot shows the measured LNA gain for temperatures of -70°C , -25°C and $+20^{\circ}\text{C}$. The lower plot shows the difference in gain between the measurement at -70°C and the two measurements at -25°C (green) and $+20^{\circ}\text{C}$ (blue).

up to about 600 MHz. A maximum gain value of circa 45 dB is reached for 300 MHz. The gain falls off for frequencies below 70 MHz. For frequencies below 50 MHz a rise of the gain is visible that is not expected and might come from external noise coupling into the measurement setup. Measurements with a network analyzer do not show this behavior (see sec. 5.4.3).

The average gain stays stable within a 1.5 dB window over the measured temperature range. Comparing the gain differences for different temperatures against the gain at -70°C , it is visible that the gain increases slightly with decreasing temperature. This behavior is expected since the gain of the first-stage LNA amplifier increases slightly for lower temperatures [91]. To give an idea of the impact of this gain variation with temperature, a 1.5 dB gain difference between the two extreme temperature scenarios of $+20^{\circ}\text{C}$ and -70°C would lead to a 3.7% uncertainty on the signal amplitude regarding a nominal LNA gain of 40 dB. Since the strength of the radio signal is directly correlated to the shower energy, this uncertainty is directly influencing the measurement uncertainty of the primary particle energy E_0 . The maximum LNA temperature during an operation at the South Pole is unknown and will be measured during future measurement campaigns but will probably be less than $+20^{\circ}\text{C}$. For a more realistic approximation, we set the maximum LNA temperature to -25°C which reduces the gain variation to 1 dB in maximum and the signal-amplitude uncertainty to 2.5%.

Taking also the targeted frequency bandwidth of 100–190 MHz into account, the gain variation decreases to less than 0.5 dB which results in an uncertainty of only 1.25%. This uncertainty can additionally be reduced when the ambient temperature during the measurement is taken into account for the analysis which is easily possible using available weather monitoring data. In Fig. 5.13 the gain results for all measured temperatures are presented which show a clean and stable gain behavior at all temperatures.

The presented measurements were performed with a constant input impedance into the LNA of $50\ \Omega$. This is not the situation when the LNA is connected to the antenna. The antenna impedance oscillates around $100\ \Omega$ and changes with frequency. This leads to impedance mismatching between the antenna and the LNA and a different gain spectrum than it has been shown in the presented measurements. In Fig. 5.14 a comparison of the measured gain spectrum for 20°C and the simulated gain spectrum of the LNA loaded with the antenna impedance is shown. The simulation overshoots the measurement for frequencies smaller than 300 MHz and shows an oscillating behavior that has its origin in the impedance mismatch between the antenna and the LNA electronics. Therefore the presented measurements should not be used to reconstruct measured signals. Here, calibration measurements of the whole system consisting of antenna and LNA are needed. The presented measurements proof that the LNA can be used to operate the antenna in the cold and highly dynamic South Pole environment and that the expected gain during operation is in the foreseen region of 35–45 dB for frequencies of 70 MHz to 600 MHz.

5.4.3 Network analyzer measurements

The presented LNA characterization measurements were repeated with the network analyzer *N9923A* to confirm and extend the information gained from former characterization measurements. The network analyzer (NA) *N9923A* is a two-port device and can perform S_{21} measurements. S_{21} measurements determine the forward gain of a device under test by comparing the input and output signal. For the measurements, the $50\ \Omega$ output of the NA was connected to the LNA input ports using the same connection like in the previous measurements (see Fig. 5.11). The LNA output was guided through a bias tee which powered the LNA with 5 V. The amplified RF signal was attenuated at the output of the bias tee with about 25 dB to protect the network analyzer input. To be able to correct the measurement results for attenuation effects due to the additional attenuators, cables, and bias tee, additional S_{12} measurements were performed without the LNA in the signal chain.

In Fig. 5.15, the gain spectra of the LNA measurements are shown. The network analyzer measurement confirms the gain behavior obtained with prior measurements. Also here, the gain of the LNA increases with decreasing temperature. The gain differ-

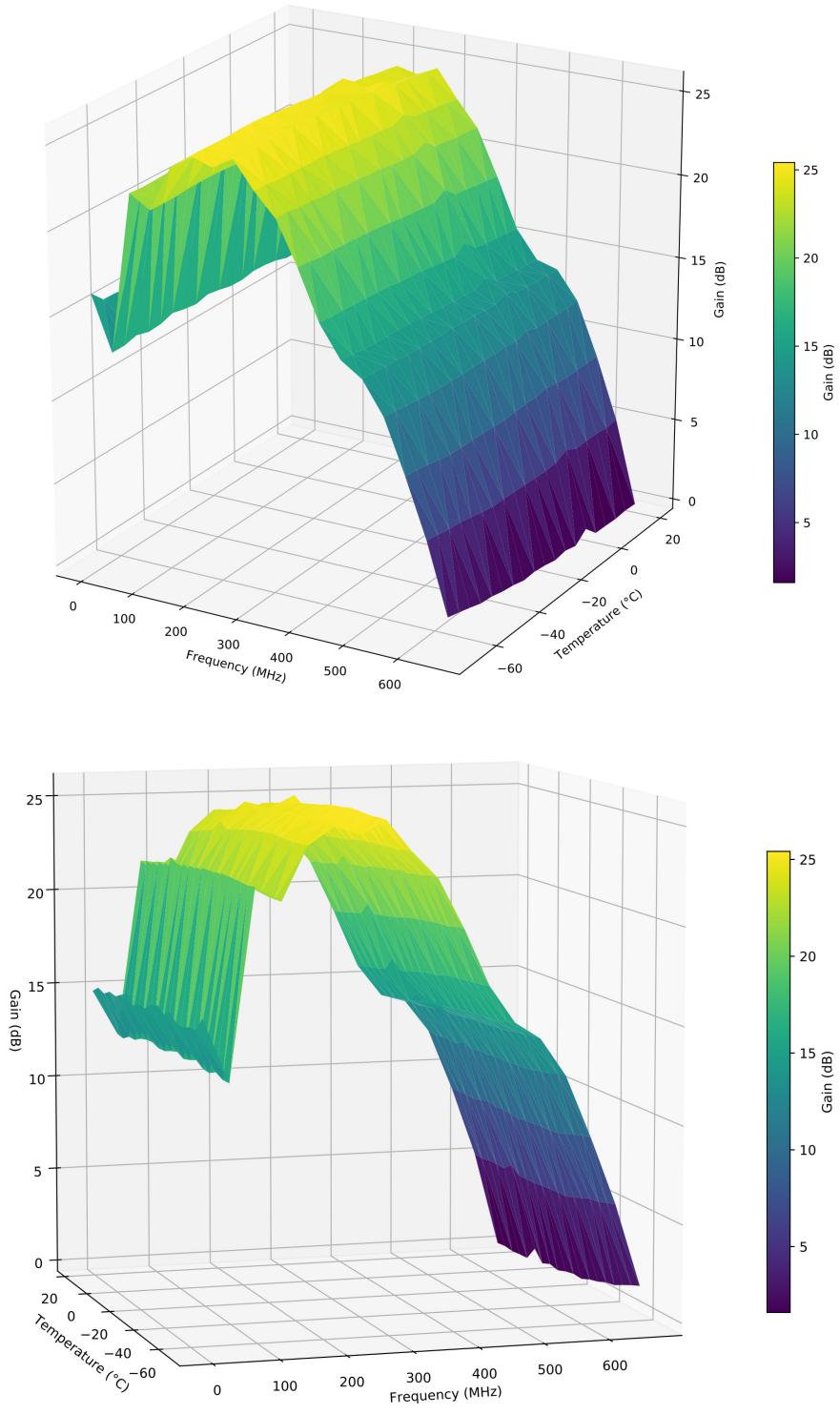


Figure 5.13: Spatial presentation of the LNA gain depending on the frequency and the temperature. The upper and the lower plot show the same graph in different viewing angles. The plots show a smooth LNA gain behavior over the full frequency and temperature range.

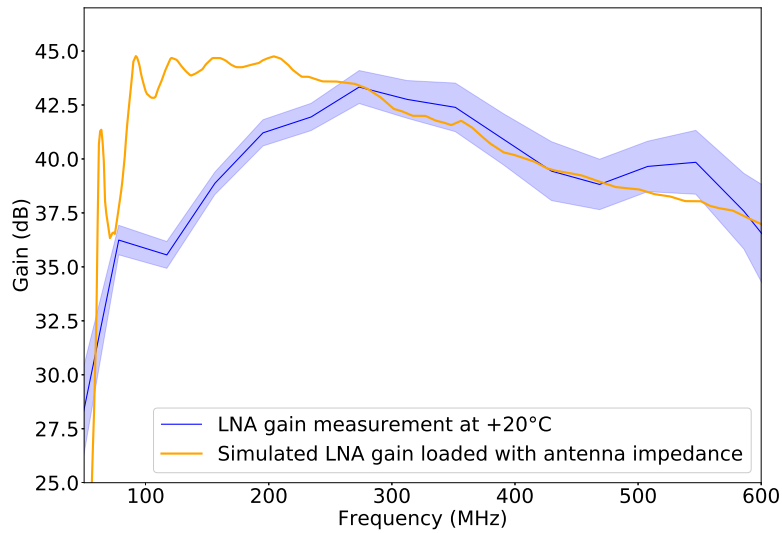


Figure 5.14: Comparison of the measured gain with a 50Ω input source at 20°C and the LNA gain simulation with the LNA loaded with the actual antenna impedance of the SKALA version-2 antenna. Effects of impedance mismatching between LNA and antenna and therefore a diverging gain pattern can be seen especially for low frequencies. (Data of simulated LNA gain taken from [76])

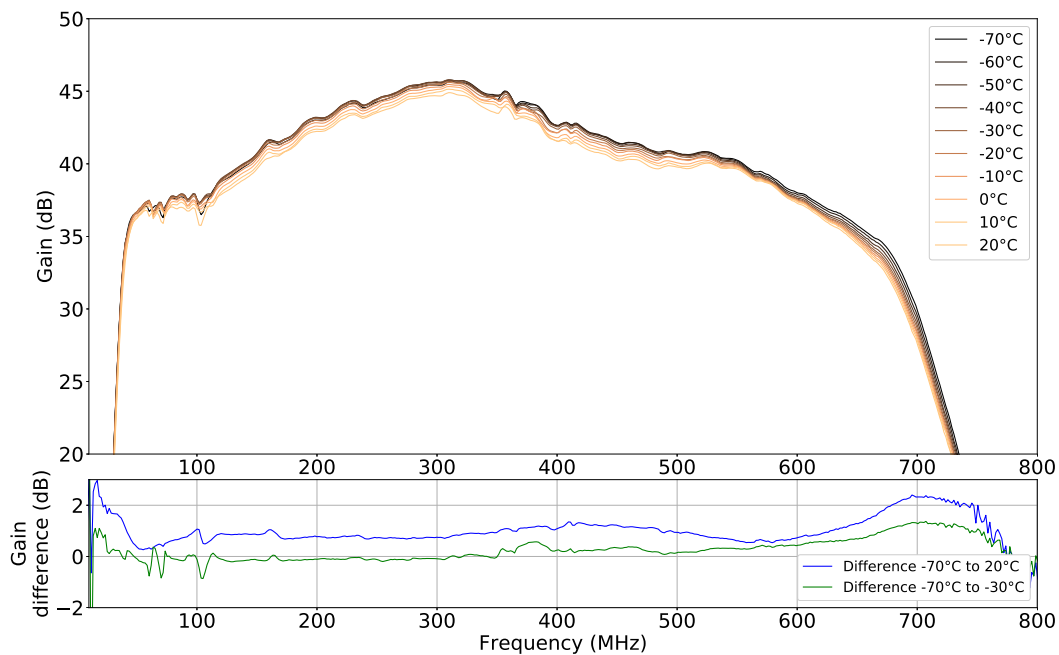


Figure 5.15: S_{21} measurements of the LNA at different temperatures from $+20^\circ\text{C}$ down to -70°C . The lower plot shows the difference in gain between the measurement at -70°C and the measurements at -30°C (green) and $+20^\circ\text{C}$ (blue).

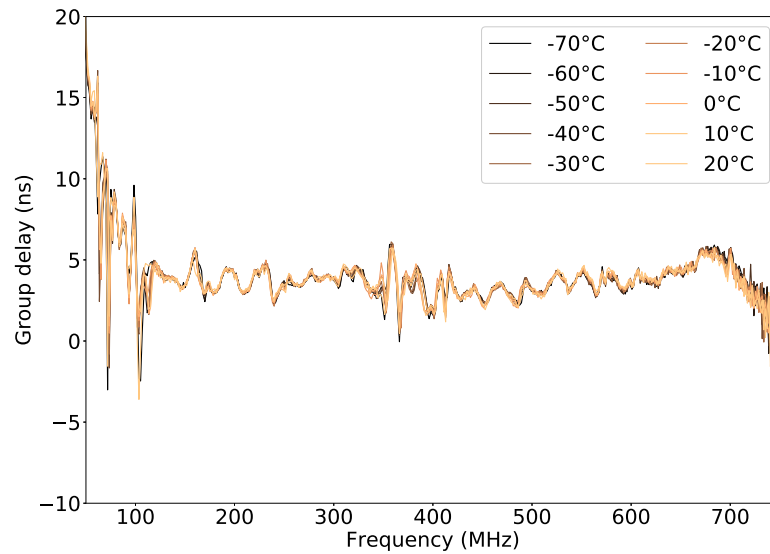


Figure 5.16: Measurement of the LNA group delay at different temperatures from +20°C down to -70°C.

ence between the measurement at -70°C and the +20°C and -30°C measurements are shown in the lower plot of Fig. 5.15. The temperature values for the comparison have been chosen to be able to compare the results with earlier measurements shown in Fig. 5.12. In the pass band of the LNA from about 70–650 MHz the maximum difference of the LNA gain between -70°C and 20°C is about 1.35 dB. Comparing the more realistic temperature values during an operation at the South Pole between -70°C and -30°C the maximum difference decreases to about 0.8 dB.

The group delay originating from the LNA electronics for temperatures from 20°C to -70°C is shown in Fig 5.16. Between 100–650 MHz the group delay stays constant within a maximum 5 ns window. No change of the group delay with temperature can be observed.

The network analyzer measurements confirm the prior measurements using the oscilloscope to record the data and calculate the gain by comparing the input and the output signal. This is pointed out here since the same measurement setup was used to characterize the radio front-end board which is introduced in the next chapter.

5.5 CONCLUSION AND REMARKS

The SKALA radio antenna is the candidate for the IceTop radio extension. The antenna comes with a good acceptance for signals with an inclination higher than 61°, a large frequency bandwidth of 70–650 MHz, a low noise temperature of under 50 K and a robust antenna design. To prepare the antenna deployment at the South Pole, a new

antenna mechanical structure has been designed consisting of glass-fiber enhanced plastic materials and plywood. These materials should withstand the cold temperatures and the high radiation of UV light during the South Pole summer. To test different antenna heights for snowdrift around the antenna and snow accumulation at the antenna site, designs with three different heights were developed. The deployment of two prototype antennas successfully took place in January 2019 at the South Pole and the latest reports show the antenna structure in good shape (see chapter 8). To ensure the antenna operation under South Pole conditions, the antenna LNA was characterized at low temperatures down to -70°C . The characterization shows a stable LNA gain with a slight increase in amplification for low temperatures. In a realistic scenario, the temperature-dependent gain variations introduce a systematic uncertainty of about 1.25% in the target bandwidth of 100–190 MHz that was found to yield the best signal-to-noise ratio [44]. This uncertainty will be reduced if available temperature data is taken into account for the analysis of the measurement. For a more accurate gain-variation correction, the deployed antennas could be equipped with temperature sensors in the LNA housing. This temperature monitoring could be used for the gain correction.

THE HYBRID ENGINEERING ARRAY

A hybrid engineering array consisting of particle detectors and SKALA radio antennas was set up on the area of the Campus North of the Karlsruhe Institute of Technology (KIT) within the frame of this thesis to be able to test newly developed detectors, electronics, and data acquisition (DAQ) systems. Regarding the development of the radio detector for the IceTop radio extension, the engineering array enabled crucial tests of the SKALA antennas, the SKALA mechanical design for South Pole operation, and the tests of dedicated radio electronics and DAQ systems. Additionally, radio measurements performed with SKALA antennas in the array proofed the functionality of the radio antennas and marked an important step towards a deployment of radio antennas at the South Pole in season 2018–19. Another aim of the array was the deployment and operation of an 'IceScint' scintillation-detector array with the same hardware setup as it was deployed at the South Pole in season 2017–18 for testing new DAQ firmware versions and perform characterization measurements of the detectors and the detector electronics. The following chapter will focus on radio-related topics of the engineering array. Further information on particle detector specific results can be found in refs. [92–94]. A master's thesis dedicated to the measurements with radio antennas in the hybrid engineering array can be found in reference [95].

6.1 INTRODUCING THE HYBRID ENGINEERING ARRAY

The hybrid engineering array is located on the grounds of Campus North of KIT. In Fig. 6.1, the surrounding infrastructure with a zoom into the exact array location is shown. The array is surrounded by buildings on all four sides housing offices, laboratories and workshops which increases the radio background for air-shower measurements with antennas (more information about the radio background will follow in sec. 6.3). The hybrid engineering array consists of particle detectors and radio antennas. As particle detectors, eight IceCube scintillation detectors (IceScint) and 12 detectors of the former trigger array of the KASCADE experiment [96] (Mini-KASCADE) are used. The Mini-KASCADE detectors are scintillation detectors read out by one photomultiplier tube (PMT). Each Mini-KASCADE detector panel houses two separate detectors. For more information about the Mini-KASCADE detectors, the reader is referred to the refs. [93, 97, 98]. In Fig. 6.2, a map of the detector layout is shown. The IceScint detectors are set up inside the array building to protect them from humidity and rainfall. An image of the detector layout inside the building is shown in Fig. 6.4 (left). Mini-KASCADE detectors are located inside and outside of the array building to increase lever arm

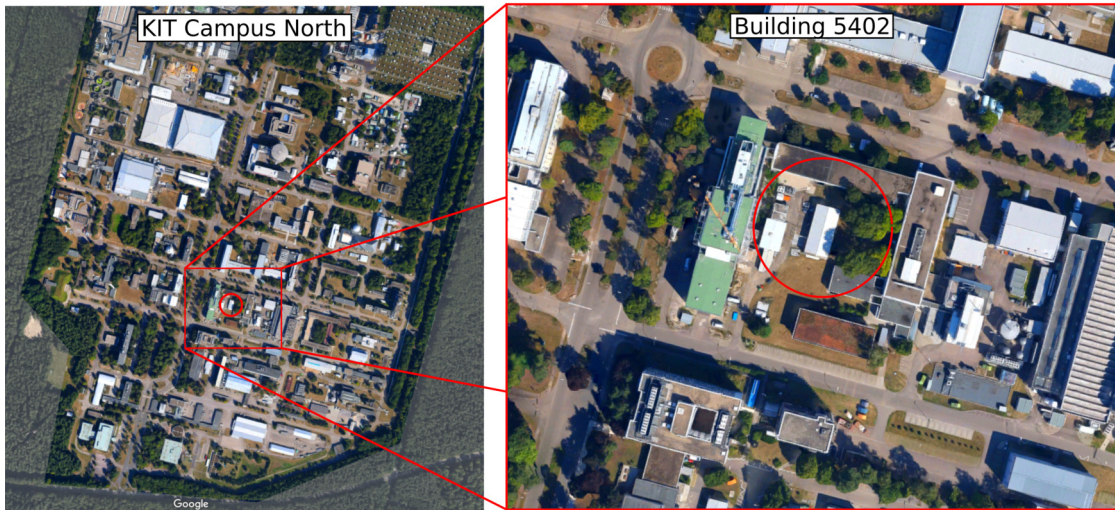


Figure 6.1: Location of the hybrid engineering array on the Campus North of KIT. The array is set up around building 5402.

and therefore the accuracy of the direction reconstruction of air-showers. Before the antenna deployment at the South Pole in season 2018–19, four SKALA radio antennas were installed around the array building. Three of the four antennas were shipped to the South Pole in September 2018. Together with the radio antennas, the engineering array covers an area of about 28 m width and 32 m length (referring to the layout map in Fig. 6.2).

For reading out the Mini-KASCADE detectors, original KASCADE electronics and software is used. The KASCADE analysis provides a calculation of the center-of-gravity of the shower core for x- and y-coordinates as well as the total energy deposited in the Mini-KASCADE detectors and the direction of the shower in azimuth and zenith coordinates. In Fig. 6.3, an example event recorded with the Mini-KASCADE detectors is shown. The denser array of eight detectors in the lower left are the detectors installed inside the array building. The outside detectors are visible in the lower right and upper left. The measured charge deposited in the detectors (left) and the time differences of recorded signals (left) are in visible agreement with the reconstructed values for the arrival direction. The IceScint detector signals are sampled and digitized with the IceTAXI DAQ system which is an exact copy of the deployed DAQ at the South Pole and allows a direct comparison of events measured with the system at the South Pole and the scintillation-detector array at KIT.

6.2 THE RADIO ARRAY

Four SKALA radio antennas were set up in the hybrid engineering array around the array building like it is shown in the detector map in Fig. 6.2. The antenna polarizations

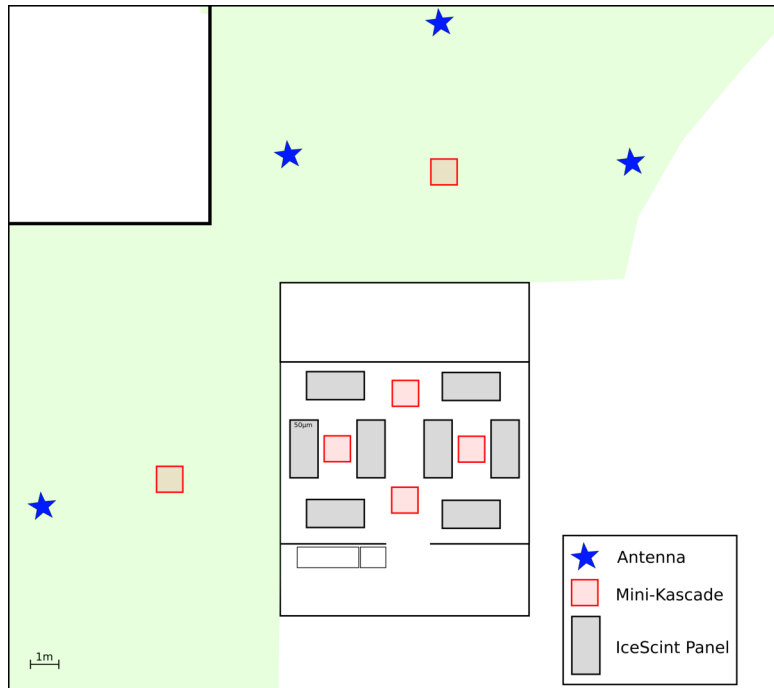


Figure 6.2: Map of the detector layout of the hybrid engineering array. The detector array consists of radio antennas (blue stars), Mini-KASCADE scintillation detectors with PMT read out (red squares) and IceCube scintillation detectors (IceScint, gray squares). Detector sizes and not to scale.

of each antenna were aligned to the east-west and north-south direction. A picture of the antenna setup is shown in 6.4 (right). The antenna LNAs were connected with 50 m coaxial cable (type *RG213*) to the radio electronics installed inside the array building. To read out the antenna signals, a commercial desktop digitizer *DT5730* was used that has eight input channels and samples the incoming signals with a sampling frequency of 500 MHz and a sampling depth of 14 bit. A calibration of the digitizer was performed in ref. [83]. The *DT5730* digitizer was operated using a modified version of the *WaveDump* software that was extended for the option to save recorded events into SQL databases. For each polarization, a bias tee *ZFBT-4R2G-FT+* powered the antenna LNA with 5 V. Before entering the *DT5730* digitizer, the radio signals were filtered with a high-pass filter *ZX75HP-44+*, a low-pass filter *SLP-200+* and a band-stop filter for the FM radio-band *ZX75BS-88108+* which is the most dominant noise source at this location. To proof the functionality of the radio array, the full radio setup including the SKALA antennas, LNAs, electronics and DAQ was successfully tested with a calibration antenna, described in [83].

To trigger the radio DAQ, a trigger signal provided by the Mini-KASCADE electronics was used. The Mini-KASCADE trigger is a coincidence trigger with a variable number

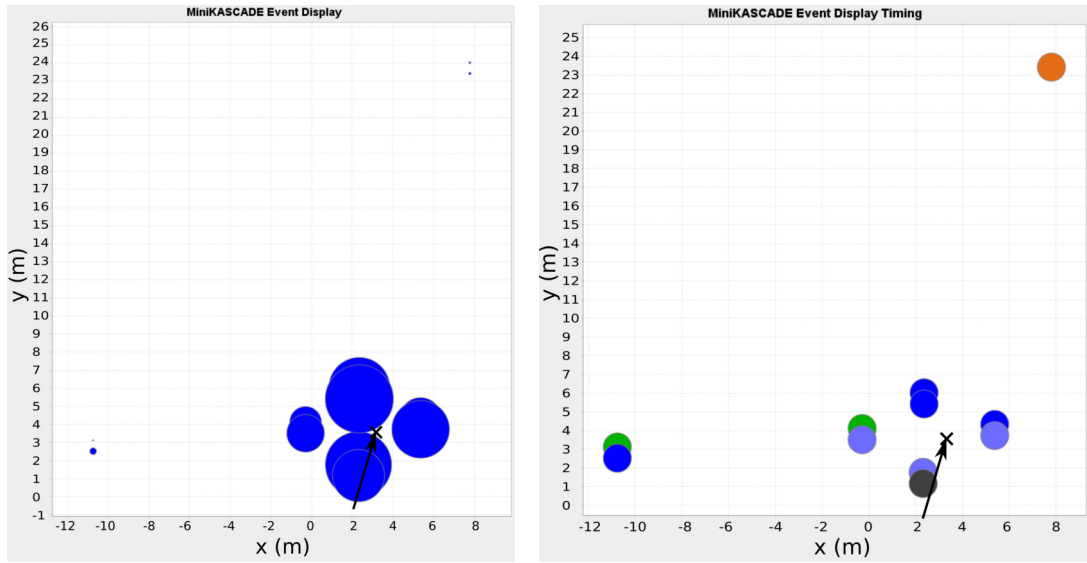


Figure 6.3: Example of an event recorded with the Mini-KASCADE particle detectors. The right plot shows the measured charge in the detector. The left plot shows the time of signal detection in the different detectors. Darker colors indicate earlier detection, lighter colors indicate later detection. The reconstructed shower direction and center of gravity are drawn in the plot for comparison. The reconstructed values for the arrival direction are $\theta = 10.9^\circ$ and $\phi = 106.4^\circ$.

of coincident detectors. For the presented radio measurement, a full coincidence of all 12 Mini-KASCADE detectors was used to trigger the radio readout. A full coincidence trigger was chosen to only record the highest-energetic showers which maximizes the probability of a detectable radio signal. The trigger delay for the radio readout was measured with the full electronic setup and was found to be 400 ns. When a trigger event occurred, the traces of all eight antenna polarization were read out with a trace length of 12 μs and stored in a SQL database together with the event timestamp.

6.3 RADIO BACKGROUND MEASUREMENTS

To better understand the radio background at the hybrid engineering array site, the background was monitored over several weeks with one SKALA antenna and the measurement setup introduced in the last section. Radio traces were automatically recorded every 60 seconds. For this measurement, no high-pass filter, cutting frequencies lower than 50 MHz, was used to gain additional information about the low-frequency part of the background spectrum. In Fig. 6.5, the average background spectrum is shown over the full measurement bandwidth up to 250 MHz. Between 80–120 MHz, the effect of the band-stop filter is visible that attenuates the FM radio band. The band-stop filter attenuates the frequencies in the stopband with a maximum of -60 dB which gives an impression of how strong the FM radio band is in the measured



Figure 6.4: Left: Image of the detector setup inside the array building. Right: Image of the outside detector setup with radio antennas and Mini-KASCADE detectors.

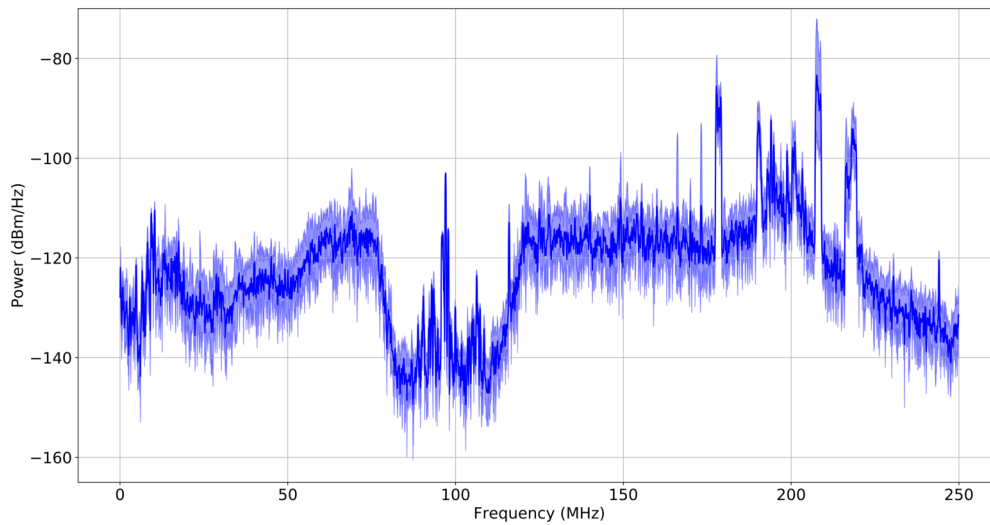


Figure 6.5: Average background spectrum recorded with the radio antennas set up around the array building. Strong RFI lines are visible especially for high frequencies. The radio FM band at 80–110 MHz was filtered using a band-stop filter.

frequency spectrum. For frequencies lower than 70 MHz, the LNA amplification decreases which leads to a decrease of spectrum power. At 200 MHz, the low-pass filter starts to attenuate. The spectrum shows strong RFI peaks at high frequencies starting around 165 MHz. The frequency range from 120–160 MHz seems quietest and was chosen as the analysis bandwidth for the search for cosmic-ray events.

To analyze possible time variations in the background spectrum, the spectral power in several quiet frequency bins is plotted over time in Fig. 6.6. The plots show the spectral power for frequencies from 120–150 MHz over the time in days. For better visibility, the data was smoothed using a floating mean with a kernel size of 300 minutes. A clear variation of the spectral power with working days is visible in the plot. The background noise increases in the morning of every working day and decreases again in the evening. During weekends, the noise stays low with only minor variations. Re-

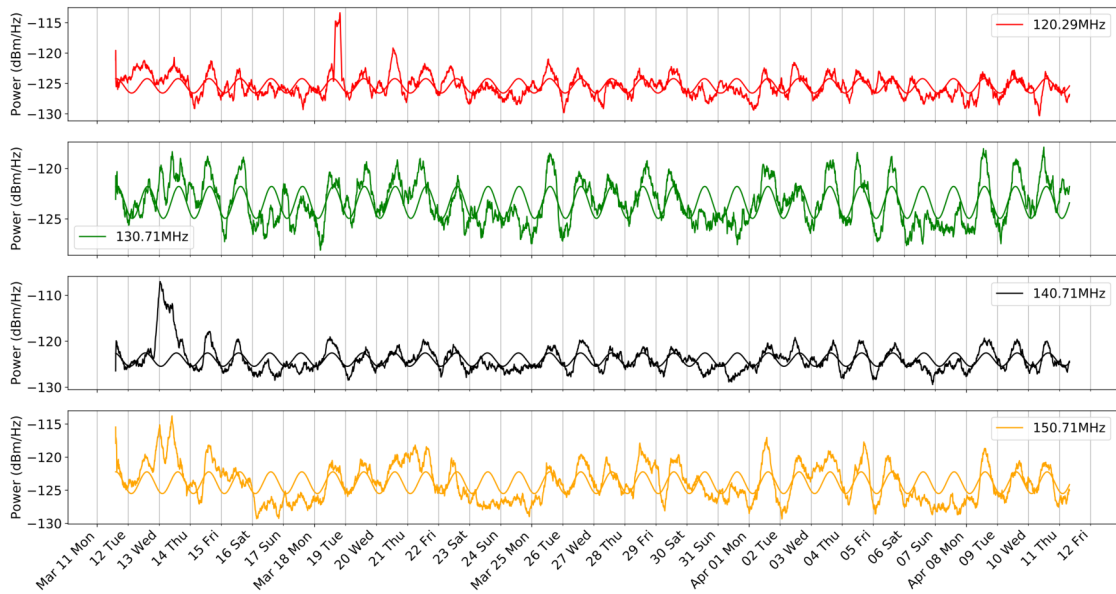


Figure 6.6: Variation of the measured power in different frequency bins between 120–150 MHz. The measured variation of the background noise is strongly correlated to working days with variations between day and night of more than 5 dB.

guarding the correlation of the noise with working days of the employees in the surrounding buildings, the origin is clearly human-made. Sine waves were fitted to the spectral power variation that result in a fitted period of the variations of 24 hours. The difference in spectral power between working days and weekends is more than 5 dB. Human-made RFI produces transient signals similar to those expected from cosmic-ray air showers and a strong pollution with human-made noise, like it is prevailing at the measurement site, complicates the radio measurement of cosmic-ray signals.

6.4 THE SEARCH FOR COSMIC-RAY SIGNALS

Although the radio background at the measurement site as well as the array layout (due to the small number of antennas and a limited area) are not ideal, radio signals of cosmic-ray air shower were searched for during multiple measurement campaigns with several thousand recorded radio events. For all measurements, the radio DAQ was triggered by a full coincidence of the Mini-KASCADE detectors. Then, the radio signals were processed and digitized as presented in sec. 6.2. The following paragraphs give a brief description of the efforts made to identify cosmic-ray signals in the noise-polluted radio traces.

6.4.1 Direction reconstruction of radio signals

In a first approach, the direction of possible radio signals was reconstructed to search for a directional coincidence with the Mini-KASCADE event that triggered the radio readout. A signal in the radio trace was defined as a peak with a sufficient signal-to-noise ratio (SNR)¹. A minimum SNR of 3 was chosen since higher SNR cuts decreased the number of event candidates significantly. If more than two radio antennas saw a radio signal in a certain time window, the direction of the signal was calculated using the time differences between the signals in the individual antennas and assuming a plane radio front. Different time windows were tested from 30 ns to 100 ns where the later would resemble a radio signal with a horizontal direction.

Before searching for radio signals, the recorded waveforms were processed offline to use different frequency bandwidths and to reduce RFI pollution. A low-frequency bandwidth from 50–80 MHz and a high-frequency bandwidth from 120–150 MHz were chosen for analysis. For low frequencies, the radio signal of cosmic rays is stronger and easier to detect above the baseline noise. The LOPES experiment confirmed the detection of cosmic-ray signals in a bandwidth of 30–80 MHz while measuring at a very similar site on the KIT campus north [99]. However, it should be noted, that the LOPES measurement site was not surrounded by buildings and that cosmic-ray signals were identified by cross-correlating more than eight antennas which is not possible within the engineering array. On the other hand, the LNA gain decreases for frequencies lower than 70 MHz which reduces the detection probability. In the high-frequency analysis window above 120 MHz, the cosmic-ray radio-signal strength decreases, but the background spectrum shows a reasonable flat behavior.

The traces were cleaned from narrow-band RFI noise using different approaches. As already introduced in the LOPES experiment, RFI peaks can be suppressed by digitally setting the RFI amplitude to the spectrum's mean value [100]. Since the spectrum of a cosmic ray is broadband, this operation should reduce the RFI but does not influence the radio signal of the cosmic-ray air shower critically. In a second, more drastic way, a floating-average function was applied on the measured spectrum smoothing the spectrum shape and removing narrow-band variations in the spectrum. Again, since cosmic-ray signals are broadband, this operation should reduce RFI pollution but spare general features of the cosmic-ray signal. After applying changes to the measured frequency spectrum, the time-domain signal was calculated with an inverse Fourier transformation and analyzed as described above.

In Fig. 6.7, the sky map of the radio direction reconstruction is shown for one measurement run together with the direction-reconstruction results from the Mini-KASCADE detectors. For each Mini-KASCADE event (see Fig. 6.3 for an example), the radio traces were analyzed for reconstructable radio signals and the calculated direction was plotted in the sky map. Comparing both sky maps, it is obvious that the radio signals

¹ The SNR is here defined as $SNR = \frac{V}{RMS(Trace)}$

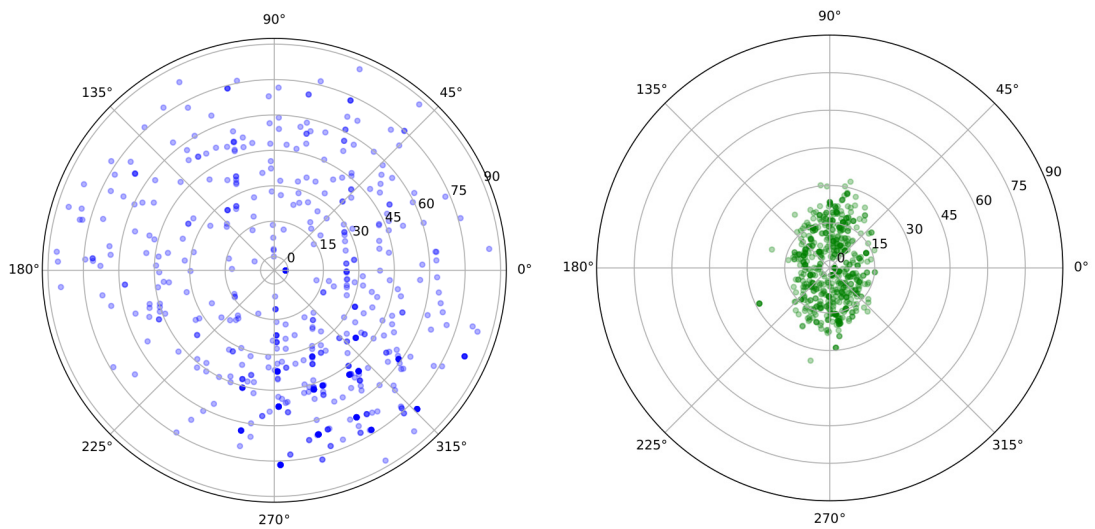


Figure 6.7: Sky Maps of reconstructed signals with the antennas (left) and the Mini-KASCADE detectors (right) which were used to trigger the radio readout. Air showers detected and reconstructed with Mini-KASCADE are mostly vertical whereas signals reconstructed with the radio antennas show a large spread over the whole sky with hot spots especially in the fourth quadrant.

have a much larger spread over the sky than the Mini-KASCADE events which are all fairly horizontal showers with inclinations below 30° . The search for directional coincidence between the reconstructed directions of the radio signal and the Mini-KASCADE event resulted in all studies in a few coinciding events which are statistically not significant. But, although no cosmic-ray events were confirmed using this approach, the resulting radio sky map nevertheless shows interesting features which are visible as hotspots in the map. Single events are plotted in the sky map as light-blue dots that get darker when they are overlaying with other reconstructed directions. Several hotspots of reconstructed signals are visible especially in the fourth quadrant of the sky map. These measured and reconstructed signals could originate partly from the photomultiplier tubes (PMT) in the Mini-KASCADE detectors which are firing and recharging every time a radio trace is recorded. The PMTs would be visible as pairs of two nearby sources in the sky map since one detector panel houses two detectors with each one PMT. This pattern can be assumed for some of the hotspots in the fourth quadrant. Since the PMTs as well as other sources like air-condition systems and electronic equipment are near to the antennas or, for the PMTs, even within the array, the direction reconstruction for these sources obviously fails and predicts the source somewhere in the sky map.

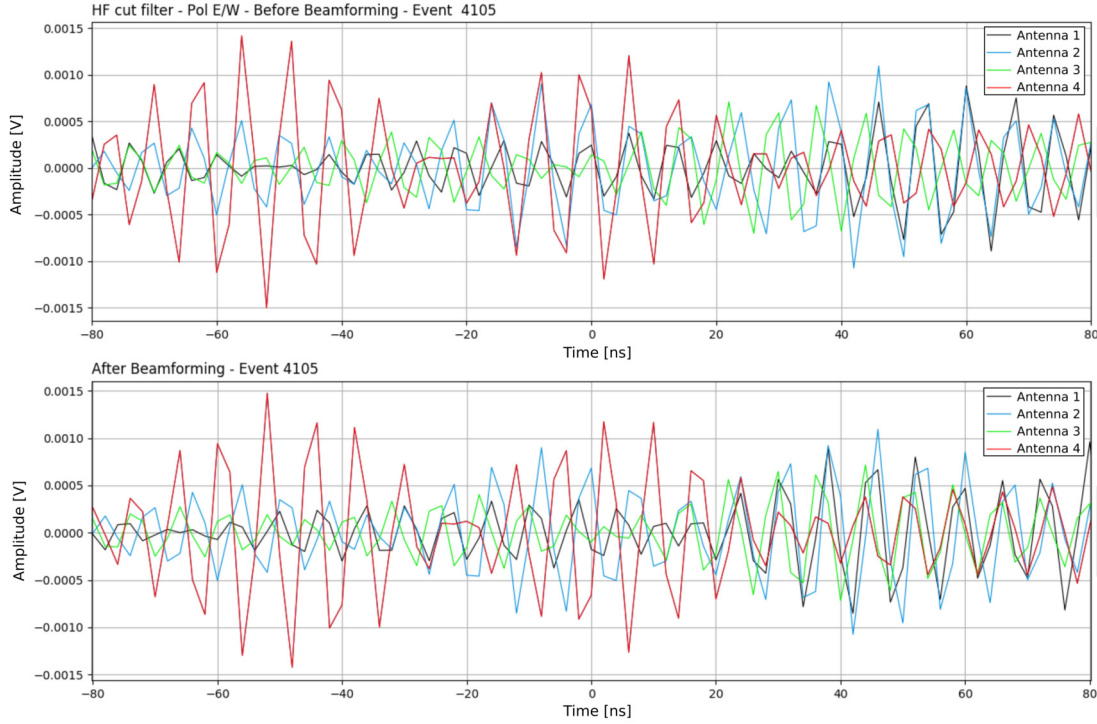


Figure 6.8: Example of a recorded radio event before (top) and after (bottom) beamforming. For this analysis a box filter was used to cut the analysis bandwidth to 120–150 MHz. RFI peaks rising above one standard deviation of the frequency band were set to the mean value. Shown is the East-West polarization signal. (Figure adopted from [95])

6.4.2 Beamforming and cross-correlation beam analysis

To reduce the appearance of artificial sources in the results of the cosmic-ray analysis of the measured radio data, beamforming and an analysis of the cross-correlation (cc) beam was used in the next approach. In general, beamforming means shifting the radio signals of individual antennas in a way that the antenna array gets most sensitive in a certain direction. For the search for cosmic rays, the direction aimed for is the incoming direction of the cosmic-ray air shower and beamforming becomes the correction of the geometrical delay of the radio signal received in each antenna. To calculate the geometric delays, the antenna positions x_i, y_i, z_i have to be transformed into the shower plane coordinate system x'_i, y'_i, z'_i with

$$\begin{pmatrix} x'_i \\ y'_i \\ z'_i \end{pmatrix} = \begin{pmatrix} -\sin(\phi) & \cos(\phi) & 0 \\ \sin(\theta)\cos(\phi) & \sin(\theta)\sin(\phi) & -\cos(\theta) \\ \cos(\theta)\cos(\phi) & \cos(\theta)\sin(\phi) & \sin(\theta) \end{pmatrix} \begin{pmatrix} x_i \\ y_i \\ z_i \end{pmatrix}. \quad (6.1)$$

Here, the angles θ and ϕ are the zenith and the azimuth angle of the cosmic-ray air shower. Assuming a plain radio wavefront, the geometric delay is the amount of time that the radio wavefront needs to overcome the distance z'_i which is

$$\Delta t_i = \frac{z'_i}{c}. \quad (6.2)$$

Assuming a more realistic radio-signal form like a spherical wave with a curvature radius R_{curv} , the distance from the shower front to antenna i becomes

$$r_i = \sqrt{x_i'^2 + y_i'^2 + (R_{\text{curv}} - z'_i)^2} - R_{\text{curv}} \quad (6.3)$$

which results in a geometrical delay of

$$\Delta t_i = \frac{r_i}{c}. \quad (6.4)$$

For the presented measurements, the difference between a plain radio wavefront and a spherical wave is negligible due to the small size of the array and the small number of four available antennas.

After successfully beamforming the recorded radio signals, the cross-correlation (CC) beam can be used as a quality value for the coherency of the radio signals in the antennas. The cc-beam is defined as

$$\text{cc}(t) = \pm \sqrt{\left| \frac{1}{N_{\text{pairs}}} \sum_{i=1}^{N-1} \sum_{j>i}^{N-1} s_i(t) \cdot s_j(t) \right|} \quad (6.5)$$

with the radio trace $s_i(t)$ of antenna i and the number of antenna pairs N_{pairs} . The overall sign of the cc-beam is the sign of the summation before the absolute value is calculated. If the beamformed radio traces are coherent, the multiplication of the time traces during this time will always lead to a positive value that will be summed up over all antenna pairs. If the traces are not coherent, the multiplication will in some or all cases lead to negative results that decrease the cc-beam value or shift it into the negative range. For further information about beamforming and the CC-beam, the reader is referred to ref. [41, 42, 100].

For the analysis of the measured signals, the individual traces were beamformed using the shower direction reconstructed by the Mini-KASCADE detectors. The cc-beam was calculated individually for both polarizations. Possible radio events were selected by searching for a maximum of the cc-beam in coincidence with local or global maxima of the radio traces. With this procedure, several events were found that show a promising beamforming behavior. In Fig. 6.8, a comparison of the original radio traces and the beamformed radio traces of a recorded event is shown for the east-west polarization. For this plot, the time axis has been shifted so that possible radio signals should occur around 0 ns. Comparing both plots, the beamforming technique points out a possible

radio signal at around 40 ns whereas signals at -60 ns and at 0 ns are obviously incoherent when the radio signals are beamformed into the air-shower direction.

Individual interesting events were found with this method but no final confirmation of a cosmic-ray signal was possible for one of them which would need to include a simulation of the cosmic-ray event and a comparison with the actual measurement. Also, no statistically relevant accumulation of maxima in the cc-beam were found around the expected time of arrival of the radio signal. Performing beamforming of the radio signals and evaluating the beamformed radio signals by calculating the cc-beam certainly led to an improved analysis but the abilities of this method were mostly limited by the number of available antennas and the resolution of the direction reconstruction with the Mini-KASCADE detectors. In particular, an uncertainty in the direction reconstruction of 1° of the Mini-KASCADE reconstruction can lead to a uncertainty in the beamforming time delay of several nanoseconds which directly decreases the quality of the cc-beam. Since a proper analysis of the direction reconstruction of the deployed Mini-KASCADE detector array was not carried out yet, an uncertainty of 1° or more on the reconstructed zenith and azimuth might be reasonable.

6.5 CONCLUSION, PROSPECTS AND REMARKS

The hybrid engineering array is of great importance for the development, test, and maintenance of new particle and radio detectors for the IceCube Enhancement and played a key role in enabling the deployment of prototype antennas at the South Pole during this thesis. The antenna array provided proof of the ability to operate and perform measurements with the SKALA prototype antennas. Radio electronics for the South Pole deployment were designed based on the radio-noise strength recorded with the array and new antenna mechanical designs were first deployed and tested within the engineering array.

The engineering array provides the possibility to test new DAQ systems which was used regularly in the last year for several versions of the TAXI DAQ and will be of great importance regarding the development of a new generation DAQ system providing interfaces for three radio antennas and eight scintillation detectors (see chapter 4). Apart from the radio-detector development, the engineering array benefited also the development, maintenance, and improvement of the IceScint scintillation detectors. The engineering array provides the possibility to operate the scintillation detectors with an exact copy of the detector and DAQ hardware as it has been deployed at the South Pole. With this, tests and characterization measurements can be performed with an accessible detector system, new hardware and software can be tested under controllable conditions, and new detector systems can be tested and compared to old designs. This ability will benefit the test and characterization of a new scintillation-detector design that will digitize the recorded signals already in the scintillation-detector electronics and that is planned to be deployed at the South Pole in the season 2019–20.

During the test deployment of four SKALA radio antennas in the engineering array, measurements of the radio background and triggered measurements of cosmic-ray events were performed with the aim to identify cosmic-ray radio signals. The engineering-array site is not ideal for radio measurements due to the high pollution with RFI coming from offices, laboratories, and workshops very close to the radio antennas. Additionally, the radio FM band from 80–110 MHz dominates all other sources in this frequency range. Several promising radio events were measured but no cosmic-ray signals could be finally confirmed. Regarding the search for cosmic-ray radio signals with the hybrid engineering array, several improvements are possible that were not realizable during this thesis. An expansion of the Mini-KASCADE detector array would lead to a more accurate direction reconstruction that is necessary for a successful beamforming of the radio signals. Also, a more accurate antenna and detector position survey using GPS would directly lead to more accurate results. Additional frequency filters for filtering strong RFI bandwidths and a stronger amplification of the radio signal could benefit the signal-to-noise ratio of possible signals. Building upon the work presented in this chapter, the detection of cosmic-ray radio signals with the hybrid engineering array might be only one step ahead.

RADIO FRONT-END ELECTRONICS

The RadioTAXI DAQ is used to sample and digitize scintillation-detector and radio signals at the South Pole. RadioTAXI can sample 24 input channels by using *DRS4* sampling chips that operate at a sampling frequency of 1 GHz (see chapter 4). The DAQ is equipped with three *DRS4* chips with eight input channels each. One of the three *DRS4* chips samples the scintillation detector signals, the other two chips sample the radio signals of two radio antennas with two polarization channels each. For sampling the radio signal, the *DRS4* chips are operated in channel-cascading mode which reduces the number of effective input channels from eight to two per *DRS4* chip but increases the sampling length to 4096 sampling cells instead of 1024 cells of a single channel. A longer radio trace improves background studies, RFI suppression, and signal filtering. To be able to operate radio antennas and process the radio signals with RadioTAXI, new radio-specific electronic components have to be introduced into the electronic chain. Radio front-end electronics were designed, built and characterized that include power supplies for the antenna LNA, filter stages and additional amplifiers. Since the DAQ electronics at the South Pole are deployed without artificial heating, the resistance against low temperatures of down to -70°C of to be deployed electronics has to be investigated with care. Especially for the radio-signal processing, variation of the amplifier gain, the filter response or the frequency behavior of other components can lead to wrong results if the temperature dependence of the electronic response is unknown. Due to this, the radio front-end was characterized for temperatures from $+20^{\circ}\text{C}$ to -70°C to investigate and parameterize possible response variations. Due to a time-critical deployment of the radio hardware, detailed characterization measurements of the radio front-end electronics were carried out after deploying the electronics at the South Pole. These characterization measurements revealed several possibilities for improvement of the electronics which will enter new versions of the radio front-end.

A master's thesis dedicated to the development of the radio front-end and its characterization measurements can be found in ref. [101].

7.1 REQUIREMENTS ON THE RADIO FRONT-END ELECTRONICS

To include the radio signal processing into RadioTAXI, new electronic components like bias tees, frequency filters, and additional amplifiers have to be introduced into the system. Since a modification of the actual RadioTAXI was not possible, new electronics were placed on additional printed circuit boards (PCBs) that are in the following re-

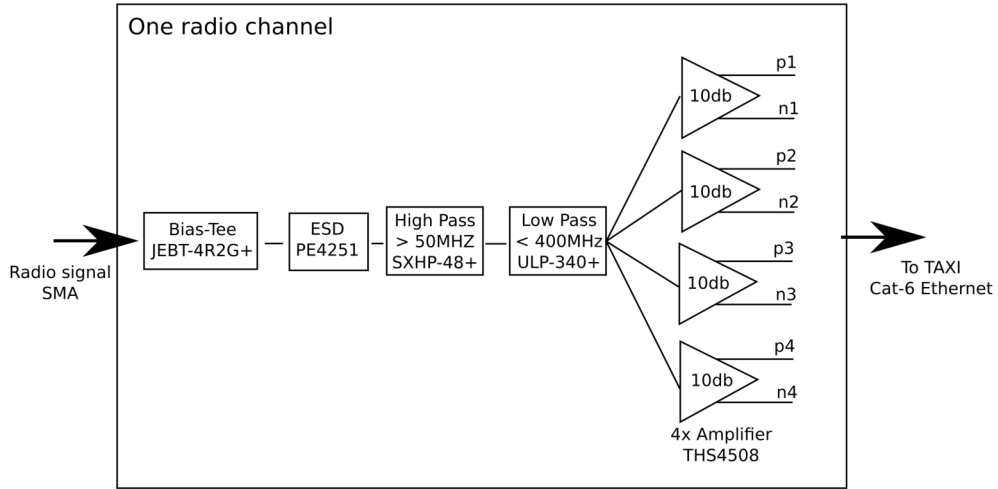


Figure 7.1: Block diagram of the radio front-end electronics.

ferred to as the radio front-end of the DAQ. In addition to technical requirements discussed in the following section, a low power consumption of additional radio electronics and a cost-effective design have to be aimed for especially regarding a future deployment of 32 detector stations with each one DAQ system.

In Fig. 7.1 a block diagram of the front-end electronics layout is shown. The front-end input is connected to the antenna LNA that outputs a $50\ \Omega$ -terminated, single-ended signal (see sec. 5.4 for more information about the LNA). The radio front-end includes a bias tee to power the antenna LNA, a protection against electrostatic discharge (ESD), a filter stage consisting of a high-pass and a low-pass filter and a fan out of the signal into four parallel amplifier circuits for each antenna polarization. As bias tee, a *JEBT-4R2G+* is used to set the +5 V bias point for the antenna LNA on the signal cable. After the bias tee, an ESD protection *PE4251* protects the following electronic parts and the RadioTAXI against sudden voltage peaks originating from electrostatic discharge. Such a protection is especially important for operation at the South Pole since wind and snow can charge metal structures like antenna arms that cannot discharge conventionally due to a not-existing ground and zero humidity at the South Pole. A high-pass filter *SXHP-48+* and a low-pass filter *ULP-340+* cut the signal bandwidth to 48–365 MHz. A filtering of the input signal is necessary to cut the dominant noise of the Galactic Center for low frequencies and to reject possible radio frequency interference (RFI) predicted at high frequencies above 400 MHz [57].

After filtering the radio signal, it is passively fanned out into four parallel amplifier circuits equipped with the differential amplifier *THS4508*. The signal fan-out enables the operation of the *DRS4* sampling chips on the RadioTAXI in channel-cascading mode which requires the input of an identical signal into all of the cascaded *DRS4* channels. The amplification is set to 10 dB which counteracts the attenuation resulting from the

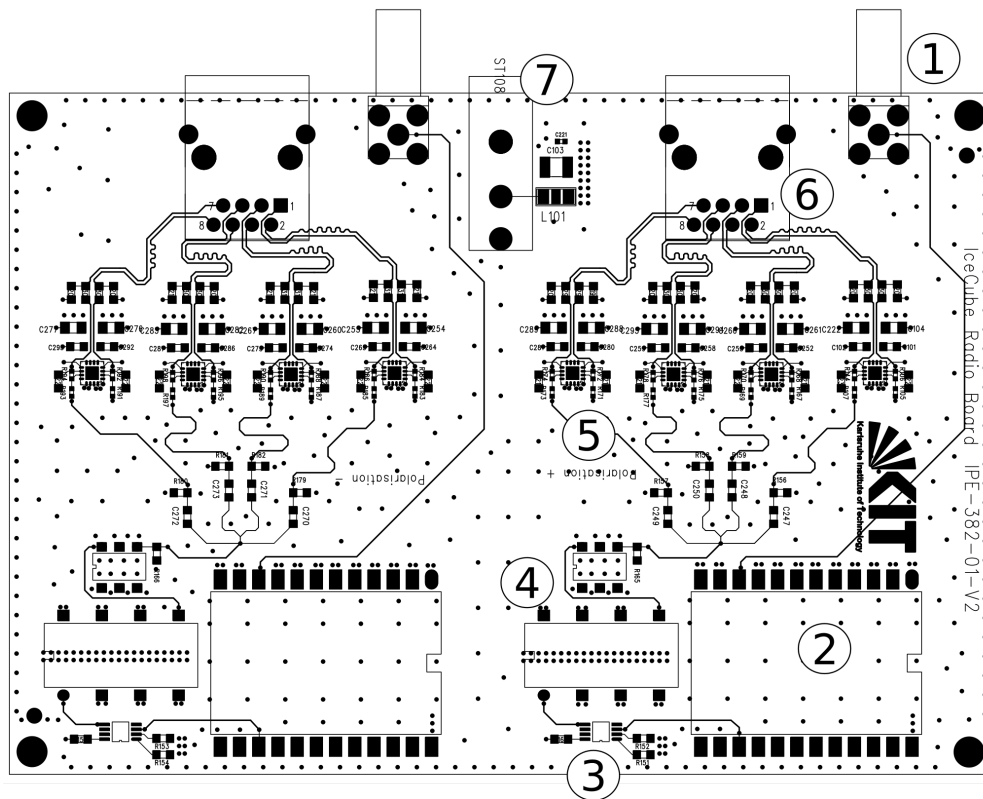


Figure 7.2: PCB layout of the front-end board. (1) SMA input, (2) bias tee, (3) ESD protection, (4) high-pass filter and low-pass filter, (5) amplifier circuits, (6) output RJ45 connector, (7) power input.

cables and the prior radio electronics. With this amplification, the amplifiers are sensitive up to frequencies of 1 GHz [102]. Each amplifier outputs a differential signal that is guided to the respective RadioTAXI inputs using CAT-7 Ethernet cables.

To route the CAT-7 cable outputs to the corresponding TAXI inputs an additional PCB is used that also houses DC/DC-converters which provide the bias voltage for the front-end electronics and the antenna LNA of +5 V. The DC/DC-converters were not placed on the actual front-end board to reduce possible RFI emitted by the converters.

7.2 A DETAILED VIEW TO THE RADIO FRONT-END BOARD

In Fig. 7.2 the PCB layout of a radio front-end board is shown. One board consists of two identical circuits and can process one antenna with two polarizations. Below, the electric circuit for one polarization (one channel) is described in detail.

The signal from the antenna LNA enters the board via an SMA connection (1). The bias tee (2) sets the bias point on the signal line and decouples the DC voltage of the signal

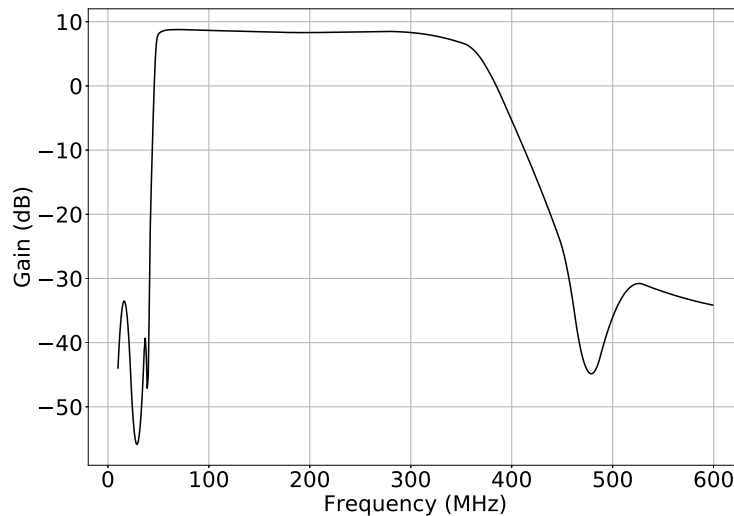


Figure 7.3: Calculated expectation of the gain pattern of the radio front-end electronics. The expected gain assumes an amplification set to 10 dB at the amplifier and takes the attenuation of the bias tee, ESD protection, high-pass and low-pass filter, and the frequency response of the amplifier into account. Attenuation values of the components were taken from their datasheets.

line from the further signal path. The following ESD protection (3) and the bias tee are connected to a power plane in the board which is delivering a constant voltage of +5 V against the ground. High-pass and low-pass filters are located at (4). After the low-pass filter, the signal is passively fanned out into four identical amplifier circuits using a via connection (5). The amplifier circuit is shown in Fig. 7.4 and will be described in more detail below. Exiting the amplifiers, a second capacitor in the signal lines of both positive and negative signal parts cancels the DC-voltage component introduced by the amplifiers. The DC point of the signal line is set with a 1 k Ω resistor to ground after the capacitor. Finally, the signal lines are routed to the RJ45 output connectors (6). The +5 V bias voltage and the ground level are provided through a 2-pol connector (7). The incoming +5 V line is filtered for electromagnetic interference (EMI) using a NFM60R EMI filter between the voltage input and the voltage plane on the board.

Each amplifier circuit is set to amplify the radio signal with a gain of 10 dB. This gain value was chosen to counteract the attenuation of the LMR400 signal cable, which is about -2.5 dB for 400 MHz, and the attenuation introduced by the prior electronics and the later interface to RadioTAXI. Since the amplification of the radio signal is directly influencing the upper and lower energy threshold of the radio array, the ideal amplification factor has to be set with care and the currently chosen value of the amplification of 10 dB will change in future front-end designs. The expected gain behavior of the current front-end board is shown in Fig. 7.3 assuming an amplification of 10 dB. The expected gain includes the attenuation of the bias tee, the ESD protection, and the

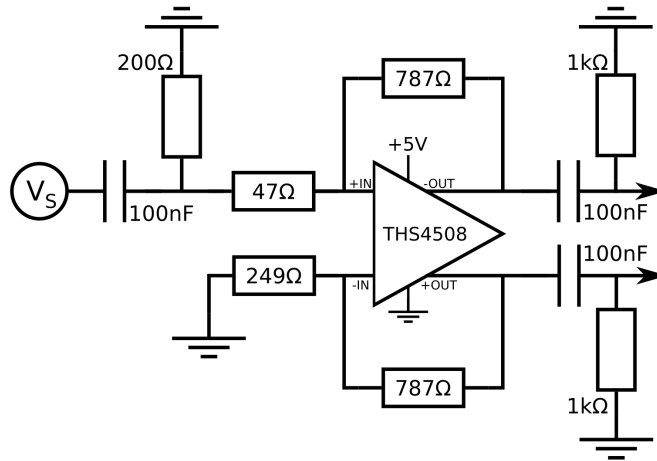


Figure 7.4: Schematic of the front-end amplifier circuit for one amplifier. The input signal V_S is the radio signal after filtering and after fan-out into the four parallel amplifiers. After the signal passes the presented amplifier circuit, it is guided to the TAXI inputs.

filters and also takes the decrease of the amplifier's gain with higher frequencies into account. Therefore, the expected gain does not reach its setpoint of 10 dB. Regarding the radio electronics, the highest amount of attenuation in the pass-band is originating from the ESD protection that attenuates the signal with about 0.5 dB [103].

A closer look to the amplifier circuit

Since the amplifier circuit is the key element in the radio front-end, a more detailed block diagram of the amplifier circuit for one of the four amplifiers is provided in Fig. 7.4. The filtered, fanned out, and $50\ \Omega$ -terminated single-ended signal enters the amplifier circuit as V_S . Each amplifier circuit is decoupled with a $100\ \text{nF}$ capacitor from the fanout point and the other amplifier circuits. The gain of the amplifier is defined by the resistors in the feedback loop. Regarding the positive amplifier input, the $200\ \Omega$ resistor and the $47\ \Omega$ resistor in the signal line can be seen as one resistor with an effective resistance of $247\ \Omega$. The gain is

$$G = \frac{787\ \Omega}{247\ \Omega} = 3.19 = 10.08\ \text{dB}. \quad (7.1)$$

The resistors at the negative amplifier input and in its feedback loop are chosen to match with the resistors at the positive input. To test the single amplifier circuit and the response of four parallel amplifier circuits, the circuits were simulated with the *TINA-TI* simulation framework¹ [104] which is a *SPICE*-based software provided by the manufacturer of the amplifiers. The simulated gain predictions do not always

¹ *Tina-TI* was used in version *v9.3.200.277 SF-TI*

agree with the actual measurement. The reason for this is probably the limited amplifier model used in the simulation which does, for example, not include any effects of impedance and impedance mismatch. Nevertheless, the simulation framework was used for tests of first designs and the development of possible amplifier circuits. Further information about the simulations performed with *Tina-TI* can be found in [105]. After investigating the amplifier circuit in detail and performing characterization measurements that will be presented below, several deficits in the proposed amplifier circuit were found. These deficits affect mostly the amplifier input impedance matching and the attenuation of standing waves in the amplifier outputs. An improved second version of the circuit was designed and is presented in the appendix section A.1.

7.3 CHARACTERIZATION MEASUREMENTS

Initial tests of the front-end functionality were performed before the deployment of the electronics at the South Pole to guarantee successful operation. Detailed tests of the electronics and a characterization for temperatures down to -70°C were performed after the deployment of the DAQ system with a replica of the deployed hardware. The results of these detailed measurements will enter new iterations of the electronics design.

7.3.1 *Low-temperature characterization*

The characterization procedure for the front-end electronics was similar to the characterization setup used for the LNA characterization shown in section 5.4. Fig. 7.5 shows sketches of the two measurement setups that will be described in the following. The radio front-end board was placed inside the temperature chamber *VT 7021* which can cool down the interior temperature to a minimum of -72°C . The calibration source *RSG 1000* was used as an input-signal generator which emits a pulse containing frequencies up to 1 GHz. The differential outputs of the front-end electronics were recorded with a *WaveRunner 610Zi* oscilloscope with a sampling rate of 20 GS/s. The single-ended signal was calculated from the recorded differential signals by subtracting the positive and the negative differential output of each amplifier in the offline analysis. The total gain of the front-end electronics was derived by comparing the calibration-source input signal and the output of the electronics.

The front-end electronics are equipped with a *RJ45* output connector which guides the output signals to a connector board attached to the TAXI DAQ that fans out the signals into the TAXI inputs. To include the effects of the *RJ45* connector and the CAT-7 Ethernet cable in the characterization, an additional PCB was designed and built to fan-out the Ethernet-cable lines coming from the front-end electronics into *LEMO* connectors that can be connected to the oscilloscope via *RG58* coaxial cables. Doing so, an impedance mismatch is introduced into the system since the Ethernet cable has a

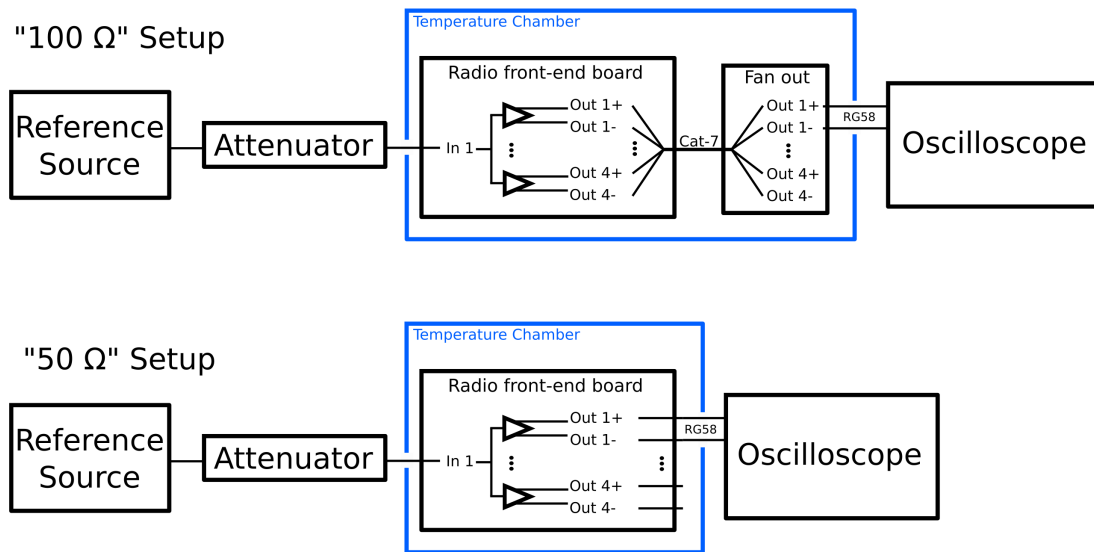


Figure 7.5: Sketches of the measurement setup to characterize the radio front-end board. Only one input channel (*In 1*) of the radio front-end board is shown for simplicity. For both setups, the attenuated reference-source signal was measured by directly attaching the attenuator output to the oscilloscope. **Top:** Characterization setup including the CAT-7 Ethernet cable and an additional fan-out board to fan out the Ethernet signal lines into *RG58* cables. **Bottom:** Characterization setup with a direct connection of the radio front-end board to the oscilloscope using *RG58* cables.

100 Ω line impedance which is connected to a *RG58* cable with 50 Ω line impedance and the oscilloscope that measures the voltage over a 50 Ω termination resistor.

To avoid the effects of the impedance mismatch in the characterization results, the *RJ45* connector was removed in one of the two circuits of a front-end board. *RG58* cables were soldered directly to the outputs of one amplifier and the remaining amplifier outputs were terminated with 50 Ω to ground. With this setup, an impedance mismatch after the front-end electronics output should not occur. Characterization measurements were performed individually for both setups and the results will be presented in the following.

Attenuation effects originating from different cable lengths during the measurement of the calibration-source and the front-end electronics measurements are corrected for in all presented results.

7.3.2 Characterization results

In Fig. 7.6, the results of the characterization measurement at room temperature are shown. The plot shows the results for both setups, one with a known impedance

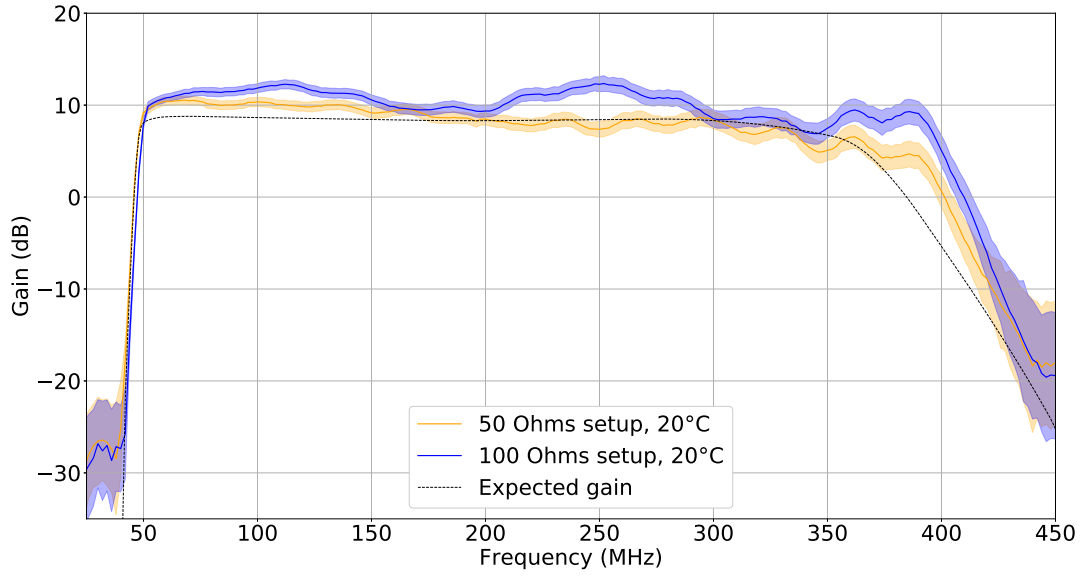


Figure 7.6: Gain measurement of the front-end board at room temperature. The gain was measured using the $100\ \Omega$ setup including the Ethernet cables and a fan out into Lemo connectors and the $50\ \Omega$ setup with coaxial cables soldered directly to the front-end board. The expected gain behavior from Fig. 7.3 is included as dashed black line for comparison.

mismatch in the signal output line ($100\ \Omega$) and one with a constant $50\ \Omega$ impedance matching. The plot also includes the expected gain behavior shown in Fig. 7.3.

For both measurement setups, the radio front-end amplifies the incoming signal with about 10 dB and the effect of the high-pass and low-pass filter are visible. Both measurements show a non-flat gain behavior in the pass-band frequency range from 50–350 MHz. Regarding the measurement setup with a known impedance mismatch in the signal output line, this behavior is expected. The other measurement setup shows this behavior too, even if it is not as strong as in the first case. This could indicate that there is a remaining impedance mismatch in the output signal line or in the amplifier circuit.

In Fig. 7.7, the gain in the pass-band frequency range of both setups is shown in detail. Linear functions are fitted to the gain spectrum in the frequency range of 60–390 MHz that result in

$$G_{50\Omega}(f) = (-13.35 \pm 0.52) \cdot 10^{-3} \frac{\text{G}}{\text{MHz}} \cdot f + (12.13 \pm 0.012) \text{ dB} \quad (7.2)$$

$$G_{100\Omega}(f) = (-10.28 \pm 0.85) \cdot 10^{-3} \frac{\text{G}}{\text{MHz}} \cdot f + (12.13 \pm 0.012) \text{ dB}. \quad (7.3)$$

The maximum deviation of the measured gain values from the fit ΔG_{\max} with

$$\Delta G_{\max,50\Omega}(f) = 1.63 \text{ dB} \quad (7.4)$$

$$\Delta G_{\max,100\Omega}(f) = 2.39 \text{ dB}. \quad (7.5)$$

is significantly higher for the 100Ω impedance mismatching setup which is expected due to the obvious impedance mismatch.

Comparing the results with the expected gain spectrum plotted as dashed black line in Fig. 7.7 and 7.6 it is clearly visible that the measured gain is higher than expected and has an overshoot for high frequencies above 350 MHz which should be attenuated by the low-pass filter. In the next iterations of the front-end electronics, which include a new design of the amplifier circuit, this unwanted behavior should vanish.

Although the gain spectrum is not as flat as expected, the variations of the gain in the bandwidth of the pass-band stay constant over time and can be taken into account when reconstructing a measured signal. Thus, the measured gain variations over frequency have no negative effect on the result of a cosmic-ray measurement. However, the measurement uncertainty does influence the cosmic-ray measurement. The uncertainty in the measured gain increases with frequency due to a decreasing signal strength of the reference source and reaches values of about ± 1.5 dB at 400 MHz. This uncertainty is directly influencing the uncertainty of the measured signal amplitude and would introduce an uncertainty in the amplitude of $\pm 18\%$. Although the reduction of this measurement uncertainty plays a subdominant role for the presented prototype electronics, it has to be reduced for future versions of the radio front-end. This could be realized by improving the measurement setup with a direct conversion of the differential output signal to a single-ended signal before the measurement with the oscilloscope and by using a frequency generator with adjustable bandwidth and higher output power for high frequencies. The measured amplification is sufficiently high to ensure a successful measurement of cosmic-ray air showers with this radio front-end. The target gain will be reevaluated for next front-end versions for which also the measured gain oscillations will be investigated and fixed, if possible.

7.3.3 *Temperature dependencies*

Special care was taken to investigate the possible effects of a changing ambient temperature and low temperatures on the electronics response. For this, characterization measurements were performed at various temperatures from $+20^\circ\text{C}$ to -70°C . In Fig. 7.8, the front-end gain spectra for the highest and the lowest available temperature of $+20^\circ\text{C}$ and -70°C are shown for both measurement setups. A slight increase in gain with decreasing temperature is expected since the attenuation of the filters and the ESD protection decreases with decreasing temperature [103, 106, 107]. Regarding the measurement setup in which the Ethernet cable has been used to guide the amplified

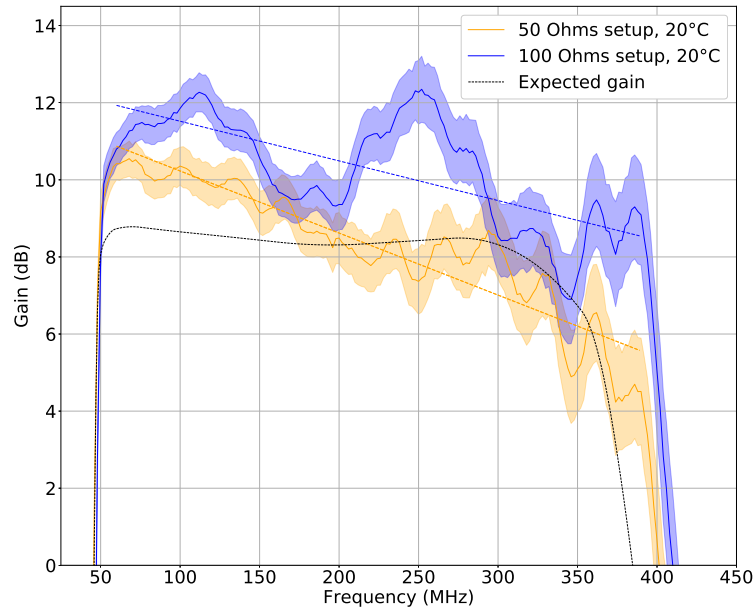


Figure 7.7: Gain measurement of the front-end board at room temperature with a zoom into the bandwidth of the pass-band. Linear fits to the slope of both measured spectra are plotted as dashed lines in the respective color of the measurement. The expected gain behavior is plotted as dashed black line for comparison.

signals to the RadioTAXI inputs, also a slight decrease of attenuation of the Ethernet cable with a decrease in temperature is expected although this effect should be not significant due to the short length of the Ethernet cable of 30 cm.

To investigate the gain variation with temperature in detail, the gain difference in the pass-band bandwidth between the -70°C and the $+20^{\circ}\text{C}$ measurement for both measurement setups is shown together with the error-propagated standard deviation of the measurements in Fig. 7.9. The average gain difference of both measurements has a similar shape and increases with frequency from about 0.5 dB at 60 MHz to about 1.5 dB at 390 MHz. A similar temperature dependency of both measurements is expected since the change in gain should originate mostly from temperature dependencies of the electrical components, PCB lines and cables which should behave similarly in both setups. For both setups, the gain difference increases with frequency up to a maximum of 1.5 dB for the measurement including Ethernet cables. If the variation of gain with temperature would be left uncorrected for the signal reconstruction and if we assume a gain variation of 1.5 dB, this would introduce a 18% uncertainty on the measured signal amplitude¹. This uncertainty is, of course, overestimating the actual temperature differences the deployed electronics will experience. The DAQ of

¹ $1.5\text{dB} = 20\log_{10}(1.18)$, variation in gain $1-1.18$, gives 18% uncertainty

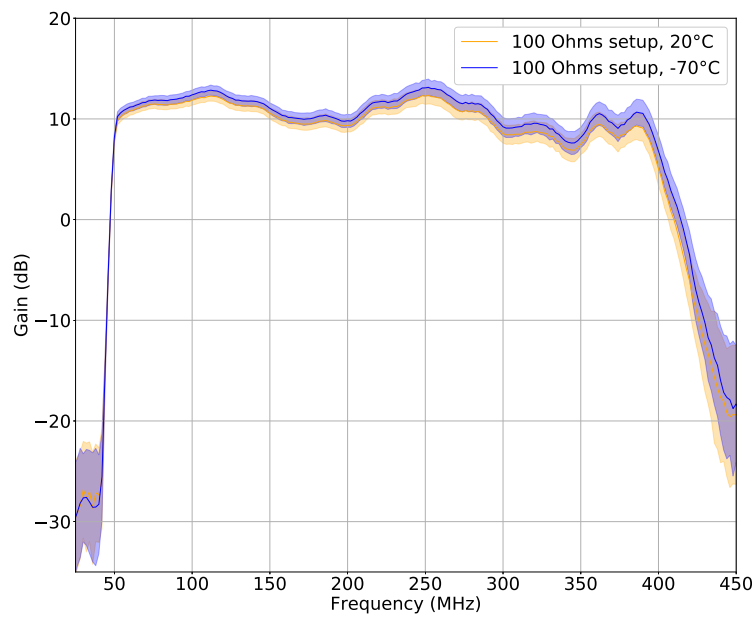
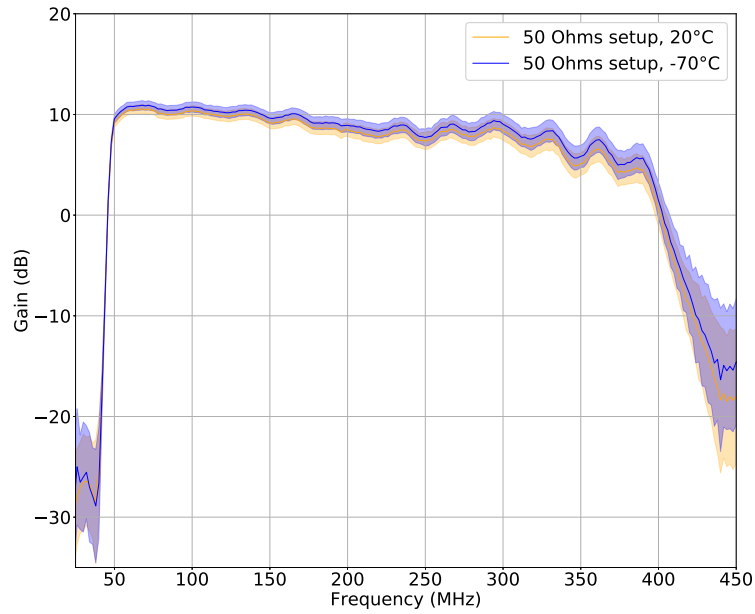


Figure 7.8: Gain measurement of the front-end board with both measurement setups at temperatures of +20°C (orange) and -70°C (blue).

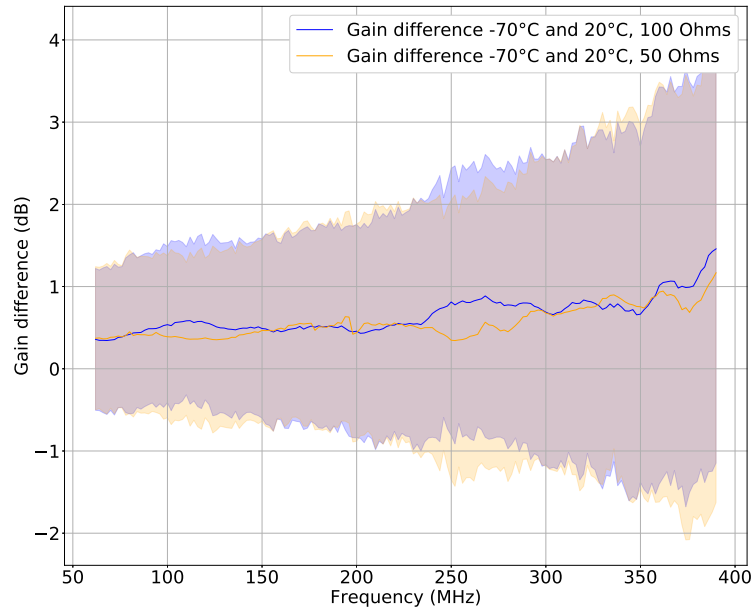


Figure 7.9: Gain difference between measurements at -70°C and $+20^{\circ}\text{C}$ for both measurement setups. Since the temperature-dependent difference in the gain should not be dependent on the measurement setup but the front-end electronics, a similar behavior for both setups is expected.

the prototype station is placed in plastic housings buried into the snow and will for future deployments be located in a thermally insulated metal box on the snow surface. With this, the temperature changes should be significantly reduced. As a comparison, if we assume a temperature fluctuation of -20°C to -70°C (which is still an overestimation), the gain variation reduces to 0.8 dB in maximum that gives a 9% uncertainty on the signal amplitude if the temperature is unknown. In the target bandwidth of 100–190 MHz the gain uncertainty stays below 0.6 dB which resembles an uncertainty of 7.1%. The measurement uncertainties for this analysis are high but can be reduced for measurements of next-generation electronics by improving the measurement setup. During the actual operation, the ambient front-end temperature will be monitored and the gain can be corrected according to the characterization results of the front-end electronics. With this, temperature effects changing the amplification can be corrected in the later analysis and the uncertainty in the signal amplitude introduced by the radio front-end reduces to the measurement uncertainty of the gain measurement.

Several changes will be included in the next generation of the radio front-end. First of all, the amplifier circuit will be improved to enable a proper termination of the input signal and an attenuation of reflections in the output signal line (see appendix section A.1). An ESD protection in the radio front-end electronics is not necessary

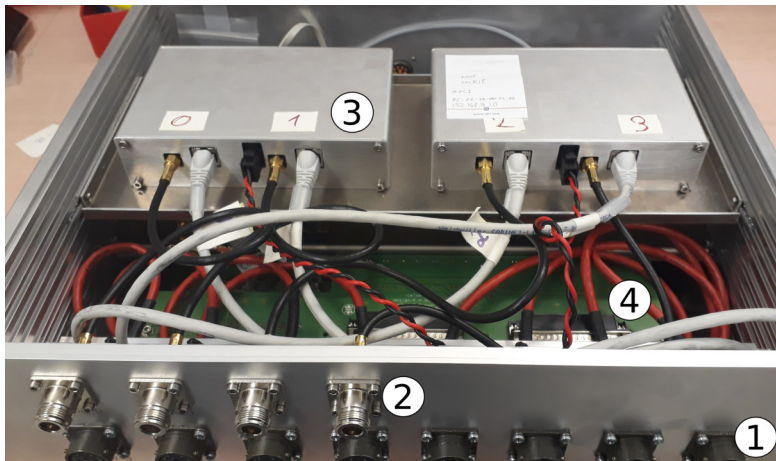


Figure 7.10: Picture of the DAQ system as it was deployed at the South Pole in January 2019. (1) scintillation-detector inputs, (2) radio-antenna inputs, (3) radio front-end boards inside a metal housing that is used for additional shielding of the radio electronics against RFI, (4) (below the cables) *IceTad* board connecting the scintillation detector cables to the TAXI inputs.

since the antenna LNA is equipped with an ESD protection at the LNA inputs and the RadioTAXI electronics are protected with Schottky diodes from voltage peaks. Therefore, the ESD protection will be removed on the radio front-end board. Next front-end versions will directly connect to the TAXI input connectors which will reduce noise introduced by the additional radio hardware. New input connectors for connecting the radio front-end to the RadioTAXI inputs are under discussion to avoid the strong attenuation for high frequencies of the current *Sub-D 37* connectors. The deployment of the next front-end generation is planned for January 2020.

7.4 INTEGRATION INTO THE DAQ SYSTEM

In the DAQ setup deployed in January at the South Pole, two radio front-end boards are connected to the RadioTAXI to process the signals of two radio antennas with two polarization channels each. An additional PCB is used to interface the front-end board outputs to the RadioTAXI inputs. This interface PCB fans out the incoming signals from the Ethernet cables into the inputs of TAXI and houses the DC/DC converters which transform the 24 V TAXI power output into 5 V bias voltage for the front-end amplifiers and the antenna LNAs. The DC/DC-converters were not placed on the front-end board to prevent possible RFI noise. The radio boards are surrounded by a metal shielding to further prevent RFI noise from the TAXI electronics.

Fig. 7.10 shows a picture of the DAQ setup as deployed at the South Pole. Ports for signal cables from the scintillation detectors (1) and the antennas (2) are located at the front. The antenna-signal inputs are connected inside of the TAXI housings via 30 cm

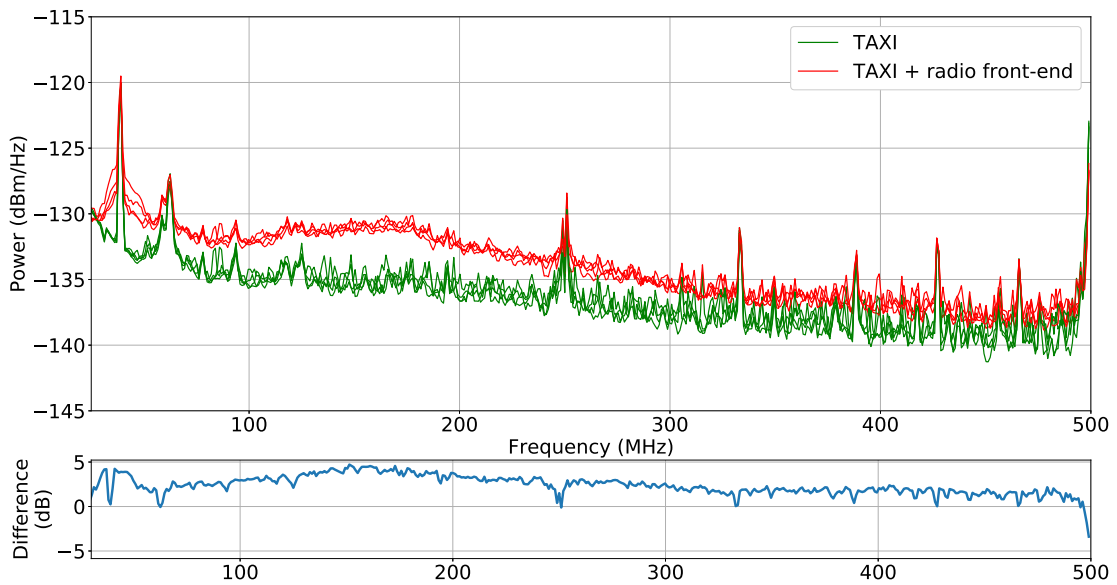


Figure 7.11: Measurement of the TAXI baseline noise with and without radio front-end electronics attached to TAXI. The baseline noise is visibly increasing when radio electronics are attached to the TAXI inputs and powered. The bottom plot shows the difference of the measured baseline spectra.

RG58 cables to the radio front-end boards which are sitting inside an additional metal housing (3). The filtered, amplified and fanned out radio signals are transferred with Ethernet cables to the TAXI inputs. The interface PCB to TAXI is not visible in this picture. The scintillation detector cables inside the TAXI housing are guided to the IceTad board (4) which is connected to one TAXI input connector.

7.4.1 Influence of the front-end electronics on the background noise

Measurements were performed to investigate the influence of the additional radio electronics on the baseline noise of TAXI. A low internal noise is especially important for the proposed search for gamma rays at the very low edge of the detection limit reachable with radio detectors. The lowest detection limit should be set by external noise sources, which are radio sources in our galaxy, and should not be set by artificial noise produced in the read-out electronics itself. Due to this, every additional noise contribution to the overall electronic noise in the DAQ system is critical and should be reduced as much as possible.

Fig. 7.11 shows the noise contribution of the radio front-end electronics to the overall baseline noise of TAXI. For the measurement, the radio front-end electronics were attached to the TAXI inputs and powered with open inputs. For both setups, four TAXI channels were read out and are drawn in the plot. An increase in noise when the ra-

dio front-end electronics are attached to TAXI is clearly visible. The bottom plot in Fig. 7.11 shows the difference in units of dB of the mean values of the four channels for both setups. For frequencies between 100 MHz and 200 MHz the increase of noise introduced by the radio electronics goes up to 5 dB. This increase of baseline noise would decrease the detection threshold of a radio signal by about a factor of two¹ if the electronic noise sets the lower limit for a detection.

Reasons for this increase in baseline noise produced by the radio electronics are the additional PCB surfaces of the radio front-end board and the connector board to TAXI, the additional electronic components in the signal line like filters, bias tee and amplifiers, as well as the CAT-7 Ethernet cable connecting the radio front-end board to the connector board. In all cases, external noise can be picked up by the signal lines in the PCBs and the cable which adds up to the internal TAXI noise. The additional electronic components in the signal line can introduce thermal noise contributions. In further iterations of the electronics design, the radio front-end will be directly connected to the TAXI inputs. Doing so, an additional interface PCB to TAXI and Ethernet cables connecting the front-end board to the interface are no longer needed which will decrease the noise introduced by the radio electronics.

7.4.2 Test of the full signal chain

After characterizing the radio front-end, a measurement of the full system including the radio front-end, the interface to RadioTAXI and the actual RadioTAXI DAQ to digitize the signal is essential to fully characterize the DAQ system. This is especially important since the behavior of the TAXI system for high-frequency signals in the radio regime was never investigated before. Since the actual RadioTAXI was not available, the presented measurements are performed with a prior-version IceTAXI which only differs in the number of input channels (IceTAXI: 8, RadioTAXI: 24). The analog and digital electronics are the same for both versions. This is also true for the procedure of how the baseline is adjusted to the center of the dynamic range of the *DRS4* sampling chips. As described in chapter 4, the baseline for IceTAXI and RadioTAXI is per default set to the lower limit of the dynamic range which is ideal for processing particle-detector signals with only positive signal deflections. Since radio signals are oscillating around the baseline with positive and negative signal contributions, the baseline has to be shifted to the center of the dynamic range. For IceTAXI and RadioTAXI, this is realized by applying an offset voltage to the differential signal lines before the preamplifier of the TAXI board. Apart from using IceTAXI instead of RadioTAXI, which makes no difference for the actual measurement, the measurement setup resembles the one deployed at the South Pole in season 2018–19, including the radio front-end, an interface of the front-end to the TAXI inputs with Ethernet cables, an interface PCB and the TAXI system. The bias voltage for the radio electronics is supplied

¹ $5\text{dB} = 20 \cdot \log_{10}(1.77)$ which gives an increase of noise level of 1.77.

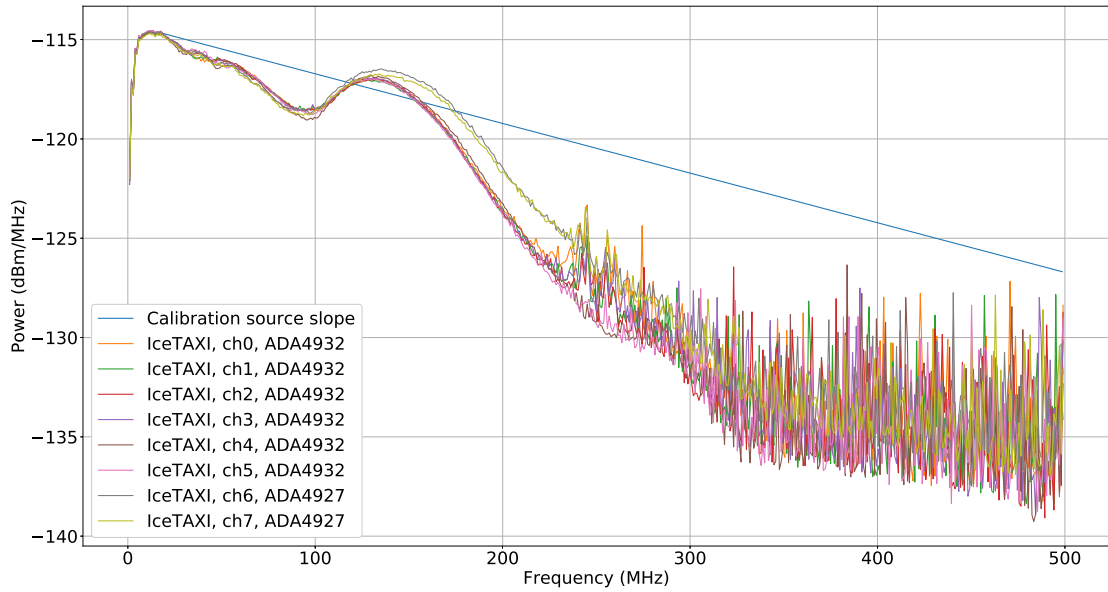


Figure 7.12: Frequency response of the TAXI DAQ system. A calibration source was used as input and the slope of the calibration source signal is plotted as blue line in the spectrum for comparison. The measurement was performed with an IceTAXI DAQ system that resembles the DAQ system deployed at South Pole in season 2018–19 best. Channel 6 and 7 of the IceTAXI DAQ were equipped with a high-frequency amplifier *ADA4927*, the other IceTAXI input channels used the default amplifier *ADA4932*.

by TAXI and transformed to 5 V using the DC/DC converters on the interface PCB. Like in the characterization measurements discussed in sec. 7.3, the calibration source *RSG 1000* was used as input of the radio front-end and as reference. For the direct measurement of the calibration source signal with TAXI, the single-ended calibration source signal was transformed to a differential signal using a *ADT-IWT* transformer and the same measurement setup as for the characterization of the TAXIs ADCs in [94].

Frequency spectrum measurements

To measure the general radio-frequency response of the TAXI system, the calibration source was directly attached to the TAXI input without additional radio front-end electronics. Fig. 7.12 shows the frequency spectra of the signal sampled with TAXI for all eight TAXI input channels. Fig. 7.12 also includes the expected frequency slope of the calibration-source signal for comparison. It is clearly visible, that the digitized signal spectrum is not corresponding to the expectation. For frequencies below 150 MHz a spectrum behavior similar to an impedance mismatch is observed. For frequencies higher than 150 MHz, the spectrum rapidly falls off into the noise floor starting at around -130 dBm/Hz with a slight bump at frequencies of around 270 MHz. This be-

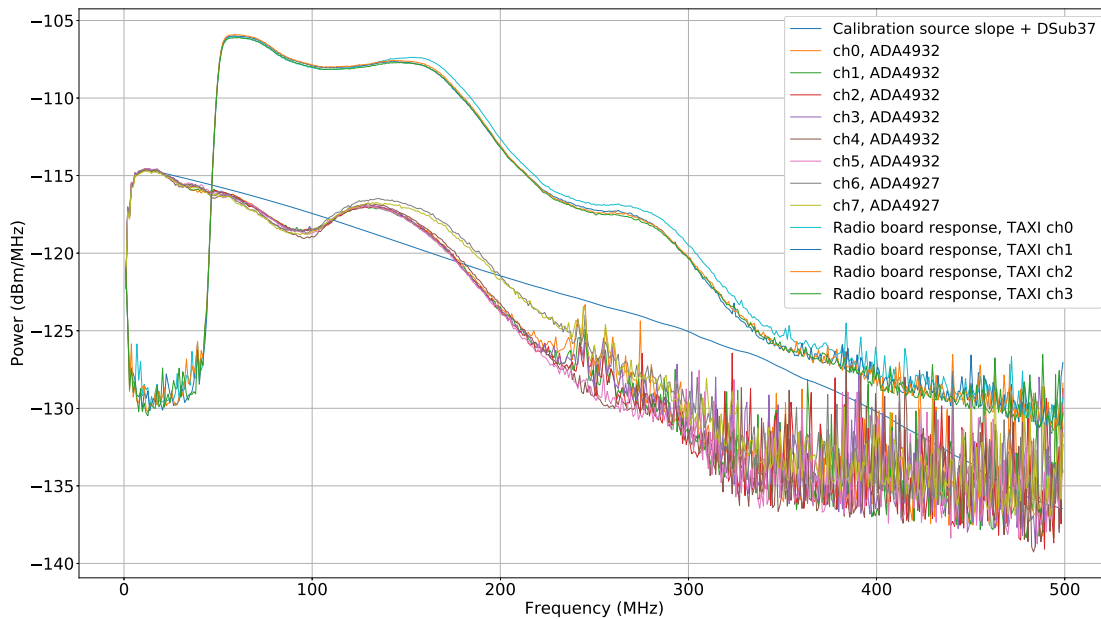


Figure 7.13: Frequency response of the IceTAXI DAQ system as it was shown in Fig. 7.12 together with the frequency spectrum of the full signal chain including the radio front-end electronics. The same calibration source was used for both IceTAXI-only and full-system measurements. The additional amplification of the radio front-end electronics is visible starting at 50 MHz. The calibration source slope was corrected for the attenuation of the TAXI input connector for comparison.

havior stays the same for different amplitudes of the input signal which excludes any effects of saturation of the TAXI electronics.

As a first approach to prevent this high-frequency attenuation, the pre-amplifier *ADA4932* in the TAXI analog signal path before the DRS4 sampling chip was exchanged for TAXI channels six and seven with an alternative amplifier *ADA4927* that has a -3 dB bandwidth for frequencies up to 2.3 GHz at a gain of 1. With these high-frequency amplifiers, the overall situation stays the same although the decrease in power is slightly shifted to higher frequencies due to the stronger amplification of the new amplifier.

Including the radio front-end into the signal chain to test the full-system behavior does not change the overall spectrum form as it is visible in in Fig. 7.13. Like is was seen in the measurements with the calibration source directly attached to TAXI, the radio front-end measurements show an impedance-mismatching-like spectrum for frequencies lower than 150 MHz and a rapid decrease in power for frequencies higher than 150 MHz with a bump around 270 MHz. Due to the strong attenuation of high frequencies, the effect of the front-end low-pass filter at around 400 MHz is not visible anymore.

Both setups show the same spectrum shape but only have the TAXI input connector

and the TAXI analog signal path in common which suggests that the origin of this behavior has to be searched for on the TAXI side. The TAXI input connector is a *Sub D* connector with 37 contacts. Measurements of the *Sub D* connector attenuation show an increasing attenuation with frequency up to an attenuation of about 5 dB for a frequency of 500 MHz (see Fig. 7.14). Since a differential signal is transferred through the connector, the attenuation of the connector has to be doubled when analyzing the resulting single-ended signal. In Fig. 7.13, the attenuation originating from the *Sub D* connector is included in the slope expectation of the calibration source. Although the resulting connector attenuation is strong, it cannot explain the sudden decrease of signal power for frequencies higher than 150 MHz.

Regarding the analog signal path of TAXI, all electronic components should guarantee

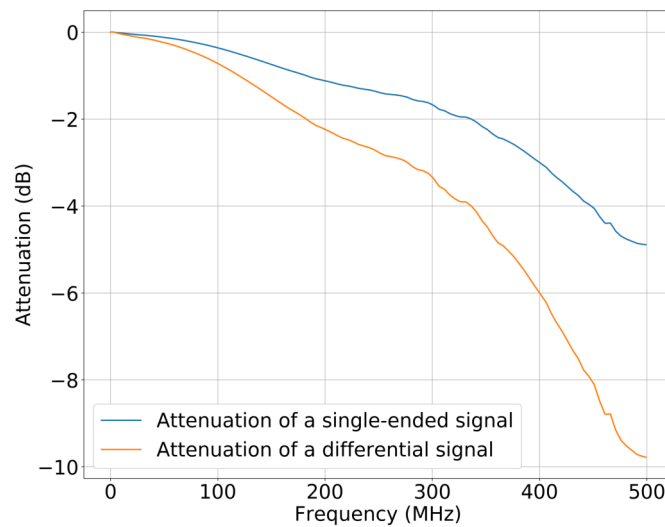


Figure 7.14: Attenuation measurement of the *Sub D* 37 TAXI input connector with a network analyzer. The measurement shows the attenuation of a single-ended signal passing the connector. If a differential signal passes the connector, both positive and negative signal parts are attenuated which results in twice the attenuation as for a single-ended signal. This is indicated as orange line in the plot.

a stable operation up to at least 560 MHz. Care has to be taken on the baseline shift that enables the sampling of positive and negative radio signals. For the TAXI version deployed at the South Pole and used in the presented measurements, the baseline shift has been realized by setting the DC level of the positive part of the differential input signal to 0.5 V. Although the output voltage range of the TAXI preamplifier *ADA4932* should be capable of handling this additional DC component, the amplifier response might differ from nominal operation. In the next versions of the TAXI DAQ (Uber-TAXI), the needed DC voltage level in the signal line will be set as a common-mode voltage directly at the amplifier which should eliminate possible problems introduced by setting the baseline DC voltage before the amplifier input. Concluding results on

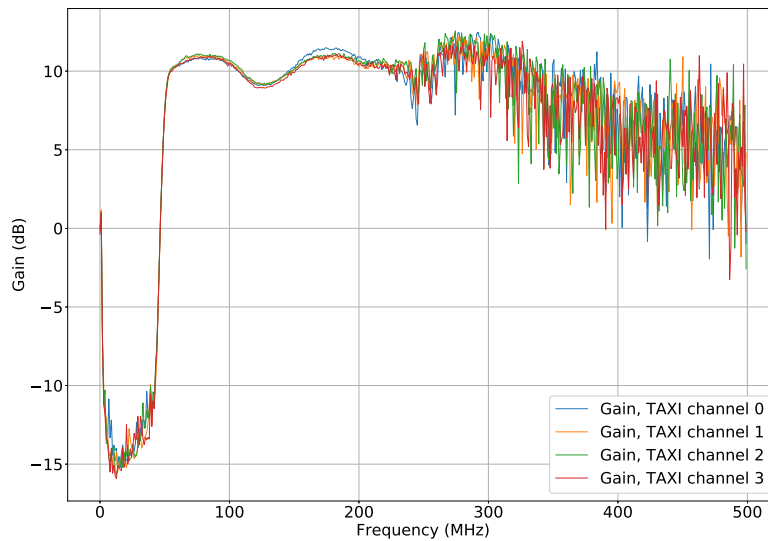


Figure 7.15: Measured gain of the full system including IceTAXI, the radio front-end electronics and the interface between both. The gain oscillates around the target gain of 10 dB before it vanishes into the noise floor of the IceTAXI measurement.

the origin of this unwanted behavior or even a solution to this problem was not obtained during this thesis. Final remarks will be given after looking at the full-system amplification in the next section.

Overall gain of the full signal chain

Due to the strong attenuation of high frequencies by the TAXI electronics described above and shown in Fig. 7.13, a final result for the total gain of the full system cannot be obtained for the full frequency range. Fig. 7.15 shows the measured gain that is defined as the difference of the reference calibration-source signal and the output of the radio front-end electronics, both measured and digitized using the TAXI DAQ. In the gain spectrum, the increasing flank of the front-end high-pass filter is visible. In the pass-band bandwidth starting at 50 MHz, the gain oscillates around the expected value of 10 dB. This oscillation can be understood by looking at the measured spectra of the calibration source and the front-end electronics (see Fig. 7.13): Although the structures in the gain, like a dip in the spectrum at around 100 MHz, a peak at 120 MHz, and a second peak at around 270 MHz, seem to be correlated in both spectra, they are slightly shifted in frequency between each other which generates the oscillating gain pattern. For frequencies higher than 250 MHz, the signal of the calibration source measured with TAXI starts to vanish into the noise floor and the calculated gain is no longer meaningful. Due to the higher noise floor in the front-end measurement than in the calibration-source measurements, the gain does not decrease below zero but converges to a 5 dB level which is just the difference of the two noise

floor levels. A reasonable conclusion about the gain of the full system is only possible until 200 MHz and, regarding this unexpected and until now not explainable TAXI frequency response, it is not clear how much trust can be put into this result.

Conclusion and remarks on the full-system measurement

The results of the presented attempt to characterize the full radio-signal chain with the TAXI DAQ are obviously depressing. The measurements reveal an unexpected steeply falling frequency response of the TAXI system for frequencies higher than 150 MHz of that the origin is yet unknown. The frequency bandwidth in which a total gain of the system is predictable is hardly reaching 200 MHz before the measurement is dominated by baseline noise. This covers the target measurement bandwidth of 100–190 MHz [44] which makes measurements possible but it is for sure not the behavior aimed for. Better measurement results would have been pleasant but important lessons can be learned to improve next versions of the DAQ.

To categorize these results, the reader shall be reminded that this is the very first measurement of a radio data-acquisition system in the prototype phase. Since the TAXI DAQ was designed to read out signals from photomultiplier tubes and silicon photomultipliers, the frequency response for radio frequencies was not measured or evaluated until now. Also, the TAXI DAQ system used for this measurement is still under development which especially holds for the firmware of the system¹. Signal artifacts were recorded during the presented measurements like a floating signal position in the trace, double peaks and empty traces that point towards a timing or trigger-distribution issue in the TAXI field-programmable gate array (FPGA). For the presented analysis of the measurements, the recorded signals were cleaned for these obviously wrong measurements but a remaining influence on the cleaned data cannot be excluded. Next firmware versions will for sure lead to a better understanding of the TAXI frequency response.

Nevertheless, the overall spectrum form cannot be explained with FPGA firmware issues but has to have its origin in the analog electronics of the TAXI input. As a first guess, the artificial shift of the *DRS4* baseline of +0.5 V for the positive part of the input signal can influence the *ADA4932* amplifier response and can distort the frequency bandwidth of the amplifier in a way like it has been measured. By replacing the *ADA4932* with the high-frequency alternative *ADA4927*, the frequency bandwidth should stay stable until circa 1 GHz for large signal amplitudes [108] which was not observed in the measurement (see Fig. 7.12). In the next TAXI version, UberTAXI, the baseline shift will be introduced as a common-mode voltage at the amplifier itself which should eliminate any problems originating from the current solution.

Second, the 37-pol *Sub D* TAXI input connectors attenuate high-frequency signals with an unwanted high attenuation that cannot explain the overall spectrum shape

¹ Firmware version *icescint_180904_00*

but might contribute to the problem. For next TAXI versions, the connector could be replaced by more high-frequency suited alternatives to prevent this unwanted attenuation.

More measurements with different versions of the TAXI DAQ are necessary to circle in the problem and to investigate the effect of different hardware versions and electronic components. Unfortunately, these measurements were not doable during the work of this thesis due to an unavailability of ready TAXI systems.

7.5 CONCLUSION

To be able to include the read-out and processing of radio signals into the RadioTAXI data acquisition, radio front-end electronics were designed, tested and characterized during this thesis. The front-end electronics include the power supply for the antenna LNA, a protection against electrostatic discharge, high-pass and low-pass filter and an additional amplification of the radio signal of 10 dB. The radio signal of each antenna polarization is fanned out inside the front-end electronics into four RadioTAXI inputs to be able to operate the RadioTAXI *DRS4* sampling chips in channel cascading mode. First tests of the radio front-end electronics and characterization measurements down to -70° show a sufficiently good frequency response with a gain fitting to the expected gain of 10 dB and a pass-band bandwidth of 50–400 MHz. Unexpected oscillations in the gain pattern are visible in the pass-band frequency range that need to be investigated further. An improved amplifier circuit for the radio front-end is at the moment under development that might lead to a more clean gain pattern [105]. Also, the overall gain requirements might change for the next versions of the DAQ since studies about a more ideal amplification taking the presented results of the full-system test and the measured radio background at the South Pole into account (see chapter 9) are ongoing. Characterization measurements of the radio front-end down to -70° show a reasonably stable gain behavior over the whole temperature change. The gain increases for about 1.5 dB between measurements at $+20^{\circ}$ and -70° . This temperature dependence can be corrected for when the ambient temperature around the radio-front end is known by using the characterization results obtained during the presented measurements.

Test measurements of the full DAQ system including the radio front-end electronics, an interface to the TAXI inputs and the TAXI DAQ itself reveal an unexpected frequency behavior of the TAXI electronics that was confirmed by measurements with two different measurements setup having only the TAXI DAQ in common. The frequency spectrum recorded with TAXI shows signs of an impedance mismatch for low frequencies and a steeply falling spectrum for frequencies higher than 150 MHz. Reasons for this unwanted behavior might be the artificial shift of the baseline to be able to sample both positive and negative signal parts or, at least partly, the high attenuation of the TAXI *Sub D* input connector. A deeper investigation of the measured effects can be realized when next TAXI versions are available and a comparison between different

hardware layouts is possible.

The presented results originate from measurements of the first version of the radio front-end electronics and a DAQ system that is still considered to be in a prototype phase. Conclusions resulting from these measurements will enter the next versions of the radio front-end and the TAXI DAQ system which are both under active development.

ANTENNA DEPLOYMENT AT THE SOUTH POLE

Within the frame of this thesis, two prototype antennas were deployed together with new DAQ electronics at the South Pole. The deployment took place in January 2019 which corresponds to the South Pole season 2018–19. The deployed antennas extend the existing scintillation-detector prototype array that is successfully operating at the South Pole since the season 2017–18. Details on the antenna deployment will follow in section 8.1. The final station layout will be presented in section 8.3. Details on the antenna shipment can be found in the appendix section A.4. A more personal view on the deployment campaign is also given in the Appendix section A.6.

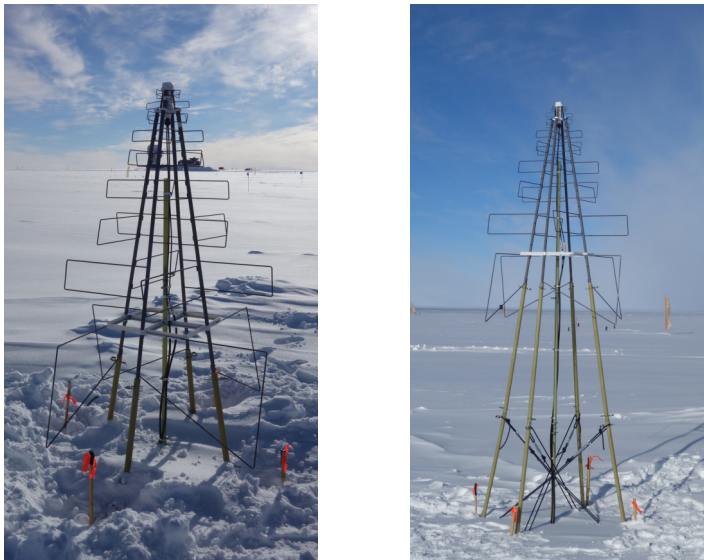


Figure 8.1: Pictures of the two SKALA version-2 antennas deployed at the South Pole in season 2018–19.

8.1 DEPLOYMENT OF THE ANTENNAS

Two prototype antennas with a new mechanical structure adopted for the conditions at the South Pole (see sec. 5.3) were deployed in season 2018–19. Each antenna has two polarization channels with two separated low-noise amplifiers (LNA). Out of the three designs for the antenna mounting with different antenna heights, the smallest and the tallest antenna designs were chosen for deployment. With this, snow accumulation effects around the antenna and effects of snow burying parts of the antenna can be

investigated. The small antenna has a height above ground of 0.3 m and a total height of 1.8 m. The tall antenna has a height above ground of 1.7 m and a total height of 3.3 m. In Fig. 8.1, pictures of the two deployed antennas are shown.

The prototype-station site is about 200–250 m away from the IceCube Lab (ICL) which is located near the center of the IceTop array. The antenna metal structure was pre-assembled in the ICL and transported to its dedicated position by hand. For both antennas, the remaining antenna structure consisting of GFK antenna legs, GFK middle pole and the plywood base was assembled in the field and attached to the antenna metal structure at the final antenna position. The snow spikes securing the antenna structure at the surface were put into the snow by hand or with the help of a sledgehammer if needed. In Fig. 8.2 close-ups of the antenna deployment at the South Pole are shown. The signal cable connected to the LNA is a 60 cm long *LMR240* cable which is then attached to a 30 m long *LMR400* cable. These cable types are in use by several other South Pole experiments like the Askaryan Radio Array (ARA), an in-ice radio detector for neutrinos, and found to withstand the South Pole environment. All deployed cables were temperature cycled and tested at -70°C before deployment. The *LMR240* cable is used as an interface between the LNA and the *LMR400* cable since the thicker *LMR400* cable would not fit into the LNA housing. The *LMR400* is used to transfer the radio signal over the long distance since this cable has a lower signal attenuation of 0.08 dB/m (400 MHz) which is half of the attenuation of the thinner *LMR240*. The signal cables leaving the LNA housing were secured with pipe clamps at the middle pole to prevent the cable from shaking in the wind. A height scale was drawn on the middle pole to evaluate the rise of the snow level with time.

The wooden base of the tall antenna was buried about 20 cm deep into the snow to stabilize the antenna against wind gusts. Additionally, the tall antenna was secured with ropes around the antenna legs visible in Fig. 8.1 and in more detail in Fig. 8.2. The ropes increase the overall stability of the antenna structure which would otherwise be a bit shaky due to the long antenna legs with a length of 2 m. For the small antenna, ropes were not needed and the wooden base was placed directly on the leveled snow surface.

The deployment of both antennas was found to be fast and easy. Both antennas were deployed within 2 days with a team of two people. With an experienced deployment team and some preparation, the deployment of three antennas in one day is possible. As a requirement for South Pole detector installations, cables have to be secured using cable trenches in the snow to prevent accidents with cables laying on the snow surface. A cable trench is an about 1 m deep snow channel in which the cable is laid out and which is closed in the end by filling it up with snow. For the deployment in season 2018–19, cable trenches had to be trenched by hand without using heavy machinery. Two circa 25 m long trenches were shoveled with a team of six people in about 1.5 days. The cable trenches were secured with metal foil in the trench before closing to be able to find and recover the deployed cable.



Figure 8.2: Details of the antenna deployment at the South Pole. **Top left:** Connection between *LMR240* cable from the antenna LNA to *LMR400* cable leading to the DAQ (antenna A1). **Top right:** Antenna Middle pole with height scale to read off snow accumulation around the antenna (antenna A2). **Bottom left:** Interface between two middle-pole GFK poles with cottor pins. Cables are fastened at the middle pole using cable clamps (antenna A2). **Bottom right:** Additional stabilization of the tall antenna with ropes around the lower antenna legs (antenna A2).

8.2 DEPLOYMENT OF THE DAQ

A new RadioTAXI DAQ was deployed at the South Pole together with the prototype antennas. The DAQ electronics are located in the field hub which is consisting of two modified Pelican plastic cases buried in the snow. In Fig. 8.3 (left), the dug-out field hub boxes are shown which gives an impression of the depth of the field hub under the snow surface. The field hub was already housing the last generation DAQ (IceTAXI). The old DAQ was replaced by the new RadioTAXI and four new *LMR400* cables connecting the radio antennas were guided into the field hub box through existing cable ports. In Fig. 8.3 (middle), the installed RadioTAXI in the top part of the box is shown with connected radio cables (silver heads) and scintillation-detector cables (one level below the radio cables). Cables to the field-hub power supply and glass-fiber cables to



Figure 8.3: Deployment of the RadioTAXI DAQ. **Left:** ‘Field Hub’ DAQ housings (Picture credits: Lu Lu [109]). **Middle:** Opened ‘TAXI Field Hub’ with new RadioTAXI installed. *LMR400* radio cables enter RadioTAXI from the top visible by silver heads. The Field Hub also houses a power supply, A *White Rabbit* timing system providing time information to the IceAct telescope and a fiber-cable hub. **Right:** Cable trenches connecting the Field Hub and the antennas. Cables enter the Field Hub area at the corner pointing to the IceCube Lab which is visible in the background (Picture credits: Lu Lu [109]).

the ICL were reused from the earlier IceTAXI DAQ.

The cable trenches from both antennas are leading to the field-hub as visible in Fig 8.3 (right). The antenna cables and the IceAct cables enter the field-hub area under the snow surface in the corner pointing to the ICL. The cable trenches were closed after deployment.

8.3 STATION LAYOUT AFTER DEPLOYMENT IN SEASON 2018–19

Directly after the deployment, the antenna positions were surveyed using a differential GPS system. Four GPS measurement points were measured per antenna which were aligned with the antenna polarization directions. In the images of the antennas in Fig. 8.1, the GPS measurement points are marked with little orange flags for the survey team. In Fig. 8.4, the closer area around the antennas is shown like it has been measured during the GPS survey. For all antenna polarizations, two measurement points indicate the polarization direction. The numbers from 0 to 4 at the antennas indicate the numbering of the polarization channels like they are connected to the DAQ system. The tall antenna is the southern antenna A2 in the map, the small antenna A1 is located in the east. The distance between the antennas is approximately 18.5 m. The map shows also the positions of the two scintillator panels near the antennas and the IceAct

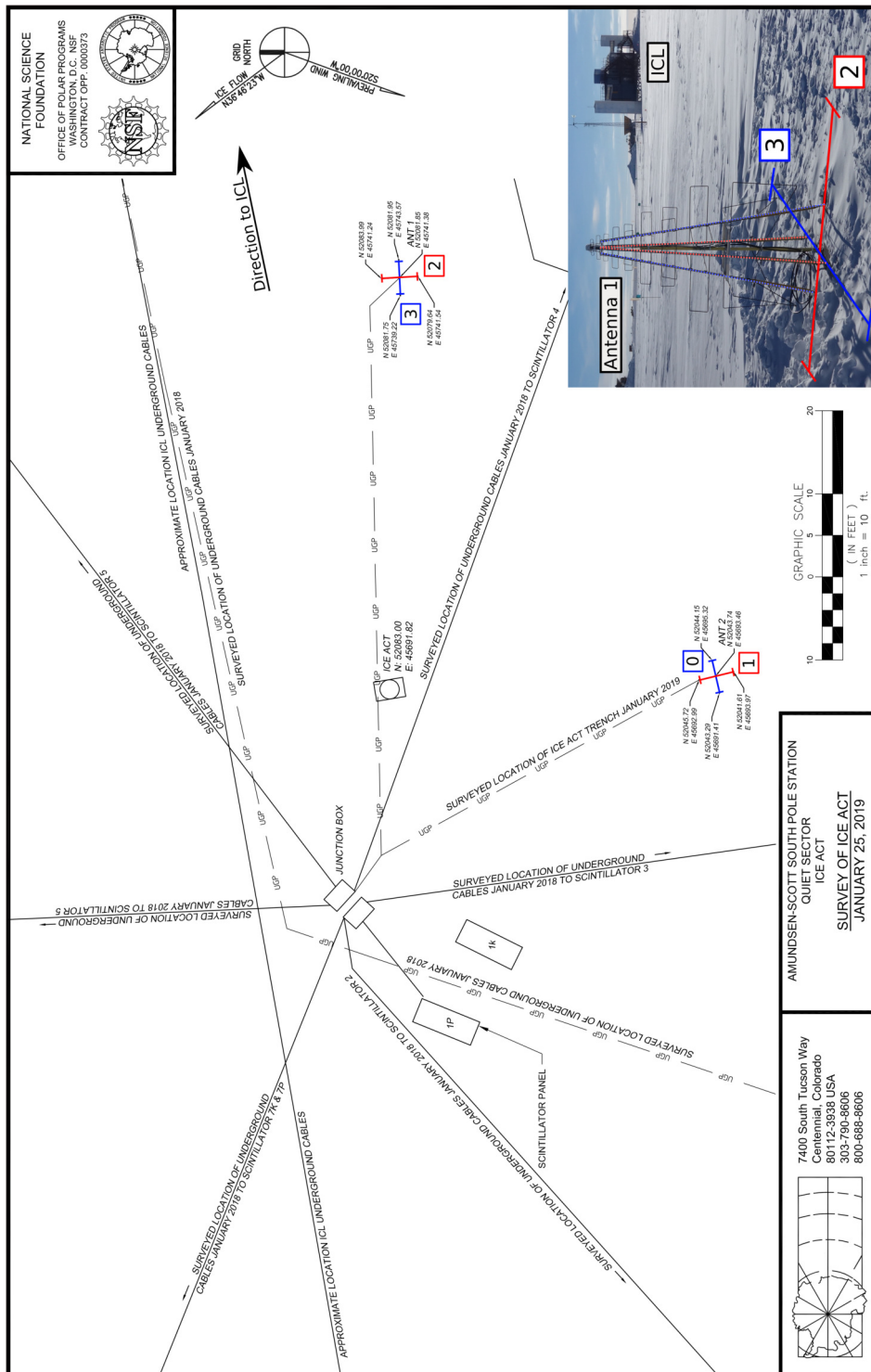


Figure 8.4: Locations of the radio antennas, the IceAct telescope, the Field Hub and the cable trenches measured during a GPS survey after deployment in season 2018–19. Colored lines of the antenna polarization channels show the orientation of the dipoles of each channel. A picture of Antenna A1 shows the orientation of the antenna for comparison. The polarization channels 1 (antenna A2) and 2 (antenna A1) are aiming towards the ICL and should be most sensitive to noise coming from this direction.

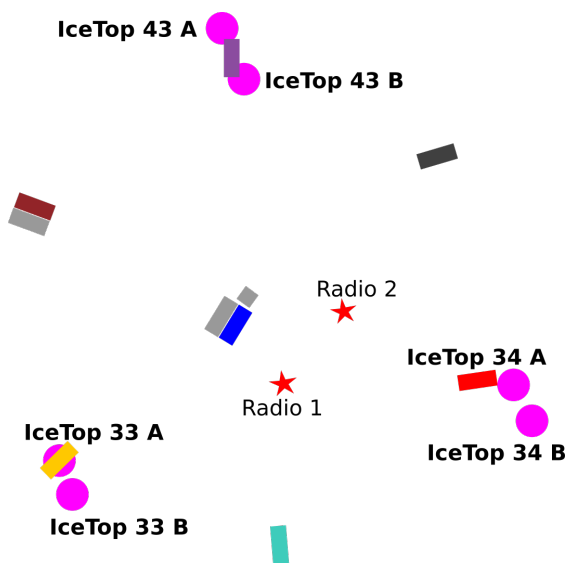


Figure 8.5: Not-to-scale station layout after including the two antennas deployed in season 2018–19.

telescope which was deployed at the same time as the antennas. The field hub housing the DAQ electronics of the scintillation detectors, the radio antennas, and parts of the IceAct timing system is marked as ‘junction box’ in the map. The cable trenches are visible as dashed lines going from the junction box to the antennas. The cable trench of the small antenna on the east side is partly shared with the IceAct telescope cables. The antenna polarizations aim¹ at the possible noise sources in the area. An arrow in Fig. 8.4 points into the direction of the ICL which is about 200–250 m away from the detector positions. The ICL is expected to emit noise but noise power and bandwidth are unknown yet. Other possible noise sources are the IceAct telescope located between the small antenna and the junction box, the electronics in the junction box and the scintillator panels. By comparing the noise levels in the different antenna polarizations of the two antennas, a better understanding of the noise emitted by these possible noise sources might be possible: Looking at polarization 2 (see Fig. 8.4) all possible noise sources are in the field of view whereas polarization 3 should be as quiet as possible. Polarization 0 aims to the junction box electronics and the IceAct camera and polarization 1 might pick up noise mainly from the ICL.

In Fig. 8.5 a not-to-scale sketch of the full detector station layout is shown. The sketch includes the positions of the scintillation detector stations, the IceTop stations in the area and the two deployed antennas. The distance between the single scintillator sta-

¹ Aiming the antenna polarization into one direction means to aim the polarization’s axis of maximum sensitivity into this direction. The dipoles of this polarization are aligned perpendicular to this direction. As an example: If the antenna polarization is aiming to north-south, the dipole elements of this polarization are aligned east-west.



Figure 8.6: Snow accumulation on the antenna structure of the small antenna in March, April, May and June 2019 (from left to right) [110].

tions is about 60 m and the IceTop stations are arranged in a grid of 125 m spacing. The scintillator station in the middle of the array is the same as visible in Fig. 8.4. The radio antennas are positioned in the middle of the detector array. Two scintillator panels overlap with IceTop tanks which enables a direct coincidence measurement of both detectors. The radio antenna read-out is triggered by a coincidence threshold of triggered scintillation detectors. It has been shown that shower events measured with the scintillation detectors can be linked to showers measured with the IceTop detector. By adding radio antennas to the array, individual cosmic-ray air showers can be measured with the IceTop ice-Cherenkov detectors, the scintillation detectors, and the radio antennas. Ideally, also the IceAct telescope can be included in this enumeration that would enable a truly hybrid cosmic-ray air shower measurement consisting of the detection of particles, radio emission and air-Cherenkov radiation of the shower.

8.4 SNOW ACCUMULATION ON AND AROUND THE ANTENNA OVER TIME

Snow accumulation around the antenna and especially on the antenna structure itself can change the antenna response pattern and sensitivity unpredictably. Also, environmental impacts have to be minimized by the policy of the IceCube experiment. This especially means, that deployed detectors have to be removable. Information can be gained from the prototype antennas about how snow is accumulating on the antenna and how the antenna structure is affecting the snowdrifts around the antenna.

The most obvious and significant subdivision of the South Pole climate is the day (summer) and night (winter). The sun starts to rise above the horizon about mid of

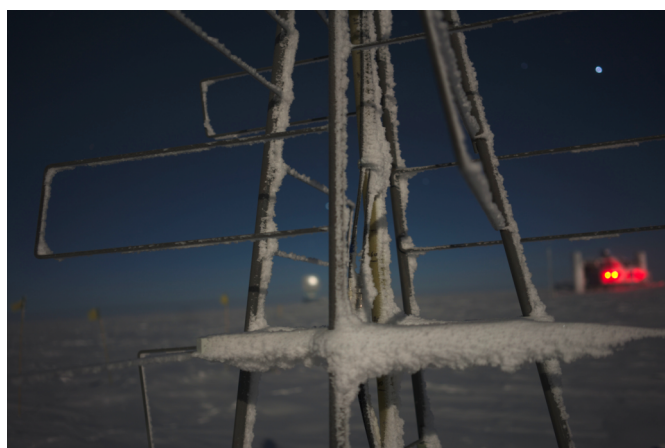


Figure 8.7: Detail of the snow accumulation on the antenna structure of the small antenna in June 2019 [110].

September which is the start of the South Pole summer. The sun stays above the horizon until the end of March of the following year when it disappears for the next half year which marks the beginning of the Antarctic wintertime. During summer, the snow surface is constantly exposed to the sun's UV radiation. Average temperatures rise to circa -30°C around new-year. During winter, the average temperature drops below -55°C with minimum temperatures below -70°C [111].

Since the antenna deployment in January 2019, the antennas mostly experienced winter time with very low temperatures but without a constant UV radiation. Images of the antennas were taken by the IceCube Winterovers every month from March until June which is the first half of the South Pole winter. In Fig. 8.6 pictures of the small antenna during these four months from March to June are shown. Fig. 8.7 shows the accumulation of snow on the antenna mechanical structure and the larger antenna lobes of the tall antenna in Jun 2019 in more detail. When comparing the snow accumulation on the antenna throughout the months, it is visible that snow builds up on the antenna structure during this time with the highest amount of snow on the antenna in the picture from June. Looking at the snow bulb that is only accumulating at one particular side of the top part of the antenna and the snow structure in the close-up in Fig. 8.7, a preferred direction for snow accumulation is visible. Comparing this to the wind direction by observing flags near the antenna positions and the general wind direction at the South Pole coming from roughly north-west [111], snow is accumulating in the windward direction.

According to Winterover reports, the snow on the antenna structure is powder snow but is too much clumped together to be blown away by wind. Here it is important to mention that the wind direction at the South Pole does not change much but is usually coming year-round from north-west direction [111]. Due to this, the natural removal of the snow accumulation on the antenna is unlikely. Further observations of the snow

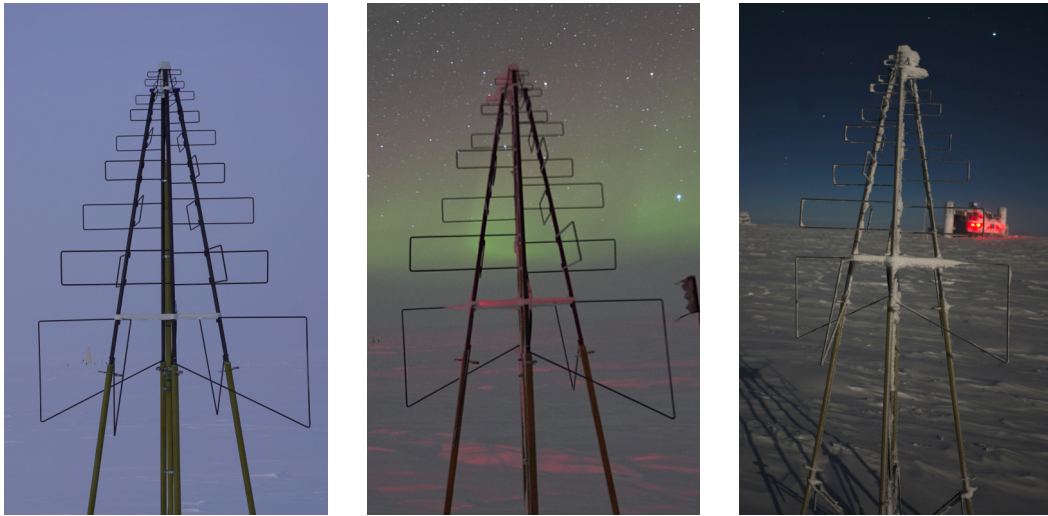


Figure 8.8: Snow accumulation on the antenna structure of the tall antenna in March, May and June 2019 (from left to right) [110].

accumulation will show whether this behavior is only apparent during the dark and cold wintertime or whether snow is also accumulating on the antenna structure during summer. Until this point, no ice has been reported on the antenna structure but also this needs further observations in the summertime since the probability for ice deposition might increase when the sun is shining on metal parts of the antenna.

The same snow accumulation behavior can be observed for the tall SKALA antenna. In Fig. 8.8, images of the tall antenna for March, May, and June of 2019 are shown. The snow accumulation on the antenna structure is very similar to the one on the small antenna although the tall antenna is about 1.5 m farther away from the snow level than the small one.

Snow accumulation, especially around the LNA housing, can affect the radio measurement since snow can bury parts of the dipole elements or establish a connection between neighboring elements. No detailed investigation of the effect of snow on the antenna is available yet but will be done by measuring the antenna signals while monitoring the snow accumulation on the antenna. It should be noted that the observed snow layer with dimensions of several cm is much smaller than the wavelengths in the measurement bandwidth of up to 500 MHz. Snow is covering the highest three dipole elements which have only a minor effect on the measurement of signals with frequencies lower than 500 MHz. However, based on the results of this work, future antennas will be coated with Teflon (PTFE) to prevent snow accumulation on the antenna metal. The effect of the Teflon coating on the antenna response is assumed to be negligible but will be investigated in future measurements.

For both antennas, no signs of snow accumulation on the ground around the antenna due to the antenna structure can be observed. This is positive since snow accumula-

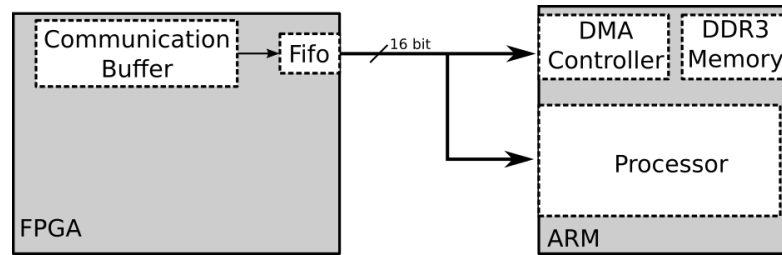


Figure 8.9: Sketch of the communication between FPGA and ARM

tion around the antenna would decrease the time until the antenna gets buried under snow. Having the antenna structure not affecting the natural snowdrift guarantees a maintenance-free measurement time as long as possible.

8.5 HARDWARE FAILURE OF THE DEPLOYED DAQ SYSTEM

Deploying hardware in general and especially in a remote and harsh environment like the South Pole is always associated with the risk of running into a hardware failure. Sometimes these failures only appear after the deployment when physical intervention is no longer possible. This was the unfortunate fate of the deployed RadioTAXI DAQ system. Although function tests of the RadioTAXI were performed before shipment to the South Pole and were followed by tests before the actual deployment, a hardware failure in the communication bus between the ARM microprocessor and the field-programmable gate array (FPGA) on the TAXI board was only found during later remote operation of the RadioTAXI system. The ARM μ CPU and the FPGA communicate over a 16 bit communication interface like it is sketched in Fig. 8.9. For the deployed RadioTAXI, one of the 16 communication bits in the bus cannot be changed anymore but stays on a constant level ('sticky bit'). This behavior is probably a result of a broken solder spot due to mechanical shocks during transport and deployment, maybe amplified by the cold temperatures. Due to this, communication with the FPGA was not possible which prevented every attempt to take data from the scintillation detectors and radio antennas connected to RadioTAXI.

It was elaborated that this failure can be fixed by reducing the communication interface between ARM and FPGA to 8 bit and to avoid the broken bit in the communication bus. This change requires modifications to the FPGA firmware as well as to software running on the ARM μ CPU and, therefore, is a complex task. Attempts to fix the communication were done during 2019 that led to preliminary data taking in September '19. Due to this, the amount of radio data is much less than expected and the data quality not ideal since other planned improvements of the FPGA firmware were delayed for repairing the communication. Information about the finally received data can be found in chapter 10.

8.6 SUMMARY

Two prototype antennas were successfully deployed at the South Pole in season 2018–19 together with a new hybrid DAQ system. The deployed antennas have different total heights of 1.8 m and 3.3 m to investigate the effects of snow accumulation around the antenna and on the antenna structure. The deployment of the antennas at the South Pole was performed with a team of two people in two days and can be sped up with more people and the experience gained during the deployment of the prototype antennas. The antenna polarizations aim to possible noise sources in the area like the ICL, other detectors, and the DAQ electronics. With this, a better understanding of the noise situation at the detector site might be possible. A first analysis of data received by the deployed antennas can be found in chapter 10. Reports and pictures of the antennas during the South Pole winter show snow accumulation on the antenna structure, especially around the stabilizing plastic plate between the antenna arms and the LNA housing. Whether this affects the measured signal is yet unknown and has to be studied in detail by analyzing measurement data while monitoring the snow accumulation. The antenna metal will be coated with Teflon to prevent snow accumulation for future deployments.

RADIO BACKGROUND MEASUREMENTS AT THE SOUTH POLE

When measuring radio emission from cosmic-ray air showers, especially at the very low edge of sensitivity like it is planned for the IceTop radio extension, the radio noise prevailing at the measurement site becomes the limiting factor of the measurement. This noise can be human-made, be produced by the readout electronics or can finally be radio emission originating from the Galactic Center and other sources in the Galaxy that represents the lowest noise level possible. For the proposed search for PeV cosmic rays with the IceTop radio extension, the radio background should be dominated by the Galactic noise to achieve the sensitivity necessary for a successful radio-signal detection [44]. To estimate the radio-background situation near the detector site, first background measurements were performed at the South Pole during the deployment of two prototype antennas in season 2018–19. The purpose of the measurements was to obtain first information about the general radio background and possible human-made radio-frequency interference (RFI) in the proposed measurement bandwidth of 100–190 MHz. The measured background spectra and information about the strength of human-made and Galactic noise contribute to new designs of the radio front-end electronics and improve future simulation studies.

9.1 NOISE IN RADIO MEASUREMENTS

Background noise in radio measurements can be subdivided into internal and external noise. Internal noise is steady thermal noise originating from the radio electronics, mostly from the antenna LNA, and noise introduced by the analog-to-digital converters in the signal line. Thermal noise can be reduced in some amount by choosing low-noise electronic components for the antenna LNA and further electronic stages. For the SKALA antenna, the internal noise of the LNA has been measured to be below 50 K (see Fig. 5.7).

External noise is radio emission originating from external sources which are measured by the antenna. The sources of radio emission are numerous and range from transient, human-made radio frequency interference (RFI) to the radio emission of the cosmic microwave background (CMB). In Fig 9.1 the strength of different noise sources is shown for comparison. In the frequency range of cosmic-ray radio detection going from tens of MHz to some hundreds of MHz, the dominant sources are man-made radio emission and the radio emission originating from sources in the Galaxy, mainly the Galactic Center. Other sources like the atmospheric noise or the radio emission from the cosmic microwave background (CMB) are too low or high in frequency to

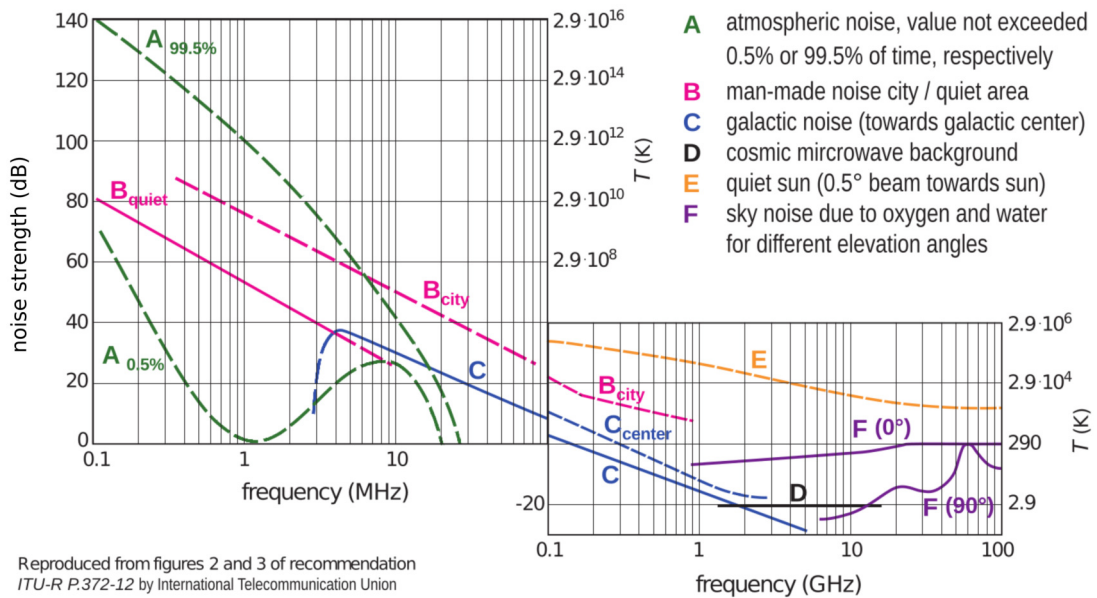


Figure 9.1: Comparison of different sources of radio emission that are expected to be possible background of cosmic-ray measurements with radio antennas. Regarding a radio detector array at the South Pole, the Galactic noise is expected to dominate the radio background. Human-made RFI is expected to be narrow-band and small in number. (Figure from [41, 112])

interfere with cosmic-ray measurements. Galactic noise has a broadband frequency spectrum covering the whole MHz frequency range up to several GHz. Human-made radio signals can be narrow-band or broad-band. Narrow-band signals can be digitally filtered when the frequency resolution of the measurement is sufficient to resolve the noise frequency and the recorded trace is long enough. Human-made broad-band signals can produce waveforms which look very similar to the signals expected from a cosmic-ray air shower.

Human-made RFI can be avoided by designing and choosing electronic parts carefully, in case the RFI is emitted by the experiment electronics itself, or by setting up the radio experiment in a remote and radio-quiet place on Earth. In contrast, the Galactic noise cannot be avoided or attenuated since it is emitted by external sources in our Galaxy. Therefore the Galactic noise will always set the lowest limit for radio detection.

A third, not avoidable but reducible noise source is the thermal noise of the surrounding antenna environment. Although this noise cannot be avoided completely, it can be reduced by choosing an antenna with a gain pattern that has a high attenuation in direction to the ground. With this, the prevailing thermal noise of the ground, i.e. this is about 200 K for the South Pole, can be reduced to a much lower value.

By choosing a remote place like the South Pole, human-made RFI can be reduced in the radio background. This assumption has been confirmed during several measurement

campaigns at the South Pole by ARA and RASTA. RASTA measurements of the radio background at the IceTop site before 2007 show an RFI-quiet frequency spectrum up to frequencies of 100 MHz with only a few weak mono-frequency lines around 100 MHz [113, 114]. More recent measurements performed by the ARA experiment with surface antennas around 2010 show sporadic radio interference with two main sources that are weather balloons, which are launched every day at the South Pole, and aircraft operation. Besides these RFI, also the ARA measurements see the Galactic noise as the dominating background and measure a sinusoidal variation of the Galactic noise due to the rotation of the Galaxy around the antenna [57, 115]. Therefore, the main radio background at the South Pole is assumed to be Galactic noise. RFI signals are visible at the South Pole but they are less frequent than in other places and the absence of FM radio broadcasting enables the use of the full resolvable spectrum.

Three models exist to describe the radiation emitted from different sources in the Galaxy. The global sky model (GSM [116]) and LFMap describe the sky brightness for individual frequencies in a direction-dependent way by predicting the brightness for every visible zenith and azimuth angle depending on the location and time of observation on Earth. An example of a GSM sky map is presented in Fig. 9.2 that shows the sky over the South Pole in January 2019 for a frequency of 100 MHz. The Galactic Center is visible in the western sky at an inclination of about 61° .

Although these models might be used to generate sky maps for later evaluations of the Galactic noise with the full array, at this point the simplified Cane model is used to predict the average Galactic noise at the prototype antenna positions. This model averages the Galactic noise measured by different experiments over the whole sky and gives an average sky brightness for frequencies covering the full MHz range. Using an averaged model for Galactic-noise predictions at the South Pole is acceptable since sources seen in the South Pole sky only change slightly and slowly in inclination due to the special location of the geographic South Pole.

9.2 THE CANE MODEL AND IMPLICATIONS FOR THE MEASURED ANTENNA FREQUENCY SPECTRUM

The Cane model describes the average brightness of the surrounding Galaxy at high measurement latitudes for the full MHz frequency range [117]. The model was obtained by interpolating measurements of the sky brightness at different frequencies measured by various experiments. The average sky brightness predicted by the Cane model follows

$$B_{\text{Cane}}(f) = B_g(f) \frac{1 - e^{-\tau(f)}}{\tau(f)} + B_{eg} \cdot e^{-\tau(f)}. \quad (9.1)$$

with

- the galactic component $B_g(f) = 2.48 \cdot 10^{-20} \cdot f^{-0.52}$

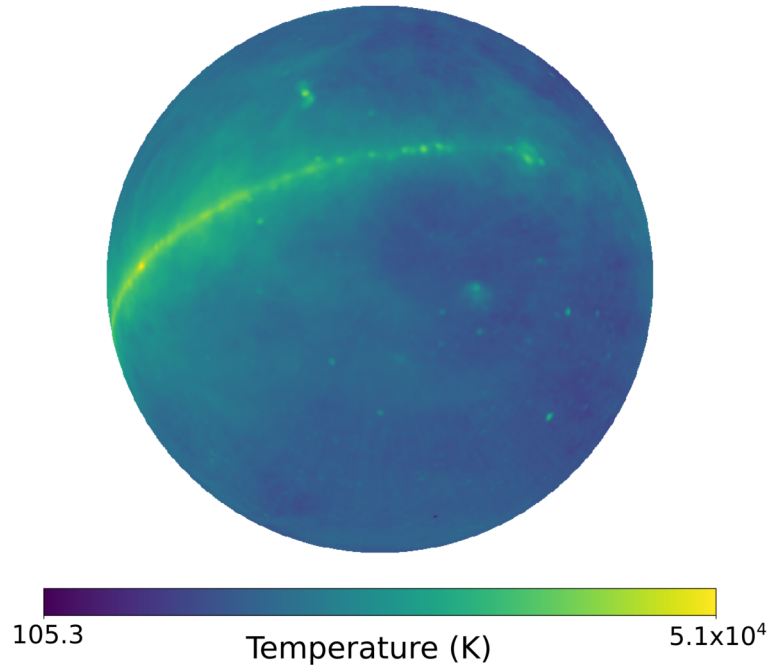


Figure 9.2: The sky in 100 MHz radio radiation as it is seen from the South Pole. This plot has been made with the global sky model (GSM) [116]. The Galactic Center is visible as the brightest source in the sky in the west at an inclination of about 61° .

- the extra-galactic component $B_{eg}(f) = 1.06 \cdot 10^{-20} \cdot f^{-0.80}$
- and the optical depth of absorption $\tau(f) = 5.0 \cdot f^{-2.1}$.

Since the Cane model describes the average sky brightness, its prediction is not always fully applicable to measurements because the measured background noise is changing with the position of mainly the Galactic Center in the field of view of the measurements. Nevertheless, prior measurements show a good agreement with the prediction of the Cane model for the South Pole [57].

The Cane model describes the average brightness of Galactic sources which can be transformed to a noise temperature in units of Kelvin using the Rayleigh-Jeans law

$$T(f) = B(f) \cdot \frac{c^2}{2k_b f^2}. \quad (9.2)$$

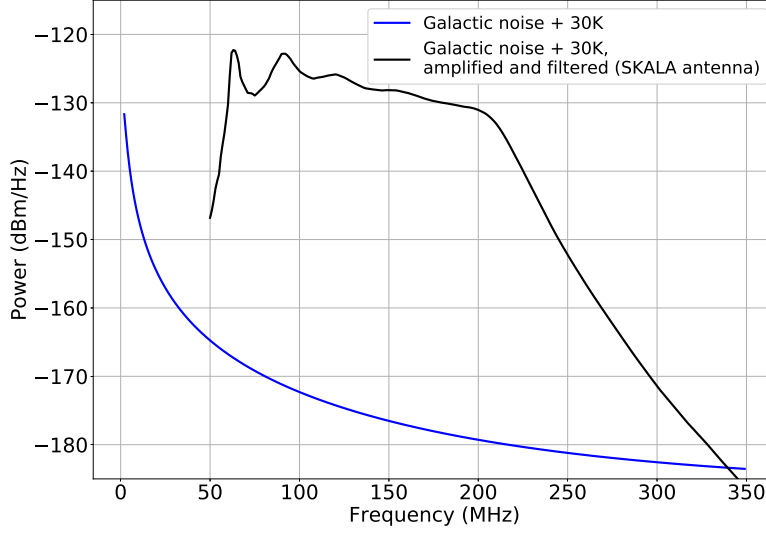


Figure 9.3: The Galactic noise predicted by Cane with an additional thermal noise contribution of 30K. The blue curve shows the raw Galactic noise behavior, the black curve shows the Galactic noise measured by the antenna, amplified with the antenna LNA and filtered with a low-pass filter to resemble the measurement setup.

9.3 PREDICTION OF THE MEASURED GALACTIC-NOISE FREQUENCY SPECTRUM

The total electromagnetic power P received by an antenna from a source with brightness $B(f, \theta, \phi)$ in the frequency bandwidth δf is

$$P_f(\theta, \phi) = B(f, \theta, \phi) \cdot A_{eff}(f, \theta, \phi) d\Omega \delta f \quad (9.3)$$

with the power P measured by the antenna, the brightness B and the effective area of the antenna A_{eff} . The Cane noise brightness is an average over all directions and is therefore not direction dependent. Since the Galactic noise can have arbitrary polarization but the antenna can only measure one polarization, the measured power with the antenna is only one half of the actually emitted one. Considering this, it follows for the Cane noise brightness

$$P_f(\theta, \phi) = \frac{1}{2} B(f) \cdot A_{eff}(f, \theta, \phi) d\Omega \delta f. \quad (9.4)$$

Using the relation between the antenna gain G and its effective area A_{eff} from 5.2

$$A_{eff}(f, \theta, \phi) = \frac{G(f, \theta, \phi) \cdot \lambda^2}{4\pi} \quad (9.5)$$

and the Rayleigh-Jeans law from equation 9.2, the measured power in equation 9.4 can be formulated using the total noise temperature T_{tot} giving

$$P_f(\theta, \phi) = \frac{1}{2} \cdot 2 \cdot k_B T_{tot}(f) \cdot \frac{G(f, \theta, \phi)}{4\pi} d\Omega \delta f. \quad (9.6)$$

Here, the total noise temperature is the noise temperature from the Galactic noise T_{GC} plus a possible thermal noise contribution due to the antenna electronics and the thermal radiation from the surrounding environment T_{th}

$$T_{tot} = T_{GC} + T_{th}. \quad (9.7)$$

In the following, an additional thermal noise contribution of $T_{th} = 30$ K has been assumed that corresponds to the prediction given in [82].

To obtain the total power received by the antenna, an integration over the solid angle $d\Omega$ is performed. In formula 9.6, the only direction-dependent variable is the antenna gain which is given as power gain for zenith and azimuth angles (θ and ϕ). The integrated antenna gain becomes

$$G(f) = \sum_{\phi} \sum_{\theta} G(\theta, \phi, f) \cdot \sin(\theta) \cdot \frac{2\pi}{365} \cdot \frac{\pi}{180} \quad (9.8)$$

with the binning of ϕ of $\frac{2\pi}{365}$ and the binning of θ of $\frac{\pi}{180}$. The total power received by the antenna is

$$P(f) = k_B T_{tot}(f) \cdot \frac{G(f)}{4\pi} \delta f. \quad (9.9)$$

In the actual measurement presented in the next section, the signal in the antenna was amplified by the antenna LNA gain G_{LNA} and attenuated by 100 feet *LMR400* cable (A_{cable}) and a low-pass filter (A_{filter}) at the end of the signal chain before the DAQ. For the measured total power P_{meas} follows

$$P_{meas} = P(f) \cdot G_{LNA}(f) \cdot A_{cable}(f) \cdot A_{filter}(f) \quad (9.10)$$

To compare this prediction with the measurement, the expectation of the measured power is expressed in units of dBm/Hz using

$$P_{dBm/Hz}(f) = 10 \cdot \log_{10} \left(\frac{P(f)}{1 \text{ mW} \cdot \delta f} \right). \quad (9.11)$$

In Fig. 9.3, the predicted Galactic noise according to Cane is shown together with the expected frequency spectrum of the Galactic noise like it is measured with the SKALA antenna and following electronics. As LNA response, simulations of the LNA loaded with the antenna impedance were used. The Galactic noise follows an exponential decrease with frequencies. The antenna LNA amplifies the received signal by more than 40 dB starting at around 70 MHz (see sec. 5.4). The oscillating structure of the expected Galactic-noise frequency spectrum is due to the LNA gain which oscillates because of impedance mismatching with the actual antenna impedance. At 200 MHz, the low-pass filter starts to attenuate the signal for higher frequencies.



Figure 9.4: Picture of the antenna location for the background measurements during the deployment in season 2018–19. The antenna was set up at a distance of about 25 m to the IceCube Lab visible in the back of the picture. (Picture taken by Lu Lu [109])

9.4 BACKGROUND MEASUREMENTS SETUP

The background measurements at the South Pole were performed in parallel to the deployment of the prototype antennas and the DAQ electronics. Due to an unavailability of the actual DAQ system, a commercial digitizer was used to digitize the antenna signals. Measurements were performed with the not-deployed SKALA antenna equipped with a mid-size antenna mounting which was shipped to the South Pole together with the two deployed antennas. The antenna was assembled leaving out the snow spikes and the middle pole which were not needed to stabilize the antenna during the measurements. The antenna was connected with one 100 feet *LMR400* cable to the readout electronics which were installed inside of the IceCube Lab (ICL). Due to the cable length, the distance between the antenna and the ICL was limited to about 25 m. In Fig. 9.4 a picture of the SKALA antenna in front of the ICL during the measurement is shown to give an impression of the location. Since only one *LMR400* cable was available for the measurements, the antenna was rotated between measurements to cover the full azimuth range. Because the ICL was the nearest and therefore the most likely source of radio noise, the antenna polarization directions were chosen to aim one time in direction of the ICL and one time perpendicular to the ICL. With this, the noise emitted from the direction of the ICL is more dominant when aiming to the ICL and a preliminary conclusion about noise emitted by the ICL is possible.

As readout electronics, the commercial DAQ system *CAEN DT5730* was used that can sample eight input channels with a sampling frequency of 500 MHz and a sampling depth of 14 bits. A low-pass filter *SLP-200+* attenuated frequencies higher than

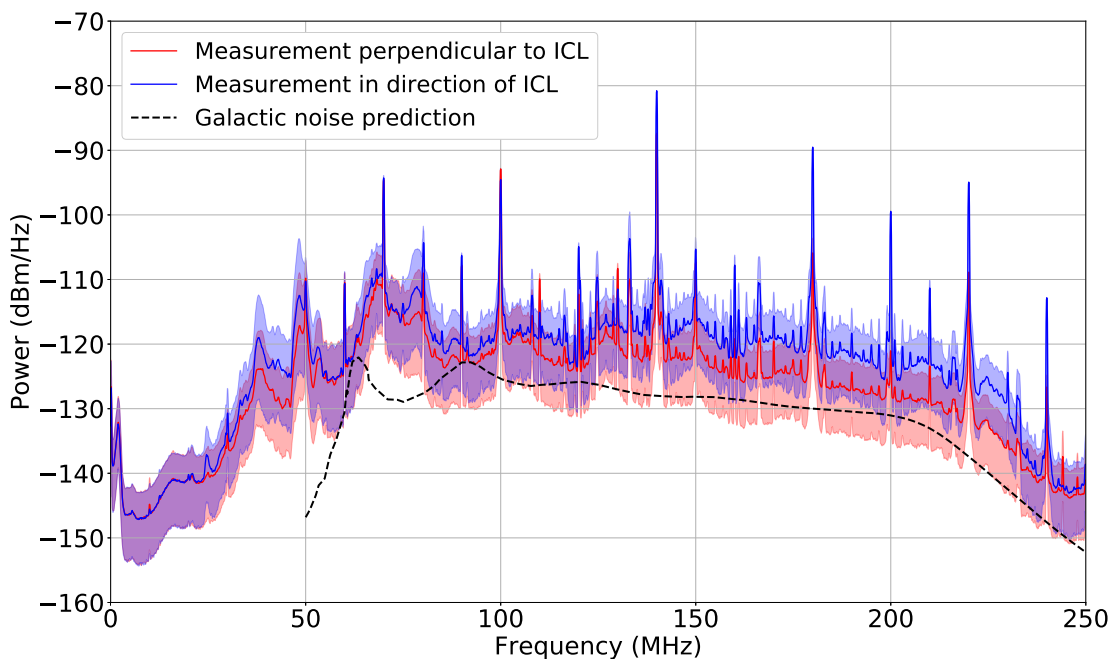


Figure 9.5: The measured frequency spectrum of the radio background near the ICL for two one-hour measurements in direction of the ICL (blue) and perpendicular to the ICL (red). The prediction of the Galactic noise is shown as black dashed line including the amplification of the antenna and the antenna LNA and the attenuation of the cable (at -20°C) and the low-pass filter.

200 MHz to prevent the reflection of high frequencies due to the limited bandwidth of the electronics. For these measurements, no high-pass filter was used to be able to record the spectrum down to the lowest possible frequencies. The antenna LNA was powered with a *ZFBT-4R2G-FT+* bias tee. The electronics including the low-pass filter and the bias tee were installed inside of the ICL at room temperature and the antenna cable was guided from there to the antenna outside of the ICL. The outside temperature at the South Pole during the measurement days was changing between -30°C and -20°C . During the actual data taking, the temperature changed for about 4°C in maximum.

9.5 THE RADIO BACKGROUND AT THE SOUTH POLE

The measured average frequency spectra of two one-hour measurements with the antenna polarization aiming towards the ICL (blue) and perpendicular to the ICL (red) are shown in Fig. 9.5 together with their standard deviation as uncertainty. For each polarization direction, one spectrum was recorded every second resulting in over 5000 single spectra for each measurement.

We first look at the general spectrum behavior. In the low-frequency part below 70 MHz, the LNA amplification drops and the spectrum power decreases to low frequencies (see section 5.4). For the highest frequencies, the spectra fall off due to the attenuation of the low-pass filter which starts to attenuate at 200 MHz. The frequency spectrum measured towards the ICL shows, in general, a higher power than the spectrum measured while pointing the antenna polarization away from the ICL. This separation of both measurements increase with frequency up to 7 dB on average before both measurements fall off due to the low-pass filter.

Analyzing the spectra in more detail, the first obvious features in both measurements are the strong RFI peaks which are visible over the full frequency range of the measurements. RFI peaks with different strengths are arranged in 10 MHz steps from 50 MHz up to 240 MHz which is the full sensitive bandwidth of the measurement. RFI peaks might also occur at lower frequencies but the strong decrease in LNA gain for frequencies lower than 50 MHz would make them vanish. To compare the RFI peaks of both measurements, the measured average spectra are shown in Fig. 9.6 with an artificial shift of +5 MHz to separate the peaks of the measurements. The relative strength of the RFI peaks of both measurements changes from a similar strength for low frequencies up to 125 MHz to a much smaller RFI power in the measurement perpendicular to the ICL for higher frequencies. The different strength of the RFI peaks can explain the overall difference in noise power of the two spectra especially for high frequencies due to frequency leakage.

Until this point, it is not clear what the origin of the RFI noise is. Due to the small distance of the antenna to the ICL, the only valid conclusion is that the noise is coming from the rough direction of the ICL. The scintillation detectors and the hybrid-station DAQ systems were not powered during the background measurements and can be excluded as sources. An investigation of possible noise candidates like communication devices or beacons together with the Antarctic Science Contractor did not lead to a result. No registered emitters are known which would emit in these frequencies. Due to the periodicity of the RFI, a possible assumption is that the origin of this noise is a clock signal in an electronic device inside the ICL. The first floor of the ICL houses many electronic devices and a workshop area and the second floor houses the IceCube server room. The IceCube server area is shielded against RFI signals with a Faraday cage, the first floor is not shielded. Therefore, the ICL is a likely source of noise signals in radio frequencies.

For comparison, Figure 9.5 shows the prediction of the Galactic noise spectrum (see sec. 9.2 for more information). This prediction includes the integrated SKALA antenna gain, the simulated LNA gain when loaded with the antenna impedance and the attenuation of the 100 feet *LMR400* cable at -20°C , the bias tee and the *SLP-200+* low-pass filter. The predicted Galactic noise spectrum is for all frequencies below the measured spectra although the spectral form resembles the measured spectra at least for frequencies higher than about 125 MHz. Assuming that the measured spectra should, in

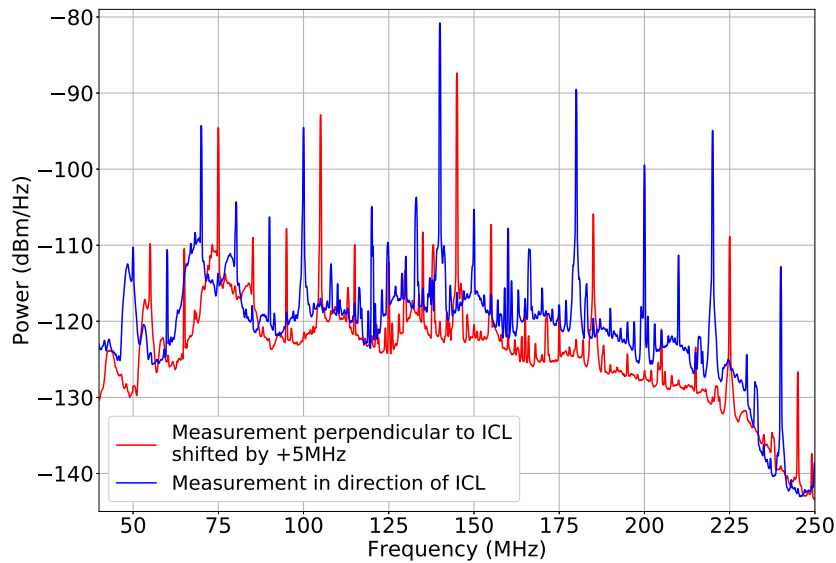


Figure 9.6: The measured frequency spectra in the direction of the ICL (blue) and perpendicular to the ICL (red). To be able to compare the strength of the RFI peaks in both measurements, the measurement perpendicular to the ICL was shifted for +5 MHz.

general, resemble the Galactic noise prediction, the discrepancy in power can have multiple reasons. First, it has to be noted that the LNA gain used to amplify the Galactic noise prediction is a simulation of the LNA gain loaded with the antenna impedance. The real gain spectrum can differ in amplitude and also in the frequency behavior, especially for low frequencies where the spectral form of the measurements and the Galactic noise do not match. Besides, the LAN simulation assumes the LNA and also the antenna at room temperature. The antenna impedance might change with temperature which can result in a different gain pattern. That the antenna impedance has a crucial effect on the gain spectrum of the LNA can be seen in Fig. 5.14, which shows the LNA gain measured with a $50\ \Omega$ input signal and the simulation of the LNA gain when loaded with the antenna impedance.

Second, also the antenna gain pattern is a result of a simulation performed by the SKA collaboration (see [76, 82]). This simulation assumes an infinite ground which is of course not the case for the actual snow surface on that the measurements were performed. The antenna pattern changes with different ground types (see Fig. 5.3). This can affect the overall gain of the antenna and can also change the amount of reflected radiation at the surface which is again measured by the antenna. Qualitative studies on how the snow and ice surface at the South Pole change the antenna pattern were not available when analyzing these measurements.

Last, the reader shall be reminded that the Galactic noise described by the Cane model is averaged over the whole sky and does not include any direction dependencies of the actual measurement. Depending on the actual direction of the antenna polariza-

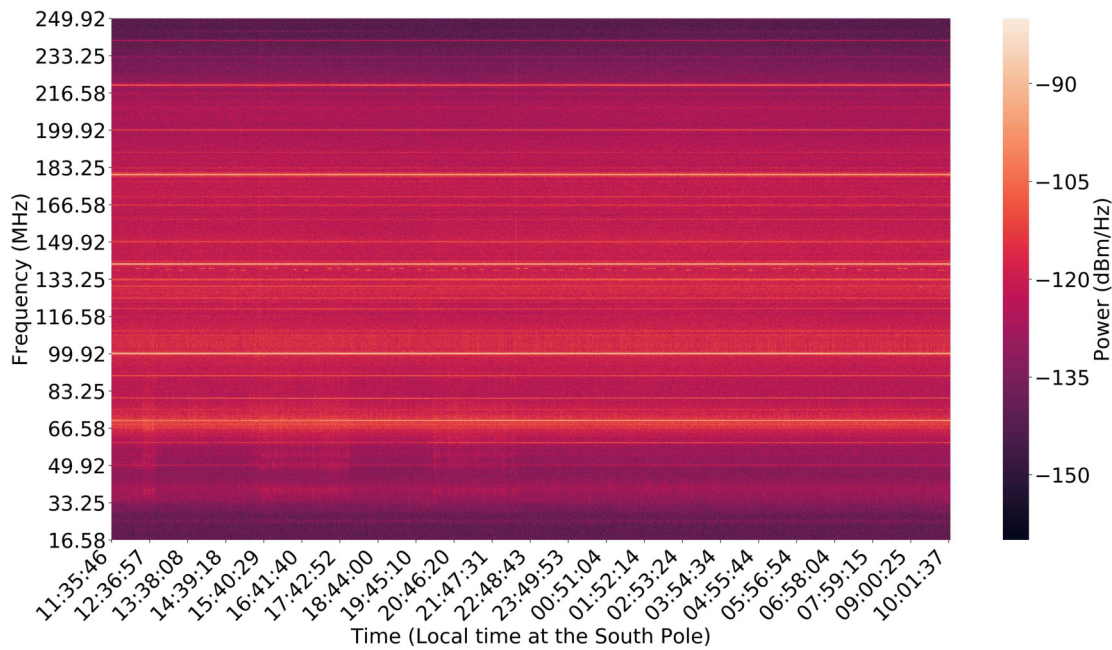


Figure 9.7: Dynamic spectrum measured during a 23 hour measurement at the South Pole. The time axis shows the local time at the South Pole. The measurement was performed over the night from the 24.01.19 to the 25.01.19.

tion and the inclination of the Galactic center, deviations from the average prediction are expected.

Regarding these considerations and the possible effect of the RFI signals on the general spectrum form, a deviation of the prediction of the Galactic noise compared to the measurement in terms of a higher power in the measurements is reasonable. Since the measured spectrum form resembles the prediction especially for high frequencies where possible antenna-impedance variations play only a minor role, the hypothesis that the dominating background of this measurement is the Galactic noise is valid. An analysis of a measurement that monitored the background for 23 hours follows in the next sections that strongly indicates that the Galactic noise is indeed the main background.

9.6 DYNAMIC BACKGROUND SPECTRUM AT THE SOUTH POLE

Additionally to the one-hour background spectrum measurements presented in the last section, the radio background was monitored for about 23 hours with the measurement setup presented in sec. 9.4. Due to the limited time available at the South Pole, the measurement time could not be extended before the measurement setup had to be disassembled. In Fig. 9.7, the dynamic spectrum of the measurement is shown.

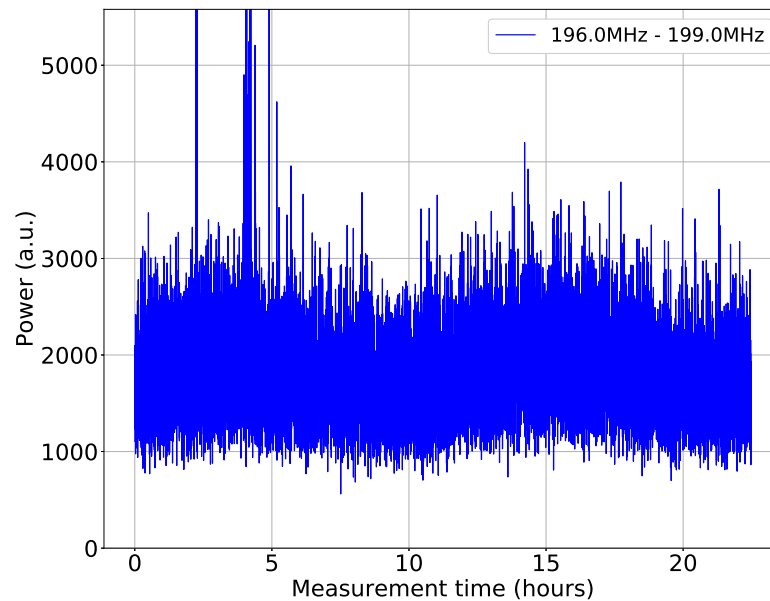


Figure 9.8: Average power in the frequency range 196–199 MHz in arbitrary units over the measurement time in hours. A variation of the background noise is visible with two maxima at circa hour 4 and hour 16 of the measurement.

No time variation of the RFI signals are visible in the measurement. Subdominant structures are visible like periods of higher background noise in the low frequencies around 16:35 and 21:35 and a stronger RFI peak visible in all frequencies around 15:40 and 22:30. Besides this, the spectrum stays constant. At the end of this measurement at around 08:00, an airplane landed on the South Pole runway about 2–3 km away from the measurement site. No additional beacon or communication signals are visible in the dynamic spectrum at this time which is a hint that airplane arrivals and departures might not interfere critically with radio measurements of cosmic rays.

9.7 THE SEARCH FOR GALACTIC NOISE

To search for evidence of the Galactic noise in the 23 hour measurement, the frequency bandwidths apart from the RFI peaks were investigated in more depth. For this, the average power in 3 MHz frequency ranges apart from RFI peaks was calculated for every single measurement within a frequency window of 100–230 MHz. In Fig. 9.8, the average power in the bandwidth 196–199 MHz is plotted over the measurement time in hours. A variation of the measured power with time is expected since the Galactic Center, as the brightest source of Galactic noise, rotates during the time of the measurement one time around the antenna. If the antenna polarization and the Galactic Center are aligned, the measured noise should be stronger compared to the constellation

Frequency (MHz)	Amplitude (a.u.)	Period (hours)	Phase (hours)	Noise offset (a.u.)
106.0–109.0	580.06±46.59	10.718±0.228	-0.16±0.26	14497.06±33.55
116.0–119.0	463.76±15.38	11.662±0.117	-0.06±0.12	4443.6±11.28
121.0–124.0	412.97±16.05	11.718±0.139	-0.07±0.14	5226.19±11.82
186.0–189.0	133.41±8.58	11.189±0.208	-0.13±0.22	3190.83±6.32
196.0–199.0	144.81±6.94	11.736±0.172	-0.05±0.18	1789.81±5.08
206.0–209.0	137.97±4.74	12.072±0.133	-0.02±0.13	1739.7±3.5
226.0–229.0	23.52±1.68	10.904±0.222	-0.17±0.25	254.03±1.24

Table 9.1: Table of the fit results with 1σ uncertainties of the sine fit to the average background power in different frequency bins. The amplitude and the noise offset are given in arbitrary units (a.u.).

when the antenna polarization points perpendicular to the Galactic-Center position which happens 6 hours later. Therefore, a sinusoidal time variation of the noise power with a period of 12 hours should be visible in the measured data if the Galactic noise is the dominating noise source. The behavior can be observed in the spectral power shown in Fig. 9.8. Sine functions of the form

$$P(t) = a \cdot \sin(2\pi \cdot b \cdot t + c) + d \quad (9.12)$$

were fitted to the data of each frequency range. For the fit, outlier measurements with peak powers unreasonably high compared to the rest of the measurement were disregarded to not falsify the fit results.

Due to RFI noise pollution of the measurement, the expected variation in the measured power is not visible in all analyzed frequency ranges. In Fig. 9.9, measurements with a successful fit and reasonable fit results are plotted together with the fitted sine function and a floating mean of the measured data with a kernel size of 155 s. The fit results of the presented measurements are shown in table 9.1. A summary of all analyzed frequency bandwidths can be found in the appendix section A.5.

A sinusoidal variation is found in various frequency bins in the analyzed frequency bandwidth of 100–230 MHz with a frequency that fits to the expected frequency of the rotation of the Galactic Center around the antenna polarization of circa $1/12 \frac{1}{\text{hour}}$. Since the spectrum at high frequencies starting at around 175 MHz is less polluted with RFI than the lower frequencies, the sinusoidal variation is more visible for higher frequencies which can be most clearly seen in the comparison plots of all frequencies in the appendix (sec A.5). The amplitude of the fitted sine function decreases with increasing frequency which fits to the prediction of the Galactic noise like it is shown in Fig. 9.5.

Due to the low statistics of the measurement with only 23 hours measurement time,

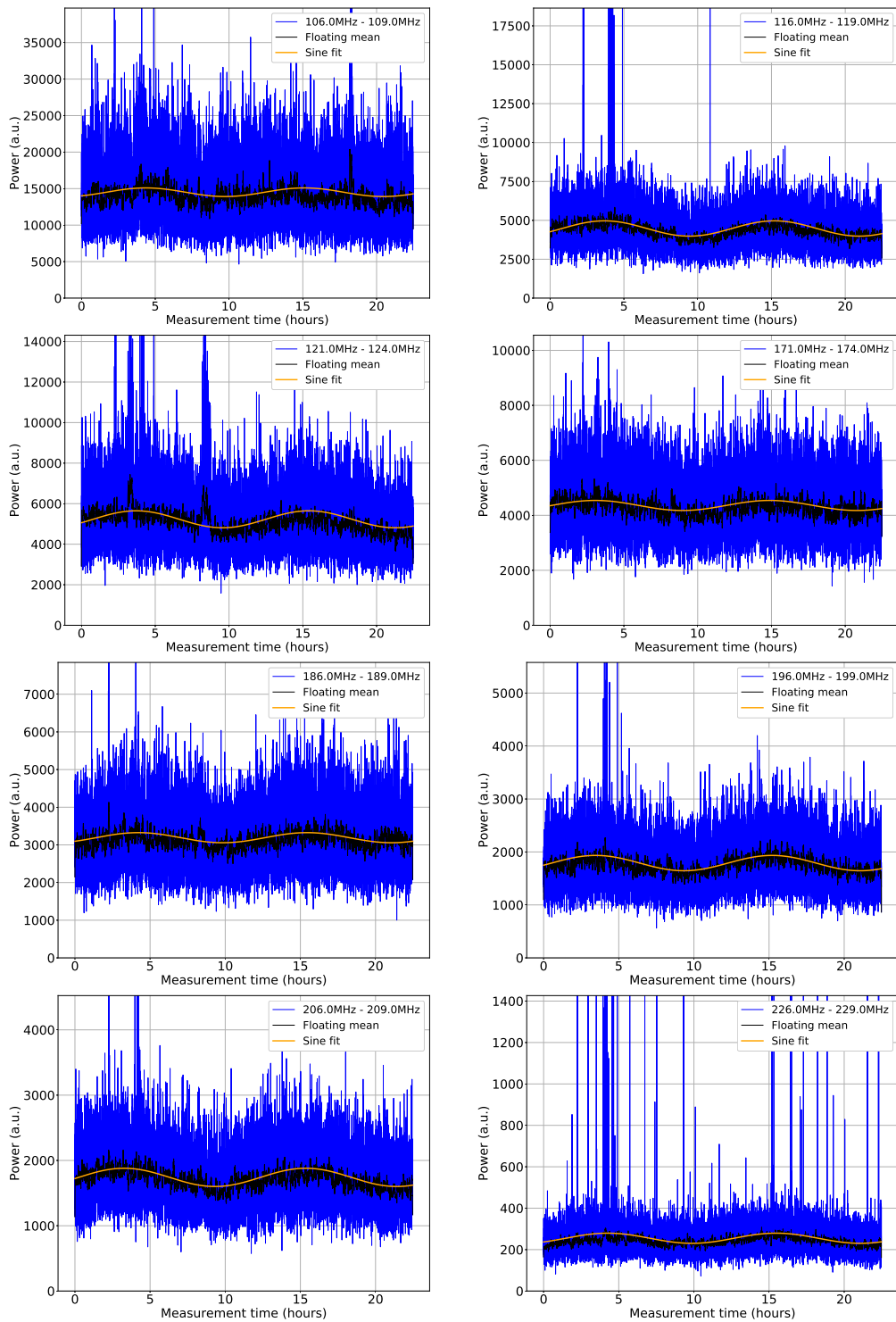


Figure 9.9: Variation of the background noise for different frequency bins between 105–230 MHz. The measured and averaged power in the frequency bin is shown in blue, a floating mean with a kernel size of 155 s is shown in black. A sine function fitted to the measured data is shown in orange. The results of the presented sine fits can be found in table 9.1. Plots for all frequency bins between 100 MHz and 230 MHz can be found in the appendix A.5.

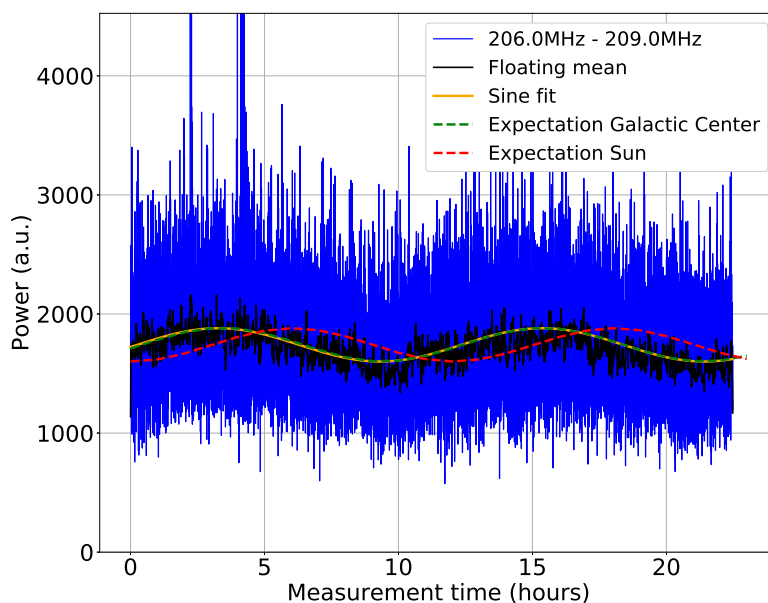


Figure 9.10: Average power in the frequency range 206–209 MHz in arbitrary units over the measurement time in hours. The measured and averaged data is shown in blue, a floating mean with a kernel size of 155 s is shown in black and a sine fit to the measured data is shown in orange. The simulated variation of the noise from the Galactic Center is shown as a dashed green line and the simulated variation of the noise from the Sun is shown as a dashed red line. The amplitude and baseline of the simulations were scaled with the sine-fit results to allow an easy comparison.

other sources of this variation besides the Galactic Center have to be investigated carefully. Human-made noise as the origin of a time variation in radio data is, in general, a probable explanation. On average, human-made noise follows a 24 hour variation with a peak intensity during the day. The measured variation differs from this usual behavior due to the faster variation of 12 hours and peak intensities at around 3 p.m. and 3 a.m. of which at least the latter does not correspond with working times. Second, variations of the ambient temperature could lead to variations in the gain of the antenna LNA or attenuation of the *LMR400* signal cable. These variations should be visible in all frequencies and the variation amplitude should increase with frequency since the LNA gain and the *LMR400* cable attenuation show larger temperature variations for high frequencies than for low frequencies (see sec. 5.4.2). Both noise features are not found in the data: The variations disappear with decreasing signal power for low frequencies when the LNA amplification drops and the variation amplitude decreases with frequency instead of increase like it would do if the variation would be caused by a variation in gain or attenuation of the electronics and cable.

To check, whether the measured phase of the background variation matches with the expected variation resulting from the rotation of the Galactic Center around the antenna, the positions of the Galactic Center, and the Sun for comparison, were simulated using the skyfield python3 package [118]. The zenith and azimuth observation angle of the Galactic Center and the Sun were simulated for the exact measurement time and the South Pole location. Since the antenna polarization was aimed perpendicular to the ICL, the rotation of the ICL with 113.2° E in regards to true North was taken as the polarization azimuth angle. The angle between the azimuth direction of the Galactic Center or the Sun and the azimuth direction of the antenna polarization was taken as a measure for the expected variation of the noise. In Fig. 9.10, the expected variation of the Galactic Center and the Sun are plotted together with the measured data and the performed sine fit for the frequency bin 206–209 MHz. For the plot, the simulated variation was scaled with the amplitude of the sine fit and baseline-shifted according to the baseline of the sine fit to easily compare the simulation to the measurement and the fit. The prediction of the noise variation due to the Galactic Center fits remarkably well to the measured data. The expected noise variation due to the sun is shifted in phase for several hours and cannot explain the measured variation.

Following this, the recorded data disfavors explanations of the measured time variation by human-made noise, ambient temperature variations or the Sun. Regarding the strong correlation between the measured noise variation and the rotation of the Galactic Center around the antenna, the Galactic noise is very likely to be the dominating broadband noise at the measurement site. As final proof, the variation should be recorded over a longer time to investigate the change of the phase over day time. Due to the slightly smaller rotation frequency of the Earth than $1/24$ hours, the phase of the variation plotted over the day time should shift for about 2 hours per month.

The observed shift in spectral power of the two background measurements presented in Fig. 9.5 cannot be explained by Galactic noise. The difference in the spectral power between a minimum and a maximum of Galactic noise is below 2 dB and with this much less than the observed difference in spectral power between the different measurement directions of more than 5 dB.

9.8 COMPARISON WITH EARLIER MEASUREMENTS

The radio background at the South Pole was investigated during earlier measurements by RASTA and ARA around the year 2010 and before. The presented measurements can be best compared with the later measurements made with the ARA testbed. ARA is an in-ice radio experiment and aims to measure radio signals generated by neutrino-induced particle showers in the South Pole ice. Besides of in-ice antennas in depths of tens to hundreds of meters, the ARA testbed also features surface radio detection with two antennas deployed near the snow surface.

In Fig. 9.11 (left), the radio background spectrum measured with the ARA surface

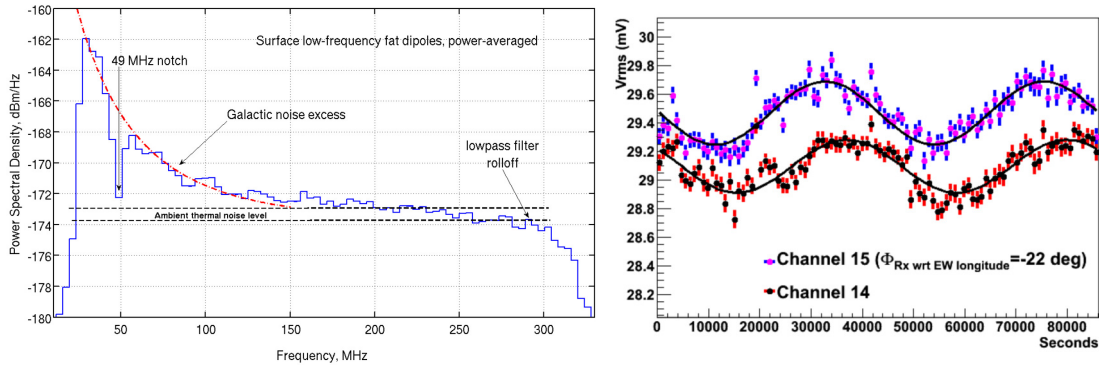


Figure 9.11: Left: Measurement of the radio background spectrum at the South Pole by ARA with an antenna buried shallow under the snow surface (Picture from [57]). **Right:** Measurement by ARA of the variation of background noise during one solar day. For the presented measurement, radio signals were filtered using a low-pass filter with a cut off at 70 MHz to increase the Galactic noise contribution in the signal. (Figure from [57]).

antennas is shown. A galactic thermal noise excess is visible for frequencies lower than 150 MHz at which the ambient thermal noise starts to dominate. Compared to the measurement performed with the SKALA antenna in Fig. 9.5 it should be mentioned, that a higher ambient thermal noise is expected for ARA antennas than for the SKALA since ARA antennas are buried in the snow and therefore cannot attenuate thermal ground radiation as it is possible with an antenna above the surface. In Fig. 9.11 (right), the variation of the background noise measured with the ARA surface antennas is shown over one solar day. A sinusoidal variation of the background noise is visible in both antennas with a period time of about 12 hours. This variation is similar to the one seen in the background measurements with the SKALA antenna shown in Fig. 9.9.

9.9 CONCLUSION

The radio background measurements performed at the South Pole during the deployment of the two prototype antennas indicate the Galactic noise to be the dominant noise floor for frequencies up to 250 MHz. The measured variation of background noise resembles the expectation of the variation due to the rotation of the Galactic Center around the antenna. Earlier measurements performed by ARA also show this behavior. RFI noise is visible in the measurement that comes from the direction of the ICL. Since the distance of the measurement antenna to the ICL was only 25 m, electronics located inside of the ICL are the most probable source candidate for this noise and it should decrease in strength for measurements performed at the actual detector site farther away from the ICL.

Regarding the search for low-energy cosmic rays, especially PeV-gammas from the Galactic Center, the measurement in a higher frequency band above 100 MHz only

improves the results, if the Galactic noise remains the dominant noise source. Due to the drop of the Galactic-noise spectrum power with frequency, electronic noise will at some point outweigh the Galactic noise which makes measurements at higher frequencies inefficient. Since the LNA noise temperature of about 30–40 K is very low, the intersection of Galactic noise and electronic noise is predicted for a frequency of around 350 MHz. The presented measurements indicate that the Galactic noise is indeed dominating over electronic noise for frequencies up to 250 MHz. This covers the important frequency bandwidth aimed for regarding signal detection during reconstruction of 100–190 MHz that provides the best signal-to-noise ratio [44].

PRELIMINARY ANALYSIS OF RADIO DATA FROM THE PROTOTYPE DETECTORS

Due to a hardware failure of the RadioTAXI DAQ system (see section 8.5), measurements with the detector station deployed at the South Pole were only possible starting September 2019, eight months after the actual deployment in January. The hardware failure of the RadioTAXI system affects the communication bus between the ARM μ CPU and the field-programmable gate array (FPGA) on the TAXI board. Probably due to a broken solder spot, one bit in the 16bit communication bus is static and cannot be changed anymore. As a solution, the 16bit communication between ARM and FPGA was scaled down to an 8bit communication that required changes in the FPGA firmware and the software running on the ARM (see section 8.5 for further information). Due to additional issues in the FPGA firmware after the scale-down of the communication bus, the quality of the recorded data is worse than the data obtained with prior TAXI generations or during lab tests of the DAQ system at KIT. However, the currently available data will be presented in this chapter as proof of the functionality of the radio antennas and the DAQ and to draw first conclusions on the noise background at the prototype-station site.

10.1 RADIO WAVEFORMS RECEIVED BY THE SOUTH POLE PROTOTYPE STATION

Before going into detail on the shortcomings of the FPGA data processing, the reader shall be reminded that the RadioTAXI DAQ is still in a prototype phase. Thus, the following results should not be seen as setbacks on the way towards a final hybrid DAQ but as important steps towards a working system.

With the available FPGA firmware version, the radio-signal readout can be triggered by a scintillation-detector event with a variable number of coincident scintillation detectors or by a software trigger. When a trigger occurs, the data of only one of the three available DRS_4 chips can be read out at a time. Event packages include 1024 ADC values per DRS_4 channel. Examples of radio traces measured with the antennas A1 and A2 are shown in Fig. 10.1. For the presented measurements, the radio read-out was triggered by a single scintillation detector event which is in most cases not correlated to an air-shower event in the array.

The deployed SKALA antennas have two polarization channels each. To enable the DRS_4 channel cascading in hardware, the signal of each antenna polarization is fanned out inside the radio front-end electronics into four DRS_4 inputs. Since channel cascading is not implemented in the preliminary FPGA firmware version used for these mea-

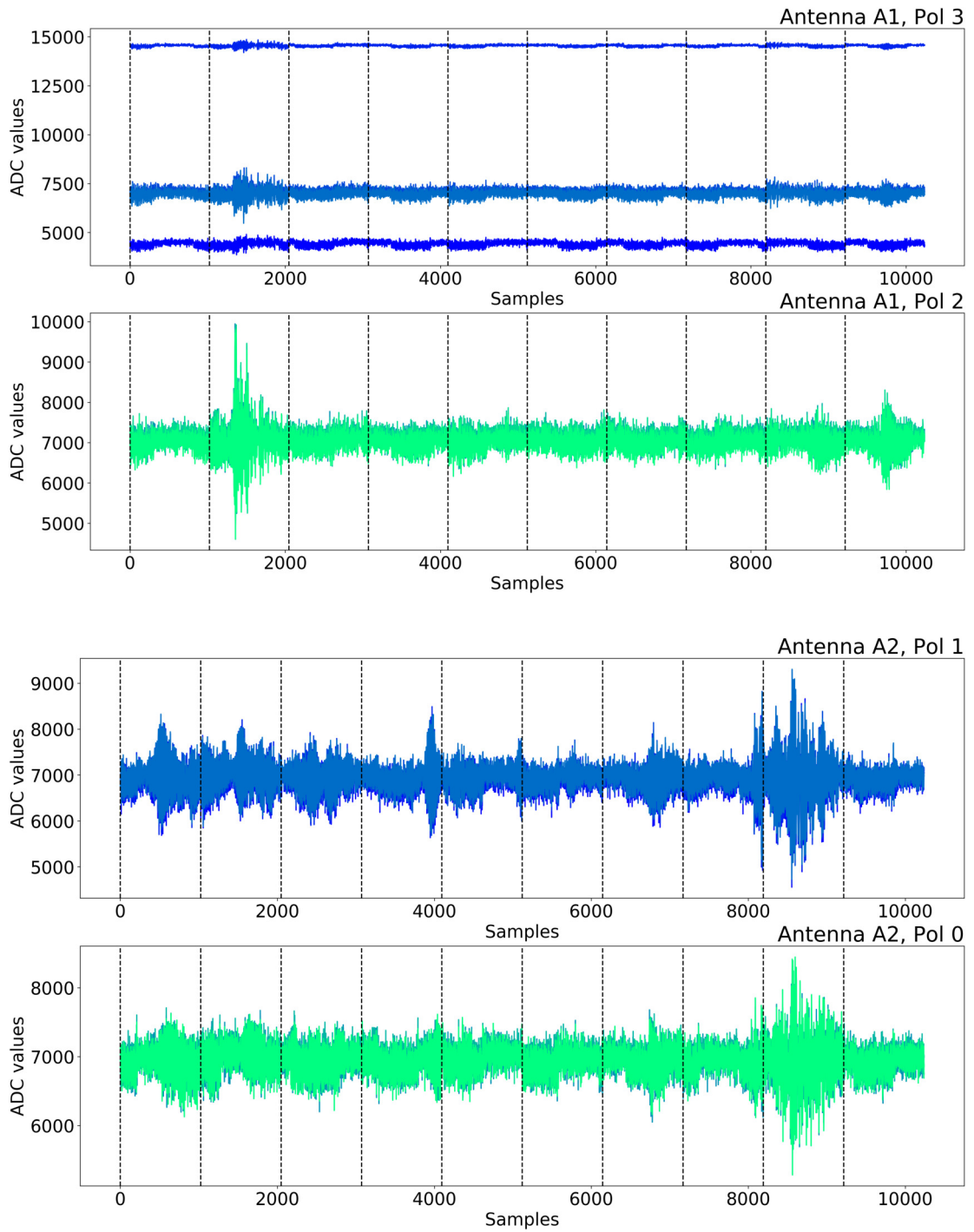


Figure 10.1: Example of radio events measured with both antennas. The polarizations are numbered from '3' to '0' according to the station map shown in Fig. 8.4. The plots show 10 events of 1024 ADC samples each that were concatenated. Dashed vertical lines indicate the beginning of the next event. The radio read-out was triggered by a single scintillation-detector event. Only background signals are expected to be visible in the data.

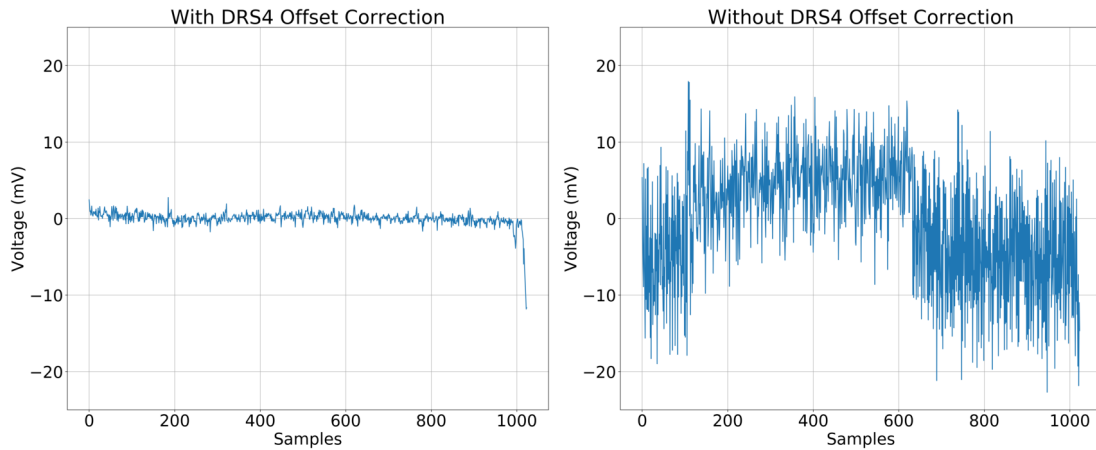


Figure 10.2: Measured DRS_4 baseline of one DRS_4 channel with (left) and without (right) offset correction. For this measurement, the voltage supply of the radio front-end electronics and the antenna’s LNA was switched off.

measurements, the identical signal is in parallel sampled with DRS_4 -channel 0–3 for one antenna polarization channel and DRS_4 -channel 4–7 for the other polarization channel of the respective antenna. In the plots shown in Fig 10.1, the ADC values of all eight channels of each DRS_4 chip are shown separated in two subplots per antenna for each antenna polarization channel. The four polarization channels of the two antennas at the South Pole were aligned to possible noise sources and numbered from ‘0’ to ‘3’ like it was shown in the detector-station map in Fig. 8.4.

We first look at the most obvious feature in the presented waveforms which is a baseline shift of two DRS_4 channels in polarization channel ‘3’. For the RadioTAXI which was deployed at the South Pole, the baseline of the DRS_4 is set by applying an offset voltage to the differential signal prior to the TAXI pre-amplifier $ADA4927$. Since the DC component in the signal line leaving the radio front-end electronics is filtered with a capacity, the reason for the observed baseline shift is most likely to find on the TAXI side. A final conclusion cannot be made at this point and might require an examination of the deployed RadioTAXI hardware. The other channels show a well-aligned baseline. Small baseline deviations are expected and can be corrected in the offline analysis.

Offsets in the DRS_4 sampling cells shift all recorded samples and increase the baseline noise over the whole frequency range. The DRS_4 stores the sampled waveform in capacities before they are read out during a trigger event. Each sampling cell has an individual constant offset that has to be subtracted from the recorded data to reduce this internal ‘noise’ contribution. This DRS_4 offset correction is usually performed in the FPGA on the TAXI board directly after the read-out of the DRS_4 chips. For the recorded data presented in this chapter, the internal DRS_4 offset correction was not available in the preliminary FPGA firmware. The effect of a missing DRS_4 offset cor-

rection can be observed as a baseline shift within one event which is visible, i.e., in the last event of polarizations '0' and '1' in Fig. 10.1. The *DRS4* offset correction reduces the noise introduced by the *DRS4* chips significantly from more than 30 mV baseline noise to about 1 mV [81]. For the recorded data, the *DRS4* offset correction was performed offline by calculating the mean value of each *DRS4* sampling cell over all recorded events and using these results as correction values. In Fig. 10.2, the result of the offline *DRS4* offset correction is shown in comparison to the not corrected baseline waveform. Usually, the calculation of the *DRS4* sampling cell offsets is done prior to the deployment of the DAQ in a laboratory setup or by recording *DRS4* baseline events with the deployed DAQ while switching off following detector electronics to reduce artificial noise. This procedure was not possible with the deployed system due to uncertainties in the sampling cell number coming from the preliminary DAQ firmware. Due to this, *DRS4* offset values were obtained with the already mentioned method to calculate the mean of all recorded traces and use these values as offset correction. Although this procedure can already reduce the noise significantly, a further decrease of the noise floor can be expected for future DAQ versions with properly measured offset values.

A more detailed view of two radio signals measured with the antennas is provided in Figure 10.3. The *DRS4* offset correction was performed on the presented data which reduces the baseline noise from tens of mV without correction to several mV. The *DRS4* channels 0–3 and 4–7 of both antennas should show the identical signal due to the signal fan-out in the radio front-end electronics. This is the case for the signals of the antenna polarizations '1' and '2'. Deviations between the signals are visible for the polarization channels '0' of antenna A1 and '3' of antenna A2. For the antenna A1, this is correlated with the baseline shift of *DRS4* channel '1' and '2'. For antenna A2, the reason is unknown and has to be investigated in more detail. A possible reason could be a reduced gain of two amplifiers on the radio front-end board or in the TAXI analog electronics.

A time offset between the channels of an antenna polarization is not visible. This is an important result since all signals will later be concatenated in the FPGA when channel cascading is realized. A time difference between the four channels of an antenna polarization would introduce time gaps in the cascaded signal. A slightly different amplification of the signals of an antenna polarization in the radio front-end or the TAXI analog electronics can be corrected in the offline analysis.

10.2 THE PRELIMINARY BACKGROUND FREQUENCY SPECTRUM

Preliminary background spectra for both antennas were obtained by averaging over the spectra of about 400 recorded radio traces. During these measurements, the radio read-out was triggered by single scintillation-detector events. Due to the high number of scintillation-detector events that are uncorrelated to cosmic-ray air shower, the 'pollution' of the recorded spectra with cosmic-ray signals can be estimated as very low

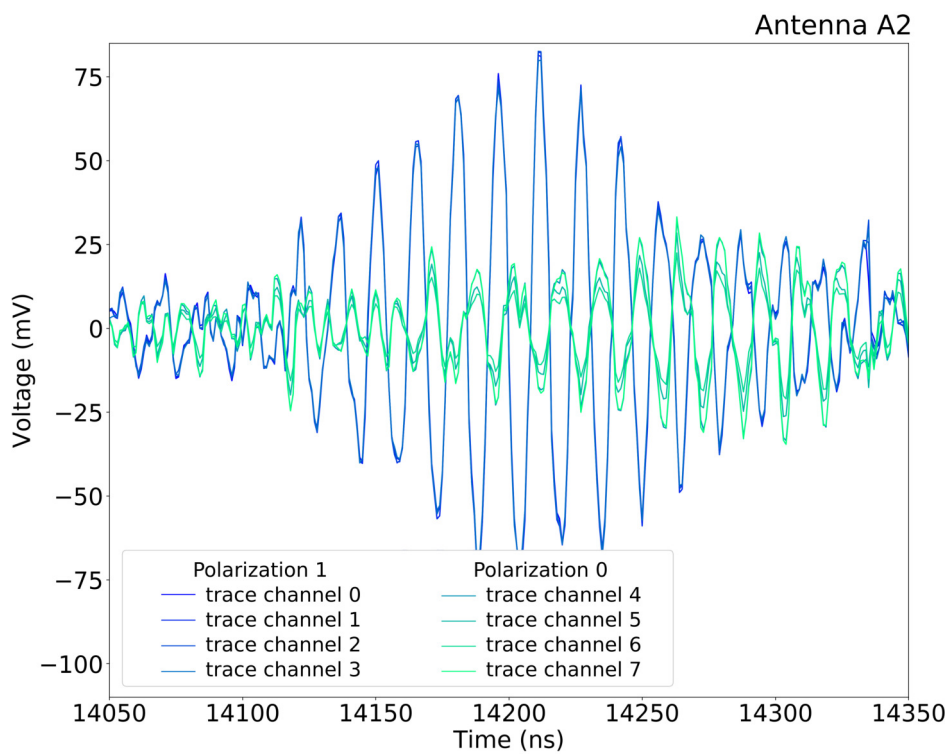
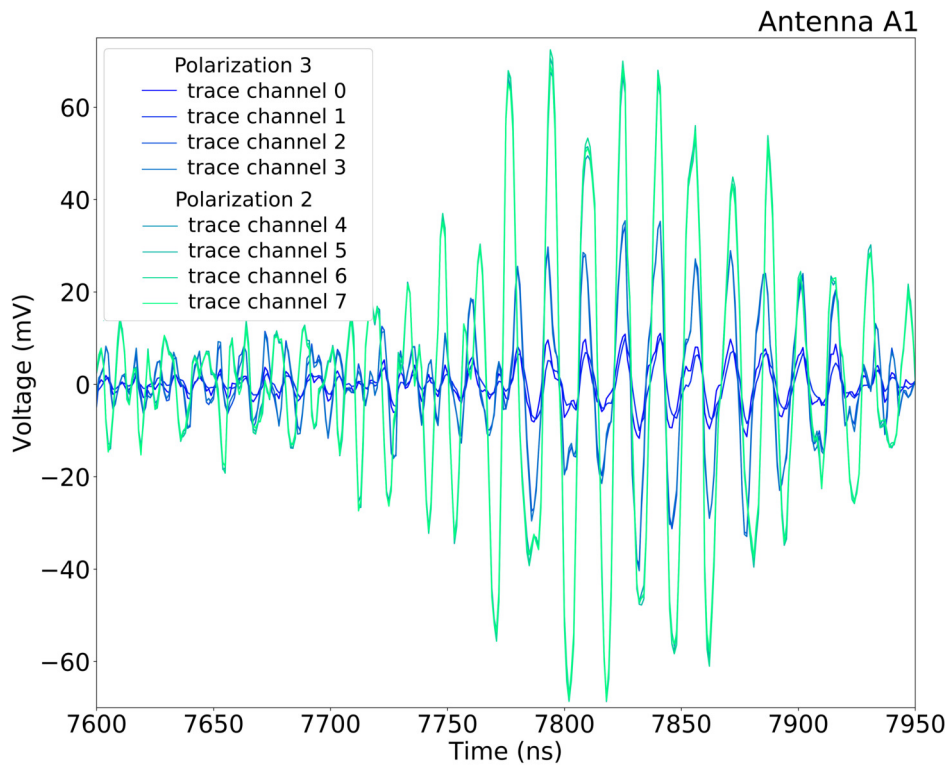


Figure 10.3: Zoom into two recorded radio signals with the antenna A1 (top) and the antenna A2 (bottom). The *DRS₄* offset correction was performed offline on the presented waveforms.

and negligible. To improve the spectrum quality, the recorded data was corrected for *DRS4* offsets.

The measured background spectra of both antennas are shown in Fig. 10.4. The RadioTAXI strongly attenuates frequencies higher than 150 MHz (see sec. 7.4.2) which explains why the measured spectrum vanishes already between 200–300 MHz in the noise floor. The noise floor of the measurement sits between -130 dBm/Hz and -135 dBm/Hz which is slightly higher than earlier measurements in the lab indicated (see Fig. 7.11). Also, the noise level seems to be higher in the antenna polarizations aiming towards the ICL. Why the noise level differs between the different antenna polarizations is unclear yet and might require an investigation of the DAQ system in the lab after its disassembly in January 2020.

As it was already observed in the analysis of the time domain signals, two *DRS4* channels of polarization '0' seem to be improperly amplified and are reduced in signal amplitude. This is also visible in the mean spectrum of antenna polarization '0' as a reduced spectral power in these two channels. The observation that the spectra of the two outlier channels have the same shape as the spectra of the two properly working channels indicates again an issue in the amplification in the radio front-end or the TAXI analog electronics.

A reduced power in two *DRS4* channels of polarization '3' is correlated with an improper setting of the signal baseline as seen in the time-domain signal in Fig. 10.1. Whether the shifted baseline is causing the decrease in spectral power due to saturation effects in the TAXI pre-amplifier or the *DRS4* or whether these two effects are correlated differently cannot be said yet but requires an investigation of the actual hardware.

Several radio frequency interference (RFI) peaks are visible in the spectra of all polarizations. For both antennas, the RFI peaks are stronger in the spectra of the polarizations aiming towards the IceCube Lab (ICL) which are polarization '1' of antenna A2 and polarization '2' of antenna A1. In Fig. 10.5 a detailed view of the frequency bandwidth of 50–180 MHz is presented with dashed lines indicating multiples of 10 MHz that can describe several of the RFI peaks in the spectrum. The strongest RFI peak is visible in all spectra at 67 MHz. Until now the source for the RFI noise is unknown. Since the RFI gets stronger when aiming at the ICL, a noise source inside the ICL is likely. RFI peaks at multiples of 10 MHz were already visible in earlier background measurements shown in 9.5. Earlier measurements were performed in close distance to the ICL (~25 m) and show RFI peaks at multiples of 10 MHz with a significantly higher strength than observed with the deployed antennas which have a distance to the ICL of about 200 m. This again points to the ICL as a possible noise source. RFI can also be produced by the RadioTAXI electronics itself or by electronics nearby. The RadioTAXI is deployed in the field hub together with a power transformer, a *White Rabbit* node and the DAQ electronics of the scintillation detectors of the University of Madison (the latter is placed in a separate plastic box in a distance of about 2 m). This

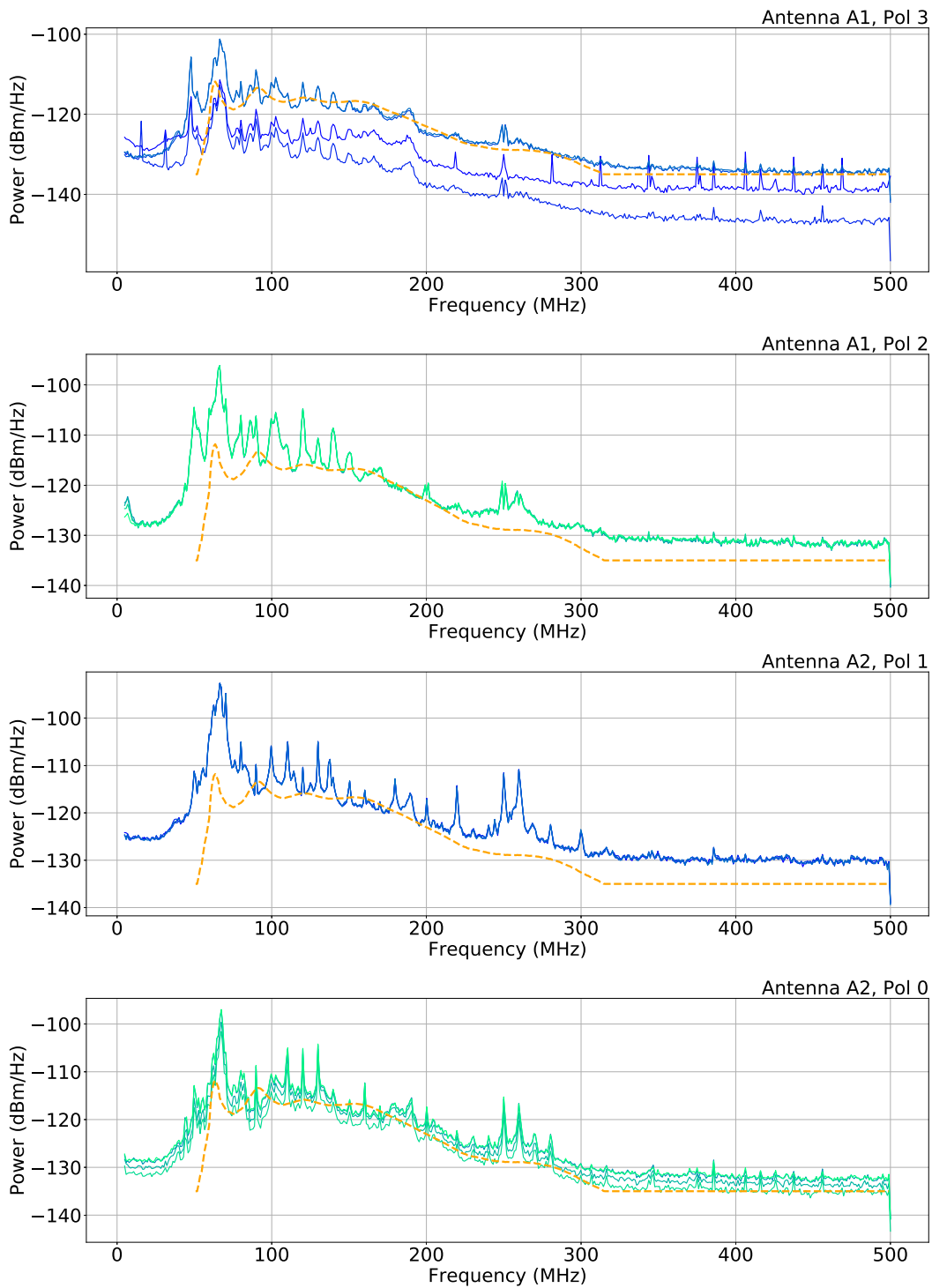


Figure 10.4: Average background spectra of all four polarizations of both antennas. The antenna polarizations are numbered as shown in the deployment map in Fig. 8.4. The measured data was corrected for DRS_4 offsets. A prediction of the Galactic noise is included in the plots as orange dashed line. A noise floor of -135 dBm/Hz of the DAQ was assumed for the prediction of the Galactic noise.

RFI does not have to be picked up by the antenna but could also couple into the signal lines of the antenna or the signal lines inside the RadioTAXI housing. Also, the IceAct camera, a prototype imaging air-Cherenkov telescope installed in the detector station, that is located in several meters distance to both antennas is a likely source of radio noise although the source direction indicated by the different strength of RFI in the antenna polarizations is disfavoring the IceAct camera as a source. A more detailed investigation is foreseen by switching off different possible nearby sources and monitoring the antenna background spectrum. A measurement with a directional antenna at the measurement site is planned for January 2020. Polarization '3' is aligned perpendicular to all possible noise sources near the antenna site and shows the less RFI pollution of all polarizations, as expected.

Apart from the RFI pollution, the spectrum shape resembles the prediction of the Galactic noise for high frequencies which is shown in Fig. 10.4 as a dashed orange line. This prediction follows the Galactic noise described by the Cane model as it is introduced in section 9.2. The prediction includes the gain of the radio front-end electronics and the attenuation of the RadioTAXI system as it was measured and presented in section 7.4. For frequencies lower than about 100 MHz, the measured spectrum shape and the prediction deviate as it was already observed in earlier measurements shown in Fig. 9.5. This might indicate, that the simulated low-noise amplifier (LNA) gain, which was used to obtain the Galactic noise prediction, might have a different frequency pattern than expected. Future characterization measurements of the antenna and the LNA can clarify this assumption.

10.3 CONCLUSION

Due to a hardware failure of the deployed DAQ system that was only recognized after the deployment, data from the two prototype antennas was only available starting September 2019. At the end of the time of this thesis, work was still ongoing to stabilize the data taking with the RadioTAXI DAQ at the South Pole. Features like a *DRS4* offset correction, channel cascading, and a parallel readout of all available *DRS4* chips were not yet implemented in the firmware of the field-programmable gate array (FPGA) on the RadioTAXI board. Therefore, the presented analysis of available data should not be regarded as final but is intended to give a first glimpse of the current situation and provide important information on the ongoing work to improve future data analysis and next versions of the radio front-end electronics.

After eight months of inactivity during the South Pole night, all deployed antennas and the RadioTAXI DAQ system are operating. Some issues in the signal of single channels are visible like an improperly set baseline for two channels and a lower amplification in two other channels. These issues have to be investigated when direct access to the DAQ hardware is possible after the disassembly of the DAQ at the South Pole in January 2020. The results of all other channels show a stable gain and a neg-

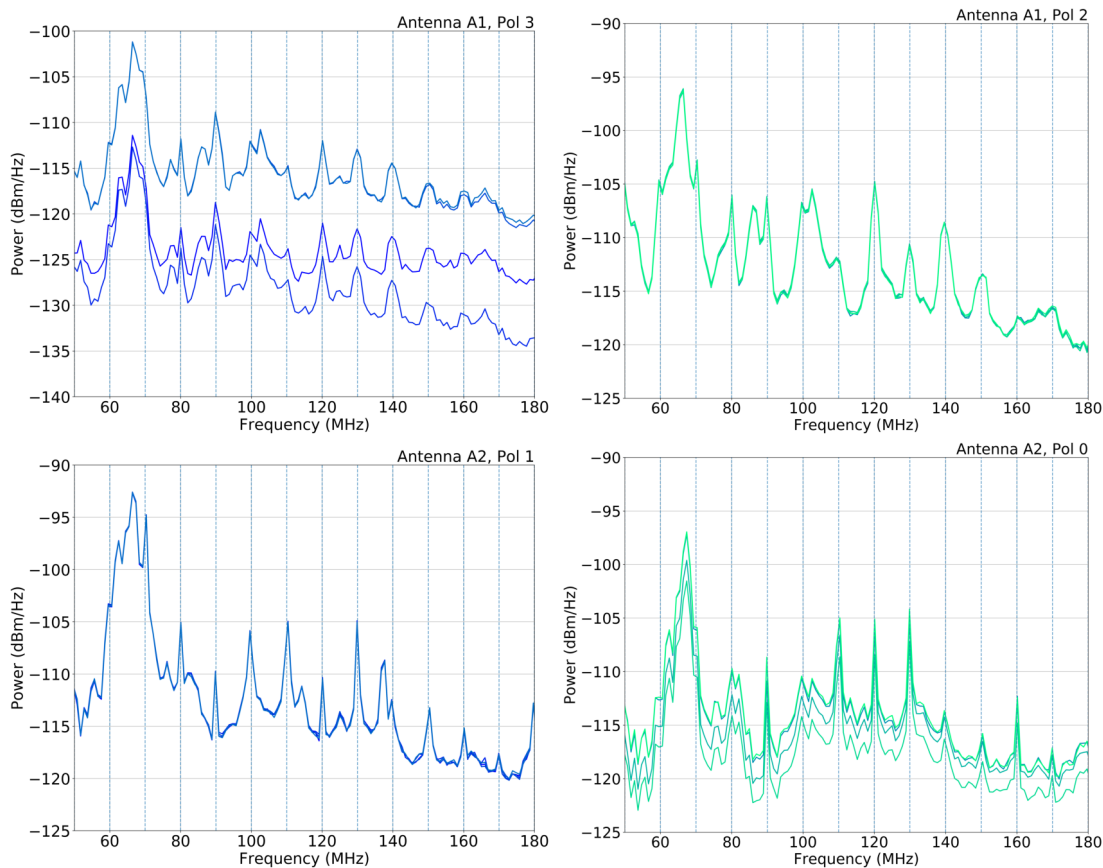


Figure 10.5: Averaged background spectra in the frequency range of 50–180 MHz. Dashed lines indicates multiples of 10 MHz. The presented data is corrected for *DRS4* offsets.

ligible time difference between the four signals of each polarization. The background spectra measured with both antennas show multiple RFI peaks in the frequency range from 50–200 MHz and partly above. A comparison of the strength of RFI peaks in the different antenna polarizations indicates the IceCube Lab as a possible source of noise signals. RFI peaks are visible at multiples of 10 MHz as it was already observed in an earlier measurement during the deployment of the antennas in January 2019. Other sources of noise near the prototype antennas are the IceAct camera close to both antennas and the station electronics buried in the snow inside plastic boxes. The latter also houses power transformers which are in general a likely source of radio emission. The presented measurements motivate an in-depth investigation of noise sources at the measurement site. These could consist of a replica station of scintillation detectors and antennas with the same electronics as used at the South Pole to investigate noise generated in the station electronics or an investigation of noise sources at the South Pole by switching off different electric systems while monitoring the noise. Apart from the

RFI pollution, the measured spectrum resembles the prediction of the Galactic noise for frequencies higher than 100 MHz. For lower frequencies, the measured spectrum and the expectation deviate as it was already seen in earlier measurements. This might indicate a not-as-expected frequency pattern of the antenna and LNA gain which both were based on simulation results for the work of this thesis.

The unexpectedly high pollution with RFI noise and the higher noise floor of the DAQ compared to earlier measurements affect the energy threshold of the measurement. The presented results indicate an increased energy threshold if no changes are made. However, the recorded data show that also including the actual noise floor and the RFI pollution, the measured radio signals are far from saturation and the RFI and baseline-noise situation are not fundamental problems.

CONCLUSION AND OUTLOOK

The IceTop surface array of the IceCube experiment will be enhanced in the next years within the frame of the IceCube Upgrade. By this, new detectors will be installed in the array to increase the capabilities of IceTop and to make a first step towards a next-generation IceCube detector, IceCube-Gen2. We propose the installation of radio antennas in addition to new scintillation particle detectors inside the IceTop array. Measuring the radio signal of cosmic-ray air showers in combination with the particle signal increases the accuracy of cosmic-ray measurements and reconstruction, in particular the mass-composition sensitivity, can improve the veto capabilities of IceTop, helps in understanding hadronic interactions during the shower development through the atmosphere, and opens new fields of research like the search for PeV-gammas from the Galactic Center. Within the frame of this thesis, efforts in the implementation of radio antennas into the IceTop surface array were started. The presented work led to the deployment of two prototype radio antennas at the South Pole in January 2019 within this thesis.

The SKALA antenna is the preferred antenna candidate of the IceCube radio extension. The SKALA antenna is developed by the Square Kilometer Array collaboration and designed for an operation at experiment sites in Australia and South Africa. To test the ability of the antenna to operate under conditions prevailing at the South Pole, tests of the antenna's plastic-material structure and characterization measurements of the antenna low-noise amplifier (LNA) were performed down to temperatures of -70° . The LNA characterization shows a slight increase in LNA gain with temperature that can introduce an uncertainty of about 1.25% in the target measurement bandwidth of 100–190 MHz.

To meet requirements regarding the antenna's mounting structure like a sufficient material resistance against low temperatures and UV radiation, a good stabilization on the snow ground, and a variable antenna height, a new antenna mounting structure was designed. The mounting structure consists of glass-fiber enhanced plastic materials (GFK) and a plywood base that is fastened with GFK snow spikes in the snow. Antenna mountings in three different heights of the antenna above the snow level of 0.3 m, 0.7 m and 1.7 m were designed with the purpose to test the amount and effect of snow accumulation on the antenna structure and the snow-drift behavior around the antenna.

Test measurement with the SKALA antennas were performed before the deployment at the South Pole with the hybrid engineering array at KIT that was installed within

the frame of this thesis. The engineering array serves not only as a test and characterization stand for the SKALA antennas but for all newly developed detectors, like the IceCube scintillation detectors, and played a key role for a successful deployment of the SKALA radio antennas at the South Pole. Besides testing the antenna electronics during real measurement operation and test deployments of the antenna mountings, four SKALA radio antennas were operated over several months to search for cosmic-ray radio signals. Although a final confirmation of cosmic-ray induced radio signals based on simulation analysis was not possible during the time of this thesis, several promising events were found.

A concept of a hybrid DAQ system was developed during this thesis based on the TAXI DAQ system that was originally used as DAQ for the IceScint scintillation detectors. The TAXI DAQ samples incoming signals using domino ring sampler chips (*DRS4*) that provide a variable sampling rate of 0.7–5 GHz and eight input channels. TAXI can be equipped with three *DRS4* sampling chips with, in total, 24 input channels. One of these chips samples the analog signals of the scintillation detectors, the other two can be used to sample radio signals. For this, the *DRS4* chips are operated in channel-cascading mode that reduces the number of effective input channels to two per chip and increases the sampling length of the radio signals. With this setup, two radio antennas with two polarizations each can be operated together with eight scintillation detectors.

To be able to operate radio antennas, additional radio-specific components have to be introduced into the DAQ system. To do so, radio front-end electronics were designed, built and characterized during this thesis. The radio front-end electronics include bias tees to power the antenna LNAs, filter stages including a high-pass filter and a low-pass filter to cut the measurement bandwidth to 50–350 MHz and an additional amplification of the radio signal of 10 dB. Characterization measurements of the radio front-end electronics were performed for temperatures between $+20^\circ$ and -70° . The change in gain in the bandwidth of the front-end pass-band and a realistic temperature range of -20° to -70° would introduce an uncertainty on the signal amplitude of 9% if the temperature would not be monitored. In the actual operation, the ambient temperature in the DAQ housing can be monitored and changes of the gain due to temperature variations can be corrected.

Measurements of the frequency response of the TAXI DAQ system revealed an unexpected attenuation behavior of the TAXI analog electronics with a non-flat response for frequencies up to 150 MHz and a strong attenuation for frequencies higher than 150 MHz. The reason for the attenuation is unknown until now and could be investigated with future versions of the TAXI DAQ that were not available for measurements during this thesis. Due to this, results for the characterization of the full DAQ system including the radio front-end electronics and the TAXI DAQ are only reasonable for frequencies below about 200 MHz. This covers the target measurement bandwidth of

100–190 MHz but does by far not cover the whole possible bandwidth of at least up to 350 MHz at a minimum sampling frequency of 0.7 GHz of the *DRS4* chips.

Two SKALA prototype antennas were deployed in January 2019 at the South Pole together with a hybrid DAQ system consisting of the TAXI DAQ and front-end electronics. The two SKALA antennas extend the existing prototype scintillation-detector array that was deployed in January 2018. The deployment of the electronics and especially the prototype antennas went smooth and the developed antenna mounting structure was found to be easy and fast to deploy with a team of two persons. A monitoring of the snow accumulation on the antenna structure and around the antenna took place during the South Pole night (winter). Although the antennas seem to not affect snowdrifts around the antenna, snow accumulation on the antenna was observed that grew during the South Pole winter. Future monitoring will show whether this snow vanishes during the summertime or whether snow will accumulate year-round. Information gained during the deployment and from the antenna monitoring over the wintertime provides important input for future designs of new antenna mountings and deployment campaigns.

Measurements of the radio background near the IceCube Lab located in the center of the IceTop array were performed during the deployment in January 2019. The background frequency spectrum shows strong RFI lines every 10 MHz that might be emitted from electronic devices inside the ICL. Since the measurement antenna was located only 25 m away from the ICL, the ICL is the most probable noise source. Measurements in other directions additionally reinforce this assumption. The overall background spectrum resembles the expectation of Galactic noise in shape for frequencies above 100 MHz. Variations of the background noise with a period of 12 hours were observed in the measured data of a 23 hour measurement. Simulations show, that this variation is in agreement with the expected noise variation generated by the rotation of the Galactic Center around the antenna. Concluding from these results, the Galactic noise can be assumed as the dominating background noise at the measurement site. This is an important result since only with a dominating Galactic noise, the measurement in a higher frequency band will improve the measurement results and lower the radio energy threshold down to single PeV energies.

Due to a hardware failure during the deployment of the TAXI DAQ, data taking with the antennas was impossible until September 2019. The finally received data shows strong RFI lines in the measured background spectra of all antennas that are resembling the RFI signals observed in earlier measurements. A comparison of the signals in the four polarizations of the two deployed antennas indicates the IceCube Lab to be a possible source for background noise. RFI peaks are visible in the spectrum at multiples of 10 MHz like it was already observed during measurements of the radio background near the ICL in January 2019. The general spectrum shape follows the

prediction of the Galactic noise.

The presented work is a first step towards an IceCube cosmic-ray radio array inside the IceTop surface detector. Based on the presented results, improvements in various parts of the prototype detector are already under development or planned for the near future. The most obvious and critical task might be the investigation of the unexpected DAQ response that is negatively influencing the measurement. The firmware of the TAXI DAQ is still under development and new, more stable firmware versions will increase the understanding of the actual problem. Measurements with next versions of the DAQ hardware with modified analog input electronics will then provide important input to solve this issue.

Closely connected to the DAQ development is the improvement of the radio front-end electronics. Based on the printed-circuit-board layout developed during this thesis, new versions of the radio front-end will be designed with an adjusted amplification of the radio signal and an improved interface to the TAXI DAQ. Since the amplification of the analog radio signal is directly influencing the energy threshold of the radio array, the amplification factor has to be set with care. This is done by performing simulation studies that take the presented background measurements and new data from the South Pole into account. An improved interface of the radio front-end to the TAXI DAQ will decrease the noise introduced by the radio front-end electronics and can be realized with a direct board-to-board connection.

An improved design of the antenna mount is at this moment under development that foresees a liftable mounting structure to raise the antenna after several years of operation. Based on the observed snow accumulation on the antenna structure, a coating of the antenna material with Teflon and a redesign of individual antenna parts is under discussion.

The prototype detector station will be extended with one additional antenna and an updated version of the TAXI DAQ and scintillation detectors in January 2020. A deployment of 32 detector stations with, in total, 96 radio antennas and 256 scintillation detectors is planned for the next years. The production of the detectors and the electronics of the proposed 32 station will happen in the next two years at the Karlsruhe Institute of Technology. The deployment of the surface stations is foreseen to happen before and after the deployment of the IceCube Upgrade and is planned to be finished in 2024.

With this enhanced IceTop detector including scintillation detectors and radio antennas, we can look forward to more accurate cosmic-ray measurements, new opportunities to gain knowledge, and the discovery of exciting things we never expected to find.

APPENDIX

APPENDIX

A.1 AN IMPROVED AMPLIFICATION CIRCUIT FOR THE RADIO FRONT-END ELECTRONICS

The original amplification circuit of the radio front-end electronics shows some issues in the design of the circuit that were only found out after the first version of the front-end electronics were produced and deployed. In this section, an improved amplification circuit is presented that should result in a more stable gain pattern.

In Fig. A.1, an improved version of the amplification circuit is shown that consist of

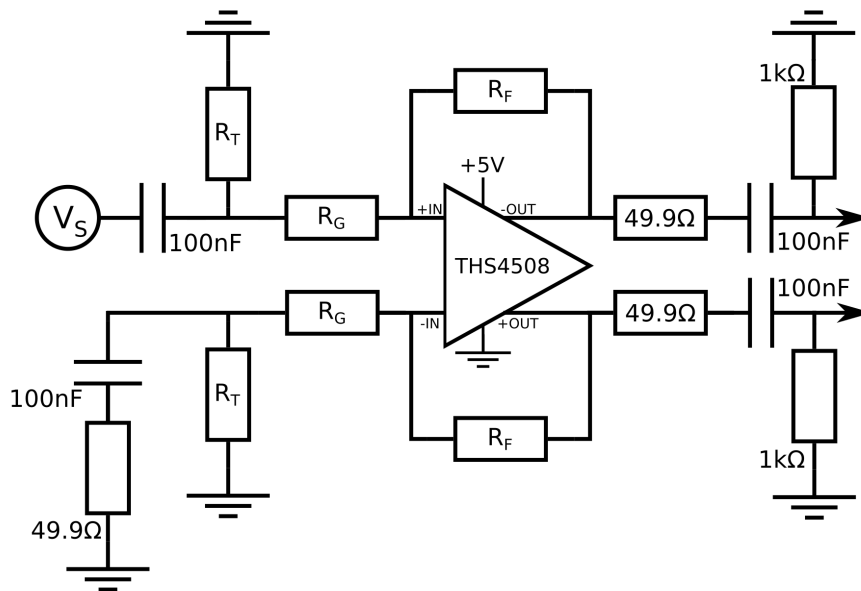


Figure A.1: Schematic of a new front-end amplifier circuit for one amplifier. The input signal V_S is the radio signal after filtering and after fan-out into the four parallel amplifiers. The input signal V_S is assumed to be $50\ \Omega$ terminated. After the signal passed the presented filter circuit, it is guided to the TAXI inputs.

an additional resistor in the negative input signal way of the amplifier to match the impedance with the $50\ \Omega$ input signal and an more clear placement of the termination resistor R_T , the amplifier input resistor R_G and the feedback resistor R_F . Leaving the amplifier, the positive and negative signals pass a $50\ \Omega$ resistor to reduce standing waves that might be generated in the output lines due to reflections of the signal. In

the end, the DC voltage on the signal line introduced by the amplifier is canceled with a capacity and the output line is linked to ground using a 1 k Ω resistor, as it was the case in the last-version circuit.

The gain of the amplifier is set to 10 dB by choosing the resistors R_T , R_G , and R_F for a 50 Ω input signal as

$$R_T = 69.8 \Omega$$

$$R_G = 100.0 \Omega$$

$$R_F = 348 \Omega.$$

It has to be kept in mind, that the 50 Ω resistor after the amplifier decreases the signal amplitude. Therefore, the total gain of the circuit will not reach 10 dB. This can be counteracted by setting the amplifier to a higher gain which decreases the frequency bandwidth of the amplifier.

A final decision on the target gain is not made at this point but is under investigation. In the end, the amplifier circuit has to be redesigned to meet this requirement or a different amplifier has to be chosen if the amplifier THS4508 it not sufficient.

A.2 GAIN MEASUREMENTS WITH DIFFERENT INPUT ATTENUATION

To investigate possible effects of the input signal height on the recorded frequency response of the TAXI DAQ, the calibration-source measurement with IceTAXI was repeated with lower attenuation of the input signal. For more information about the measurement setup and an interpretation of the results, the reader is referred to chapter 7. In Fig. A.2 the TAXI frequency response is shown for different attenuation levels of the input signal. For comparison, the frequency response of the full DAQ system including TAXI and the radio front-end electronics is included in the plot. It is visible, that the TAXI frequency response does not change with input attenuation.

A.3 THE CALIBRATION SOURCE RSG 1000

As the reference source for the characterization measurements of the antenna's low-noise amplifier, the radio front-end electronics and the TAXI DAQ, the frequency generator *RSG 1000* developed by *Teseq* is used. The frequency generator has an output frequency range of 1–1000 MHz and can output pulses with a pulse frequency of 1 MHz, 5 MHz and 10 MHz. Fig. A.3 shows the output frequency spectrum, measured with at 50 Ω input. For the presented measurements, a pulse frequency of 1 MHz was used. The signal stability is given as ± 0.3 dB for an operation at a constant temperature of 20°C, which can be assumed for the operation in the air-conditioned laboratory.

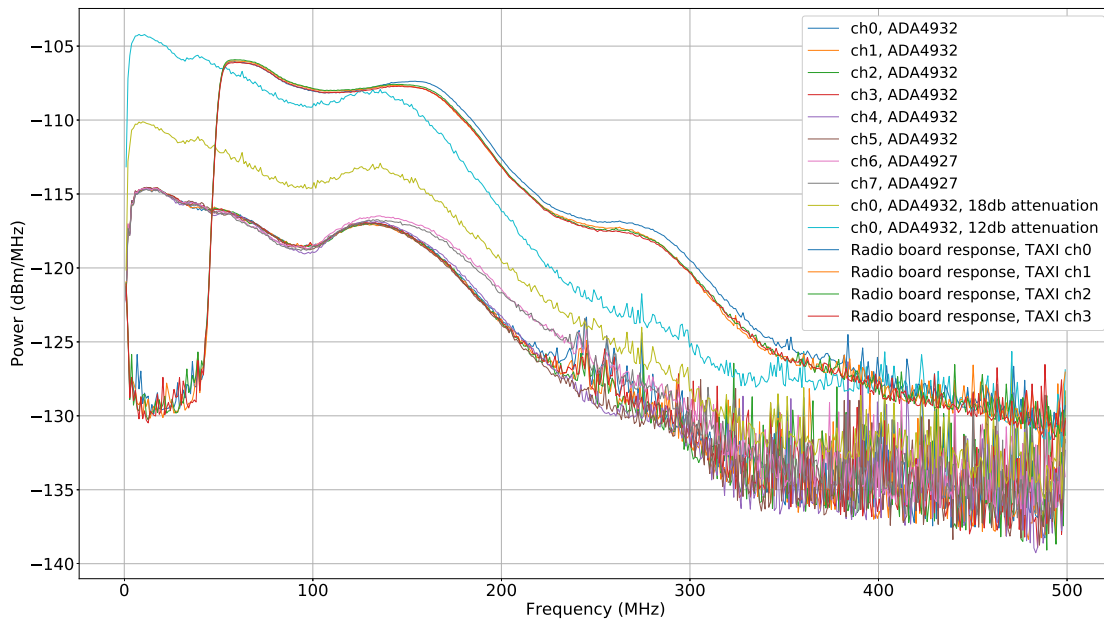


Figure A.2: Spectra with different calibration source attenuations

A.4 SOUTH POLE ANTENNA TRANSPORT

For the transport of three antennas together with cables, antenna mounting structures and tools, a transport box was designed during this thesis and is presented here to provide advice for future transports, if needed. In Fig. A.4 a sketch of the transport box is shown. The height of the transport box was 0.3 m, which was more than sufficient for three antennas. The transport box was made out of plywood which is an important detail since the import of wooden products into New Zealand can be tricky. Plywood seems to cross the border to New Zealand without problems. A letter containing information about the plywood and a certificate of the harmlessness of the wood was sent with the transport papers. Two separated rooms on both sides of the antennas contained the low-noise amplifier and smaller antenna parts. The antennas were secured in the middle of the transport box with ropes and cable ties at the walls of the box and at the wooden separation between the antennas and the lower storage room which contained the heavier parts that had to be shipped with the antenna. The empty transport box weighted 200 kg. The loaded and closed transport box weighted about 400 kg. The box was not sent back from the South Pole after deployment but was recycled there.

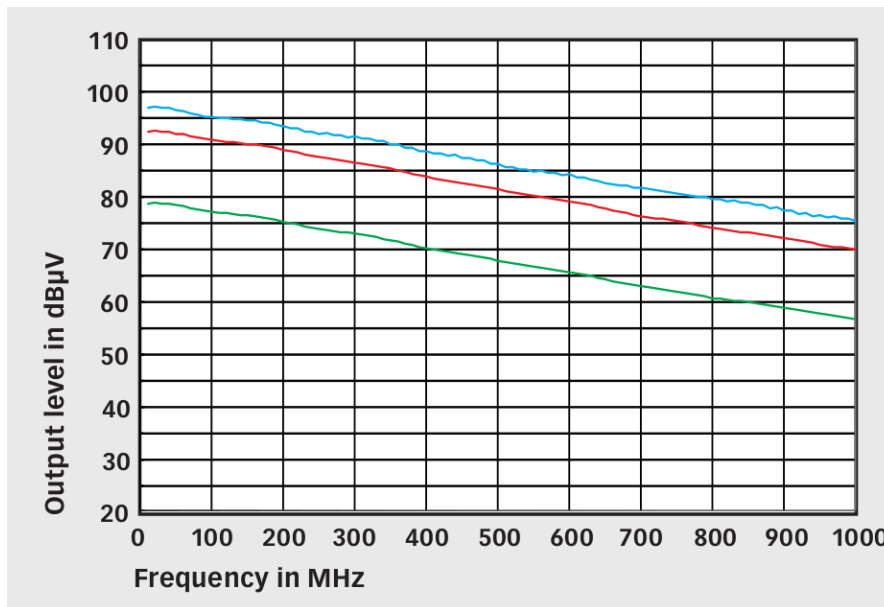


Figure A.3: RSG 1000 frequency spectrum at $50\ \Omega$ [119]

A.5 FIT RESULTS BACKGROUND MEASUREMENT TIME VARIATION

The background-noise variation was measured in different frequency bandwidth of 3 MHz apart from RFI peaks in the spectrum. For more details, the reader is referred to chapter 9. The following plots in Fig A.6 show the measured power over time, a floating mean of the data with a kernel size of 155 s and a sine fit to the data. Results for every sine fit can be found in table A.1. In every plot, the expected variation due to the rotation of the Galactic Center and the Sun around the antenna polarization is shown for comparison. Fit results between 100–200 MHz do not always meet the expectation due to a higher pollution with RFI noise. For frequencies with less RFI noise, especially above 200 MHz, the variation of the background is clearly visible in the data.

A.6 REPORT OF THE DEPLOYMENT CAMPAIGN AT THE SOUTH POLE 2018–19

This is a report on the deployment of two prototype antennas and a hybrid RadioTAXI DAQ in January 2019. The following text hopefully provides useful information for future South Pole travelers and deployment helpers.

The author hand-carried the RadioTAXI to the South Pole in a checked-in bag. To avoid problems with customs service, accompanying documents were put together with the electronics into the suitcase which provided information about what this piece of electronics is, which purpose it has and that it belongs to the Karlsruhe Insti-

Frequency	a	b	c	d
101.0–104.0 MHz	548.32	0.097	-0.55	14113.34
106.0–109.0 MHz	591.18	0.093	-0.98	14505.05
111.0–114.0 MHz	455.56	0.075	0.39	6258.92
116.0–119.0 MHz	491.96	0.087	-0.44	4476.36
121.0–124.0 MHz	418.62	0.085	-0.42	5229.4
126.0–129.0 MHz	403.75	0.048	3.28	11767.7
131.0–134.0 MHz	-7859.54	0.036	0.9	31349.02
136.0–139.0 MHz	-516.96	0.09	0.53	10371.07
141.0–144.0 MHz	464.73	0.047	2.72	7120.11
146.0–149.0 MHz	620.94	0.041	3.71	5303.63
151.0–154.0 MHz	655.43	0.044	3.48	5633.12
156.0–159.0 MHz	324.87	0.049	2.97	4240.51
161.0–164.0 MHz	216.26	0.071	0.73	3616.71
166.0–169.0 MHz	502.3	0.044	3.17	6914.25
171.0–174.0 MHz	183.05	0.085	-0.05	4358.92
176.0–179.0 MHz	132.48	0.088	-0.82	5974.74
181.0–184.0 MHz	281.86	0.081	-0.33	4848.59
186.0–189.0 MHz	134.03	0.089	-0.79	3191.23
191.0–194.0 MHz	182.8	0.048	2.98	2478.55
196.0–199.0 MHz	144.74	0.085	-0.38	1789.91
201.0–204.0 MHz	146.99	0.084	-0.39	1543.79
206.0–209.0 MHz	139.8	0.083	-0.13	1740.8
211.0–214.0 MHz	124.65	0.084	-0.3	1394.11
216.0–219.0 MHz	65.44	0.086	-0.39	1099.09
221.0–224.0 MHz	43.08	0.09	-0.71	504.58
226.0–229.0 MHz	24.5	0.089	-0.82	254.91

Table A.1: Table with fit results

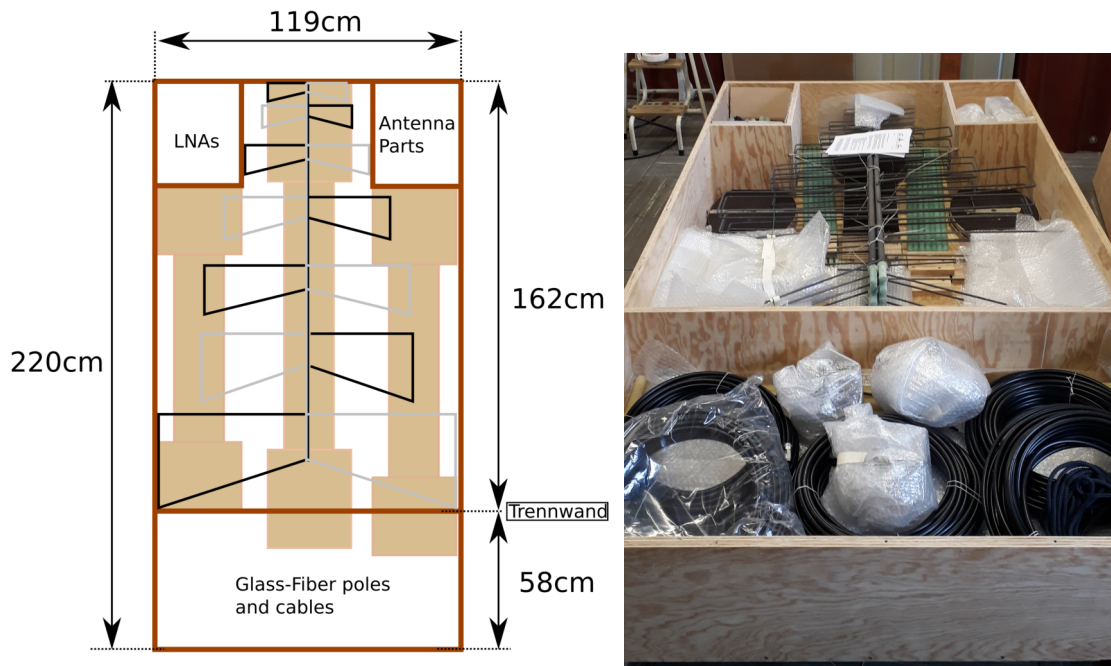


Figure A.4: Left: Sketch of the antenna transport box with dimensions. The transport-box height is 30 cm. Right: Picture of the packed transport box. Empty space was filled with cardboard and bubble foil to protect the antenna parts from mechanical shocks.

tute of Technology (KIT). However, the suitcase was not opened by customs service either on the way to the South Pole nor on the way back returning the disassembled DAQ system to KIT.

The antennas, as well as the South Pole antenna mountings and antenna cables, were sent in advance as cargo in a single crate to the South Pole. The crate was transported to the IceCube Lab (ICL) before the author's arrival at the Pole and was stored inside the ICL (see Fig A.7, left). This might not be the general case and crates may be stored outside the ICL and experience the full Antarctic coldness. Equipment that has to be protected from cold temperatures can be sent as 'Do Not Freeze'-transport which is then transported and stored in heated storage rooms.

The deployment at the South Pole began by testing the functionality of the RadioTAXI DAQ system. The integration of the RadioTAXI DAQ and the TAXI's White Rabbit node into the South Pole network infrastructure was managed by the IceCube Winterovers. After receiving IP addresses for both the RadioTAXI system and the White Rabbit node, the RadioTAXI was connected to the IceCube network system by connecting it directly to the IceCube server machines on the second floor of the ICL via glass-fiber cables (see Fig A.7, middle). The communication with the TAXI system was tested by enabling an ssh connection to TAXI from the IceCube server network. One should keep in mind that the White Rabbit node in the TAXI system cannot be reached

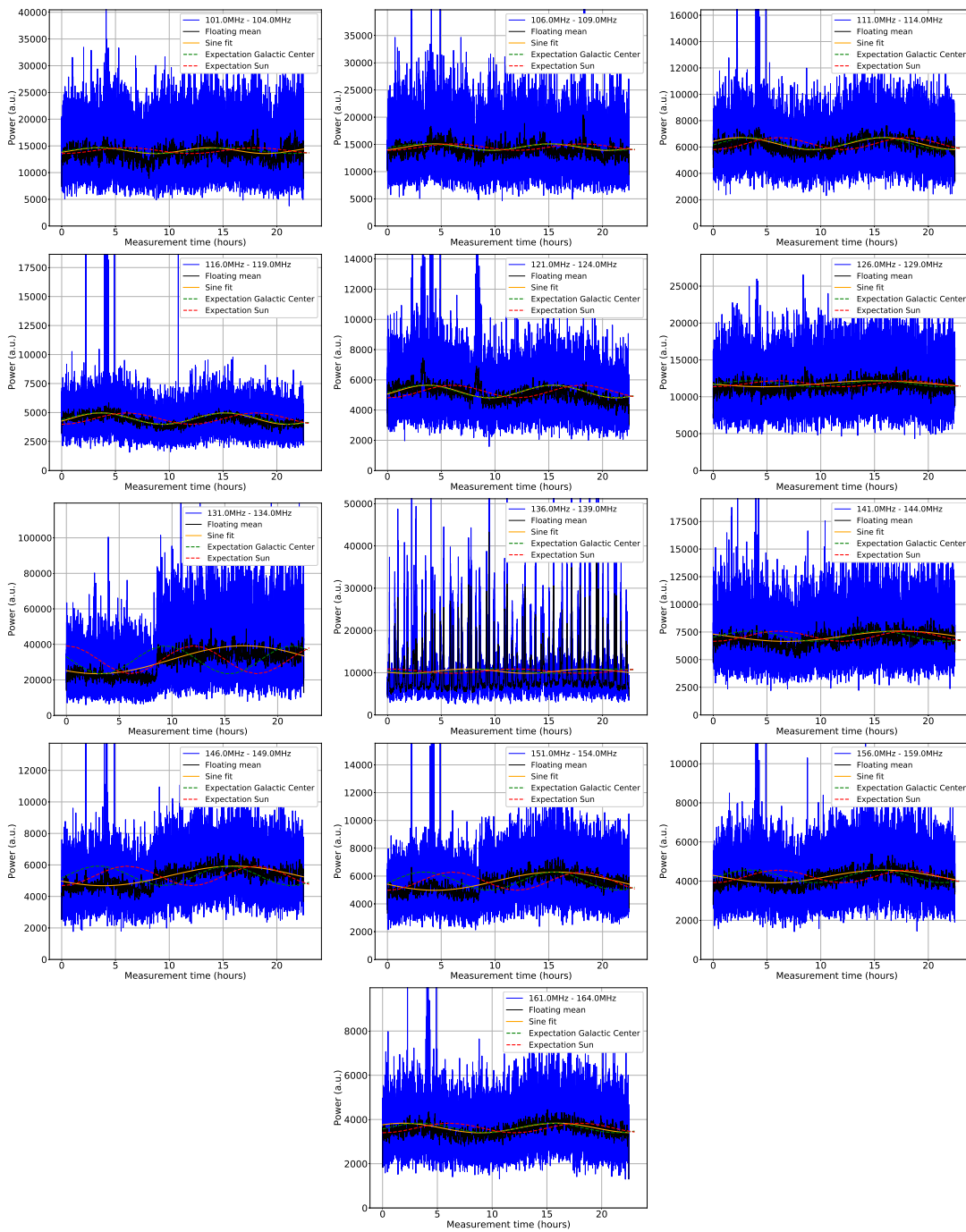


Figure A.5: Background dynamic spectrum

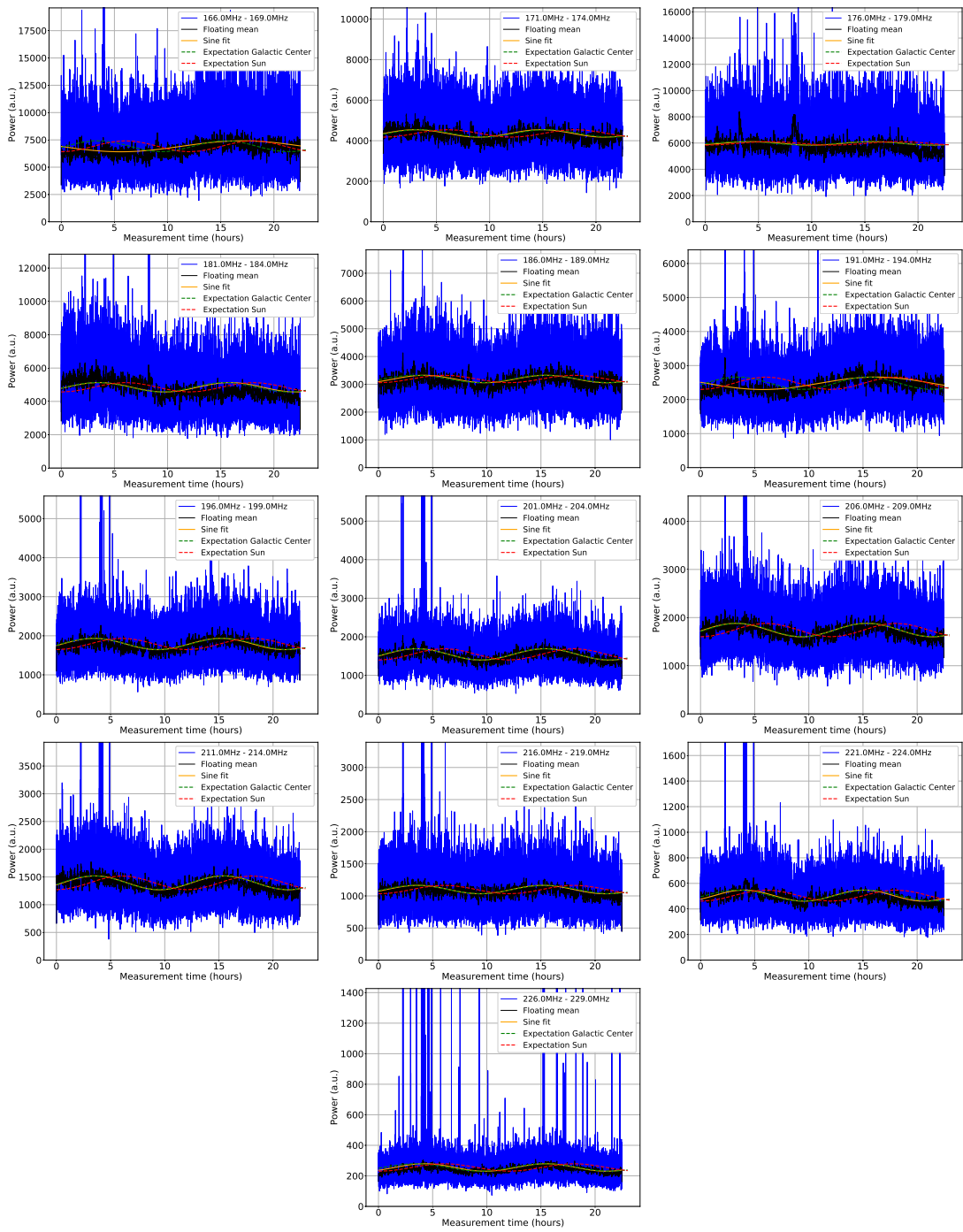


Figure A.6: Background dynamic spectrum



Figure A.7: **Left:** Antenna transport box in the ICL. **Middle:** Initial test of the new RadioTAXI DAQ system in the IceCube server room in the ICL. **Right:** Antenna structure during assembling in the ICL.

by ssh when the following systems are attached to the node via an Ethernet connection. A more in-depth test of the TAXI functionality was not possible at this time since firmware for this TAXI generation was under development at the time of deployment.

The antenna metal structure was assembled inside the ICL (see Fig A.7, right). It might be helpful for future deployments to note that the fully assembled antenna does not fit through the doors inside the ICL. Therefore, the antenna structure has to be assembled in the first entrance room of the ICL that has a direct connection to the outside. After assembling both antennas inside the ICL including the antenna's LNA, each antenna was individually carried to the deployment site that is around 200 m away from the ICL. The antenna transport happened one time by simply carrying the antenna by hand with two people to the 200 m distant site which is doable but exhausting. The second antenna was transported on a sled attached to a snowmobile while having one person on the sled securing the antenna. This was found to be an easy and safe way to carry the antenna.

At the deployment site, first, the wooden base was installed on the leveled snow surface and secured with snow spikes. The snow density varied between the two antenna locations. While it was possible to push the snow spikes at the Antenna A2 location by hand 1 m deep into the snow, this was not possible for the Antenna A1 location. However, it was no problem to push the snow spikes into the snow by using a sledgehammer. A reason for the different snow density might be heavy machinery that was used at the location of Antenna A1 in former years. This location is in one line between the ICL and the field hub electronics where cables were trenched using trench-

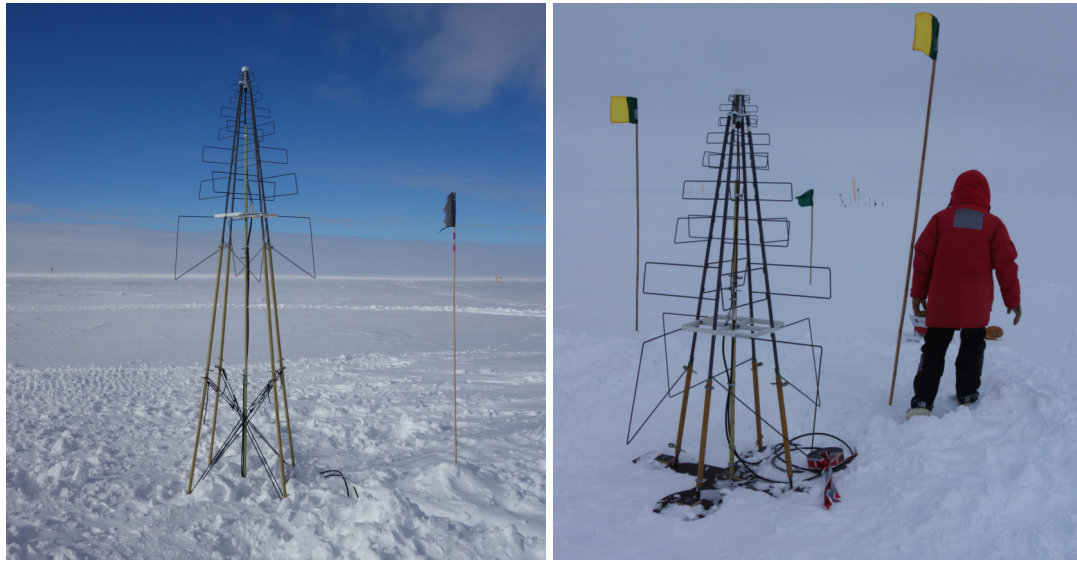


Figure A.8: Left: Big antenna A2 after the deployment. Right: Deployment of the small antenna A1 on a windy day. Wind-chill temperatures dropped down to -58°C at the day of the deployment of the small antenna.

ing machines. After installing the wooden base, the antenna mount was attached to the antenna which was doable without additional tools due to the use of cottor pins that can be fastened even with heavy gloves.

The antenna structure was fastened on the wooden base using screw connections. Fastening screws with heavy gloves is difficult. For any work with screws, the heavy gloves were removed and the work was performed only with two layers of glove liners. This was no issue during windless days. At windy days, for which the wind-chill temperature decreased to -58°C , working only with liner gloves was hard and only doable for some minutes before the hands got too cold. Hand and feet warmers are available in the ICL that can be used to stay warm during longer activities outside.

Cables going from detectors to the DAQ electronics have to be buried in cable trenches. Since a mechanical trenching of cables was not possible during the deployment in January '19, trenches had to be shoveled by hand. With a team of up to six people it was possible to prepare two trenches with a depth of about 1 m and a length of each trench of about 20 m–25 m in one day. Shoveling trenches at the South Pole is hard and physical exhaustion is amplified if one is not acclimatized to the height of about 3000 m. After shoveling trenches during the entire third day at the South Pole, the author was absolutely exhausted and went directly to bed to sleep all night through.

The location of trenches has to be marked with metal foil that is, like the cables, laid out in the trench. The cable in the trench and the metal foil should be separated by some tens of centimeters of snow to prevent accidentally damaging a cable when a trench has to be reopened. Cables and metal foil (separated by some snow) should be

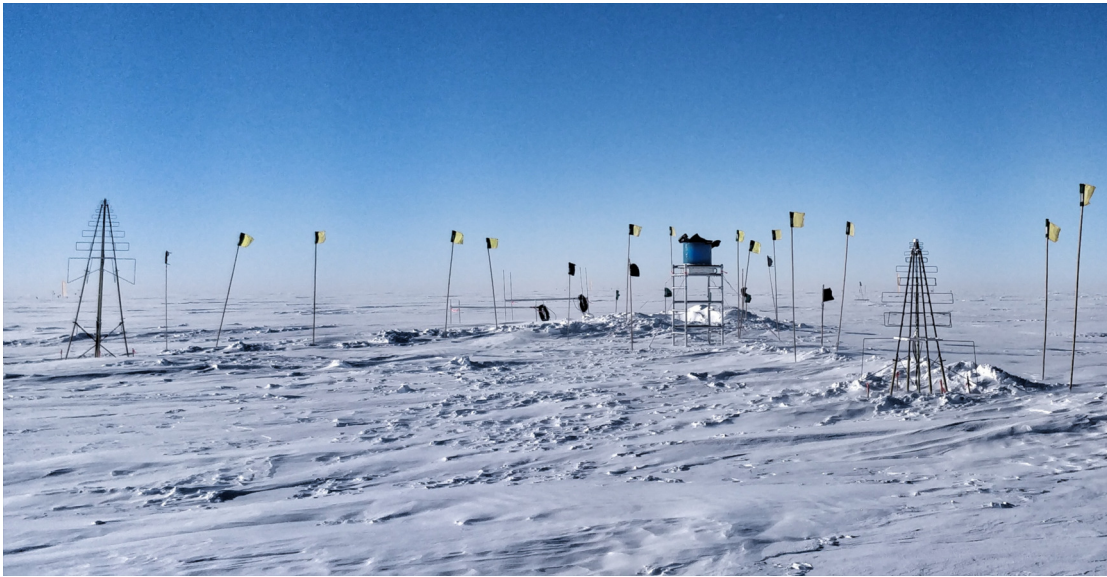


Figure A.9: Picture of the final array with the deployed antennas (Antenna A1 right, Antenna A2 left) and the IceAct telescope between the two antennas.

laid out in the trench directly after trenching. During the deployment in January, new trenches were partly filled up to more than a half of the trench height with drifting snow after one night and had to be reopened to lay out the metal foil.

A GPS survey was conducted after the deployment to measure the exact antenna position and the polarization directions. The survey points were marked with orange flags and the location of these markers was measured by the survey team. For each antenna, four markers were placed in the prolongation of the antenna polarizations to measure the antenna position and the polarization angles. For this prototype deployment, the survey markers were placed by eye which introduces additional uncertainty. A later analysis of the polarization direction of one antenna revealed an angle between the two antenna polarizations of 102° which is 12° above the actual 90° angle between the two polarizations.

Two antennas were deployed within two days by a team of two people. With some experience in deploying antennas in the field and prior preparation of the antenna structure in the ICL, a deployment of two to three antennas with a team of two people in one day is possible.

ACKNOWLEDGEMENTS

First of all, I want to thank my first referee Prof. Dr. Ralph Engel and my second referee Prof. Dr. Marc Weber for their consent to supervise this work. I very much appreciate the opportunity I was given and hope that I made good use of it.

I want to thank my supervisor Andreas Haungs who is supporting me since my master's thesis four years ago. During all this time, and especially during the time of this PhD, I always knew that I could count on him when problems appeared. I learned a lot during these years and I am very grateful for the opportunities I got. I hope that with the work I did, I was able to repay some of the trust he has placed in me.

With gratitude, I remember the help and advice of Frank Schröder. I am especially very thankful for the time he took to answer questions and to guide me in the right direction. Without him, for sure, I would not have come this far.

I thank Michele Caselle from the IPE/KIT for his time and help to develop the radio front-end electronics and Eloy de Lera Acedo from the SKA collaboration for providing the possibility to test and deploy prototype versions of the SKALA antenna. I thank Michael Riegel for his support dealing with the antenna mounting and communicating with the workshop and Harald Schieler for his help and advice during the years of this thesis. I thank Lu Lu for her help to deploy the antennas at the South Pole and for her company during this unforgettable adventure. Especially, I want to thank all the bachelor and master students who significantly contributed with their work to the deployment of the antennas at the South Pole: Reed Masek for designing the antenna mount and helping to analyze radio measurements, Mark Weyrauch for his work on characterizing the antenna LNA, Peter Steinmüller for designing and characterizing the radio front-end electronics, Noah Goehlke for his work on improving the front-end amplifier circuit, and Sara Martinelli for her analysis of radio signals measured at KIT.

I thank my colleagues in our CRT working group, Agnieszka, Anja, Aswathi, Hrvoje, Marie, Roxanne, Tom and Will for their help, their time and especially for their company. I enjoyed coming to work every day and this was mostly because of them. This also applies for Donghwa and Katrin who contributed in great ways to this warm and friendly atmosphere. It was great belonging to this group of wonderful people.

Invaluable was the support I received from Andreas Weindl and Bernd Hoffman. This does not only cover all the technical support that actually enabled the success of this work. Even more important is the absolutely friendly and helpful atmosphere which I was privileged to enjoy all these years. Thank you.

I thank Heike for all the WAB and barbecue organization, Jürgen for preparing the highly important daily coffee break, Doris for all the IT support, Sabine for taking care of everything, the Skat players for many exciting matches during lunch and the rest of the institute for the wonderful time I had.

Last but, for sure, not least, I thank my family for their support over all the years and I thank Dorothea for her love and support.

PUBLICATIONS

The following summarizes the first-author publications of the author finished during the time to this thesis.

- [1] M. Renschler et al. "Characterization of Hamamatsu 64-channel TSV SiPMs" *Nuclear Instruments and Methods in Physics Research Section A: Accelerators, Spectrometers, Detectors and Associated Equipment* 888 (2018), pp. 257–267 ISSN: 0168-9002 DOI: <https://doi.org/10.1016/j.nima.2018.01.029>.
- [2] M. Renschler et al. "Detector developments for a hybrid particle and radio array for cosmic-ray air-shower detection" *Journal of Physics: Conference Series* 1181 (2019), p. 012075 DOI: 10.1088/1742-6596/1181/1/012075.
- [3] M. Renschler et al. "First measurements with prototype radio antennas for the IceTop detector array" *36th International Cosmic Ray Conference (ICRC2019)* vol. 36 International Cosmic Ray Conference 2019, p. 401.

BIBLIOGRAPHY

- [1] V. Hess "Über Beobachtungen der durchdringenden Strahlung bei sieben Freiballonfahrten" *Physikalische Zeitschrift* 13 (1912), pp. 1084–1091.
- [2] W. Kolhörster, I. Matthes, and E. Weber "Gekoppelte Höhenstrahlen" *Naturwissenschaften* 26.35 (1938), pp. 576–576.
- [3] A. Haungs, H. Rebel, and M. Roth "Energy spectrum and mass composition of high-energy cosmic rays" *Reports on Progress in Physics* 66.7 (2003), pp. 1145–1206 DOI: 10.1088/0034-4885/66/7/202.
- [4] W. D. Apel et al., KASCADE-Grande Collaboration "Kneelike Structure in the Spectrum of the Heavy Component of Cosmic Rays Observed with KASCADE-Grande" *Phys. Rev. Lett.* 107 (17 2011), p. 171104 DOI: 10.1103/PhysRevLett.107.171104.
- [5] A. Aab "Observation of a large-scale anisotropy in the arrival directions of cosmic rays above 8×10^{18} eV" *Science* 357.6357 (2017), pp. 1266–1270 ISSN: 0036-8075 DOI: 10.1126/science.aan4338.
- [6] B. Abbott, LIGO Scientific Collaboration and Virgo Collaboration "Observation of Gravitational Waves from a Binary Black Hole Merger" *Phys. Rev. Lett.* 116 (6 2016), p. 061102 DOI: 10.1103/PhysRevLett.116.061102.
- [7] M. Aartsen "Multimessenger observations of a flaring blazar coincident with high-energy neutrino IceCube-170922A" *Science* 361.6398 (2018) ISSN: 0036-8075 DOI: 10.1126/science.aat1378.
- [8] A. Abramowski et al., H.E.S.S. Collaboration "Acceleration of petaelectronvolt protons in the Galactic Centre" *Nature* 531 (2016), p. 476 DOI: 10.1038/nature17147.
- [9] P. Bezyazeev et al. "Measurement of cosmic-ray air showers with the Tunka Radio Extension (Tunka-Rex)" *Nuclear Instruments and Methods in Physics Research Section A Accelerators Spectrometers Detectors and Associated Equipment* 802 (Sept. 2015) DOI: 10.1016/j.nima.2015.08.061.
- [10] F. G. Schröder "Radio detection of high-energy cosmic rays with the Auger Engineering Radio Array" *Nucl. Instrum. Meth.* A824 (2016), pp. 648–651 DOI: 10.1016/j.nima.2015.08.047.
- [11] M. Huynh and J. Lazio "An Overview of the Square Kilometre Array" *arXiv e-prints*, arXiv:1311.4288 (2013), arXiv:1311.4288.
- [12] P. Auger et al. "Extensive Cosmic-Ray Showers" *Rev. Mod. Phys.* 11 (3-4 1939), pp. 288–291 DOI: 10.1103/RevModPhys.11.288.

- [13] M. Tanabashi and K. Hagiwara, Particle Data Group "Review of Particle Physics" *Phys. Rev. D* 98 (3 2018), p. 030001 DOI: 10.1103/PhysRevD.98.030001.
- [14] O. Adriani et al. "Time dependence of the proton flux measured by PAMELA during the July 2006 - December 2009 solar minimum" *Astrophys. J.* 765 (2013), p. 91 DOI: 10.1088/0004-637X/765/2/91.
- [15] J. R. Hörandel "The composition of cosmic rays at the knee" *Frontier Objects in Astrophysics and Particle Physics* 2005, p. 439.
- [16] J. Blümer, R. Engel, and J. R. Hörandel "Cosmic rays from the knee to the highest energies" *Progress in Particle and Nuclear Physics* 63.2 (2009), pp. 293 – 338 ISSN: 0146-6410 DOI: <http://dx.doi.org/10.1016/j.ppnp.2009.05.002>.
- [17] L. A. Anchordoqui "Ultra-High-Energy Cosmic Rays" *Phys. Rep.* 801 (2019), pp. 1–93 DOI: 10.1016/j.physrep.2019.01.002.
- [18] D. Hooper, S. Sarkar, and A. M. Taylor "The intergalactic propagation of ultrahigh energy cosmic ray nuclei" *Astropart. Phys.* 27 (2007), pp. 199–212 DOI: 10.1016/j.astropartphys.2006.10.008.
- [19] J. Abraham, The Pierre Auger Collaboration "Observation of the Suppression of the Flux of Cosmic Rays above 4×10^{19} eV" *Phys. Rev. Lett.* 101 (6 2008), p. 061101 DOI: 10.1103/PhysRevLett.101.061101.
- [20] D. Ivanov "TA Spectrum Summary" *PoS ICRC2015* (2016), p. 349 DOI: 10.22323/1.236.0349.
- [21] H. P. Dembinski et al. "Data-driven model of the cosmic-ray flux and mass composition from 10 GeV to 10^{11} GeV" *PoS ICRC2017* (2018) [35,533(2017)], p. 533 DOI: 10.22323/1.301.0533.
- [22] F. G. Schröder "News from Cosmic Ray Air Showers (ICRC 2019 – Cosmic Ray Indirect Rapport)" *arXiv e-prints*, arXiv:1910.03721 (2019), arXiv:1910.03721.
- [23] A. Yushkov, The Pierre Auger Collaboration "Mass composition of cosmic rays with energies above $10^{17.2}$ eV from the hybrid data of the Pierre Auger Observatory" *PoS ICRC2019* (2019) to be published, p. 482.
- [24] H. S. Ahn et al. "Measurements of cosmic-ray secondary nuclei at high energies with the first flight of the CREAM balloon-borne experiment" *Astropart. Phys.* 30 (2008), pp. 133–141 DOI: 10.1016/j.astropartphys.2008.07.010.
- [25] Y. Ohira, N. Kawanaka, and K. Ioka "Cosmic-ray hardenings in light of AMS-02 data" *Phys. Rev. D* 93.8 (2016), p. 083001 DOI: 10.1103/PhysRevD.93.083001.
- [26] H. Klapdor-Kleingrothaus and K. Zuber *Astroteilchenphysik* Teubner Studienbuecher, 1997.

- [27] D. Ikeda, Telescope Array Collaboration "Hybrid Measurement of the Energy Spectrum and Composition of Ultra-High Energy Cosmic Rays by the Telescope Array" *PoS ICRC2017* (2017), p. 515 DOI: <https://doi.org/10.22323/1.301.0515>.
- [28] W. Hanlon "Telescope Array Hybrid Composition and Auger-TA Composition Comparison" *EPJ Web Conf.* 208 (2019), p. 02001 DOI: [10.1051/epjconf/201920802001](https://doi.org/10.1051/epjconf/201920802001).
- [29] H. Pandya, IceCube Collaboration "A Composition Sensitive Log-Likelihood Ratio for Cosmic Rays and Gamma Rays" *PoS ICRC2017* (2018), p. 514 DOI: [10.22323/1.301.0514](https://doi.org/10.22323/1.301.0514).
- [30] T. K. Gaisser and A. M. Hillas "Reliability of the method of constant intensity cuts for reconstructing the average development of vertical showers" *International Cosmic Ray Conference* vol. 8 International Cosmic Ray Conference 1977, pp. 353–357.
- [31] D. Heck et al. *CORSIKA: a Monte Carlo code to simulate extensive air showers*. Feb. 1998.
- [32] A. Balagopal V. "A Quest for PeVatrons Employing Radio Detection of Extensive Air Showers" PhD thesis Karlsruher Institut für Technologie (KIT), 2019 129 pp. DOI: [10.5445/IR/1000091377](https://doi.org/10.5445/IR/1000091377).
- [33] A. Haungs et al. "The KASCADE Cosmic-ray Data Centre KCDC: Granting Open Access to Astroparticle Physics Research Data" *Eur. Phys. J.* C78.9 (2018), p. 741 DOI: [10.1140/epjc/s10052-018-6221-2](https://doi.org/10.1140/epjc/s10052-018-6221-2).
- [34] A. Aab et al., The Pierre Auger Collaboration "Prototype muon detectors for the AMIGA component of the Pierre Auger Observatory" *JINST* 11.02 (2016), P02012 DOI: [10.1088/1748-0221/11/02/P02012](https://doi.org/10.1088/1748-0221/11/02/P02012).
- [35] S. Berezhnev "The Tunka-133 EAS Cherenkov light array: Status of 2011" *Nuclear Instruments and Methods in Physics Research A* 692 (2012), pp. 98–105 DOI: [10.1016/j.nima.2011.12.091](https://doi.org/10.1016/j.nima.2011.12.091).
- [36] M. Mostafa, The Pierre Auger Collaboration "Hybrid Detection of UHECR with the Pierre Auger Observatory" *Vulcano Workshop 2006: Frontier Objects in Astrophysics and Particle Physics Vulcano, Italy, May 22-27, 2006* 2006.
- [37] R. U. Abbasi "Study of Ultra-High Energy Cosmic Ray composition using Telescope Array's Middle Drum detector and surface array in hybrid mode" *Astropart. Phys.* 64 (2015), pp. 49–62 DOI: [10.1016/j.astropartphys.2014.11.004](https://doi.org/10.1016/j.astropartphys.2014.11.004).
- [38] G. A. Askar'yan "Excess negative charge of an electron-photon shower and its coherent radio emission" *Sov. Phys. JETP* 14.2 (1962) [*Zh. Eksp. Teor. Fiz.*41,616(1961)], pp. 441–443.

- [39] J. V. Jelley et al. "Radio Pulses from Extensive Cosmic-Ray Air Showers" *Nature* 205.4969 (1965), pp. 327–328 ISSN: 1476-4687 DOI: 10.1038/205327a0.
- [40] H. Schoorlemmer "Tuning in on cosmic rays. Polarization of radio signals from air showers as a probe of emission mechanisms" PhD thesis Nijmegen U., 2012.
- [41] F. G. Schröder "Radio detection of Cosmic-Ray Air Showers and High-Energy Neutrinos" *Prog. Part. Nucl. Phys.* 93 (2017), pp. 1–68 DOI: 10.1016/j.ppnp.2016.12.002.
- [42] T. Huege "Radio detection of cosmic ray air showers in the digital era" *Phys. Rept.* 620 (2016), pp. 1–52 DOI: 10.1016/j.physrep.2016.02.001.
- [43] T. Huege, M. Ludwig, and C. W. James "Simulating radio emission from air showers with CoREAS" *AIP Conf. Proc.* 1535.1 (2013), p. 128 DOI: 10.1063/1.4807534.
- [44] A. Balagopal V. et al. "Search for PeVatrons at the Galactic Center using a radio air-shower array at the South Pole" *Eur. Phys. J. C* 78.2 (2018), p. 111 DOI: 10.1140/epjc/s10052-018-5537-2.
- [45] A. Aab, The Pierre-Auger Collaboration "Measurement of the Radiation Energy in the Radio Signal of Extensive Air Showers as a Universal Estimator of Cosmic-Ray Energy" *Phys. Rev. Lett.* 116 (24 2016), p. 241101 DOI: 10.1103/PhysRevLett.116.241101.
- [46] W. D. Apel et al., Tunka-Rex, LOPES Collaborations "A comparison of the cosmic-ray energy scales of Tunka-133 and KASCADE-Grande via their radio extensions Tunka-Rex and LOPES" *Phys. Lett. B* 763 (2016), pp. 179–185 DOI: 10.1016/j.physletb.2016.10.031.
- [47] E. M. Holt, F. G. Schröder, and A. Haungs "Enhancing the cosmic-ray mass sensitivity of air-shower arrays by combining radio and muon detectors" *Eur. Phys. J. C* 79.5 (2019), p. 371 DOI: 10.1140/epjc/s10052-019-6859-4.
- [48] M. G. Aartsen et al., IceCube Collaboration "Atmospheric and astrophysical neutrinos above 1 TeV interacting in IceCube" *Phys. Rev. D* 91.2 (2015), p. 022001 DOI: 10.1103/PhysRevD.91.022001.
- [49] M. G. Aartsen et al., IceCube Collaboration "First observation of PeV-energy neutrinos with IceCube" *Phys. Rev. Lett.* 111 (2013), p. 021103 DOI: 10.1103/PhysRevLett.111.021103.
- [50] R. Abbasi "IceTop: The surface component of IceCube. The IceCube Collaboration" *Nuclear Instruments and Methods in Physics Research A* 700 (2013), pp. 188–220 DOI: 10.1016/j.nima.2012.10.067.
- [51] R. Abbasi et al., IceCube Collaboration "The IceCube Data Acquisition System: Signal Capture, Digitization, and Timestamping" *Nucl. Instrum. Meth. A* 601 (2009), pp. 294–316 DOI: 10.1016/j.nima.2009.01.001.

- [52] R. Abbasi et al., IceCube Collaboration "The Design and Performance of IceCube DeepCore" *Astropart. Phys.* 35 (2012), pp. 615–624 DOI: 10.1016/j.astropartphys.2012.01.004.
- [53] J. G. Learned and S. Pakvasa "Detecting tau-neutrino oscillations at PeV energies" *Astropart. Phys.* 3 (1995), pp. 267–274 DOI: 10.1016/0927-6505(94)00043-3.
- [54] M. G. Aartsen et al., IceCube Collaboration "Astrophysical neutrinos and cosmic rays observed by IceCube" *Adv. Space Res.* 62 (2018), pp. 2902–2930 DOI: 10.1016/j.asr.2017.05.030.
- [55] A. Ishihara, IceCube Collaboration "The IceCube Upgrade - Design and Science Goals" International Cosmic Ray Conference 36, 1031 (2019), p. 1031.
- [56] M. G. Aartsen et al., IceCube Collaboration "IceCube-Gen2: A Vision for the Future of Neutrino Astronomy in Antarctica" (2014).
- [57] P. Allison et al., ARA Collaboration "Design and initial performance of the Askaryan Radio Array prototype EeV neutrino detector at the South Pole" *Astroparticle Physics* 35.7 (2012), pp. 457–477 DOI: 10.1016/j.astropartphys.2011.11.010.
- [58] S. W. Barwick et al., ARIANNA Collaboration "A First Search for Cosmogenic Neutrinos with the ARIANNA Hexagonal Radio Array" *Astropart. Phys.* 70 (2015), pp. 12–26 DOI: 10.1016/j.astropartphys.2015.04.002.
- [59] J. A. Aguilar et al. "The Next-Generation Radio Neutrino Observatory – Multi-Messenger Neutrino Astrophysics at Extreme Energies" (2019).
- [60] S. Klepser "Reconstruction of Extensive Air Showers and Measurement of the Cosmic Ray Energy Spectrum in the Range of 1 – 80 PeV at the South Pole" PhD thesis Humboldt-Universität zu Berlin, 2008.
- [61] IceCube Collaboration "Cosmic Ray Spectrum and Composition from PeV to EeV Using 3 Years of Data From IceTop and IceCube" *arXiv e-prints*, arXiv:1906.04317 (2019), arXiv:1906.04317.
- [62] K. Rawlins "Cosmic ray spectrum and composition from three years of IceTop and IceCube" *Journal of Physics: Conference Series* 718 (2016), p. 052033 DOI: 10.1088/1742-6596/718/5/052033.
- [63] K. Rawlins "A Function to Describe Attenuation of Cosmic Ray Air Shower Particles in Snow" Aug. 2016, p. 628 DOI: 10.22323/1.236.0628.
- [64] M. G. Aartsen et al., IceCube Collaboration "IceCube-Gen2: A Vision for the Future of Neutrino Astronomy in Antarctica" (2014).

- [65] A. Haungs "A Scintillator and Radio Enhancement of the IceCube Surface Detector Array" *European Physical Journal Web of Conferences* vol. 210 European Physical Journal Web of Conferences 2019, p. 06009 DOI: 10.1051/epjconf/201921006009.
- [66] T. Bretz et al. "A compact and light-weight refractive telescope for the observation of extensive air showers" *JINST* 13.07 (2018), P07024 DOI: 10.1088/1748-0221/13/07/P07024.
- [67] M. Schaufel, K. Andeen, and J. Auffenberg, IceCube Collaboration "IceAct, small Imaging Air Cherenkov Telescopes for IceCube" *36th International Cosmic Ray Conference (ICRC 2019) Madison, Wisconsin, USA, July 24-August 1, 2019* 2019.
- [68] S. Kunwar et al., IceCube-Gen2 Collaboration "The IceTop Scintillator Upgrade" *PoS ICRC2017* (2018), p. 401 DOI: 10.22323/1.301.0401.
- [69] A. Leszczyńska "Simulation study for the IceCube IceTop enhancement with a scintillator array" *Journal of Physics: Conference Series* 1181 (2019), p. 012076 DOI: 10.1088/1742-6596/1181/1/012076.
- [70] A. Leszczyńska and M. Plum, IceCube Collaboration "Simulation and Reconstruction Study of a Future Surface Scintillator Array at the IceCube Neutrino Observatory" *International Cosmic Ray Conference* 36, 332 (2019), p. 332.
- [71] T. Karg et al. "Introducing TAXI: a Transportable Array for eXtremely large area Instrumentation studies" *6th International Workshop on Acoustic and Radio EeV Neutrino Detection Activities (ARENA 2014) Annapolis, MD, June 9-12, 2014* (2014).
- [72] D. Tosi "Instrumentation for the Scintillator Upgrade of IceTop" Talk given at the ICASiPM.
- [73] M. Kauer et al., IceCube Collaboration "The Scintillator Upgrade of IceTop: Performance of the Prototype Array" *International Cosmic Ray Conference* 36, 309 (2019), p. 309.
- [74] F. G. Schroeder, IceCube Collaboration "Science Case of a Scintillator and Radio Surface Array at IceCube" *International Cosmic Ray Conference* 36, 418 (2019), p. 418.
- [75] S. Böser and IceCube Collaboration "A Radio Air-Shower Test Array (RASTA) for IceCube" *Nuclear Instruments and Methods in Physics Research A* 662 (2012), S66–S68 DOI: 10.1016/j.nima.2010.11.164.
- [76] E. de Lera Acedo et al. "Evolution of SKALA (SKALA-2), the log-periodic array antenna for the SKA-low instrument" *2015 International Conference on Electromagnetics in Advanced Applications (ICEAA)* (2015), pp. 839–843 DOI: 10.1109/ICEAA.2015.7297231.

- [77] J. Auffenberg, IceCube-Gen2 Collaboration "IceAct: Imaging Air Cherenkov Telescopes with SiPMs at the South Pole for IceCube-Gen2" *PoS ICRC2017* (2018), p. 1055 DOI: 10.22323/1.301.1055.
- [78] L. Nellen "The observation of a muon deficit in simulations from data of the Pierre Auger Observatory" *Journal of Physics: Conference Series* 409 (2013), p. 012107 DOI: 10.1088/1742-6596/409/1/012107.
- [79] H. P. Dembinski et al. "Report on Tests and Measurements of Hadronic Interaction Properties with Air Showers" *EPJ Web Conf.* 210 (2019), p. 02004 DOI: 10.1051/epjconf/201921002004.
- [80] C. E. Shannon "Communication in the Presence of Noise" *Proceedings of the IRE* 37.1 (1949), pp. 10–21 DOI: 10.1109/JRPROC.1949.232969.
- [81] S. Ritt "Design and performance of the 6 GHz waveform digitizing chip DRS4" *2008 IEEE Nuclear Science Symposium Conference Record* 2008, pp. 1512–1515 DOI: 10.1109/NSSMIC.2008.4774700.
- [82] E. de Lera Acedo et al. "SKALA, a log-periodic array antenna for the SKA-low instrument: design, simulations, tests and system considerations" *Experimental Astronomy* 39.3 (2015), pp. 567–594 ISSN: 1572-9508 DOI: 10.1007/s10686-015-9439-0.
- [83] M. Weyrauch "Preparative Measurements for the Installation of a Radio Array at the South Pole" Bachelor thesis Karlsruhe Institut of Technology, Oct. 2018.
- [84] R. Šmída et al. "First Experimental Characterization of Microwave Emission from Cosmic Ray Air Showers" *Phys. Rev. Lett.* 113.22 (2014), p. 221101 DOI: 10.1103/PhysRevLett.113.221101.
- [85] R. Hiller et al., Tunka-Rex Collaboration "The Tunka-Rex antenna station" *Proceedings, 33rd International Cosmic Ray Conference (ICRC2013): Rio de Janeiro, Brazil, July 2-9, 2013* 2013, p. 1278.
- [86] A. Rehman "private communication" University of Delaware.
- [87] V. Lenok et al. "Current Status and New Challenges of The Tunka Radio Extension" *Journal of Physics Conference Series* vol. 1181 *Journal of Physics Conference Series* 2019, p. 012027 DOI: 10.1088/1742-6596/1181/1/012027.
- [88] B. Pont "A Large Radio Detector at the Pierre Auger Observatory - Measuring the Properties of Cosmic Rays up to the Highest Energies" *36th International Cosmic Ray Conference (ICRC2019)* vol. 36 *International Cosmic Ray Conference* July 2019, p. 395.
- [89] E. de Lera Acedo et al. "Spectral performance of SKA Log-periodic Antennas I: mitigating spectral artefacts in SKA1-LOW 21 cm cosmology experiments" *Monthly Notices of the Royal Astronomical Society* 469.3 (2017), pp. 2662–2671 DOI: 10.1093/mnras/stx904.

- [90] R. Hiller "Radio measurements for determining the energy scale of cosmic rays" PhD thesis Karlsruhe Institut für Technologie (KIT), 2016 DOI: 10.5445/IR/1000053456.
- [91] TriQuint Semiconductor, Inc "Datasheet TQP3M9039" <https://www.qorvo.com/products/d/da005565> 2015.
- [92] T. Huber "Development of a scintillation particle detector for the IceCube experiment" to be published PhD thesis Karlsruhe Institut of Technology, 2020.
- [93] A. Schneider "Software development and data analysis Mini-KASCADE" Bachelor thesis Karlsruhe Institut of Technology, 2017.
- [94] E. Raspopin "Calibration of the ADCs and discriminator threshold of the IceTAXI data acquisition system" Bachelor thesis Karlsruhe Institut of Technology, Oct. 2018.
- [95] S. Martinelli "Master thesis in preparation" Master thesis University of Turin, 2019.
- [96] T Antoni et al., KASCADE Collaboration "The Cosmic ray experiment KASCADE" *Nucl. Instrum. Meth.* A513 (2003), pp. 490–510 DOI: 10.1016/S0168-9002(03)02076-X.
- [97] U. Raidt "Setup of the Trigger and Timing Facility of the KASCADE Central Detector and Investigation of Muon Arrival Times in Extended Air Showers" *Wissenschaftliche Berichte FZKA* 5917 1997.
- [98] Karlsruhe Institute of Technology "KASCADE / KASCADE-Grande Homepage".
- [99] T. Huege et al., LOPES Collaboration "The LOPES experiment - Recent results, status and perspectives" *Nuclear instruments & methods in physics research / A* 662.SUPPL. 1 (2012), S72–S79 ISSN: 0168-9002, 1872-9576 DOI: 10.1016/j.nima.2010.11.081.
- [100] A. Horneffer "Measuring Radio Emission from Cosmic Ray Air Showers with a Digital Radio Telescope" PhD thesis Rheinischen Friedrich-Willhelms-Universität Bonn, 2006.
- [101] P. Steinmüller "Development of radio front-end electronics for a prototype radio station at the South Pole" Master thesis Karlsruhe Institut of Technology, 2019.
- [102] Texas Instruments "Datasheet THS4508" <http://www.ti.com/lit/gpn/ths4508> 2008.
- [103] Peregrine Semiconductor "Datasheet PE4251" <https://www.psemi.com/pdf/datasheets/pe4251ds.pdf> 2019.
- [104] Texas Instruments "TINA-TI circuit simulation software" <http://www.ti.com/tool/TINA-TI> 2019.

- [105] N. Goehlke "Design of an amplifier circuit for the radio front-end electronics of the IceTop radio extension" Bachelor thesis, to be published Karlsruhe Institut of Technology, 2019.
- [106] Mini-Circuits "Typical Performance Data SXHP-48+" https://www.minicircuits.com/pages/s-params/SXHP-48+_VIEW.pdf.
- [107] Mini-Circuits "Typical Performance Data ULP-340+" https://www.minicircuits.com/pages/s-params/ULP-340+_VIEW.pdf.
- [108] Analog Devices "Datasheet ADA4927" https://www.analog.com/media/en/technical-documentation/data-sheets/ADA4927-1_4927-2.pdf 2016.
- [109] L. Lu "Private communication" Chiba University, Deployment helper season 2018–19.
- [110] B. Eberhardt and K. Mallot "Private communication" IceCube Winterover season 2018–19.
- [111] M. A. Lazzara et al. "Fifty-year Amundsen–Scott South Pole station surface climatology" *Atmospheric Research* 118 (2012), pp. 240–259 ISSN: 0169-8095 DOI: <https://doi.org/10.1016/j.atmosres.2012.06.027>.
- [112] International Telecommunication Union "Recommendation ITU-R P.372-12" <https://www.itu.int/rec/R-REC-P.372-12-201507-S/en> 2015.
- [113] J. Auffenberg et al. "A radio air shower surface detector as an extension for IceCube and IceTop" *Nucl. Instrum. Meth. A* 604 (2009), S53–S56 DOI: 10.1016/j.nima.2009.03.179.
- [114] J. Auffenberg et al. "A radio air shower surface detector as an extension for IceCube and IceTop" *Nucl. Instrum. Meth. A* 604 (2009), S53–S56 DOI: 10.1016/j.nima.2009.03.179.
- [115] S. B. ARA, IceCube Collaborations "Prospects for a radio air-shower detector at the South Pole" *AIP Conference Proceedings* 1535.1 (2013), pp. 116–120 DOI: 10.1063/1.4807532.
- [116] D. C. Price "PyGSM: Python interface to the Global Sky Model" 2016.
- [117] H. V. Cane "Spectra of the non-thermal radio radiation from the galactic polar regions" *Monthly Notices of the Royal Astronomical Society* 189 (Nov. 1979), pp. 465–478 DOI: 10.1093/mnras/189.3.465.
- [118] B. Rhodes DOI: <https://rhodesmill.org/skyfield/>.
- [119] Teseq GmbH "Datasheet RSG1000" <https://www.teseq.de/produkte/RSG-1000.php> 2011.